Experimental and numerical study of deep foundations under seismic loading: vertical piles and inclined piles

Zheng Li

l'université nantes angers le mans

PÔLE DE RECHERCHE ET D'ENSEIGNEMENT SUPÉRIEUR

Centrale Nantes

Thèse de Doctorat

Zheng LI

Mémoire présenté en vue de l'obtention du
grade de Docteur de l'Ecole Centrale de Nantes
sous le label de L'Université Nantes Angers Le Mans

École doctorale : **S**ciences **P**our l'**I**ngénieur, **G**éosciences, **A**rchitecture

Discipline : Génie civil
Unité de recherche : GeM - UMR CNRS 6183

Soutenue le 24 janvier 2014

ÉTUDE EXPÉRIMENTALE ET NUMÉRIQUE DE FONDATIONS PROFONDES SOUS SOLLICITATIONS SISMIQUES : PIEUX VERTICAUX ET PIEUX INCLINÉS

JURY

Président :	**Claudio TAMAGNINI,**	Professeur,	Professeur des Universités, Università degli Studi di Perugia
Rapporteurs :	**Claudio TAMAGNINI,**	Professeur,	Professeur des Universités, Università degli Studi di Perugia
	Ioannis ANASTASOPOULOS,	Professeur,	Professeur des Universités, University of Dundee
Examinateurs :	**Alain PECKER,**	Professeur	President of Géodynamique et Structure
	Jean-François SEMBLAT	Chercheur	ICTPE-chercheur IFSTTAR
	Stéphane GRANGE	Maître de conférences	Université Joseph Fourier
Directeur :	**Panagiotis KOTRONIS**,	Professeur,	Ecole Centrale de Nantes
	Sandra ESCOFFIER,	Chercheur	IFSTTAR, Nantes

l'université nantes angers le mans
PÔLE DE RECHERCHE ET D'ENSEIGNEMENT SUPÉRIEUR

Centrale Nantes

Thèse de Doctorat

Zheng Li

ÉTUDE EXPÉRIMENTALE ET NUMÉRIQUE DE FONDATIONS PROFONDES SOUS SOLLICITATIONS SISMIQUES : PIEUX VERTICAUX ET PIEUX INCLINÉS

Experimental and numerical study of deep foundations under seismic loading: vertical piles and inclined piles

Résumé

En génie civil, les pieux inclinés sont souvent utilisés quand une importante résistance latérale est nécessaire. Cependant, de nombreux codes du dimensionnement (e.g. AFPS 1990, Eurocode 8) - ne recommandent pas leur utilisation pour des régions sismiques. Néanmoins, de plus en plus de récentes études font état d'un meilleur comportement. Gazetas et Mylonakis (1998) affirment que les pieux inclinés, si ils sont bien dimensionnés, jouent un rôle bénéfique pour la structure et les fondations. Pender (1993) and Berrill et al. (2001) rapportent aussi les effets bénéfiques de l'utilisation des pieux inclinés. La question de savoir si l'utilisation de pieux inclinés dans des zones sismiques est bénéfique est donc encore ouverte. Avoir recours à des méthodes de dimensionnement basées sur les déplacements et aux outils numériques avancés peut contribuer à une meilleure résistance sismique et à une réduction significative de coût des projets.

Dans cette thèse, la performance des pieux verticaux et inclinés est étudiée avec une approche couplant l'expérimental est le numérique. Des essais dynamiques en centrifugeuse géotechnique sont effectués afin de reproduire et quantifier le comportement des structures sur des pieux verticaux ou inclinés. Des équations empiriques sont proposées pour prendre en compte la diminution de la rigidité du sol et l'amortissement associé ainsi qu'une nouvelle loi hypoplastique pour des chargements cycliques. Des calculs éléments finis sont effectués pour obtenir la forme de la surface de rupture d'un pieu ou un système de pieux et enfin un nouveau macro-élément hypoplastique est développé est validé à partir des résultats expérimentaux.

Mots clés
Interaction sol structure, pieux, macro-élément, centrifugeuse, fondations.

Abstract

Inclined piles, also called batter piles or raked piles, are widely used in civil engineering constructions when a substantial lateral resistance is required. However, nowadays many design codes or national standards like AFPS 1990 and Eurocode-8 do not recommend using inclined piles in seismic regions. As reported by Gazetas and Mylonakis (1998), inclined piles, if properly designed, can be beneficial rather than detrimental both for the structure they support but also for the piles themselves. Pender (1993) and Berrill et al. (2001) suggest also significant beneficial effects from the use of inclined piles. The argument about whether the use of inclined piles is detrimental or beneficial is therefore still unsettled. Using displacement based design and advanced analytical tools inclined piles may result in better earthquake resistance and significant project savings.

In this Ph.D, the performance of vertical and inclined piles is studied using both experiments and finite element calculations. A series of dynamic centrifuge tests are performed to reproduce and quantify the behavior of structures rested on vertical or inclined piles. Empirical equations are introduced to calculate the soil stiffness degradation and the associated hysteresis damping and a new hypoplastic constitutive law is proposed, suitable for cyclic loadings. Numerical finite element studies are carried out in order to obtain the failure envelope for a single pile and a system of pile foundations and finally a novel hypoplastic macro-element is developed and validated using the experimental data.

Key Words
Soil structure interaction, piles, macro-element, centrifuge, foundations.

Acknowledgments

The author would like to express his sincere thanks to all the people who I worded with during this Ph.D period, without them the research could not be accomplished. **Dr. Sandra ESCOFFIER**, as the supervisor of the Ph.D study in the past three years, did do a lot of effort in improving my knowledge and academic ability in field of geotechnical earthquake engineering. Her excellent academic attitude and kind personality are greatly appreciated.

Prof. Panagiotis KOTRONIS is also my supervisor of my Ph.d study. I am greatly indebted to for his continuous help and strong support throughout this research. His wealth of ideas has enriched this dissertation and is highly appreciated.

The two supervisors of mine provided me great freedom to let me diving into the sea of research and think freely. Words are not enough to express my gratitude.

Dr. Jean-Louis CHAZELAS is greatly acknowledged by the author for his charming personalities. It is a great pleasure to work with him in the past three years. He is like a mentor, a leader and even a family member.

I am also extremely grateful to **Prof. Claudio Tamagnini** for his assistance and valuable input to various aspects of this dissertation.

I would also like to acknowledge the valuable inspirations from **Dr. Stéphane Grange**.

The help form other researchers in the centrifuge team (Dr. Luc Thorel, Dr. Matthieu Blanc and Dr. Alberto Bretscheider) were also sincerely acknowledged by the author.

The help from all the technicians in the centrifuge team are greatly acknowledged. There were many lovely stories in my memory, I will remember them forever. Patrick GAUDICHEAU, Philippe AUDRAIN, Damien MACE, Claude FAVRAUD, Alain NEEL and Stéphane LERAT, YOU ARE THE BEST EVER !

The author's best Chinese friend, Zhao SONG, who has impressive talents in computer languages and numerical methods is greatly acknowledged. Raphaël Valensi who is a master of surface wave inversion and Jazz music, or perhaps a philosopher, helped the author in the pursuing the science and the true value of the life.

Kisses to my parents and sister for their love and supports to my study abroad of CHINA. No matter where am I, rich or poor, young or old, I am your son.

Contents

List of Figures

List of Tables

Chapter 1

Research Objectives and Motivation

1.1 Research Objectives and Motivation

Inclined piles also called as batter piles or raked piles which are widely used in civil engineering constructions where substantial lateral resistance is required. However, nowadays, many building codes or standards like AFPS 1990 [21] and Eurocode-8 [22] do not recommend using inclined piles in seismic region. To be less conservative, the codes like ACI318-05 and ACI318-11 for example, although it is not absolutely prohibited to use inclined pile in earthquake-resistant structures, the potential damages at the junction of inclined piles and buildings that caused by the large forces during the earthquake are called for attentions. The main drawbacks concluded by engineers are following: large forces induced onto the pile cap, reduction in bending capacity due to the induced tensile forces, unfavorable rotation on the cap and the additional bending moment due to the settlement of soil before the earthquake [23]. Some field evidences like the failure of the wharf in the port of Okland in 1989, Loma Prieta earthquake and the port of Los Angeles during Nothridge earthquake in 1994 reveals the unsatisfactory performance of inclined piles.

However, more and more recent studies show the positive performance of inclined piles. As it was reported by Gazetas and Mylonakis [24], the inclined piles, if properly designed, could be beneficial rather than detrimental both for the structure they support and the also the piles themselves. Also studies from Pender [25] and Berrill et al. [8] suggest important beneficial effects regarding the use of inclined piles. The argument about whether the usage of inclined piles is detrimental or beneficial is still unsettled. In 2004, Harn [26] pointed out that the poor performance of inclined piles in the past earthquakes may due to the lack of knowledge and analytical tools which are available today. Under some circumstances, the use of inclined piles is desirable and favorable. Using displacement based design with carefully-detailed inclined piles may result in a significant project savings.

Giannakou et al. [9, 27] studied numerically, in the time domain, the performance of batter piles. Linear constitutive laws were assumed for the soil and the inclined pile groups. Five different inclinations were considered. The authors found that for seismic loadings and purely kinematic conditions, the negative reputation of batter piles was more-or-less confirmed. When the total response was considered however (kinematic and inertial response of the structural system founded on groups of batter piles), their influence could be beneficial. Among other parameters, their

contribution depends on the ratio of the overturning moment versus the shear force transmitted to the piles from the superstructure. This Ph.D study originally initiated from the numerical study of Giannakou et al. [9, 27]. The main task for the experimental part of the study in this dissertation is to clarify the performance of inclined piles under dynamic excitations with seismic soil-pile-superstructure interaction (SSPSI); and the influences of the gravity center of superstructure and base shaking will be highlighted by experimental parametric studies.

For the numerical aspects, 3D FEM studies of the behavior of both inclined and vertical pile groups were carried out. By using a simple hypoplastic model, the behavior of pile groups can be well captured and reproduced by the FEM model. Then based on the successfully calibrated FEM model, a hypoplastic macro-element model was finally developed. The performance of the newly developed macro-element for pile foundations is satisfactory.

1.1.1 Outline of the dissertation

- **Chapter 1**: the main objectives and motivations of this Ph.D study are presented.
- **Chapter 2** presents the literature review of existing studies on the performance of pile foundations. Although many post-earthquake observations indicate poor performance of inclined piles, in recent years, evidence has been accumulating that, under certain conditions, inclined piles may be beneficial rather than detrimental for both the structure they support and the piles themselves. Existing experimental and numerical studies for investigating the performance of inclined piles are reviewed. The seismic soil-pile-superstructure interaction of inclined piles has still not been well clarified. In addition, fast and robust numerical tools for analyzing the soil-structure interaction of pile foundations are still in lack.
- **Chapter 3**: In this chapter, the dynamic centrifuge tests based on free field conditions were performed in order to identify the Fontainebleau sand properties. A substantial amount of sensors was used to capture the response of the centrifuge model. A post processing strategy was proposed (with less dispersion compared to previous studies) based on the definition of average loops and the evolution of the shear modulus and the damping ratio was quantified. Empirical equations from the literature were validated and specific regressed numerical values are proposed for the Fontaineblau sand. It is found that confining pressure has an important influence on both the shear modulus evolution and the damping ratio. A low pressure confined sand tends to have a larger damping ratio and a greater shear modulus reduction. The high confining pressure tends to enlarge the elastic range of sand.
- **Chapter 4** presents the experimental study of the performance of inclined piles. In terms of residual bending moment, inclined piles still have poor performance compared with the vertical piles. However, with the presence of

inclined piles, compared with the vertical piles, the performance of inclined piles have been changed from detrimental to beneficial. For the same type of building (either short or tall), inclined piles have less or equal stresses to the vertical piles. It could also be observed that contrary to the vertical piles, inclined piles are less sensitive to the variation of gravity center of the superstructures which they support. For both inclined and vertical configurations, increase the gravity center will induce higher axial force in piles. However, in terms of bending moment, higher gravity center may have beneficial effect on the performance for both inclined and vertical piles. It is found that vertical piles are much more sensitive to the variation of the center of mass of the superstructures. A high gravity center of the superstructure may mitigate the detrimental performance induced by short superstructure. In terms of the rocking behavior, the presence of the inclined piles increases the rotational damping ratio without losing so much the rotational stiffness; for the horizontal translation behavior, compared with vertical pile foundation, the inclined one have greatly larger horizontal stiffness than the vertical one, while keeps almost the same dissipation ability as the vertical pile foundation. The results from a relatively large number of tests show that, the behavior of the pile foundation system is frequency in-dependent, and the influences from the gravity center could be ignored.

- **Chapter 5** mainly presents the 3D FEM modeling of the soil-pile-superstructure system. A simple constitutive of sand which incorporates the concept of hypoplasticity was introduced. By comparing the results from numerical simulations with experimental data, it can be concluded that, the FEM model can successfully capture the behavior of the soil-pile-superstructure system, which provide strong support in developing macro-element for pile foundations.

- **Chapter 6**: Based on the successful calibrated FEM model, the failure surfaces of single piles pile groups were investigated by using numerical radial displacement tests. With the identified failure surface, the macro-element for deep foundation was built-up with in the framework of hypoplasticity theory. After calibration, the macro-element can be applied successfully to predict the behavior of pile foundations. The results from the proposed macro-element have good agreement with the experimental data.

- **Chapter 7** presents the challenging aspects and perspectives of this study in the future.

Introduction générale

Les pieux inclinés sont fréquemment utilisés dans les constructions de génie civil pour lesquelles une résistance latérale non négligeable est nécessaire. Cependant, de nos jours, de nombreux codes ou standards, comme l'AFPS 1990 [21] et l'Eurocode-8 [22] ne recommandent pas l'utilisation des pieux inclinés en zone sismique. Pour certains codes moins conservatifs, comme par exemple l'ACI318-05 et l'ACI318-11, il est indiqué que bien que l'utilisation de pieux inclinés pour des structures soumises à des séismes ne soit pas interdite, une attention particulière doit être portée sur les dommages potentiels qui peuvent survenir au niveau de la jonction entre les têtes des pieux inclinés et les bàtiments du fait des importantes forces qui peuvent se dêvelopper lors d'un séisme. Les principaux désavantages cités par les ingénieurs sont les suivants: les importantes forces induites au niveau du chevêtre, la réduction de la capacité portante induite par les forces axiales, la rotation dêfavorable au niveau du chevêtre et le moment fléchissant additionnel dû au tassement du sol avant sêisme [23]. Certains retours d'expérience sur site, comme la rupture d'un quai dans le port d'Okland en 1989 (séisme de Loma Prieta) ainsi que celle dans le port de Los Angeles durant le séisme de Nothridge en 1994 mettent en évidence les mauvaises performances des pieux inclinés.

Cependant, de plus en plus d'études récentes illustrent le comportement favorable des pieux inclinés. Gazetas and Mylonakis [24] indiquent que les pieux inclinés, s'ils sont correctement dimensionnés, peuvent avoir un comportement bénéfique plutôt que défavorable à la fois pour la structure qu'ils soutiennent et pour les pieux eux-mêmes. De plus, des études menées par Pender [25] et Berrill et al. [8] suggèrent un effet bénéfique non négligeable de leur utilisation. L'effet bénéfique ou néfaste de l'utilisation de pieux inclinés n'est pas par conséquent encore clairement établit. Harn [26], en 2004, a mis en avant que leur mauvaise performance durant des séismes antérieurs est peut être due à un manque actuel de connaissances et d'outils analytiques et/ou numériques. Dans certaines circonstances l'utilisation de pieux inclinés est désirable et favorable: l'utilisation de méthodes de dimensionnement basées sur les déplacements couplées avec des outils numériques performants peut conduire à des économies de projet significatives.

Giannakou et al. [9,27] ont étudié numériquement, dans le domaine temporel, la performance des pieux inclinés. Des lois constitutives linéaires ont été utilisées pour le sol et les groupes de pieux. Cinq inclinaisons différentes ont été considérées. Les auteurs ont mis en avant que sous l'effet d'un chargement sismique d'origine purement cinématique, le comportement des pieux inclinés a tendance à confirmer leur mauvaise réputation. Lorsque la réponse sismique globale est considérée (réponse cinématique et inertielle de la structure fondée sur des groupes de pieux inclinés), leur présence peut être bénéfique. Parmi les autres paramètres également testés, la contribution des pieux inclinés dépend du rapport entre le moment de renversement et la force de cisaillement transmise par la superstructure aux pieux.

Ce travail comporte trois parties principales:

Cette thèse a été initiée suite aux résultats numériques obtenus par Giannakou et al. [9,27]. L'objectif principal de la partie expérimentale (essais dynamiques centrifugés) présentée dans ce manuscrit est de clarifier les performances des pieux inclinés sous sollicitation sismique dans le cadre de l'interaction sol-pieu-superstructure; de plus, l'influence du centre de gravité de la superstructure et de la sollicitation sont également abordés dans le cadre d'une étude paramétrique. La campagne expérimentale a été réalisée en plusieurs étapes. Dans un premier temps, afin d'améliorer la compréhension du comportement du système sol-pieux-superstructure, les propriétés dynamiques du sable de Fontainebleau ont été déterminées à l'aide d'une série d'essais en champs libre en centrifugeuse. Dans ce cadre, une nouvelle méthode simple et robuste, permettant d'obtenir la courbe de dégradation du module de cisaillement et de l'amortissement matériel associé, est introduite. En considérant les expressions proposées par Ishibashi and Zhang [28], des valeurs des paramètres de régression ont été identifiées pour le sable de Fontainebleau et l'influence de la pression de confinement sur les courbes de régression du module de cisaillement a été prise en compte. La courbe de dégradation du module de cisaillement ainsi identifiée est utilisée pour la calibration d'une loi constitutive hypoplastique simple utilisée dans le cadre d'une modélisation par éléments finis. La méthode proposée pour traiter les boucles d'hystérésis obtenues est également utilisée dans le second chapitre pour l'analyse du comportement en basculement et en translation des fondations profondes.

Dans un second temps, en se basant sur les résultats numériques obtenus par Giannakou et al. (voir chapitre 2), une nouvelle séries d'essais en centrifugeuse a été réalisée. Dans ce cadre deux structures, une de faible et une de fort élancement, ont été dimensionnées afin d'étudier l'influence du chargement inertiel provenant de différents types de structures sur la performance des pieux inclinés. La structure massive (faible élancement) représente un cas de chargement dominé par une force de cisaillement alors que la structure élancée représente un cas de chargement dominé par une force de basculement. Une configuration symétrique de 1×2 pieux inclinés de $15°$ par rapport à la verticale est adoptée et les résultats obtenus sont comparés avec ceux obtenus sur un groupe 1×2 de pieux verticaux. Pour les deux configurations, une connexion rigide est imposée au niveau de la tête des pieux au travers de l'utilisation d'un chevêtre massif. Les différences de comportement sous sollicitations sismiques des deux configurations de groupe de pieux sont analysées et discutées. Dans le cadre de cette étude, tous les essais ont été réalisés à 40g. Deux types de sollicitations ont été considérés : des séismes et des sollicitations sinusoïdales. L'objectif du premier type de tests (séismes) était de mettre en évidence la performance des pieux inclinés pour un chargement multi fréquentiel, dans le cas du second type de tests (sollicitation sinusoïdales) les objectifs étaient de mettre en évidence, ou non, l'influence de différents paramètres, sur la performance des pieux inclinés. L'effet de la hauteur du centre de gravité de la structure sur le comportement des pieux inclinés a été également dans les deux cas étudié.

Dans un premier temps des tests avec un séisme réel ont été réalisés sur les deux groupes de pieux sans superstructure et ensuite avec les deux superstructures (superstructures massive et élancée). En se basant sur les résultats obtenus au cours de ces tests, la hauteur du centre de gravité de la structure élancée a été multipliée par deux pour les essais réalisés avec une sollicitation sinusoïdale afin de mettre en évidence son effet sur la performance des pieux inclinés. Les différentes configurations utilisées dans les essais dynamiques centrifugés sont présentées sur la Fig. 4.1 dans le cas du groupe de pieux inclinés. Pour chaque configuration, la réponse est comparée à la configuration équivalente avec pieux verticaux. La configuration groupe de pieu sans superstructure a pour objectif d'évaluer la performance des pieux inclinés dans le cas d'une interaction sol-pieux.

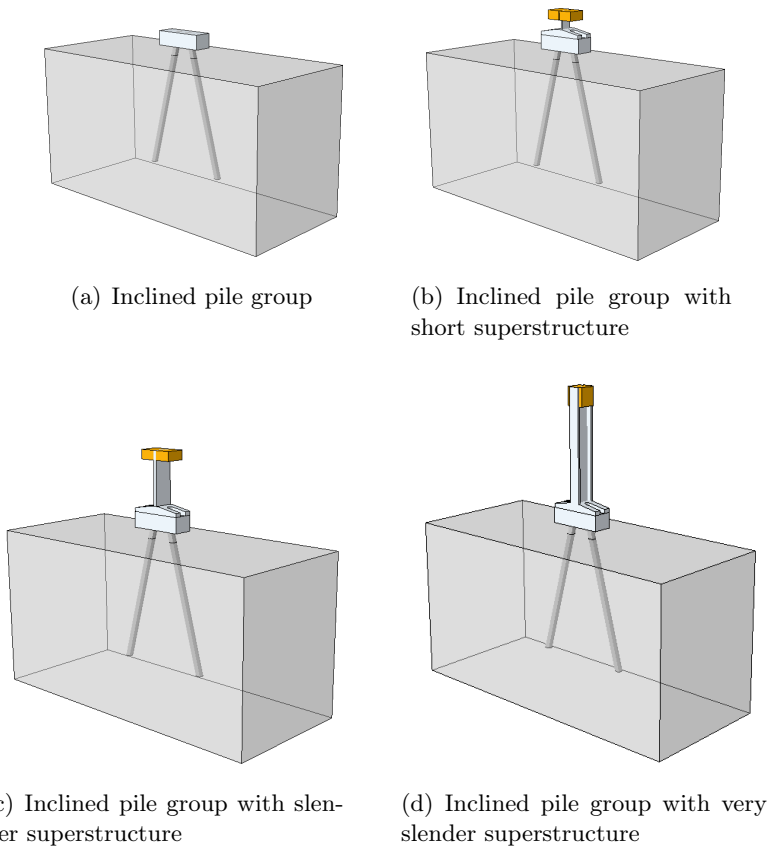

(a) Inclined pile group

(b) Inclined pile group with short superstructure

(c) Inclined pile group with slender superstructure

(d) Inclined pile group with very slender superstructure

Figure 1.1: Configurations des essais dynamiques centrifugés

Les principales conclusions sont les suivantes:

1. Par rapport au cas d'une interaction purement cinématique, la présence de la superstructure (chargement inertiel) modifie à la fois la réponse du groupe de pieux inclinés et du groupe de pieux verticaux.

2. Les superstructures fondées sur pieux inclinés ont des fréquences de réponse plus hautes. Cette augmentation est probablement due à une plus importante

rigidité horizontale introduite par les pieux inclinés. Quelle que soit la configuration du groupe de pieux (inclinée ou verticale), l'augmentation de la hauteur de centre de gravité de la superstructure diminue la fréquence de réponse.

3. La présence de pieux inclinés tend à diminuer les accélérations et les déplacements maximaux en haut de la superstructure. Pour la même superstructure, la présence de pieux inclinés réduit la rotation du chevêtre au cours des fortes sollicitations.

4. La présence de pieux inclinés a un rôle bénéfique en réduisant le chargement inertiel au niveau de la superstructure (cisaillement et moment de renversement au niveau du chevêtre). Par rapport au groupe de pieux verticaux, dans la plupart des cas, le groupe de pieux inclinés, qu'il soutienne la superstructure courte ou élancée, subit une force résultante plus faible au niveau du chevêtre. Cependant, dans le cas de forts séismes, du fait des fortes nonlinéaritées induites dans le sol, l'effet des pieux inclinés et de la hauteur du centre de gravité sont réduits.

5. Concernant les moments fléchissants résiduels, les pieux inclinés tendent à avoir de moins bonnes performances que les pieux verticaux.

6. Pour les deux configurations, groupe de pieux inclinés et groupe de pieux verticaux, une augmentation de la hauteur du centre de gravité de la superstructure induit une augmentation des forces axiales dans les pieux. Concernant les moments fléchissants, l'augmentation de la hauteur du centre de gravité semble améliorer la performance à la fois des groupes de pieux verticaux et inclinés. Il est également mis en évidence que le groupe de pieux verticaux est plus sensible à la variation de la hauteur du centre de gravité de la superstructure que le groupe de pieux inclinés.

7. Pour ce qui est du comportement en rotation, la présence de pieux inclinés augmente le coefficient d'amortissement en rotation, la raideur en rotation restant proche de celle obtenue pour le groupe de pieux verticaux. Pour ce qui est du comportement en translation, la présence de pieux inclinés augmente fortement la raideur horizontale alors que la capacité de dissipation d'énergie reste comparable à celle du groupe de pieux verticaux. Les résultats obtenus sur un nombre relativement important d'essais montent que le comportement de ces systèmes de fondations profondes est indépendant de la fréquence de sollicitation et que l'influence de la hauteur du centre de gravité peut être ignoré.

D'un point de vue numérique, une modélisation éléments finis 3D du système sol-pieux-superstructure est présentée. Une loi constitutive pour le sable, basée sur la théorie d'hypoplasticité, est introduite avec relativement peu de paramètres et dont la calibration est relativement aisée. A partir de comparaisons entre les simulations numériques et différents résultats expérimentaux, il est conclu que le modèle

éléments finis proposé rend compte de manière satisfaisante du comportement du système sol-pieu-superstructure. Par conséquent, cette stratégie de modélisation est dans la suite considérée comme un outil robuste pour l'établissement d'un macro-élément pour des pieux profonds.

En s'appuyant sur le modèle éléments finis précédemment calibré et validé par les résultats expérimentaux, un macro-élément pour des pieux verticaux dans le sable est développé. A partir de la surface limite d'un pieu isolé puis pour un groupe de pieux, établies toutes deux à l'aide du modèle éléments finis, les détails de la formulation du macro-élément sont présentés. Dans le cas des pieux inclinés, une solution approchée est également proposée. Afin de déterminer l'enveloppe de rupture 3D, des swip tests ainsi que des tests de déplacement radial ont été réalisés numériquement (comme proposé par Gottardi et al. [29] pour les fondations superficielles circulaires):

- Swipe tests: dans un premier temps un déplacement vertical est appliqué sur un pieu jusqu'à l'atteinte d'une certaine force verticale. Dans un second temps un déplacement horizontal croissant est appliqué tout en maintenant le déplacement vertical constant.
- Tests de déplacement radial: le rapport entre les incréments de déplacements ou de combinaison rotation/déplacement appliqués est maintenu constant.

L'enveloppe de rupture pour un pieu vertical isolé dans l'espace $H - M - V$ est représenté sur la Fig. 6.9. Tous les points de données numériques appartiennent à une surface 3D qui a pour surface dans le plan $H - M$ une ellipse inclinée.

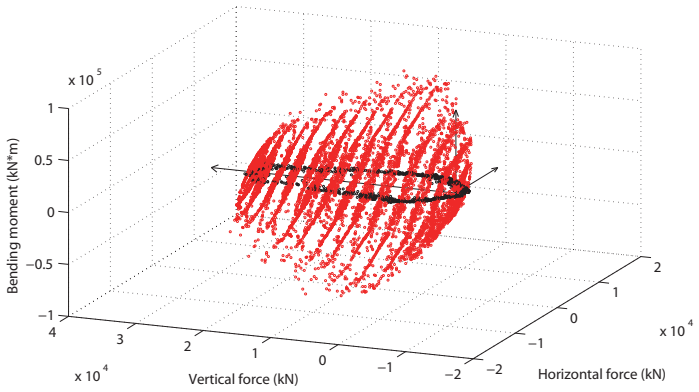

Figure 1.2: Enveloppe de rupture numérique dans l'espace H-M-V

Une équation semi-analytique est proposée pour représenter la surface de rupture 3D d'un pieu vertical isolé, voir équation (1.1); la surface 3D fournie par l'équation (1.1) est représentée sur la Fig. 1.3:

$$f = 1.0m^2 + 1.0n^2 - 1.5mn - (1 - \upsilon^2) = 0 \tag{1.1}$$

où $m = H/H_0$ est la force horizontale normalisée, $n = M/M_0$ le moment fléchissant normalisé et $v = V/V_{c0}$ ou $v = V/V_{t0}$ la force verticale normalisée (dépendant du signe de la force verticale).

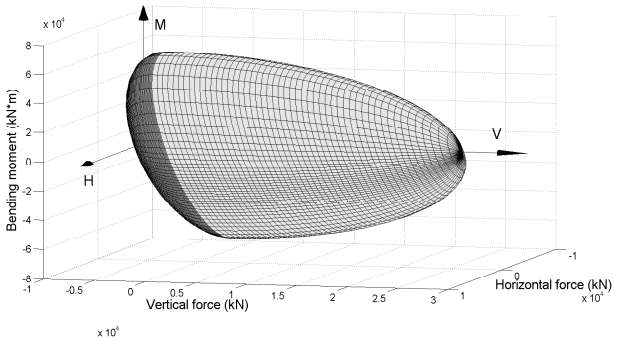

Figure 1.3: Enveloppe de rupture obtenue à partir de l'équation. (1.1)

Pour obtenir l'enveloppe de rupture du groupe de pieux verticaux la même approche a été utilisée et l'équation semi-analytique est la suivante:

$$f = \left(\frac{H}{N\mu H_0}\right)^2 + \left(\frac{M}{N\mu M_0}\right)^2 - 1.5\left(\frac{H}{N\mu H_0}\right)\left(\frac{M}{N\mu M_0}\right) - \left(1 - \left(\frac{V}{N\mu V_0}\right)^2\right) = 0 \quad (1.2)$$

où, H_0, M_0 and V_0 sont les capacités portantes ultimes pour un pieu vertical isolé, N est le nombre de pieux et μ traduit l'effet de groupe. Selon les résultats obtenus à partir des tests numériques de déplacement radial, le facteur μ pour un groupe de pieux avec 2 pieux et une distance pieu-pieu de $4D$ est d'environ 0.75; pour un espacement de $8D$, μ est approximativement égale à 1.0. En d'autres termes, l'effet de groupe peut être ignoré lorsque l'espacement entre pieux est supérieur à $8D$. Les enveloppes de rupture pour différentes configurations de groupe de pieux verticaux sont présentées sur la Fig. 1.4.

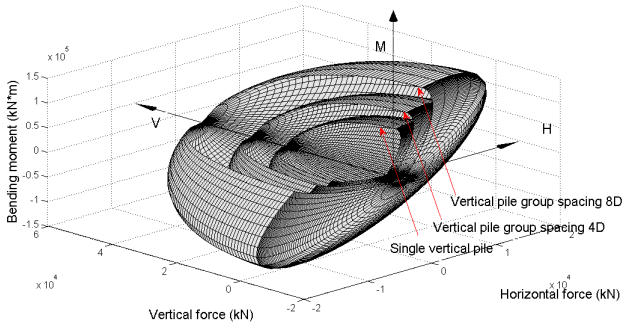

Figure 1.4: Enveloppes de rupture 3D pour des groupes de pieux verticaux avec différents espacements pieu-pieu: pieu vertical isolé, groupe de pieux verticaux avec un espacement de $4D$ et groupe de pieux verticaux avec un espacement de $8D$

Une fois les expressions semi-analytiques des enveloppes de rupture déterminées, le modèle de macro-élément est construit dans le cadre théorique de l'hypoplasticité. La structure de base du macro-élément hypoplastique est la suivante ([30] et [31]):

$$\dot{\boldsymbol{t}} = \mathcal{K}(\boldsymbol{t}, \boldsymbol{q}, \boldsymbol{d}) \tag{1.3a}$$

$$\mathcal{K} = \mathcal{L}(\boldsymbol{t}, \boldsymbol{q}) + \boldsymbol{N}(\boldsymbol{t}, \boldsymbol{q})\boldsymbol{\eta}^T \tag{1.3b}$$

$$\boldsymbol{\eta} = \frac{\boldsymbol{d}}{\|\boldsymbol{d}\|} \tag{1.3c}$$

où $\boldsymbol{d}$ est le vecteur de vitesse généralisé, $\boldsymbol{q}$ est un pseudo vecteur de variables internes qui rend compte des effets de l'histoire de chargement et $\|\|$ le symbole de norme.

Par la suite, le macro-élément est validé à l'aide des résultats expérimentaux obtenus à partir d'essais statiques et dynamiques. Quelques résultats sont présentés sur la Fig. 1.5 (chargement cyclique statique) et sur la Fig. 1.6 (chargement dynamique).

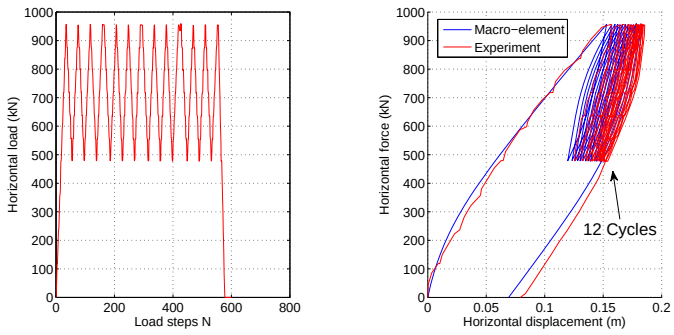

(a) (b)

Figure 1.5: Validation du macro-élément pour un pieu vertical isolé: chargement cyclique dans un sens, 12 cycles d'amplitude 480 kN (données expérimentales de Rosquët [1]): (a) chargement; (b) réponse en tête de pieu

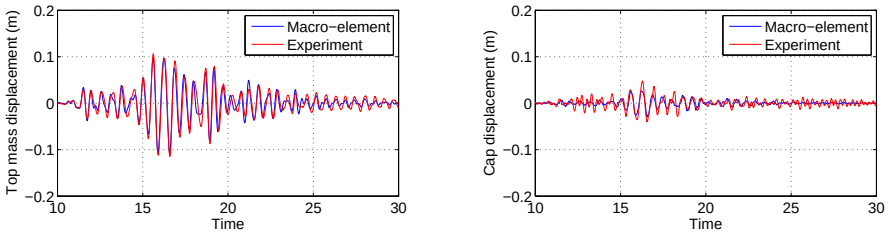

(a) (b)

Figure 1.6: Validation du macro-élément pour le groupe de pieux verticaux: groupe de pieu verticaux avec superstructure faiblement élancée soumis au séisme de Northridge -9 dB : (a) réponse au niveau de la masse surélevée; (b) réponse au niveau du chevêtre

Du fait des difficultés rencontrées pour les pieux inclinés et les groupes de pieux inclinés, une alternative a été proposée pour le développement d'un macro-élément pour un groupe de pieux inclinés. Les résultats obtenus à partir de ce macro-élément ont été comparés à ceux obtenus aux cours des essais dynamiques en centrifugeuse. Le macro-élément proposé pour les pieux inclinés permet de reproduire le comportement du groupe de 1×2 pieux inclinés, cependant des améliorations doivent être apportées.

Chapter 2

Literature review

2.1 Inclined piles in practice

Throughout most of the 20th century, inclined piles were routinely employed to carry lateral loads and to limit the lateral displacement of the foundations. Retaining walls founded upon soft soils, anchored bulk-heads, pile supported decks, breasting dolphins and bridge piers regularly employed batter piles. In fact, inclined piles were the preferred structural system for deep foundations subject to lateral loads. However and towards the end of the century, the poor performance of batter piles in a series of earthquakes discouraged engineers to use them in seismic regions. In the following section various case studies are reported, examples were inclined piles behaved either poorly or adequately.

2.1.1 Post-earthquake observations - Poor performance of inclined piles

As a general remark it can be said that inclined piles are designed to accommodate large lateral loads but they often attract forces that the pile head or the pile cap can not sustain [32].

Wharf structure, Loma Prieta Earthquake, October 1989

In 1991 in San Francisco Bay, pile damages were reported in the port facilities and marine structures. The peak ground acceleration was measured equal to 0.45 g. A lot of pile damages were observed in the wharf structures (a cross-section of a part of the wharf - 7th Street Terminal - is given in Fig. 2.1). Egan et al. [33] reported that approximately 95% of landward batter piles and roughly 50% of outboard batter piles failed from cyclic shear forces at the deck connection during the earthquake. The 7th Street Terminal suffered extensive damage as 16 inches in square prestressed concrete batter piles supporting the Public Container Wharf failed in tension at their connection to the deck, see Fig. 2.2. The battered piles were embedded in loose hydraulic fill which liquefied and settled, exerting lateral and downdrag forces on the piles. The inclined piles in the Maston Terminal Wharf suffered also similar damage. In addition, damage had been found to the back row of the vertical piles. At the Oakland Outer Harbor Pier 7, 16 inches square prestressed concrete batter piles failed at or near the connection to the pile cap. Liquefaction and settlement of the supporting soil during the earthquake were also observed.

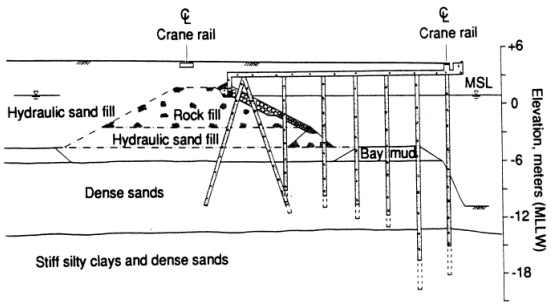

Figure 2.1: 7th Street Terminal of the Port of Oakland: Batter pile configuration (after Seed et al. [2])

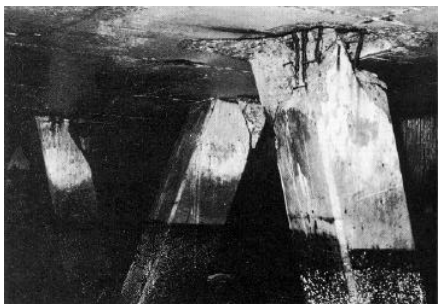

Figure 2.2: 7th Street Terminal of the Port of Oakland: Damaged batter piles after the 1989 Loma Prieta Earthquake (after SEAOC, 1991 [3])

Tensile failure at the connection of the deck to the prestressed concrete batter piles was observed in the Ferry Plaza Pier with some of the piles punching through the slab. Spalling and cracking of the bottom of the slab was found at over 100 pile locations. The damage pattern shown in Fig. 2.3 was observed on over 120 20 inches square prestressed batter piles.

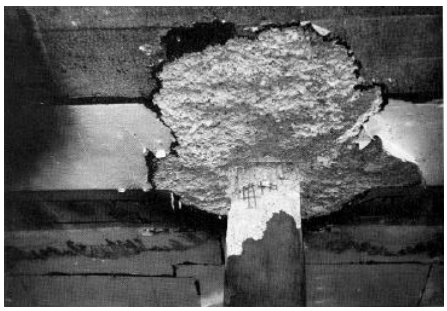

Figure 2.3: Ferry Plaza: Damaged batter piles after the 1989 Loma Prieta Earthquake (after SEAOC, 1991 [3])

Bridge 605 A, Great Alaska Earthquake, March 1964

The Great Alaska Earthquake of 1964 (moment magnitude M_w 9.2) caused some of the most devastating and widespread damage to highway bridges in United States history. The peak ground accelerations were estimated to be in the range of 0.1 g to 0.2 g.

In the area of the valley of Snow River, at the time of the earthquake, a replacement bridge (Bridge 605 A) was under construction immediately adjacent on the downstream side. The bridge was completely destroyed during the earthquake. A post-earthquake view of the bridge looking downstream is shown in Fig. 2.4.

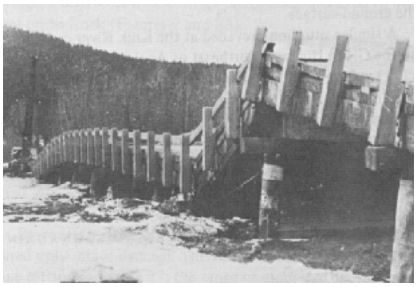

Figure 2.4: Bridge 605 A, Snow River: Post-earthquake view looking downstream (after Dickenson et al. [4])

The bridge experienced significant displacement and tilting as shown in Fig. 2.5 (a). The pier foundations were founded on concrete-fill steel-tube piles extending to an average depth of 27 m below the level of the stream bed. As a result of liquefaction, these piers displaced laterally about 2.5 m downstream and tilted upstream about 15° as illustrated in Fig. 2.5 (b).

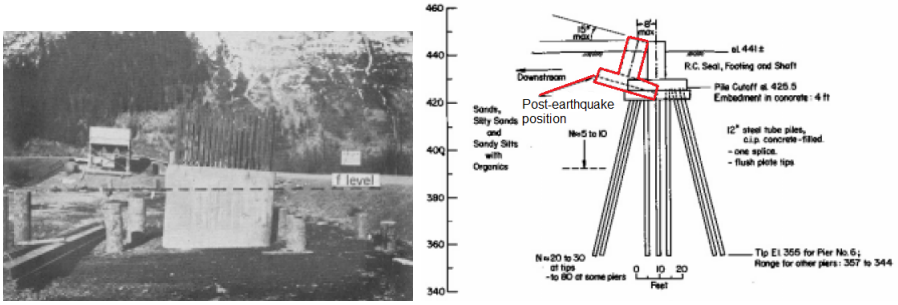

(a) (b)

Figure 2.5: Bridge 605 A, Snow River: (a) Post-earthquake view of one pier; (b) Displacement and tilting of the pier 6 after the 1964 Great Alaska Earthquake

Rio Banano Bridge, Costa Rica Earthquake, April 1991

The magnitude 7.5 Costa Rica Earthquake caused severe damage over a large area, including liquefaction related collapse of several pile-supported bridges. A three span road bridge (Rio Banano bridge, shown in Fig. 2.8) was located at a river crossing that showed extensive signs of liquefaction. Priestley et al. [5] reported the damages of this bridge after the earthquake. The south abutment of the bridge rotated about 9°, causing movement of the 36 cm^2 precast concrete piles 66 cm toward the river, shown in Fig. 2.6. The front battered piles suffered flexural and shear damage, the vertical piles at the rear were however less damaged, shown in Fig. 2.7.

Figure 2.6: Rio Banano Bridge: Liquefaction induced rotation at the pile cap after the 1991 Costa Rica Earthquake (after Priestley et al. [5])

Figure 2.7: Rio Banano Bridge: Front raked piles were more heavily damaged than the rear vertical piles after the 1991 Costa Rica Earthquake (after Priestly et al. [5])

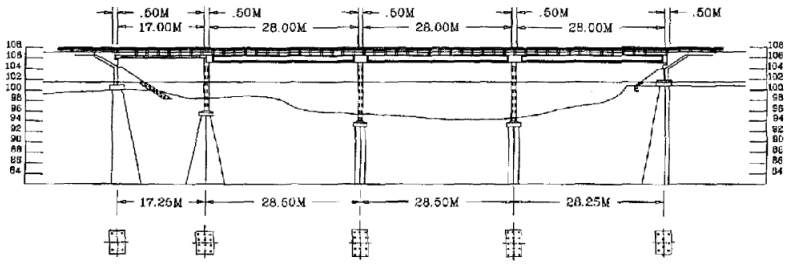

Figure 2.8: Rio Banano Bridge: Built drawing (after Priestly et al. [5])

Rio Vizcaya Bridge, Costa Rica Earthquake, April 1991

The Rio Vizcaya road bridge is a 3-span prestressed concrete bridge founded in soft sands, as shown in Fig. 2.9. After the 1991 Costa Rica Earthquake the bridge was heavily damaged: it lost two spans due to severe abutment rotation, pile distress ,the collapse of the interior support and soil liquefaction. The various failure modes in the batter piles and the soil are shown in Fig. 2.10 (a) and (b) respectively. Fig. 2.10 (a) corresponds to a situation where soil movements led to extensive damage in the batter piles.

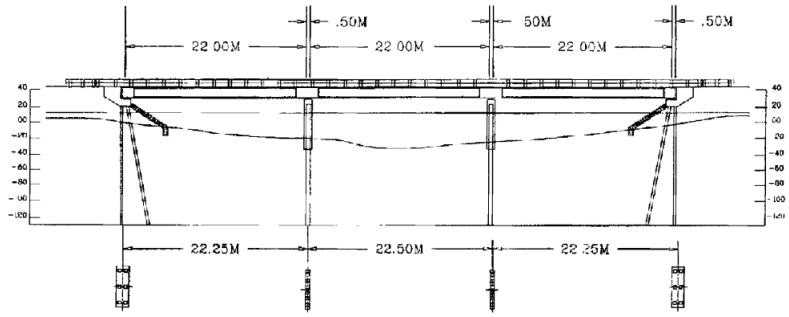

Figure 2.9: Rio Vizcaya bridge: Built drawing (after Priestly et al. [5])

(a) (b)

Figure 2.10: Rio Vizcaya bridge: (a) Damaged batter piles (north abutment); (b) Liquefaction failure mode of the birdge after the 1991 Costa Rica Earthquake (after Priestly et al. [5])

Container Terminal at San Pedrito Harbour, Manzanillo earthquake, October 1995

The Manzanillo earthquake in Mexico (9 October 1995) damaged a non negligible amount of piles and structural joints in the dock of the Container Terminal at the San Pedrito Harbour. The dock is divided into five modules 50 x 21.6 m. Each has an independent reinforced plane concrete slab of 45 cm thickness. A separation of 2 cm exists between the slabs. The piles, shown in Fig. 2.11, are made from reinforced concrete elements and their cross section is square, 50 × 50 cm. Fig. 2.12 shows the earthquake-induced damage on the batter piles of the wharf. High punching forces on the heads of the battered piles caused also damages on the slabs.

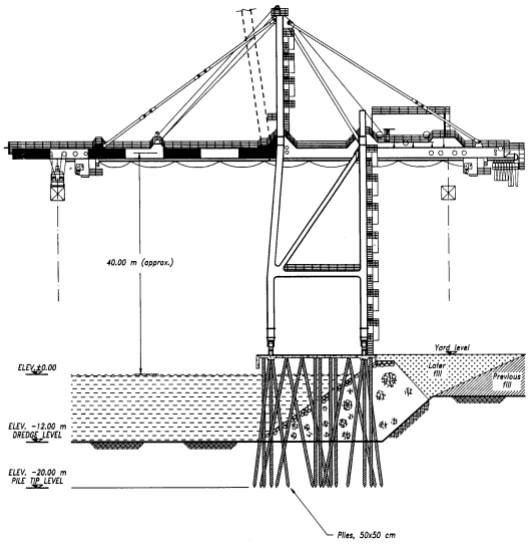

Figure 2.11: Container Terminal in San Pedrito: Cross section of the wharf (after Ovando-Shelley and Pomo [6])

Figure 2.12: Container Terminal in San Pedrito: Earthquake induced damage on the batter piles of the wharf after the 1995 Manzanillo earthquake (after Ovando-Shelley and Pomo [6])

Liquefaction also occurred at a depth of 8 to 14 m. The lateral spreading of the soil layer towards the seafront caused damages to roughly 100 piles out of 1300. Most of the damaged piles were inclined. Exhibiting a higher lateral stiffness, inclined piles took over more significant loads than the vertical ones. Failure was observed mainly in the connection with the cap.

Port of Coronel, Chile Earthquake, February 2010

The M_w=8.8 offshore Maule Chile earthquake (27 February 2010) occurred in a subduction zone in which the Nazca plate passes eastward and downward beneath the South American plate. The rate of convergence of the two plates is 70 mm/year [7]. The Port of Coronel is located in the Region of Bio-Bio, 30 km south of the city of Conception. The northern part was constructed in 1998 and is supported by conventional steel pipe piles (battered and vertical). This part was heavily damaged after the Chile earthquake as shown in Fig. 2.13.

Figure 2.13: Port of Coronel: Damaged battered piles after the 2010 Chile earthquake (after GEER [7])

Inclination was approximately 20° forward for the seaward pile and 20° backward for the landward pile. A sketch of the pile cap and the piles before and after the earthquake is provided in Fig. 2.14. After being subjected to important lateral spreading movements induced by the earthquake, the leading row pile remained embedded in the cap while the trailing row pile was pulled out. More specifically, it moved down 0.8 m and horizontally 0.3 m so that it was within 10 cm of impacting the leading row pile.

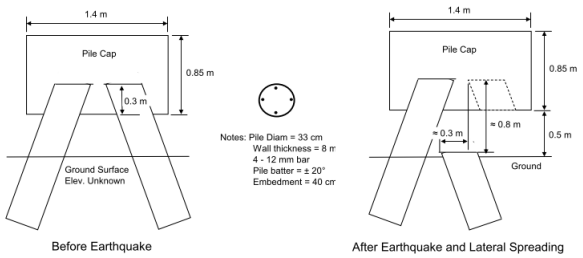

Figure 2.14: Port of Coronel: Sketches of the pile cap and the piles before and after the 2010 Chile earthquake (after GEER [7])

Port of San Antonio, Chile Earthquake, February 2010

The Port of San Antonio is Chile's largest port and the busiest port on South America's west coast. Located on the shores of central Chile in the Valparaiso Region, it is situated 80 km west from the outskirts of the country's capital Santiago. Since the port was reconstructed (1992∼1997), little damage was observed in the port. Notable exceptions are an old dock (apparently not part of the reconstruction) which suffered severe damage during the Chile earthquake and a wharf structure supported on vertical and inclined steel piles. Displacements in excess of 1 m were observed leading to failure the connections at the pile heads, see Fig. 2.15. The settlement of the piles - a consequence of liquefaction - is also evident the figure.

Figure 2.15: Port of San Antonio: Failure of the head connection between the wharf and the inclined piles after the Chile earthquake (after GEER [7])

2.1.2 Post-earthquake observation - Beneficial performance of inclined piles

Apart from the poor performance of incline piles, field evidence has been found revealing the beneficial performance of inclined piles. Some examples which have already been reported by Giannakou [9] are introduced briefly in this section.

Landing Road Bridge, Edgecumbe Earthquake, March 1987

In 2 March 1987 a 6.3 magnitude earthquake hit the east coast of north New Zealand. Extensive liquefaction occurred (especially near rivers) resulting in significant lateral spreading. Roadway embankments, rail and road bridges, buildings and lifelines suffered damages due to the important ground movements.

The Landing Road Bridge was one of these structures. The nearest strong motion record was at the Matahina Dam where a peak ground acceleration of 0.33 g was recorded. The bridge (Fig. 2.16) was built in 1962 and comprises 13 simply supported spans of 18.3 m in length. The substructure consists of concrete slab piers, each supported on eight 406 mm^2 prestressed 9 m long concrete piles battered

at 1:6. The abutments are supported on eight batter piles, five of them inclined towards the river side and the other three to the opposite direction. The bridge is founded on a soil deposit consisting of a crust of stiff clayey/silty layer (1-2 m thick) underlained by a 6 m thick layer of loose, medium to coarse sand. Below that depth, the piles are driven 2-3 m into layers of dense sand and gravels. The loose sand layer was the one that liquefied during the earthquake. Different Standard Penetration Test (SPT) and Cone Penetration Tests (CPT) were conducted. The cone resistance of the loose sand was found in the range of 4∼6 MPa, whereas for the underlain dense sand layer about 15∼20 MPa.

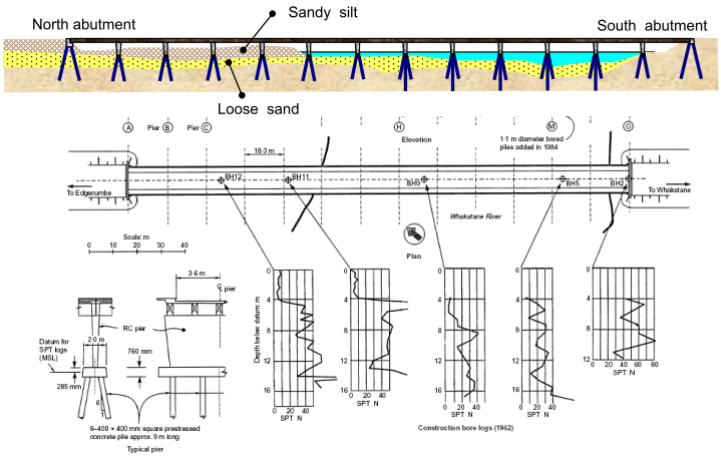

Figure 2.16: Plan of the Lading Road Bridge (after Berrill et al. [8])

Despite the observed axial compression of the deck (indicated by the closing of the joints and the buckling of the footpath slabs), the bridge superstructure did not undergo any significant stresses. On the northern abutment of the bridge, the settlement of the soil surrounding the piles was measured around 300∼500 mm exposing cracks in them. The abutment had tilted 0.5° towards the river, while the piers B and C were leaning about 1° to the same direction. All the other piers stayed vertical. The lateral displacement at the river bank was estimated about 1.5∼2 m.

Signs of soil mounding on the landward side of the piers suggested passive failure in the soil crust. Additional investigations were carried out in 1993 in order to verify the speculated failure mechanism. Trenches were excavated on each side of pier C. Soil had mounded up at the north side of the pier (Fig. 2.17) and the ground surface was 450 mm higher than the surface on the river side. Two shear surfaces were logged in the sandy silt near the ground surface and traced downwards, the lower shear towards the front face of the pile cap and the upper shear to the intersection of the pile cap and bridge slab pier at an angle of 20 ∼ 30° to the horizontal, shown in Fig. 2.18. The angle of inclination and positioning of the failure surfaces, together with the sharp offset of a lens of sandy silt, clearly indicate that these discontinuities were formed during the 1987 episode of lateral spreading. Trenching on the south side of the pier showed no upthrust mound. However, two vertical lateral spreading

cracks were revealed. The first 200 mm of the piles below the pile cap were inspected and a faint crack was found about 50 mm below the cap.

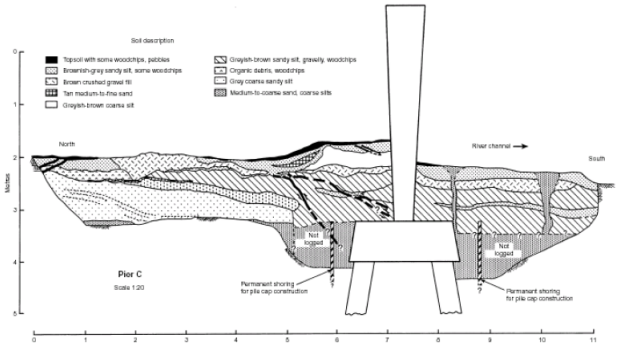

Figure 2.17: Pier C, trench log. (after Berrill et al. [8])

Figure 2.18: Pier C. The mound of the soil on the one side of the pier and the gap on the riverward side (after Berrill et al. [8])

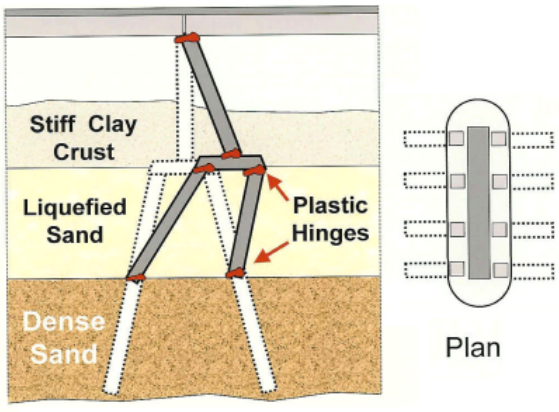

Figure 2.19: Assumed " failure " mechanism of the Pier C of the Landing Road Bridge (after Berrill et al. [8]), original from Giannakou [9]

Trenching on the south side of the pier showed no upthrust mound. However,

two vertical lateral spreading cracks were revealed. The first 200 mm of the piles below the pile cap were inspected and a faint crack was found about 50 mm below the cap.

Based on these observations and on in-situ testing data, Berrill et al. [8] concluded to the collapse mechanism shown in Fig. 2.19. The passive earth thrust was estimated to about 1 MN per pier. In the same time, the estimated force induced on piles by the liquefied layer was 50 kN. Comparing these forces it is obvious that the damages were caused by the non-liquefied crust. According to Yasuda and Berrill [34], the good performance of the bridge is attributed to the larger stiffness of the pile group due to the presence of the batter piles.

Maya Futo Wharf at the Port of Kobe, 1995 Kobe Earthquake (also called as Hygoken Nanbu earthquake)

The January 17, 1995, Hyogoken-Nanbu (Kobe) Earthquake was assigned a JMA magnitude of 7.2 by the Japan Meteorological Agency (JMA). It brought great damage to structures in the Port of Kobe, which is one of the primary ports in Japan. The post-earthquake observation showed that one quay-wall relying on inclined piles survived in the earthquake. On the contrary, however, a nearby wall relying exclusively on vertical supporting piles was completely destroyed, and disappeared during the earthquake. This documented case of exceptional and mediocre seismic response of two adjacent composite foundations leads to the inescapable conclusion that composite foundations can have significant advantages and are undoubtedly worth studying in detail. GEER [35] and Kastranta et al. [36] documented the performance of the Maya Futo Wharf during Kobe earthquake in 1995.

The port quay walls as well as the foundations of the piers of several bridges which connect the man-made islands to the mainland were subjected to large ground deformations. The quay walls were designed with strong pile foundations to resist seismic loading. Quay walls at the southeast corner of the westernmost pier were the most significantly deformed, with large gaps between quay wall blocks.

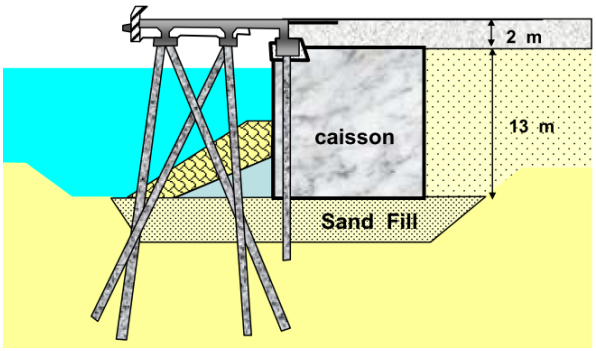

Figure 2.20: Cross section of survived quay wall in Kobe earthquake, original from Giannakou [9]

In the case of the mentioned survived quay-wall, of which the cross-section is shown in Fig. 2.20. This wall suffered only insignificant displacements (relatively speaking, in view of the magnitude of the disaster). The bearing capacity of the inclined pile seems to have far exceeded the component of the lateral imposed force. The presence of the inclined piles, which presently are internationally underrated and their use is not proposed or even forbidden in several seismic codes and regulations, was one of the reasons why the quay wall managed to withstand the severe seismic motion and experience a deformation of 20 cm only. The post-earthquake observation is shown in Fig. 2.21, no obvious damages were observed.

Figure 2.21: Post-earthquake observation of the survived quay wall in Kobe earthquake

Another two quay walls without inclined piles were damaged severely, the cross sections of these two walls are shown in Figs. 2.22 (a) and (b), respectively. The main causes for the huge displacements that these quay walls experienced (3m displacement) were the developed large inertia forces, as well as the excess pore pressures built-up especially at the foundations soils. The earthquake induced damages of the three sections, are shown in Fig. 2.23 (a) and (b), respectively.

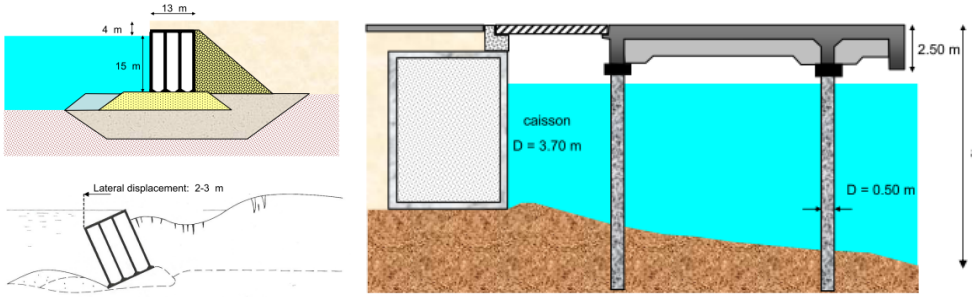

(a) (b)

Figure 2.22: Cross sections of the severely damaged quay walls in Kobe earthquake, original from Giannakou [9]

(a) (b)

Figure 2.23: Post-earthquake observations of the severely damaged quay walls in Kobe earthquake

Sheet pile bulkheads at Sendai Port, 1978 Miyagi-ken-Oki Earthquake

1978 magnitude 7.4 Miyagi-ken-Oki earthquake caused severe damage to gravity quay walls, piers and sheet pile bulkheads. The Sendai Port area has a soil profile composed of a sand layer 3 to 20 meters thick underlain by layers of medium coarse sand and silty loam. Dense sand and bedrock underlie the silty loam layer. Two nearby bulkheads serve as a comparison study, Figure 2.13. A 10 seismic lateral coefficient of 0.1 g was used in the design. Bulkhead No. 4 was anchored with vertical H-beam. The area behind this bulkhead experienced cracking and settlement. Bulkhead No. 5 was constructed in a similar manner except that it used batter piles to restrain the anchor. This bulkhead withstood the earthquake without damage. Note as shown in Fig. 2.24 (a) and (b), that the near surface soil behind Bulkhead No. 4 had lower blowcounts, which when combined with reduced anchorage could have caused the increased lateral spreading and associated damage.

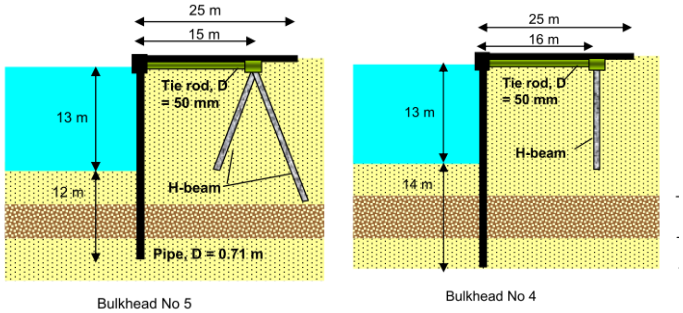

(a) (b)

Figure 2.24: Cross sections of two nearby sheet pile bulkheads at Sendai Port, original from Giannakou [9]

2.1.3 Summary of performance of inclined piles from post-earthquake observations

In this section, several post-earthquake observations of the performance of inclined piles were reviewed. To sum up, the main reasons for the poor performance of inclined piles are due to the large rotation of pile cap, the excessive forces punching or tensile on pile heads and insufficient detailing at the pile-to-cap connections etc. In addition, soil liquefaction plays an important in the failure of inclined piles. In all the earthquake events introduced above whereas inclined piles had poor performance, intensive liquefaction of the soil were also observed.

In other engineering cases, whereas inclined piles had beneficial performance, inclined piles played important roles in providing larger stiffness and restraining excessive displacement of deformation of the structures. However, in these engineering cases, the obvious liquefaction of the soil had not been observed.

It seems that without the liquefaction of soil, the performance of inclined piles is better than that of the vertical piles. The performance of inclined piles in non-liquefied soil will be introduced and investigated in the following chapters.

2.2 Experimental studies on inclined pile foundations

In this section, a short literature review is presented on experimental studies on inclined pile foundations. The tests are classified in three groups: conventional laboratory tests, centrifuge tests and in-situ tests (or field tests).

2.2.1 1 g test on reduced scale

From 1972 to 1995 Meyerhof et al. conducted important experimental campaigns to investigate the bearing capacity of piles and pile foundations in soils [37–43]. They introduced the following two definitions: a "negative inclined pile" and a "positive inclined pile" according to the direction of inclination, as shown in Fig. 2.25 (Reese and Willem [44] prefer calling them in batter and out batter piles respectively).

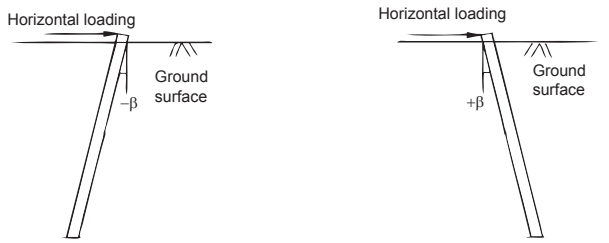

(a) "In" batter or Negative inclined pile

(b) "Out" batter or Positive inclined pile

Figure 2.25: Negative and positive battered pile

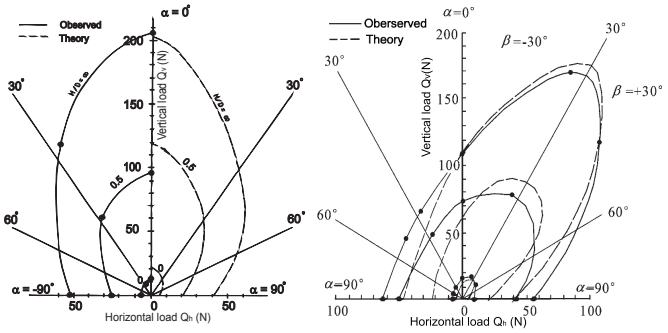

(a) (b)

Figure 2.26: Polar bearing capacity diagrams for single vertical piles (a) and single inclined piles (b) under inclined loads [10]

If the lateral load acts on the pile in the direction of batter, it is called in-batter or negative batter pile. If the lateral load acts in the direction opposite to that of the batter, it is called an out-batter or positive batter pile. Meyerhof and Ranjan [38] studied the influence of angle of inclination on the bearing capacity diagram of a

single battered pile on sand and found that it also influences the foundation stiffness. An empirical equation was proposed to predict the ultimate strength of the piles under arbitrary load combinations (horizontal and vertical forces). Fig. 2.26 shows the different bearing capacity diagrams for single vertical piles and inclined piles in layered soil. Meyerhof and Rangjan [38] highlighted also the fact that for small pile batter angles, the behavior of free standing batter piles under inclined loads appears qualitatively similar to that of free standing vertical piles. For small load inclination, vertical and positive batter piles present a more significant ultimate bearing capacity. Fig. 2.26 shows the polar bearing capacity diagrams for single vertical piles and single inclined piles under inclined loads.

2.2.2 Centrifuge tests on inclined piles

2.2.2.1 Static centrifuge test

In the static domain, many researches have been performed so far. Pinto et al. [45] performed a series of centrifuge tests on free and fixed-head plumb and battered pile groups. The battered piles without vertical dead loads were found to be less resistant than the vertical piles; lateral resistance of fixed-head pile group is higher than that of the free-head pile group; fixed-head piles developed significant axial forces.

In 1997, McVay et al [11] performed centrifuge tests to investigate the behavior of laterally loaded battered pile groups. 3×3 and 4×4 battered pile groups were tested in loose and medium dense sand, shown in Fig. 2.27. Increasing the dead load increased the lateral resistance of both pile groups. Although this change in loose sand depends on the batter piles configuration, in medium dense sand the dependence is not so strong. The dead load influenced also the rotation of the batter pile groups. With increasing dead load, the load distribution in the 4×4 groups in medium dense sand tended to shift from the lead row to the trail row, with little change in the middle rows. In the 3×3 groups and with increasing dead load the lead and trail rows took more of the lateral load than the second and third rows.

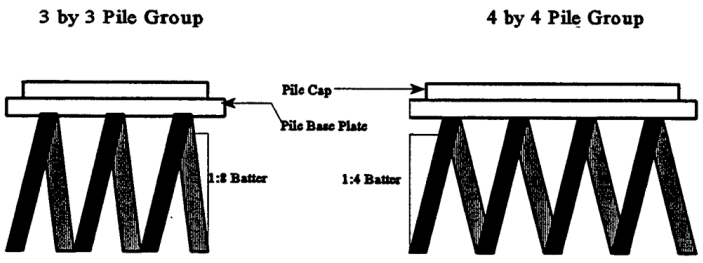

Figure 2.27: Pile groups configuration in sand for static centrifuge tests, McVay et al. [11]

In 1999, Zhang et al. [12] studied the effect of pile inclination and soil density on

the displacement of a single pile head when subjected to a horizontal static load, see Fig. 2.28. The inclination of the pile varied from −14° to 14° (i.e. from negative to positive inclined pile). Results showed that for both medium dense and dense sand, the horizontal resistance increased by 24% and 50% respectively for the negative inclined pile and decreased by 15% and 35% respectively for the positive inclined pile, shown in Fig. 2.28.

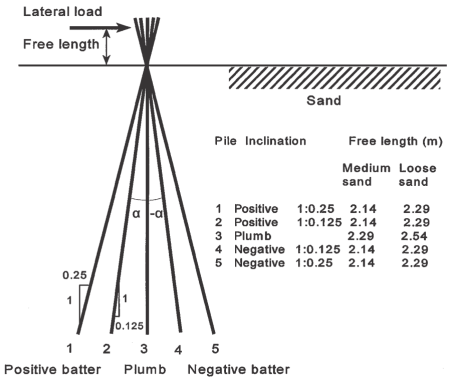

Figure 2.28: Layout of single battered pile for static centrifuge tests, Zhang et al. [12]

Zhang et al. [46] stated that the lateral resistance of individual battered piles in a given soil is influenced by the pile inclination and loading direction. The vertical load influences also the lateral behavior of the battered pile. When no vertical load exists, the horizontal movement of the negative battered pile causes a positive movement in the soil in front of the pile and therefore the lateral resistance of the negative battered pile is greater than for a vertical pile. On the contrary, the lateral movement of a positive battered pile causes an upward movement of the soil that reduces the vertical stresses and the lateral resistance is found smaller. In comparison, the lateral resistance of negative battered pile is thus found greater, followed by the lateral resistance of a vertical pile and then by a positive battered pile. Nevertheless, when a vertical load is applied, the lateral resistance of a negative battered pile is reduced because of the bending moment due to the vertical load component that causes an additional lateral displacement. The opposite is true for a positive battered pile since the bending moment counterbalances the lateral load component.

Escoffier et al. [13] conducted horizontal cyclic loading static centrifuge tests on the pile group configurations shown in Fig. 2.29. Results indicated that the initial stiffness of the inclined pile group is higher than that of the plumb pile group, and the presence of inclined pile decreased the maximum bending moment below the soil surface.

2.2.2.2 Dynamic centrifuge test

Few dynamic centrifuge tests have been conducted on inclined piles. Escoffier et al. [13] performed centrifuge tests on pile foundations in dry sand considering an impact loading applied by a magnetic hammer. Two pile groups were studied (a 1×2 vertical pile group and a 1×2 pile group with one inclined pile, shown in Fig. 2.29) and two end-bearing conditions (a floating friction pile group and an end-bearing pile group installed on bed-rock). The impact test highlighted the translation-rocking mode of the inclined pile group. Its stiffness was found higher and the resulting movement smaller that of the vertical pile group. In both groups, the center of rotation of the cap was near the vertical face of the pile cap towards the front pile side. In terms of bending moment profiles, the presence of the inclined pile induced a decrease of the maximum bending moment below the soil surface in both piles. In addition, the influence of the inclined pile on the maximum bending moment at the pile cap interface seemed to be negligible in the front pile whereas it induced an increase of the maximum bending moment in the rear pile. For the inclined pile group, the axial load was increased in the front and the rear pile by a factor of 1.7 and 2 respectively.

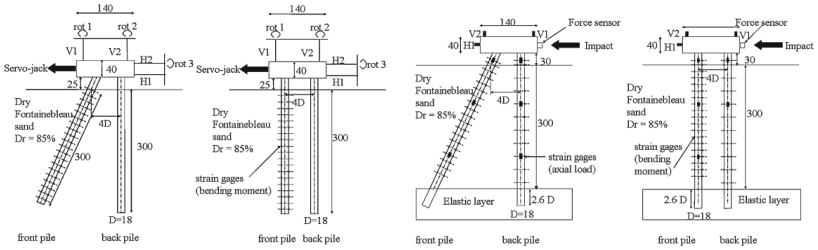

Figure 2.29: Pile group configuration for static and dynamic centrifuge tests: (a) static tests (b) dynamic tests (after Escoffier et al. [13])

Tazoh et al. [14] performed centrifuge tests to clarify the seismic behavior of batter pile foundations. A vertical pile foundation and a batter pile foundation were installed parallel to each other in a soil container filled with dry sand, shown in Fig. 2.30). No superstructures were used in order to observe the pure kinematic interaction. Considering different signals (the El Centro earthquake and a sinusoidal loading) it was found that the maximum acceleration at the footing of the vertical pile foundation is larger than that of the batter pile foundation; the bending moment and axial force of the batter pile foundation were also greater than that of the vertical pile foundation.

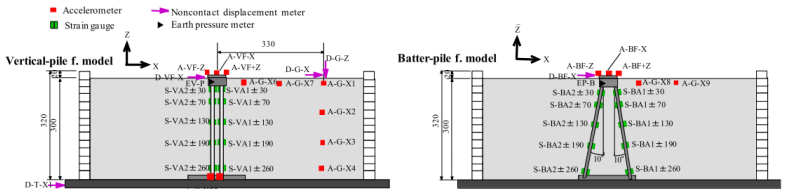

Figure 2.30: Pile group configurations for dynamic centrifuge tests, Tazoh et al. [14]

In 2012, Escoffier [47] performed new series of dynamic centrifuge tests on inclined piles. This time the dynamic loads were applied using an earthquake simulator [48] at the bottom of the model. The two configurations shown in Fig. 2.31 were studied using both sinusoidal and earthquake signals. The results of the seismic tests showed that the inclined pile caused a shift of the frequencies and reduced 2 times the maximum horizontal acceleration of the cap. The analysis of the bending moments and axial loads in the piles indicated that the inclined pile induced larger residual bending moments and did not change the sign of the axial loads in the piles. The sine tests highlighted the fact that the effect of the inclined piled is strongly dependent on the loading input frequency content. Considering the kinematic response of the cap, the input frequency significantly influenced the effect of the inclined pile on the maximum total bending moment. In addition, Escoffier reported that for inclined pile foundations the residual bending moments can not be ignored compared to the dynamic bending moments.

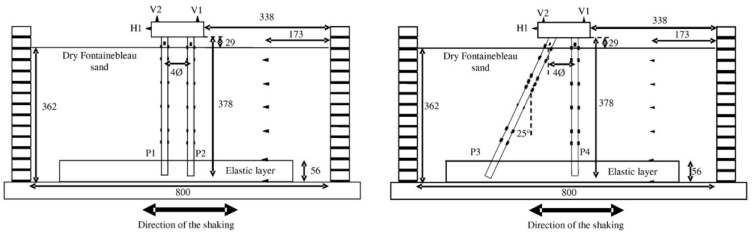

Figure 2.31: Pile group configuration for dynamic centrifuge tests, Escoffier et al. [13]

Okawa et al. [15] performed centrifuge tests with loose sand. Fig. 2.32 shows the two pile group configurations. The first was composed of 8 vertical piles (Fig. 2.32 (a)) and the second of 4 inclined piles with an inclination of 10° and 4 vertical piles (Fig. 2.32(b)). A short superstructure was placed on the footing to study both kinematic interaction and inertial effects. The presence of inclined piles decreased the acceleration amplitude at the footing and the superstructure. Higher axial forces were observed in the inclined piles.

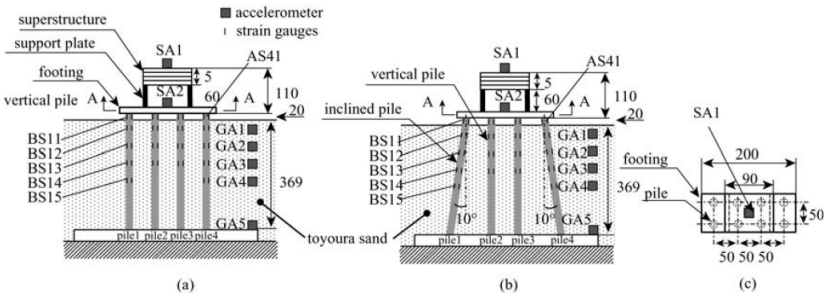

Figure 2.32: Pile group configurations for dynamic centrifuge tests, Okawa et al. [15]

Boland et al. [16,17] performed dynamic centrifuge tests with two models (named SMS02 and JCB01) constructed as a generalization of the pile supported wharf structures common at the Port of Oakland (POOAK), the Port of Los Angeles (POLA) and the Port of Long Beach (POLB) in California. The typical section of these wharf structures is similar to the 7th Street terminal at the Port of Oakland introduced previously, shown in Fig. 2.1.

For the SMS02 model shown in Fig. 2.33, a relatively simple soil configuration with a single-lift rock dike was considered. The bottom layer of the model consisted of a relatively dense (D_r=70%) sand, used to provide a bearing and termination layer for the piles. A single monolithic rock dike with a 2.0:1.0 (H:V) slope was the waterfront face of the model. The reverse face (land-side) had a 1.5:1.0 (H:V) slope. Additional dense sand was placed behind the rock dike as a backfill material.

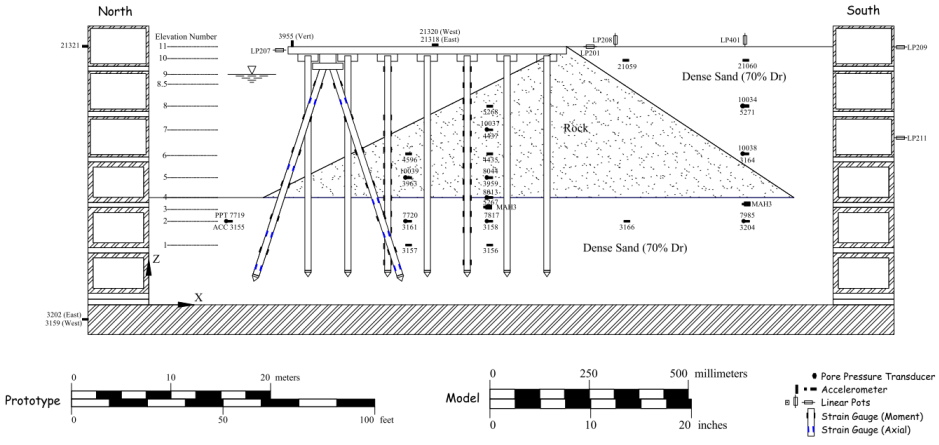

Figure 2.33: Center cross Sections of the centrifuge models, instrument locations for the SMS02 model, Boland et al. [16]

In the JCB01 model shown in Fig. 2.34, the rock dike geometry was modified to a 6-foot-thick (prototype scale) sloping rock facing (2:1 slope) placed over loose (D_r=40%) sand. This geometry represents a typical configuration where ground

improvement has been used in the backland, but omitted beneath the wharf deck where any improvement scheme would be expensive and difficult to implement due to limited access. This particular profile is similar to actual conditions at port facilities in the Oakland area that suffered earthquake related damage during the 1989 Loma Prieta earthquake. In addition to the loose sand, the backland area incorporated an improved (D_r=70%) region. This relatively simple geometry, with no loose sand regions in the backland area, was chosen to enable direct comparison with the previous monolithic rock dike configuration of SMS02.

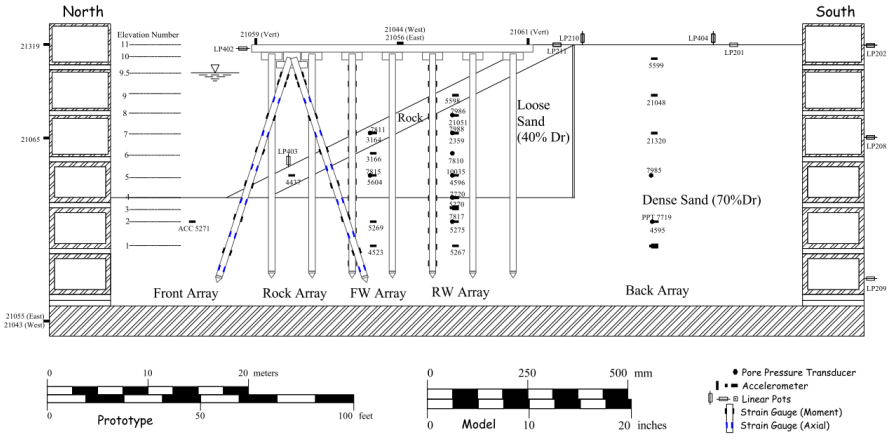

Figure 2.34: Center cross Sections of the centrifuge models, instruments locations for the JCB01 model, Boland et al. [17]

The test program consisted of spinning the model at approximately 40 g centrifugal acceleration and applying input motion through the shake table [16, 17]. The testing sequence generally consisted of two or three small motions (peak input accelerations less than 0.1 g) to examine the small-strain performance of the structure and to examine the performance of the data acquisition system. Four or five large motions were then applied to the model (peak input accelerations greater than 0.1 g). The testing sequence focused on the use of two earthquake motions. The first was recorded in the backland at the Port of Oakland Outer Harbor during the 1989 Loma Prieta Earthquake and the second was recorded at the Rinaldi station during the 1994 Northridge Earthquake. The SMS02 model was shaken with a total of eight earthquake motions consisting of three small shakes and five large shakes. The last two pairs of shakes (two Loma Prieta and two Northridge Rinaldi motions) were focused of the author's articles as they were very similar in magnitude with the only difference being the detachment of the batter piles. The JCB01 model was shaken with a total of six dynamic events consisting of two small shakes, three moderate shakes, and one large shake. As for the SMS02 model, the authors focused on the last two shakes since their events were similar with the only difference being the removal of the batter pile connections.

Boland et al. [16, 17] presented the maximum moments of the piles (at the be-

ginning of each test the moments were considered equal to zero i.e. the residual moments from the previous tests were not taken into account). It was found that the maximum moments were all recorded near the top of the piles adjacent to the fixed-head connection to the wharf deck. Results clearly showed a significant increase (1.4 to 3.9 times) in recorded pile moments when the batter piles were detached (removed) for nearly identical input base accelerations. The batter piles had peak dynamic moments of 40 to 100% of the vertical pile values near the wharf deck connection. The lateral forces within the batter pile heads were significantly greater (9 to 20 times) than those recorded in the vertical piles for the same dynamic event. The shear forces in the vertical piles increased significantly with the removal of the batter piles. Dynamic wharf displacements increased by about 30% for all tests where batter piles were detached. The displacement of the embankment also contributed to the increase in lateral loads on the wharf structure. On the other hand, increases in wharf deck and embankment displacements were observed when batter piles were detached for the same level of shaking.

The measured experimental data was consistent with the damage observed at the Port of Oakland Seventh Street Terminal after the 1989 Loma Prieta earthquake. Much of the damage to the wharf substructure was concentrated at the batter pile connections, and in many cases the connections were completely sheared. Based on these results, it can be anticipated that detailed batter piles may reduce both permanent embankment and wharf displacements.

Juran et al. [49] conducted a series of centrifuge tests on vertical and inclined micropile groups. The tests results showed that with increasing inclination angle the natural frequency of the network system increased. In general, increasing the pile inclination results to a decrease on the pile cap displacements and increase in axial forces and bending moments at the pile cap connections.

2.2.3 Full scale in-situ tests

Among all the experimental approaches, full-scale in-situ tests is one of the best approaches to understand the behavior of pile foundations. Although more uncertainties are present, they are more close to practice and overcome the physical constrains existing in laboratory modeling. Nevertheless, due to the extremely high costs only few full-scale in-situ tests have been conducted so far on piles and pile groups.

One of the earliest records of in-situ tests on inclined piles are the experiments conducted by Feagin [50] in 1953. The author reported a series of full-scale field tests on groups of vertical and battered timber piles with heads fixed in concrete monoliths. The inclination of the batter piles were 20° and driven into fine to coarse sand with occasional gravel. It was found that groups with both vertical and battered piles were more resistant than those containing only vertical piles. The resistance increased with increasing batter angle. When the direction of the external load was the same as the direction of a batter pile (i.e. combination of vertical and inclined loads) the measured resistance was the greatest. The resistance

of an inclined pile also increased with the application of a vertical compression load.

Again in 1953, Tschebotarioff [51] conducted a test to measure the capacity of a single pile battered at 15° in tension and compression. The results showed that the lateral capacity of the pile battered in compression was much smaller than the capacity of a pile battered in tension.

Kim and Brungraber [52] performed full-scale tests on battered piles and reported that negative batter piles provide more resistance than positive batter piles. In 1982, Denisov [53] studied the behavior of foundations using driven vertical and inclined piles under horizontal loadings. It was found that for equal spacing of the piles in the clusters, the bearing capacity of the foundations consisting of inclined piles with a low grating in clay soils of semihard and hard consistency was greater by a factor of 1.7-2.1 than the capacity of foundations consisting of vertical piles; the rigid embedment of the heads of the inclined piles in the slab of the low grating increased their strength by a factor of 3.9, whereas for vertical piles by factor of only 1.9 (in comparison with the strength of individual piles with free heads of equal rigidity).

Giannakou [9] reported a case study of the in-situ measurement of response of the Ohba-Ohashi Bridge in Japan. A number of researchers have studied the response of the Ohba-Ohashi Road Bridge near Tokyo to a 1983 magnitude 6.0 earthquake that caused a maximum horizontal acceleration of 0.114 g at the site, and attempted to correlate their analytical models to the observed response, with varying degrees of success. The significance of this case is that the bridge and foundations were fairly well instrumented, and the 1983 event represents the strongest shaking data for instrumented piles published in the literature. The Ohba-Ohashi Bridge is 485 m long and is supported by 11 piers (Fig. 2.35). Published reports have concentrated on the performance of Pier 6, adjacent to the river, which is supported by 64 steel pipe piles (half of which are battered) of diameter 600 mm, wall thickness 9 mm for the vertical and 12 mm for the inclined piles, and length 22 m, see Fig. 2.36. The soil conditions at Pier 6 consist of 22 m of extremely soft alluvial strata of humus and silt, with an SPT N-value of nearly zero and a shear wave velocity of 40 to 65 m/s. The underlying strata consist of diluvial deposits of clay and fine sand, with an SPT N-value > 50 and a shear wave velocity of 400 m/s. The piles are securely embedded in he underlying substratum.

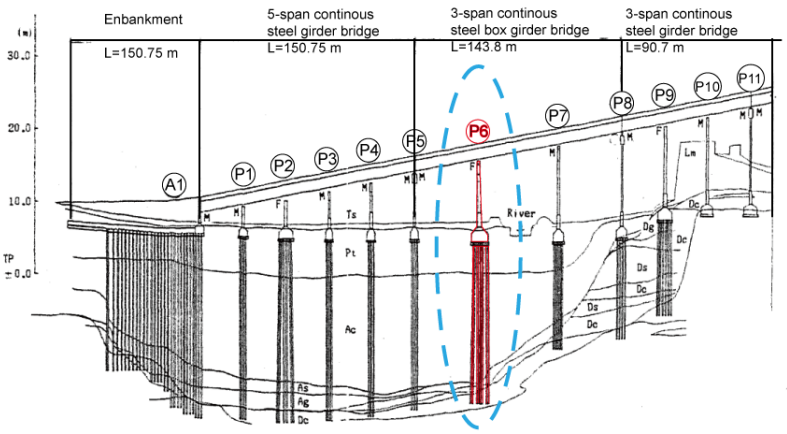

Figure 2.35: Plan view of Ohba-Ohashi bridge (modified after Ohira et al. [18])

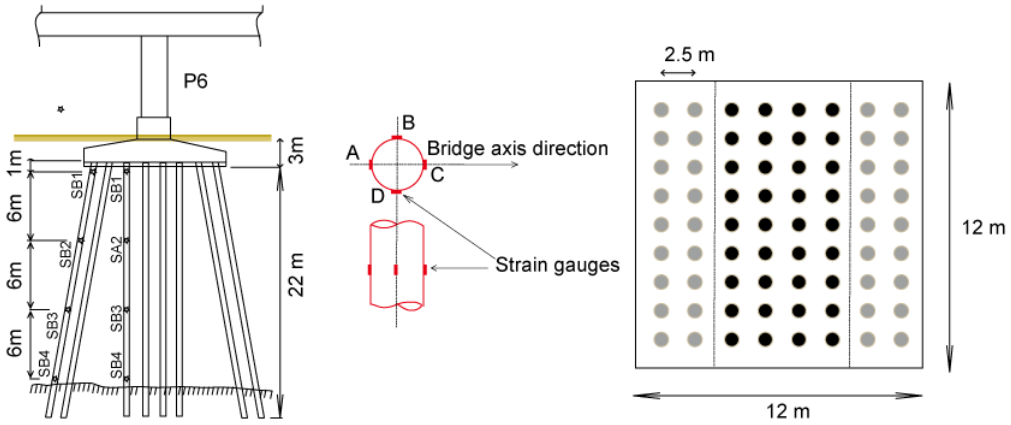

Figure 2.36: Cross section of Pier 6 of Ohba-Ohashi bridge (modified after Ohira et al. [18])

According to Ohira et al. [18], large bending strains were observed at the upper and lower ends of the piles, and axial strains decreased with depth over the length of the piles. Differences in strain distributions between vertical and batter piles was also observed, especially for the piles battered parallel to the bridge axis. The power spectra of pile strains and pier accelerations were well-correlated, indicating that the pile response was dominated by inertial interaction with the superstructure. The alternating pattern of compressive and tensile stresses in the piles also corresponded to the observed rocking motion of the superstructure. Transfer functions between the surface and the base and the footing and the base indicate spectral deamplification of 50∼80% of the pier motion relative to the free-field up to a period of 2.4 seconds, which corresponds to the site period.

Tazoh et al. [54] reported that the sign of axial strains in an instrumented verti-

cal pile was opposite that of the adjacent instrumented battered pile for all seismic observations at this site, and used finite element models to investigate this phenomenon. According to their observations the strains of the vertical and the batter piles remain opposite in sign during the entire duration of the earthquake. Moreover, they conclude that the displacement of the footing decreases for increasing values of the angle of the batter pile under static conditions. The bending strain of the batter pile has been observed to be larger than that of the vertical pile. Their models also discerned the relative contributions of inertial interaction to strains developed near the pile head, and kinematic interaction to strains near the pile tip. Gazetas et al. [55] evaluated the Ohba-Ohashi case history with a dynamic substructuring analysis method. A central conclusion of their study was that determination of the free-field motion in this very high plasticity clay (PI=100∼250) in the narrow alluvial valley (base dipping at 15 degrees) was no trivial matter. Complex basin effects may have influenced the free-field motion to the extent that the footing to free-field transfer function may not provide a clear basis for comparison.

2.3 Numerical analyses of inclined piles

2.3.1 Analytical studies

In 1971, Poulos [56] used Mindlin's elasticity equations to solve for stresses and displacements between pairs of piles due to horizontal point loads applied in an elastic half space. He came out with charts of interaction factors for both fixed and free head piles subject to lateral and moment loadings, functions of the flexibility of the piles, the spacing, the diameter, the length and the (initial) departure angle (the angle between the piles and the loading direction). The analysis was accomplished by superposition, calculating the interaction of each pile with all the others in the group, and ignoring the presence of intervening piles. Subsequently, results underestimated the pile group interaction for small pile spacing and overestimated the interaction for large spacing. The author elaborated furthermore the method to include soil limit pressures, soil-pile axial slip, variation of the soil modulus with depth and for batter piles.

In 1999, Poulos [57] studied the behavior of a 2×5 pile group subjected to static vertical ground movements (induced by the presence of an embankment). He found that when vertical ground movements act on the group, additional lateral deflections, bending moments and axial forces develop on the raked piles compared to a group with only vertical piles.Therefore, their presence might be detrimental.

2.3.2 p − y curves for inclined piles

The $p-y$ nonlinear curves relate the soil resistance to the pile deflection at different points along the pile. They are used to analyze the ability of deep foundations to resist lateral static or dynamic loads. The influence of inclination of the piles on the $p-y$ curves was investigated by Kubo [58], Awoshika [59] and Zhang et al. [12]. The

authors found that the shape of the $p-y$ curves for battered and vertical piles were similar. However, the pile inclination influenced the ultimate soil resistance and the subgrade modulus, two parameters that govern the pile response: The subgrade modulus defines the initial slope of the $p-y$ curve; the ultimate resistance governs the pile response at large deflections.

Zhang et al. [12] suggested that the changes in the subgrade modulus and the ultimate resistance for battered piles should be proportional to the ratio of the passive earth pressure coefficient for batter piles and for vertical piles. The authors introduced charts to estimate the factor, see Fig. 2.37. The modified $p-y$ curves for battered piles in sand are shown in Fig. 2.38, [12].

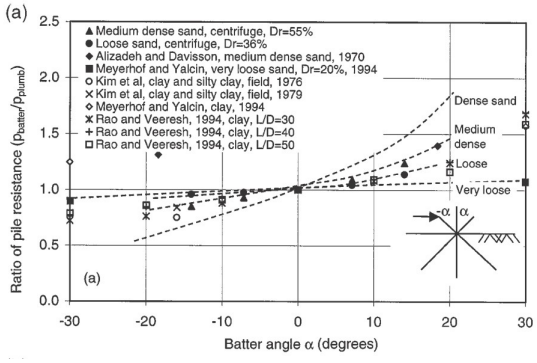

Figure 2.37: Influence of the batter angle on the lateral pile resistance [12]

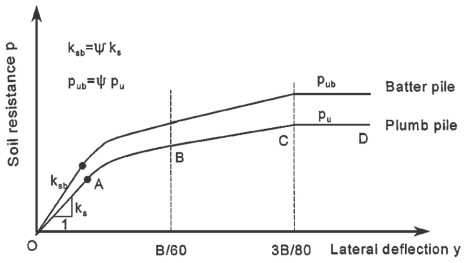

Figure 2.38: $p-y$ curves for batter and plumb piles in sand [12]

Another parameter that has a considerable influence on the lateral resistance of batter piles (and thus on the $p-y$ curves) is the soil pile interface friction angle. According to Sherif et al. [60], the magnitude of the friction angle depends not only on the soil properties but also on the amount and direction of the soil movement. Jardin and Chow [61] found that the value of the friction angle is independent of the relative density and tends to decline with the particle size.

2.3.3 Finite element modeling

Giannakou et al. [9, 27] studied numerically, in the time domain, the performance of batter piles. Linear constitutive laws were assumed for the soil and the inclined pile groups. Five different inclinations were considered. The authors found that for seismic loadings and purely kinematic conditions, batter piles tended to confirm their negative reputation. When the total response was considered however (kinematic and inertial response of the structural system founded on groups of batter piles), their influence could be beneficial. Among other parameters, their contribution depends on the ratio of the overturning moment versus the shear force transmitted to the piles from the superstructure.

Mroueh and Shahrour [62] performed numerical analyses on single inclined piles to investigate the bearing capacity under combined horizontal and vertical forces. The numerical bearing capacity diagram was similar to the experimental results coming from Meyerhof and Ranjan [37]. A Mohr-Coulomb constitutive law was used for the soil deposit and contact elements were introduced to reproduce the interface between the soil and the pile. The influence of the friction angle on the soil pile interface was studied and it was found that if the inclination of the load with respect to the horizontal direction does not exceed 10° this influence can be ignored.

Shahrour and Juran [63] performed numerical analysis of the seismic behavior of a micropile system containing inclined piles. Results were compared with centrifuge tests data and it was found that the inclination of the micropiles allowed an effective mobilisation of their axial resistance, leading to an increase in the stiffness and to a reduction in both shear forces and bending moments.

More advanced numerical studies were performed by Cheng and Jeremić [64] that took into account the soil skeleton pore fluid interactions. The authors have used the well known Dafalia-Manzari constitutive law [65] for soils and a perfect bonding was adopted between the pile and the soil. Okawa et al [15] and Zhang et al. [66] used the same constitutive model [67] for inclined piles. The numerical simulation has good agreement with centrifuge test results.

The impendance functions of deep vertical foundations attracted the attention of various researchers [68–72]. Regarding inclined piles, Mamoon et al. [70] studied the impedance function of 3×3 pile group via an hybrid boundary-element method. Giannakou et al. [73] studied the case of a single pile embedded in a homogeneous or non-homogeneous soil deposit and Padón et al. [74] the impedance function of deep foundations with inclined piles via a combined boundary element-finite element model.

Finally, specific software has been developed to calculate and apply the $p - y$ curves. For example, the nonlinear finite element program FLPIER [75] was developed at the University of Florida to analyze bridge pier structures. Zhang et al. [12] successfully implemented the proposed $p - y$ curve for battered piles into this software to simulate centrifuge tests. The numerical results showed an excellent agreement with the experimental results.

2.3.4 Macro-elements

With the development of the finite element method (FEM) and the rising of commercial FEM codes, engineers can explicitly reproduce 3D Soil-Structure Interactions (SSI) problems. However, this type of numerical analysis is computationally expensive as calculations may need days or weeks to finish. Furthermore, a very demanding professional expertise training is required for the engineers to be able to use sophisticated finite element codes and advanced constitutive laws introducing a multitude of material parameters. In this sense, more simple, fast and robust numerical methods are needed.

The concept of a macro-element was first introduced in geotechnics by Nova and Montrasio [76]. In general, a failure envelope and a constitutive law are implemented expressed in global variables (horizontal forces, overturning moments and vertical force). The constitutive law is usually formulated within the plasticity theory and the different directions are coupled. One can thus see the macro element as 3D non linear springs with coupling terms. Today, macro-elements provide useful tools for preliminary design and also a means to check the output of sophisticated numerical modeling [77].

The concept of macro-element can be illustrated in Fig. 2.39. The soil-foundation-superstructure system is subjected to a dynamic excitation at the bedrock denoted by $\ddot{u}$. Several nonlinear effects such as irreversible deformation of soil, radiation damping and uplift of structure are involved in the response of the system. It is usually very expensive to use FEM method to solve this kind of problem. However, this complex problem can be simplified by the macro-element. In the concept of macro-element, the entire foundation-soil system is replaced by a single element that is place at the base of the superstructure. All the nonlinear soil-structure effects will be reproduced properly by the non-linear constitutive law of the macro-element. The constitutive law in the macro-element level defines the constitutive relationship between generalized forces and displacements.

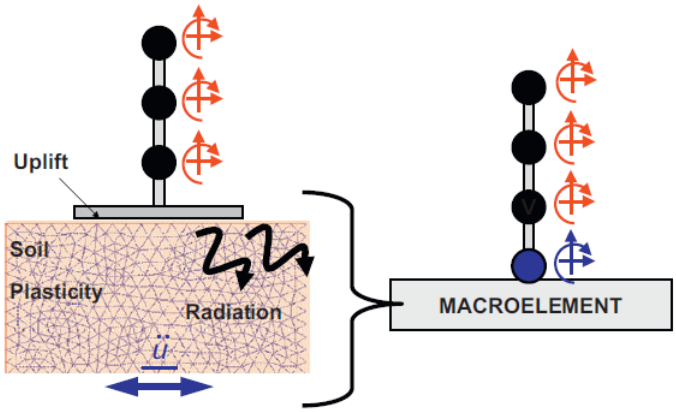

Figure 2.39: Generic soil-foundation-structure system subjected to dynamic loading and macro-element concept (after Chatzigogos et al. [18])

Various macro-elements for shallow foundations have been developed the previous years. Paolucci [78] introduced a perfect plastic model with a non-associated flow rule that can be applied for seismic calculations. Crémer et al. [79] used a non-associated plasticity model considering isotropic and kinematic hardening variables. Grange et al. [80] used the plastic theory of multi-mechanisms and failure surfaces that take into account an adequate overturning mechanism (uplift). The uplift effect is also considered in the macro-element developed by Chatzigogos et al. [81] and Shirato et al. [82]. Salciarini and Tamagnini [83] developed a hypoplastic macro-element for shallow foundations suitable for monotonic and cyclic loadings. Macro-element method and be applied on other geotechnical problems concerning soil-structure interaction. Cocchetti et al. [84] studied the soil-pipeline by means of macro-element.

For deep foundations, most of the researchers were inspired by the $p-y$ method and proposed 1D non linear uncoupled springs. Taciroglu et al. [85] and Rha & Taciroglu [86] generalized the classical $p-y$ approach by introducing the gaping and drag effects to consider soil pile interaction in a more realistic way. Boulanger et al. [87] used a dynamic beam on a nonlinear Winkler type foundation to analyze the seismic soil pile structure interaction of a single pile and validated the numerical results using dynamic centrifuge tests. Curras et al. [88] extended the dynamic beam approach for pile group systems. Gerolymos and Gazetas [89] [90] developed a Winkler model for rigid caisson foundations under static and dynamic loads. Varun [91] proposed a nonlinear Winkler type model and multiple $p-y$ curves to take into account pore pressure build-up and liquefaction.

Recent research works are however more close to the original idea of the macro-element proposed by Nova and Montrasio [76]. Davies and Budhu [92] proposed relatively simple formulations to evaluate the lateral stiffness of long elastic piles embedded in elastic soil but also to handle nonlinear soil pile interaction. Using their work as a starting point, Pender [77] introduced a pile head macro-element and improved the nonlinear response of the macro-element for cyclic loadings. However, the nonlinear behavior is reproduced by more or less a stiffness reduction method, no yield surface was defined in the macro-element. The performance of the macro-element was validated using results coming from a 3D finite element simulation. Gerolymos et al. [93] proposed the failure envelop curve and flow rules in the horizontal force overturning moment plane for caisson foundations. In 2011, António [94] developed a pile head macro-element for a single vertical pile in clay. He derived the failure envelop in a semi-analytical way and applied the classical bounding surface theory to implement the constitutive law. However, the influence of vertical load on the response is not considered.

In this dissertation, a macro-element in 3D H-M-V (horizontal force, overturning moment and vertical force) space was developed. The macro-element can be applied for both pile free-head and fixed-head conditions for single vertical pile; and also it can be applied for pile groups by simply introducing the group effect.

Chapter 3

Identification of dynamic properties of Fontainebleau sand by dynamic centrifuge tests

3.1 Introduction

In this chapter, the dynamic properties of Fontainebleau sand are identified by using dynamic centrifuge tests. Since the pile foundations are embedded in the sand deposit, the nonlinear properties of the sand play important role in the seismic response of pile foundation. A simple, robust and novel method to obtain the shear modulus degradation curve and the associated damping ratio is introduced in this chapter. The specific regression parameters, suitable for Fontainebleau sand, of the unified equation proposed by Ishibashi and Zhang [28] are identified and the influence of the confining pressure on the shear modulus reduction curves is taken into account. The identified shear modulus degradation curve is used to calibrate a simple hypoplastic constitutive law which is used in the finite element modeling. The proposed method for handling the hysteresis loops is used in the following chapter for analyzing the rocking and translation behavior of the pile foundations.

Taking into account the dependence of the shear modulus and the damping ratio on the shear strain is crucial in order to apprehend and simulate the cyclic behavior of soils. The accuracy of a numerical simulation largely depends on the quality of the identification of these soil dynamic properties. The calibrated constitutive law should be able to reproduce satisfactorily the monotonic loading back-bone curve and the cyclic (loading - reloading) behavior [95].

Laboratory tests on specimens (triaxial cyclic or resonant column tests) are usually used to estimate the dynamic properties of soils. Centrifuge tests can also be chosen as an alternative solution. Although definitely most costly, they avoid the physical constrains of the laboratory element tests [96], such as boundary conditions due to testing equipment and consolidation conditions. Furthermore, the stress path followed in the centrifuge tests is more realistic.

Several studies concerning the determination of soil properties from experimental strain-stress loops can be found in the literature. Pitilakis et al. compared the results obtained by numerical simulations with the stress-strain loops coming from centrifuge tests (calculated using the method proposed by Zeghal and Elgamal [97]) to verify the soil hysteretic response [98]. Elgamal et al. [99] studied the dynamic response of a saturated dense sand in a laminated centrifuge container to estimate

the shear modulus reduction and the damping ratio and identified a confinement dependence. Brennan et al. [96] reported some key techniques (such as influence of filtering, double integration technique and calculation of shear stress and shear strain) to evaluate the soil properties from dynamic centrifuge tests. Conti and Viggiani [100] proposed analytical expressions for the shear modulus and damping ratio of sand using nonlinear calibration with the experimental data.

This chapter presents a series of dynamic free field centrifuge tests on Fontainebleau sand with an embedded earthquake (dynamic loading) simulator [48] and an equivalent shear beam (ESB) container [101,102]. A general methodology is proposed for processing the experimental data avoiding large dispersion and the dependency of the shear modulus and the damping ratio on the shear strain is studied. The specific regression parameters, suitable for Fontainebleau sand, of the unified equation [28] are identified and the influence of the confining pressure on the shear modulus reduction curves is taken into account.

3.2 Dynamic centrifuge experimental program

3.2.1 Centrifuge tests set-up

3.2.2 Material properties and experimental set-up

The sand used in all the dynamic centrifuge tests is NE34 Fontainebleau sand with fine grain size and uniform distribution [103]. The sand mass was prepared by air pluviation technique at 1g gravity level. Its density was controlled to be 80%. Various measured material properties are listed in Table. 3.1.

Soil	e_{min}	e_{max}	e	ν	$D_r(\%)$	$\gamma_d(kN/m^3)$
Fontainebleau NE34	0.545	0.866	0.58	0.25	80%	16.155

Note: e:void ratio; ν:poisson ratio; γ_d:weight of sand; D_r: relative density of sand

Table 3.1: Fontainebleau sand NE34: Material properties [20]

During the experimental program, two tests (Test-01 and Test-02) were performed corresponding to two different input signals. To ensure that the properties of the sand in the tests were the same, in-flight cone penetration testing (CPT) was used. The maximum difference of the two CPT tests is about 5% which shows good repeatability of the experiments.

All the dynamic centrifuge tests were performed using dry sand under $40g$ gravity level (to avoid confusion in scales and dimensions, all the scales and dimensions in this chapter hereafter will be in the prototype scale). Accelerometers were buried into the sand during the air pluviation to measure accelerations at different depths, see Fig. 3.1. In the middle of the ESB container, a dense vertical array of accelerometers (from channels CH-02 to CH-16) was placed to capture the behavior of the soil column and thus to check any possible boundary effect of the container. The vertical distance between each sensor is about $1.2m$ in the prototype scale (i.e. $30mm$ in the

model scale). CH-29, CH-31 and CH-32 are used to verify the displacements from the measured accelerations using double integration.

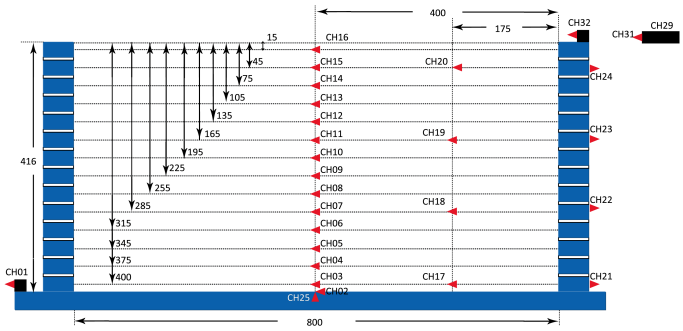

Notes: Dimensions are in mm (model scale).

Figure 3.1: Dynamic centrifuge tests: Experiment set-up

3.2.3 Input signals

The design of the base shaking is done considering different signal types, input intensities and frequency contents. Firstly, in order to make the identification process (relatively) easier, simple sinus signals were adopted. Secondly, signals with different intensities are used in order to be able to identify the shear modulus and damping ratio at different shear strain levels. Finally, signals with different frequency, within the shaker capacity, were selected to study the frequency dependence of the soil response.

The following two input signals were used: (1) a sine input signal with increasing and decreasing cycles (Signal-1), as shown in Fig. 3.2; and (2) a sine input signal with constant amplitude (Signal-2), as shown in Fig. 3.3. Two centrifuge tests were performed, and Signal-1 and Signal-2 were used in Test-1 and Test-2 respectively.

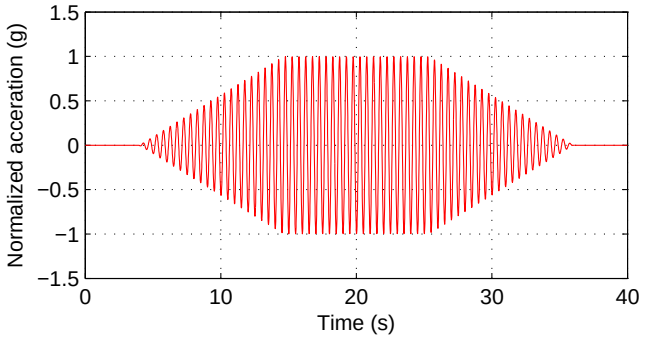

Figure 3.2: Dynamic centrifuge test - 1: Input wave Signal-1 with increasing and decreasing (normalized) amplitude cycles

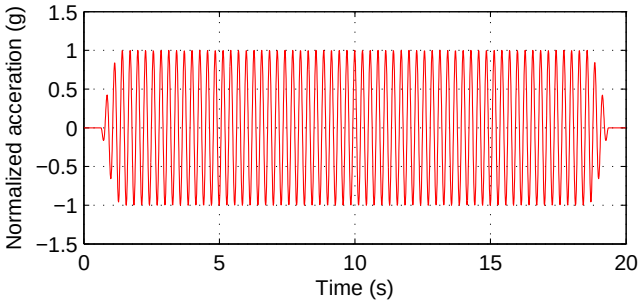

Figure 3.3: Dynamic centrifuge test - 2: Input wave Signal-2 with constant (normalised) amplitude cycles

The input signal sequences for Test-1 and Test-2 are given in Tables. 3.2 and 3.3. For Test-1, both frequency and amplitude varied. For Test-2 only the amplitude varied.

No.	Signal type	Max. Amplitude	Frequency
1	Signal-1	0.05g	2Hz
2	Signal-1	0.05g	2Hz
3	Signal-1	0.1g	2Hz
4	Signal-1	0.1g	2Hz
5	Signal-1	0.2g	3.5Hz
6	Signal-1	0.2g	3.5Hz
7	Signal-1	0.2g	4.5Hz
8	Signal-1	0.2g	4.5Hz
9	Signal-1	0.4g	4.5Hz
10	Signal-1	0.4g	4.5Hz

Note: Signal-1 is the sine signal with increasing and decreasing parts

Table 3.2: Test-1: Input sequence for Signal-1

No.	Signal type	Max. Amplitude	Frequency
1	Signal-2	0.05g	3.5Hz
2	Signal-2	0.05g	3.5Hz
3	Signal-2	0.1g	3.5Hz
4	Signal-2	0.1g	3.5Hz
5	Signal-2	0.2g	3.5Hz
6	Signal-2	0.2g	3.5Hz
7	Signal-2	0.4g	3.5Hz
8	Signal-2	0.4g	3.5Hz

Note: Signal-2 is the sine signal with constant amplitude

Table 3.3: Test-2: Input sequence for Signal-2

Based on previous experimental campaigns performed at the centrifuge facility, the fundamental frequency of the soil column was estimated approximately equal to $3.5Hz$ in the prototype scale ($140Hz$ in the model scale). This is why the frequency content of the input waves was set in the range between $2Hz$ to $4.5Hz$ (prototype scale).

3.3 Shear modulus

3.3.1 Maximum shear modulus profile

The maximum shear modulus G_{max} profile at small-strain level is a key parameter for geotechnical problems. Different studies have shown that for fine grained sand, the G_{max} profile depends on the void ratio and the effective confining pressure [104–106]. The following formula proposed by Hardin and Drnevich [107] is often used to estimate the G_{max} profile:

$$G_{max} = A \cdot \frac{(B-e)^2}{(1+e)} \cdot {\sigma_c}^C \tag{3.1}$$

where: G_{max} is in MPa, e the void ratio (0.52 for the Fontainebleau sand at relative density 80%) and σ_c the confining pressure. A, B and C are constants taken as 200, 2.17 and 0.47 respectively (Delfosse-Riday et al. [103]). The confining pressure σ_c is calculated by :

$$\sigma_c = \frac{(1+2K_0)\gamma_d z}{3} \tag{3.2}$$

z being the depth and γ_d the unit weight of the sand. K_0 expresses the lateral soil pressure coefficient exerted by the soil at rest. The general form of K_0 is:

$$K_0 = \frac{\nu}{1-\nu} \tag{3.3}$$

where ν is the Poisson ratio of the sand. For the specific case of centrifuge physical modeling, Gaudin [108] proposed the following equation to determine K_0 (with D_r the relative density of the sand, see Fig. 3.1):

$$K_0 = -\frac{1}{2.9} D_r + 0.63 \tag{3.4}$$

In our case, the values obtained from Figs. 3.3 and 3.4 are 0.333 and 0.354 respectively. In the following, K_0 is taken equal to 0.354.

Another way to calculate the G_{max} profile is to use the shear wave velocity at different soil layers. In dynamic centrifuge experiments, the shear wave velocity profile can be calculated by determination of the time delay (cross-correlation) of the signals between pairs of accelerometers. In order to be certain that the shear wave velocity corresponds to a small-strain level (i.e. the sand being in the elastic or in the nearly elastic range), only the experimental data from low intensity exciting signals are adopted hereafter. During the experimental campaign, two low intensity

signals were introduced (the sine signal input $2g - 2.0Hz$ and the sine signal input $2g-3.5Hz$). Since the natural frequency of the sand column is approximately $3.5Hz$ in the prototype scale only the data from the $2g - 2.0Hz$ signal are used hereafter to calculate the shear wave velocity to avoid possible nonlinear responses due to amplification phenomena. The strain level is estimated to be about $6.16 \times 10^{-3}\%$ (calculated by double integration). The qualitative representation of the signal delay is shown in Fig. 3.3.1.

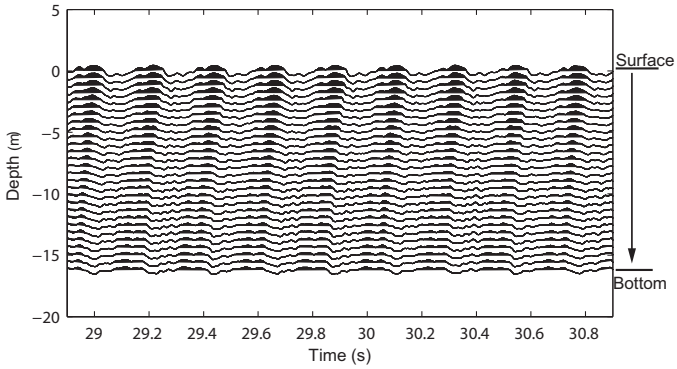

Figure 3.4: Dynamic centrifuge tests: Seismogram of the input signal sine $2g-80Hz$

Based on the signal delay (computed by cross-correlation) between the soil layers, the shear wave velocity is calculated and the shear modulus profile can be determined from Fig. 3.5.

$$G_{max} = \rho V_s^2 \tag{3.5}$$

where ρ and V_s are the density of the soil and the shear wave velocity respectively.

The shear wave velocity for depths $0 \sim -6m$, $-6m \sim -12m$ and $-12m \sim -16m$ are respectively calculated as $205.7m/s$, $246.0m/s$ and $311.8m/s$. The maximum shear modulus profiles are calculated using Eqs. 3.1 and 3.5 and the results are compared in Fig. 3.5. The comparison can be only qualitative, however the two curves follow the same trend and show significant correlation.

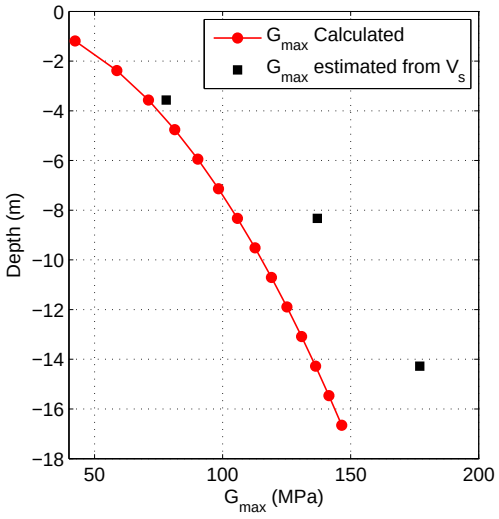

Figure 3.5: G_{max} profiles using Eqs. 3.1 (red) and 3.5 (black)

3.3.2 Shear modulus evolution

3.3.2.1 Shear stresses

In centrifuge tests, shear stresses can be calculated indirectly using the accelerometers measurements [96], [97] according to the following equation:

$$\tau(z) = \int_0^z \rho \ddot{u} \, \mathrm{d}z \tag{3.6}$$

where τ is the shear stress at depth z and $\ddot{u}$ the absolute acceleration. It is obvious that the accuracy of the calculation depends on the acceleration profile. Thanks to the large number of accelerometers placed in the tests (see Fig. 3.1), detailed acceleration profiles can be obtained by fitting the acceleration data points as shown in Fig. 3.6. Using a simple Newton-Cotes formula for the numerical integration (e.g. trapezoidal integration) the shear stresses can thus be obtained. Results are shown in Fig. 3.6 for a specific time t (Test-01, input signal with increasing and decreasing parts (0.2g 3.5Hz)). The trend of the acceleration profile is shown by a spline fitted curve.

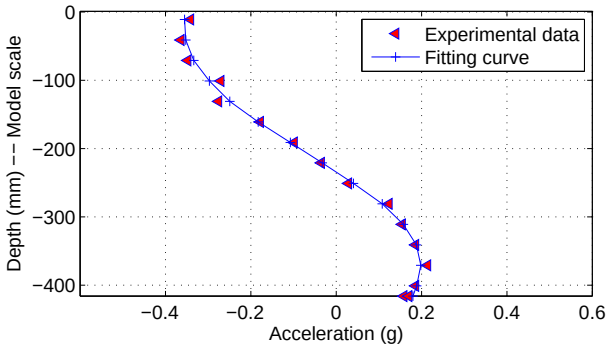

Figure 3.6: Acceleration profiles at specific time t

3.3.2.2 Shear strains

Double integration is used to calculate shear strains in the different soil layers, a procedure that is also necessary to avoid drifting of the results [96]. CH-29 (Fig. 3.1) is a laser sensor that measured the distance between the two black blocks. CH-31 and CH-32 are two accelerometers that can be used to measure the same distance. The comparison for the Signal-1 is shown in Fig. 3.7 (a similar comparison was also performed for the Signal-2). The good agreement of the comparison indicates the validation of the adopted double integration process.

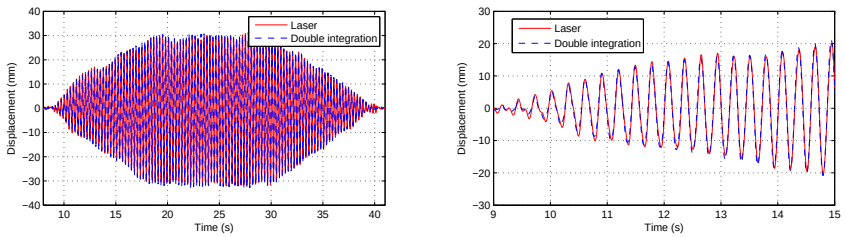

(a) Comparison of the results using double-integration and the laser sensor sensor

(b) Zoomed view

Figure 3.7: Verification of the double-integration procedure: comparison of the results using double-integration and the laser sensor (a) and zoom view (b)

By applying a double-integration process on the discrete acceleration data, the displacement u_i at each sand layer z_i can be calculated. Zeghal and Elgamal [97] used an average shear strain equation to study data from earthquake records based on the first order derivative with respect to depth. In this chapter, due to the important numbers of accelerometers used in the experiment, higher order formulas are applied for the calculation of the shear strains: first order (Eq. 3.7), second order (Eq. 3.8) and forth order (Eq. 3.9) respectively.

$$\gamma_i = \frac{u_i - u_{i+1}}{h} \tag{3.7}$$

$$\gamma_i = \frac{u_{i-1} - u_{i+1}}{2h} \tag{3.8}$$

$$\gamma_i = \frac{-u_{i-2} + 8u_{i-1} - 8u_{i+1} + u_{i+2}}{12h} \tag{3.9}$$

Remark: When using the forth order formula, four accelerometers are necessary. At the bottom or near the top of the ESB container only the first or second order formulas have thus been used.

A schematic representation of the calculated shear strains is shown in Fig. 3.8. It is obvious that when using the first order formula, the shear strain profile is not continuous. For higher order formulas however, smoother, more realistic profiles are obtained.

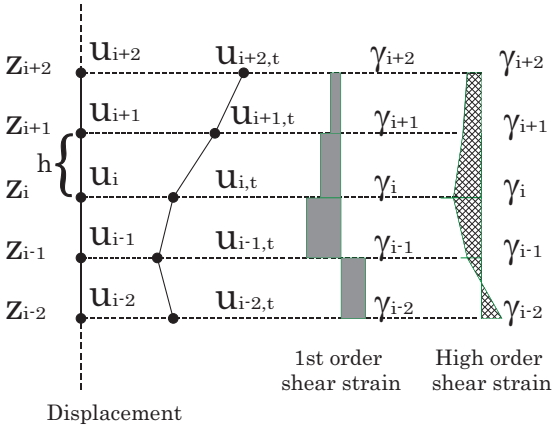

Figure 3.8: Shear strain profiles using different order formulas

3.3.2.3 Shear stress Vs. shear strain loops

The typical responses of the Fontainebleau sand in terms of hysteresis loops (shear stress Vs. shear strain) at different depths are shown in Fig. 3.9 (Test-2, input signal with constant amplitude, 0.4g, 3.5Hz). The shear strain level at the top layers is 0.55% while at the bottom layer is about 0.05%. Compared to the small shear strain level (6.16×10^{-3}%) used to estimate the shear wave velocity in the previous section, it is evident that important nonlinearites developed at different depths and different confining pressures (especially at the top layers). Almost all the loops are well centered, which makes easier the identification of the hysteretic response of the sand. It is also observed, qualitatively, that the slop of the loop axis increases with increasing confining pressure.

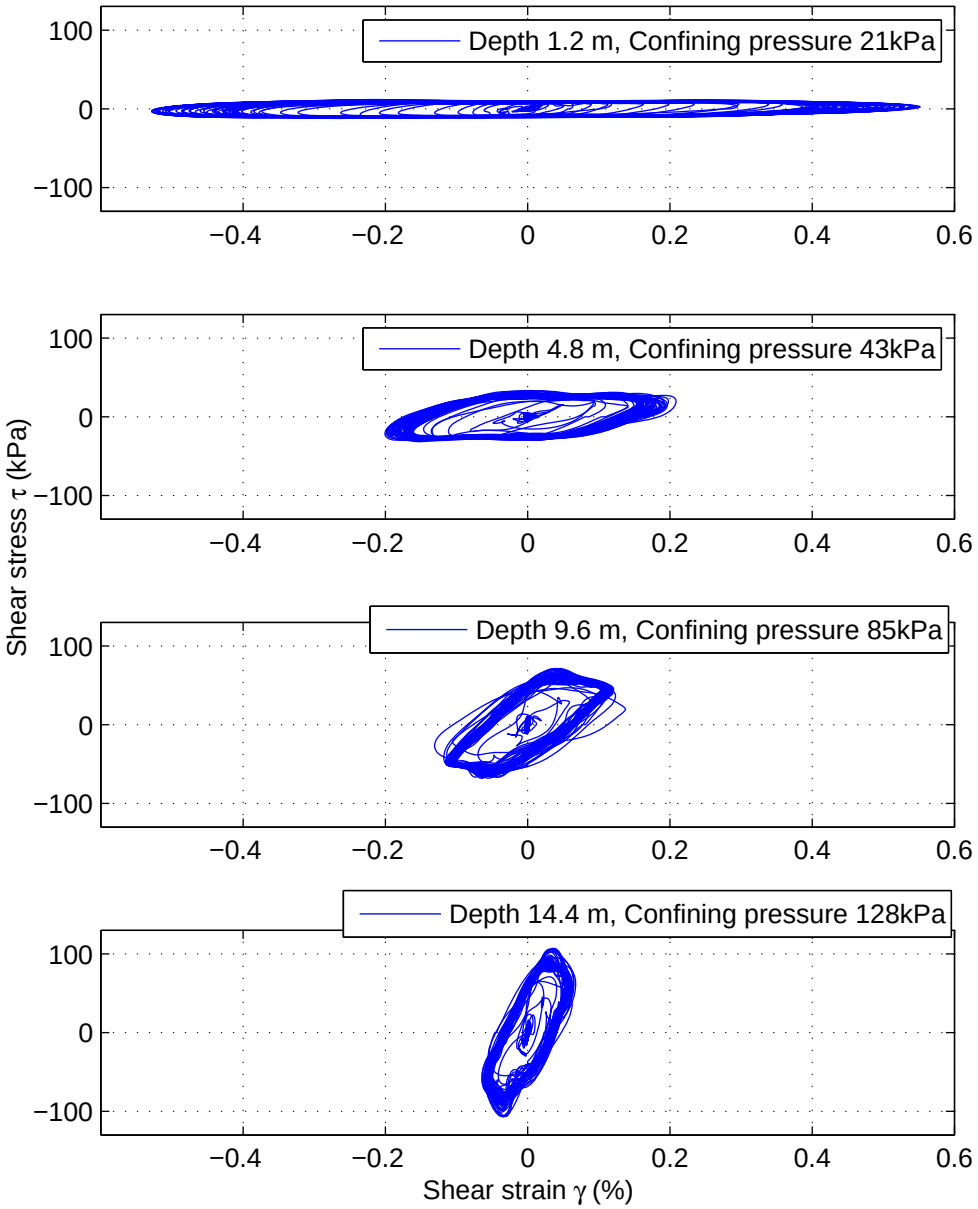

Figure 3.9: Dynamic centrifuge tests: Shear stress Vs. shear strain loops at different depths

3.3.2.4 A post processing strategy to quantify the variation of the shear modulus with respect to the shear strain

Quantifying the degradation of the shear modulus with respect to the shear strain and this for the whole range of loading is not an easy task since the experimental data are often distorted and polluted by noise (e.g. background white noise or high frequencies). This is particularly true in the small strain range ($1 \times 10^{-4}\% \sim 3 \times 10^{-3}\%$), as shown in Fig. 3.10(a) (depth 1.2m with confining pressure $11kPa$). The distorted hysteresis loops make impossible to read the "correct" shear modulus (or the damping ratio, see Fig. 3.4) [96]. A post processing strategy is proposed hereafter to quantify the variation of the shear modulus with respect to the shear strain. The main ideas are:

- It is observed that when putting together several distorted hysteresis loops, the new group tends to be more "smooth" and representative of the soil behavior. For example, in 3.10 the grouped hysteresis loops indicate a linear behavior for a small strain level around $\pm 2.5 \times 10^{-3}\%$. One should thus select adequately a group of hysteresis loops corresponding to the same shear strain level.

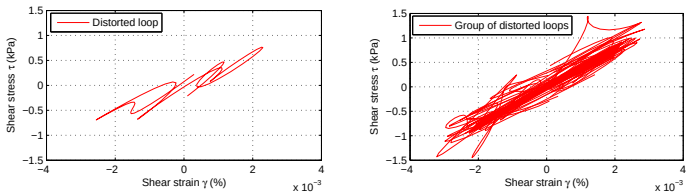

(a) Signal distorted loop (b) Group of distorted loops

Figure 3.10: Dynamic centrifure tests: Distorted hysteresis loop (a) and group of distorted hysteresis loops (b)

- For a complete centrifuge test, different groups of hysteresis loops corresponding to the same shear strain levels should be carefully chosen. For each group, the corresponding average loop can be found and used to calculate the shear modulus (or the damping ratio, see Fig. 3.4).

- The method to find the average loop is illustrated in Fig. 3.11. Each group of loops is divided into two parts using a cutting plane (in Fig. 3.11, see the double dash line connecting the two points with maximum distances from the center of the loops). For the upper and the lower part, the mean values at different cross-sections ($S1\,S2$ ... Sn) can be found. The average loop is the one passing through all the mean values points.

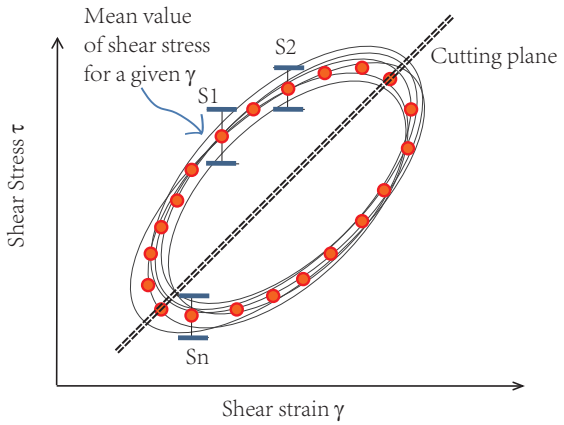

Figure 3.11: The method to find the average loop

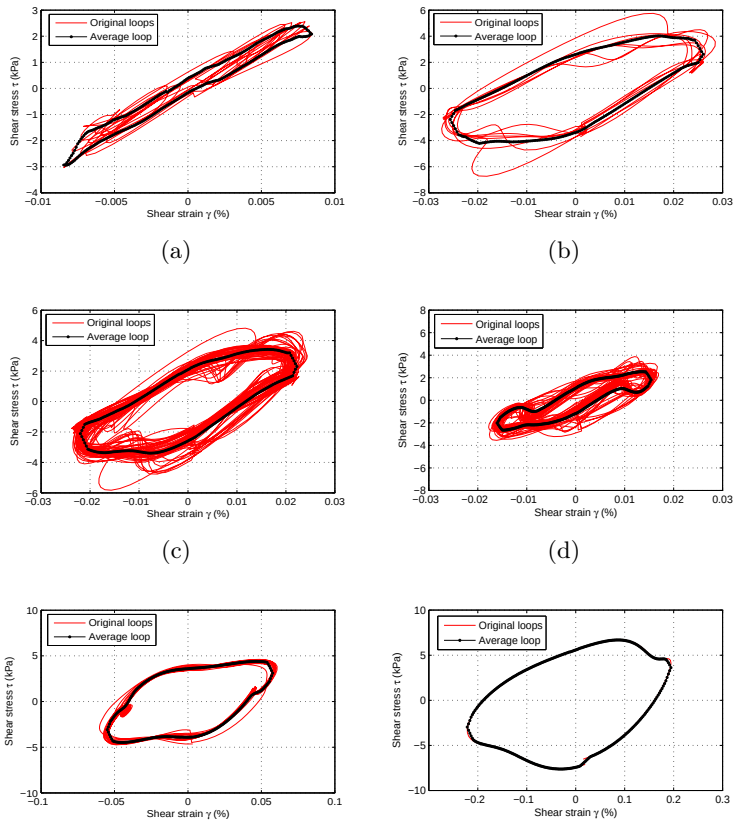

Figure 3.12: Dynamic centrifuge tests: Calculating the average loop at different depths (a) 0.6m (confining pressure 11 kPa); (b) 1.2m (confining pressure 43 kPa); (c) 4.8m (confining pressure 75 kPa); (d) 9.6m (confining pressure 96 kPa); (e) 14.4m (confining pressure 117 kPa); (f) 16.0m (confining pressure 149 kPa)

The proposed strategy is applied hereafter to the whole range of the dynamic centrifuge experimental data. As shown in Figs. 3.12(a), 3.12(b), 3.12(c), 3.12(d) and 3.12(e) the method captures the average behavior for all the different loading steps. In Fig. 3.12(a), corresponding to a small shear strain level, the average loop is characteristic of an (almost) linear response. The non linear behavior is obvious in Figs. 3.12(b), 3.12(c), 3.12(d) and 3.12(e) when looking at the size of the hysteresis loops. The proposed method gives satisfactory results even for complicated patterns (see Fig. 3.12(d)). If just one single loop exists, the average loop reduces to this single loop. Furthermore, even if this single loop is open, the average loop is closed (see Fig. 3.12(f)).

The final step is to calculate the equivalent shear modulus (Fig. 3.13) according to Fig. 3.10.

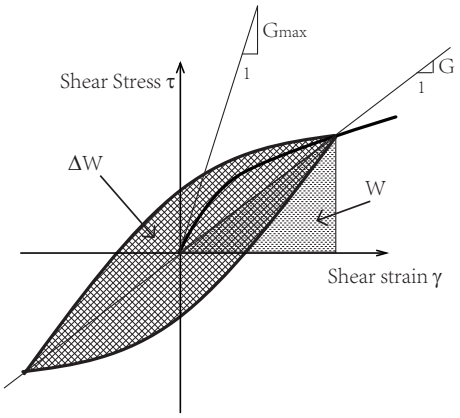

Figure 3.13: Equivalent shear modulus (G), elastic stored strain energy (W) and dissipation energy (ΔW)

$$G = \frac{\tau_{max} - \tau_{min}}{\gamma_{max} - \gamma_{min}} \tag{3.10}$$

Applying the previous procedure to the experimental data coming from the two different sine inputs (Fig. 3.2 and Fig. 3.3) the shear modulus is calculated hereafter. In Fig. 3.14 (depth of $1.8m$), one can see that results are similar for the two input loadings. This was also verified at different depths of the container, see Fig. 3.15 (depth of $5.4m$). It also proves that the response of the sand is, as often quoted in the literature [106, 109–111], hysteretic and frequency independent.

In the following, the data coming from the two sine inputs are merged in order to have a relatively large database of the sand response.

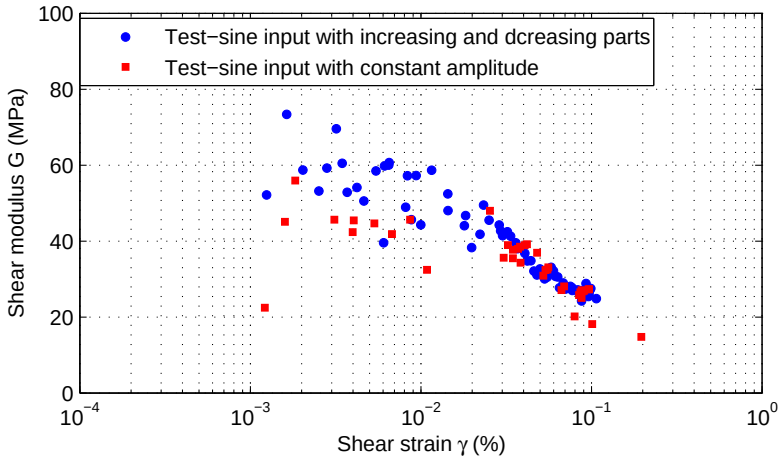

Figure 3.15: Dynamic centrifuge tests: Shear modulus Vs. shear strain of the Fontainebleau sand layer at depth $5.4m$ (confining pressure $53kPa$) – two types of loading signal

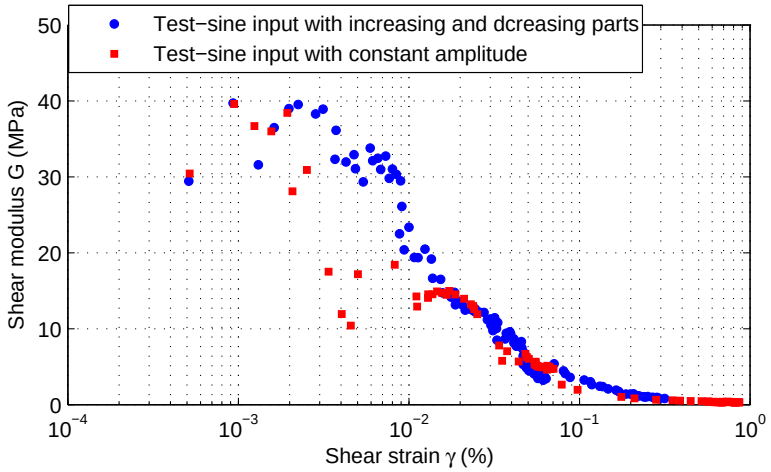

Figure 3.14: Dynamic centrifuge tests: Shear modulus Vs. shear strain of the Fontainebleau sand layer at depth $1.8m$ (confining pressure $21kPa$) – two types of loading signal

3.3.2.5 Empirical equation

The evolution of the soil shear modulus and shear strain during a cyclic are mainly controlled by the confining pressure and the soil plasticity index. The effect of the confining pressure has been studied by Hardin et al. [107] and Iwasaki et al. [106]. Kokusho [112] and Ishibashi [113] have found that its effect is more pronounced for soils with a low plasticity index. Ishibashi and Zhang [28] have proposed an empirical equation linking the maximum shear modulus G_{max}, the confining pressure σ_c,

the shear strain γ, the plastic index PI and two parameters $K(\gamma)$ and $m(\gamma) - m_0$ that control the evolution of the shear modulus. Specific values of these parameters (computed by nonlinear regression) for the Fontainebleau sand are proposed hereafter, fitted with the dynamic centrifuge experimental data.

Since dry Fontainebleau sand was used in the experimental campaign was dry, the plastic index is taken equal to $PI = 0$. The empirical equation takes the following simplified form (γ in (m/m) and σ_c in (kPa)):

$$\frac{G}{G_{max}} = K(\gamma){\sigma_c}^{m(\gamma)-m_0} \tag{3.11}$$

$K(\gamma)$ and $m(\gamma) - m_0$ are tuned to fit the dynamic centrifuge experiment data and are calculated according to Eqs. 3.12 and 3.13. The comparison of the empirical equation results and the experimental data at different depths (confining pressures) is presented in Fig. 3.16.

$$K(\gamma) = 0.5\left[1 + tanh\left\{ln\left(\frac{0.000102}{\gamma}\right)^{0.613}\right\}\right] \tag{3.12}$$

$$m(\gamma) - m_0 = 0.34\left[1 - tanh\left\{ln\left(\frac{0.000556}{\gamma}\right)^{0.4}\right\}\right] \tag{3.13}$$

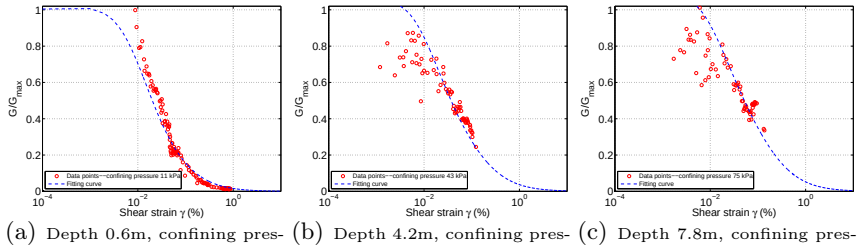

(a) Depth 0.6m, confining pressure 11 kPa (b) Depth 4.2m, confining pressure 43 kPa (c) Depth 7.8m, confining pressure 75 kPa

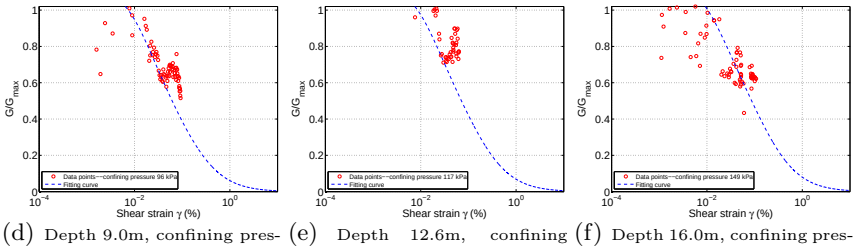

(d) Depth 9.0m, confining pressure 96 kPa (e) Depth 12.6m, confining pressure 117 kPa (f) Depth 16.0m, confining pressure 149 kPa

Figure 3.16: Evolution of the Fontainebleau sand shear modulus normalized by G_{max} at different depths. Experimental data Vs. empirical equation results

The proposed equations for $K(\gamma)$ and $m(\gamma) - m_0$ combined with Eq. 3.11 capture the behavior of the Fontainebleau sand for different confining pressure levels. The influence of the confining pressure level (CP) is more highlighted in Fig. 3.17 (the

precision of the processed data is enough to limit the dispersion of data points especially for high confining pressures). For high confining pressures the experimental data become more scattered with higher uncertainties. For the same shear strain level, the increase of confining pressure induces higher G/G_{max} ratio. Also, high confining pressures increase the elastic range of the sand.

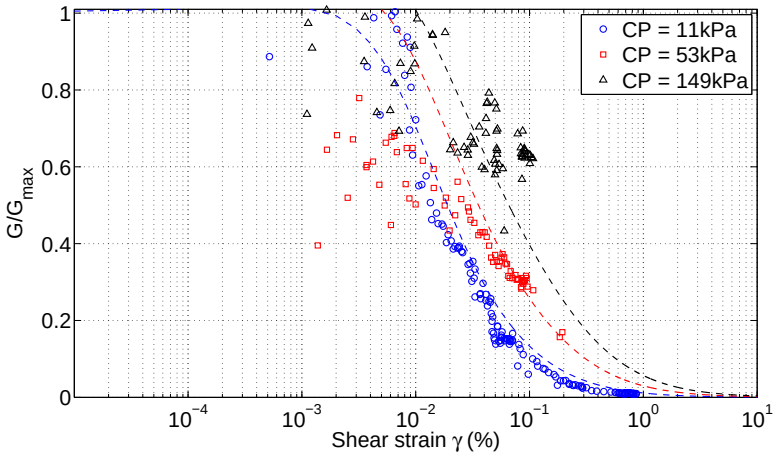

Figure 3.17: Influence of the confining pressure (CP) on the evolution of the Fontainebleau sand shear modulus. Experimental data Vs. empirical equation results

3.4 Damping ratio

3.4.1 A post processing strategy to quantify the variation of the damping ratio with respect to the shear strain

The post processing method detailed in 4.2.4 is applied hereafter in order to obtain the average loops at different depths, Fig. 3.12. The equivalent damping ratio can then be estimated using Eq. 3.14, considering the dissipated energy ΔW and the maximum elastic energy W stored at each loop, see 3.13.

$$D = \frac{1}{2\pi} \frac{\oint \tau d\gamma}{0.25 \Delta\tau \Delta\gamma} = \frac{1}{4\pi} \frac{\Delta W}{W} \tag{3.14}$$

The application of the procedure to the dynamic centrifuge experimental data gives the results presented in Figs. 3.18 and 3.19. Although results present a higher dispersion at low strain level, the damping value is estimated to be around 5%. In other words, even at small strain level there is a certain energy dissipation.

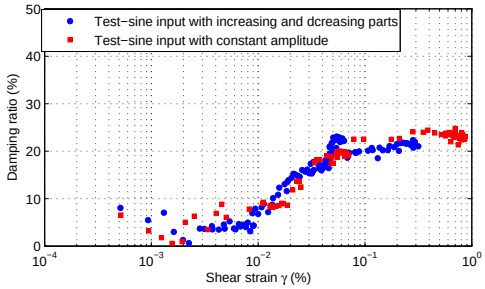

Figure 3.18: Dynamic centrifuge tests: Damping ratio Vs. shear strain of the Fontenebleau sand at depth $1.8m$ (confining pressure $21kPa$) - two types of loading signals

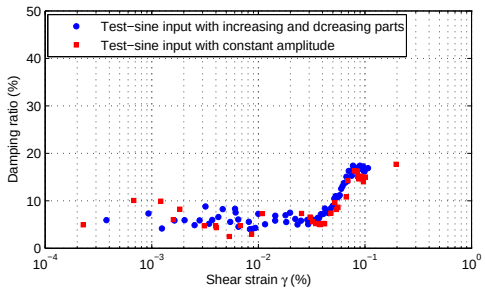

Figure 3.19: Dynamic centrifuge tests: Damping ratio Vs. shear strain of the Fontenebleau sand at depth $5.4m$ (confining pressure $53kPa$) - two types of loading signals

3.4.2 Empirical equation

Hardin and Drnevich [107] and Tatsuoka et al. [114] proposed a formula where the damping ratio D is expressed as a function of G/G_{max}, Fig. 3.15. Ishibashi and Zhang [28] extended its application for high plastic soils introducing the influence of the plastic index PI.

For the case of the (dry) Fontainbleau sand used in the dynamic centrifuge tests, the expression takes the form of Eq. 3.16 after the appropriate fitting (damping is expressed as percentage (%)):

$$D = f(\frac{G}{G_{max}}) \Rightarrow \tag{3.15}$$

$$D = 25.3 \left\{ 0.513 \left(\frac{G}{G_{max}} \right)^2 - 1.351 \left(\frac{G}{G_{max}} \right) + 1 \right\} \tag{3.16}$$

The fitting curve of the damping ratio is plotted together with the data points from all the 14 sand layers for confining pressures ranging from $11kPa \sim 149kPa$ in Fig. 3.20. It is found that the damping ratio increases with the reduction of the shear

modulus. This type of graph gives us the possibility to quantify the damping ratio directly from G/G_{max} without plotting the damping Vs. shear strain relationships. One can see that when G/G_{max} reaches its maximum value 1, the damping ratio is about 4.1%. This is in accordance with the results of Lanzo and Vucetic [115] that even at small strain levels, there exists some energy dissipation. Using Eq. 3.16, the damping ratio at different different depths (confining pressures) with respect to the shear strain is plotted in Fig. 3.21.

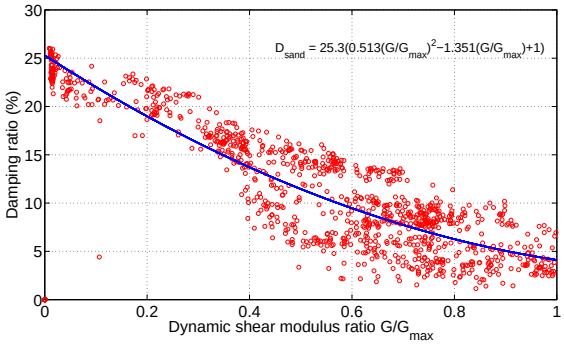

Figure 3.20: Relationship between dynamic shear modulus and damping ratio

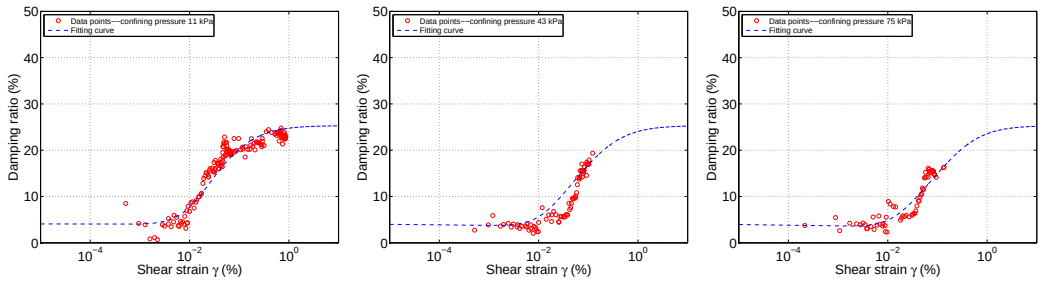

(a) Depth 0.6m, confining pressure 11 kPa

(b) Depth 4.2m, confining pressure 43 kPa

(c) Depth 7.8m, confining pressure 75 kPa

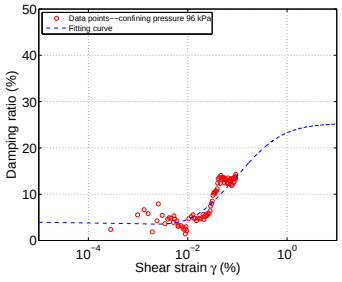

(d) Depth 9.0m, confining pressure 96 kPa

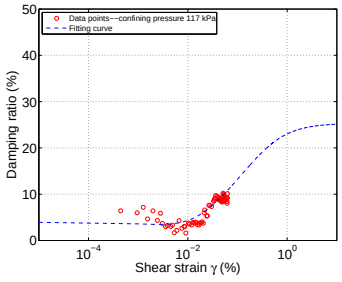

(e) Depth 12.6m, confining pressure 117 kPa

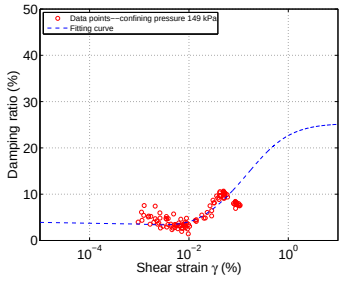

(f) Depth 16.0m, confining pressure 149 kPa

Figure 3.21: Evolution of the Fontenebleau damping ratio at different depths. Experimental data Vs. empirical equation results

The influence of the confining pressure on the damping ratio is obvious. For the same shear strain, low pressure confined sand has a larger damping ratio, Fig. 3.22.

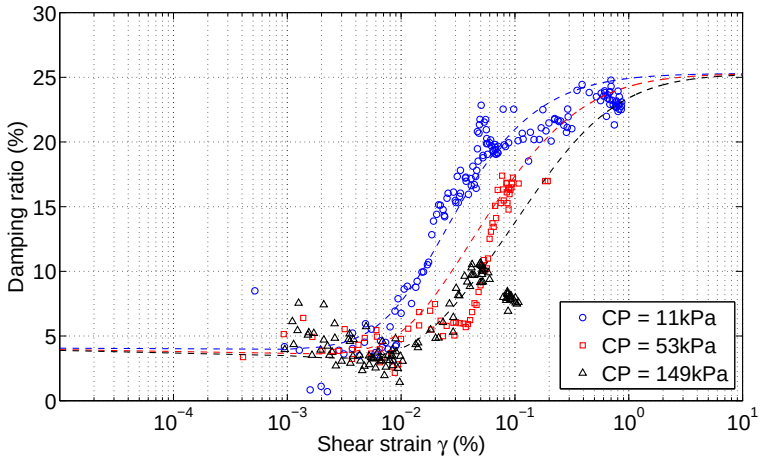

Figure 3.22: Influence of the confining pressure (CP) on the evolution of the damping ratio of the Fontenbleau sand. Experimental data Vs. empirical equation results

3.5 Conclusions

In this chapter, dynamic centrifuge tests based on free field conditions were performed in order to identify the Fontainebleau sand properties. An important number of sensors was used to capture the response of the centrifuge model. A post processing strategy was proposed (with less dispersion compared to previous studies) based on the definition of average loops and the evolution of the shear modulus and the damping ratio was quantified. Empirical equations from the literature were validated and specific regressed numerical values are proposed for the Fontaineblau sand. It is found that confining pressure has an important influence on both the shear modulus evolution and the damping ratio. A low pressure confined sand tends to have a larger damping ratio and a greater shear modulus reduction. The high confining pressure tends to enlarge the elastic range of sand.

Chapter 4

Performance of inclined piles under dynamic excitations

As mentioned in Chapter 2, the beneficial or detrimental role of inclined piles is not yet clarified. The existing studies mainly focus on the interactions between soil and piles but less attention has been paid on the influence of the superstructure on the effect of inclined piles. However, a recent numerical study performed by Giannakou et al. [9, 27] has shown that for a comprehensive evaluation of the performance of inclined piles the influence of the superstructure or the inertial response from the upper structural system have to be taken into account. Based on the numerical results obtained by Giannakou (see chapter 2), a series of centrifuge tests have been performed. Short (squat) and tall (slender) superstructures are designed in order to study the influence of the inertial loading coming from the different types of superstructure on the performance of inclined piles. The short superstructure represents a shear force dominated loading case; the tall building represents an overturning moment dominated loading case. A symmetric configuration of inclined piles with a 15° inclination is adopted and results are compared with the ones from a vertical pile group. For both configurations, rigid connections are imposed by a stiff pile cap. The different behaviors of the two configurations under dynamic excitations are analyzed and discussed. Some key issues concerning the performance of the inclined piles are the following: residual bending moment, dynamic bending moment, axial force, rocking behavior, horizontal translation behavior etc. In this chapter, the experimental program and set-up are first introduced. Then some assumptions, notions, terms and explanations concerning the analysis and interpretation of the experimental data are discussed. Finally, the results concerning the performance of inclined piles are presented.

4.1 Experimental set-up and program

4.1.1 Introduction of experimental program

For this experimental study, all the tests have been performed at 40g level. Two types of tests have been made: tests with real earthquake signals and tests with sinusoidal signals. The first group of tests aims to work out the performance of inclined piles for a general loading case, while the second to further highlight the parameters that influence the behavior of the inclined piles. In both cases, the effect of the height of the gravity center of the superstructure on the behavior of the inclined

piles is also studied. Tests with real earthquake signals have been first performed on pile groups without a superstructure and then with both short and slender superstructures. Based on the results obtained in these tests, the gravity center of the slender superstructure is increased 2 times for the tests with the sinusoidal signals in order to highlight its influence. The different model configurations used in the dynamic centrifuge tests are shown in Fig. 4.1 for the case of the inclined pile group. For each configuration the response is compared to that of an equivalent configuration with vertical piles. The case of a pile group without superstructure is aimed to investigate the performance of inclined piles in terms of "kinematic interaction".

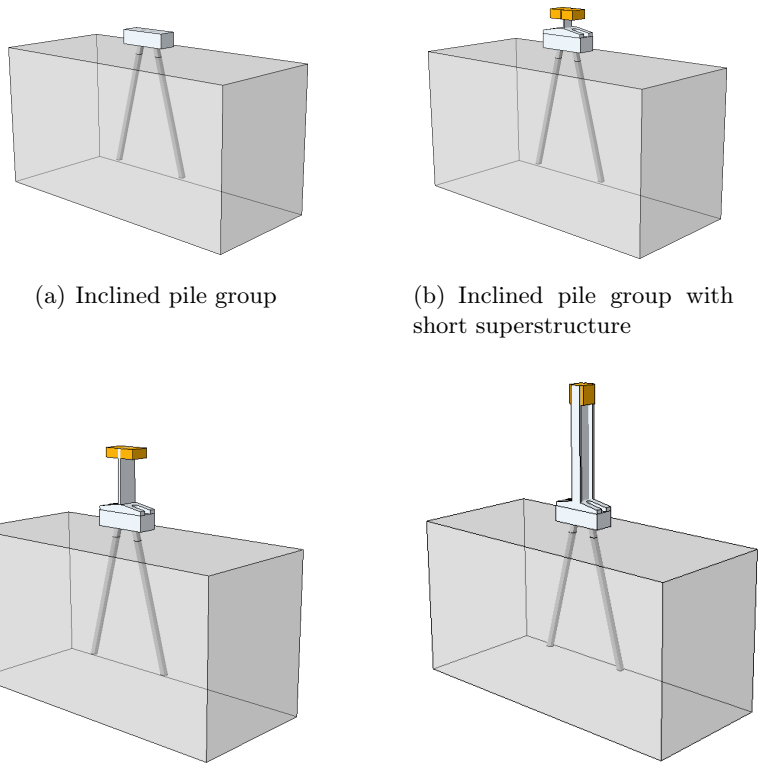

(a) Inclined pile group

(b) Inclined pile group with short superstructure

(c) Inclined pile group with slender superstructure

(d) Inclined pile group with very slender superstructure

Figure 4.1: Model configurations used in the dynamic centrifuge tests

The performed dynamic centrifuge tests can be classified according to the pile group configurations and test objectives presented in Table. 4.1. In this section, the design considerations of the centrifuge tests, the experimental set-up, the centrifuge modeling process and the sensor arrangement are introduced.

Signals	Test contents	Objectives	Configurations	Responses
Real earthquake test	Free-field test	Determination of ***soil column resonant frequency***		Soil response
	Inclined and vertical pile group tests	***"kinematic interaction"***	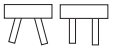	Soil - pile - cap interaction
	Inclined and vertical pile group with short and tall superstructures	Effect of inclined piles with (***kinematic interaction + inertial interaction***) taking into account the influence of ***gravity center*** of superstructure when subjected to real earthquake excitations	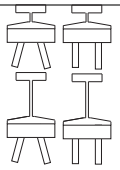	Soil - pile - superstructure interaction
Sinusoidal test	Inclined and vertical pile group with short and taller superstructures	Effect of inclined piles with (***kinematic interaction + inertial interaction***) taking into account the influence of ***gravity center*** of superstructure subjected to sinusoidal excitations	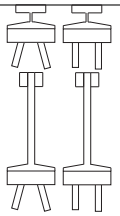	

Table 4.1: Summary of experimental program

4.1.2 Base shaking signals

In this study, the design of a dynamic centrifuge test is composed of four elements: the soil column, the pile foundation, the superstructure and the base shaking. The relations between the response frequency of each component and the frequency content of the base shaking can play an important role. Consequently, the selection of the base shaking signals should take into account the dynamic properties of the experimental centrifuge test set-up and the capacity of the shaker. Concerning the IFSTTAR shaker [48], there are two main limitations for selecting, or design the input signals. The frequency contents of the signal must be limited within the working frequency range of the shaker. The maximum displacement, velocity and acceleration cannot go beyond the limit of the shaker (+/-5mm, 1m/s and 50% of the g-level, at model scale, respectively). At 40g, the working frequency range of the shaker is, at the prototype scale, from 1.25 Hz to 5.0 Hz for the sinusoidal signal; and from 0.5 to 8.75 Hz for the real earthquake input.

Selection of real earthquake signals

The two main objectives of the real earthquake tests are to determine the response frequencies of the soil column and the soil-pile-superstructure system and to analyze the performances of inclined piles when subjected to multiple-frequencies base shaking. In this framework, 3 different earthquakes are selected. The first two earthquakes are the Martinique Jara and the Northridge signals. Both are broad-band frequency range earthquakes (the frequency contents of the two signals are shown in Fig. 4.2(a) and (b)). The use of these two earthquakes should enable the determination of the frequency response of the soil column and the soil-pile-superstructure system. For the determination of the frequency of the soil column, the two signals

are attenuated to have small intensities in order to avoid significant plasticity in the soil. The third signal is a recording of the Kobe earthquake. Most of the energy of the Kobe earthquake comes from frequencies below 2.0 Hz, see in Fig. 4.2(c), and thus below the prior response frequencies of both the soil column and the soil-piles-structure system. To be in the capacity range of the shaker, these three earthquake signals have been filtered within the frequency range of 20∼350 Hz. The Northridge signal is attenuated by -9 dB and the Kobe earthquake by -4 dB.

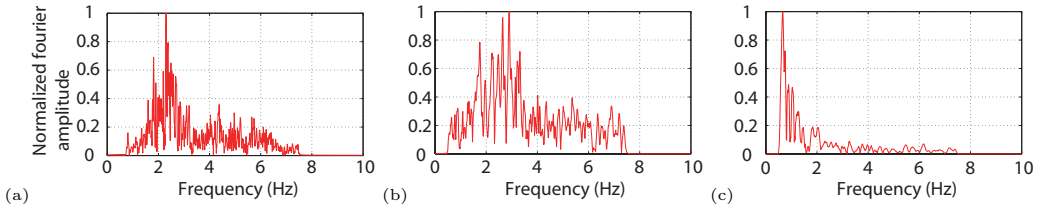

Figure 4.2: Frequency representations of the base shaking: (a) Martinique Jara, (b) Northridge earthquake and (c) Kobe earthquake

Selection of sinusoidal signals

The main objectives of the tests using the sinusoidal signals are to highlight the effect of the input frequency and its amplitude on the performance of the inclined pile group. The selection of the input frequency is made by taking into account the frequency range of the shaker and the determined frequency response of both the soil column and the soil-pile-superstructure system.

The resonant frequency of soil column was identified by series of free-field tests. The soil column was subjected to small amplitude broad-band real earthquake excitations. The resonant frequency was experimentally determined based on the analysis of the transfer function between the horizontal acceleration measured near the soil surface and near the bottom of the soil column. Appendix B, Fig. B.2 shows the amplitude and the phase angle of the transfer function estimated from the free-field tests. The frequency of soil column is estimated in the range between the two dashed lines i.e. 3.5∼3.7 Hz.

Based on the series of earthquake tests, the response frequencies of the soil-pile-group systems has been determined around 6.0 Hz for vertical pile group and around 10.0 Hz for inclined pile group. It can be noted that the frequencies for inclined pile group and vertical pile group are out of the working frequency range of shaker for sinusoidal signals.

Fig. 4.3 shows the frequency characteristics of each component in the experimental system. Considering the working frequency range of the shaker, the first selected frequency is in the vicinity of the soil column response: 3.5 Hz. In order to highlight the influence of the superstructure (inertial loading) and not be mixed up with the influence of the soil column, it is better for the frequency of the superstructure to be far away enough from the possible frequency range of soil column (from 2.5 Hz to 4.0 Hz). Naturally, 2.0 Hz is selected for the frequency of the superstructure. 2.0

Hz is the second frequency selected for the input.

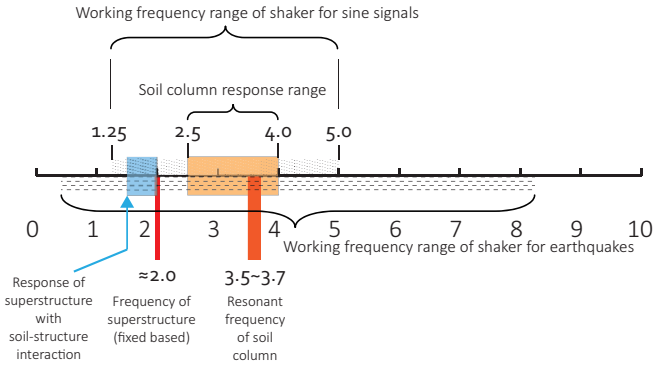

Figure 4.3: Resonant frequency of soil column in free-field condition

4.1.3 Built-up of centrifuge models

Basic elements concerning the physical centrifuge models are: soil deposit with controlled homogeneous properties, piles instrumented with strain gauges, stiff pile caps and superstructures. Besides the basic elements, accelerometers and laser sensors are also installed to get information of the behavior of the soil-pile-superstructure system.

Properties of experimental set-up components: sand, piles, pile caps, superstructures, and pile group systems

The properties and design considerations of each component are introduced hereafter (except for the properties of the NE34 Fontainebleau sand that have been presented in detail in chapter 3). The model piles are made of aluminium alloy with hollow sections. They are instrumented with strain gauges, which enable the determination of the bending moment profile and the axial stress at different depths (for the details of piles see in Appendix. H). As already mentioned, the connections between the piles and the pile cap are assumed to be rigid. The pile heads are thus rigidly connected together through stiff mass caps, which induce rotational restrains [116]. The pile caps for both the vertical and inclined piles are made of two aluminium alloy pieces in order to ensure an easy assembly with bolts after the sand pluviation. The reason for doing this it to avoid the *"shadowing effect"* during the air pluviation process. Fig. 4.4(a) shows the assembly of the inclined piles and the pile cap. In Fig. 4.4(b), a zoomed view of the assembly of the piles is shown: the piles are clamped within two pieces of the pile cap to provide a rigid connection. It can be noticed that the piles are connected with a thin plate before the assembly. Its role is to provide a temporary support to the piles during the sand pluviaton process. Table. 4.2 gives the characteristics of the piles and the pile cap in model and prototype scales.

(a) Assembly of inclined piles and pile cap

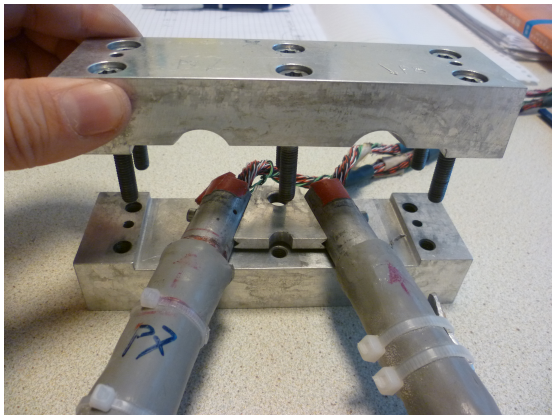

(b) Assembly of pile cap with piles

Figure 4.4: Assembly of pile and pile cap

Item	Model scale 40 g	Prototype scale 1g
Pile-embedded depth	326.5 mm	13.06 m
Pile-external diameter	18 mm	0.72 m
Pile-Internal diameter	15 mm	0.6 m
Pile-Young's modulus	74000 MPa	74000 MPa
Pile-Bending stiffness	197 N·m^2	505 MN·m^2
Pile-Yield strength	245 MPa	4245 MPa
Pile cap-Dimensions	140 mm × 40 mm × 40 mm	5.6 m × 1.6 m × 1.6 m
Cap-weight	560 g	33.8 tonne

Table 4.2: Characteristics of piles and pile cap

To simplify the problem, the possible soil-cap interaction or the lateral resistance of the pile cap is not studied during the design of the experiments. Actually, various research studies exist on the effects of the soil-cap interaction on the behavior of pile groups: due to the friction between the soil and the cap, especially when the pile cap is embedded beneath the ground surface, the lateral resistance of the pile cap can be significant [69,117–119]. To avoid soil-cap interaction, the piles are designed to stand at certain distance above the ground surface, see in Fig. 4.5. The gap between the pile cap and the ground surface is 28 mm at model scale (1.12 m in 1g prototype scale). The spacing of the piles i.e. the center-to-center distance between the piles is designed to be 4 times the diameter of the piles ($4D$) for both pile group configurations. Since the piles are only supported by the surrounding soil, so it is clear they are friction piles.

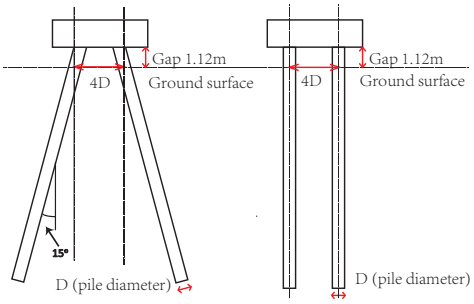

Figure 4.5: Spacing of piles in inclined pile and vertical pile groups

In order to study the influence of the gravity center on the responses of the pile foundations, two types of superstructures with different heights are designed i.e. a short (squat) and a tall (slender) building. To simplify the problem, only single degree-of-freedom superstructures are tested. The design criteria for the short and tall building are the following: they both should have

- the same resonant frequency with fixed base condition
- the same top mass weight
- the same total weight of the whole foundation and super-structure system

Fig. 4.6 shows the superstructures used in the study. The top mass (yellow) is made from brass and the column and the base (grey) is made from aluminium alloy. The short (left) was used for both sinusoidal tests and real earthquake tests; tall building (middle) was only used in real earthquake tests; taller building (right) was only used in the sinusoidal tests. Each building is made up of 3 parts: the top mass block, supporting column and base. The base is used to have a good connection when the building is installed on the pile cap, see in Fig. 4.7.

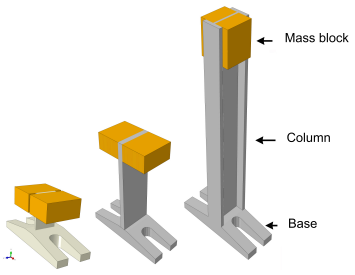

Figure 4.6: Super-structures used in the experiments: short building, tall buidling and taller building

Fig. 4.7 shows that after the installation of the superstructure the base of the building together with the pile cap gives an enlarged new foundation. The fixed-base frequency of the building is designed to be 2.0 Hz. As it was mentioned in the previous section, there is a distance (1.12 m) between the pile cap and the soil

surface. After the installation of superstructure, the height or the gravity center of the top mass is thus found increased. The foundation superstructure system can be idealized as a lumped mass system, see for example in Fig.4.7. Since the column supporting the building can not be regarded in practice as weightless, according to Harris and Piersol [120], 23% of the weight of the column should be included in the top mass while the rest 77% contributes to the weight of the base. The weight of the top mass comes from the mass block and 23% of the column; the weight of the foundation comes from the base the pile cap and 77% of the column. The height of the pile foundation H_{cap} is 1.92 m (including the gap between the pile cap and the soil surface); the gravity center H_{mass} of the building is measured from the ground surface. Detailed information for the foundation superstructure systems are listed in Tables. 4.3, 4.4 and 4.5.

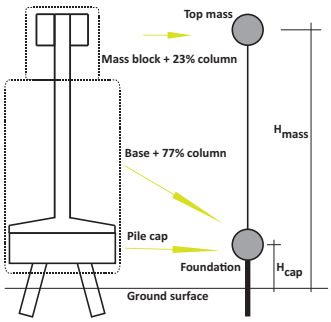

Figure 4.7: Foundation-superstructure discretization

	Short building	
Item	Model scale	Prototype scale
Top mass weight	0.85 kg	54.40 tonne
Total weight	1.05 kg	67.20 tonne
Height of gravity center	128 mm	5.12 m
Measured frequency	81.0 Hz	2.03 Hz

Table 4.3: Main parameters for pile foundation with short building

	Tall building	
Item	Model scale	Prototype scale
Top mass weight	0.84 kg	53.76 tonne
Total weight	1.18 kg	75.52 tonne
Height of gravity center	211 mm	8.48 m
Measured frequency	80.4 Hz	2.01 Hz

Table 4.4: Main parameters for pile foundation with tall building

	Taller building	
Item	Model scale	Prototype scale
Top mass weight	0.88 kg	56.32 tonne
Total weight	1.23 kg	78.72 tonne
Height of gravity center	354 mm	14.16 m
Measured frequency	79.0 Hz	1.98 Hz

Table 4.5: Main parameters for pile foundation with taller building

The top mass in Tables 4.3, 4.4 and 4.5 includes the contribution of the column; the mass of the pile cap is also included in the total mass of the foundation superstucture system. Due to physical reasons with the available materials it is very difficult to meet strictly the requirements of the design criteria: the tall building requires more material and therefore the total mass is found increased. Appendix A.5 provides detailed information of the designed superstructures used in the experiments.

Preparation of sand-pile system

As it was introduced in Chapter 3, air pluviation is used to prepare the sand for the free-field tests. The same Fontainebleau sand with similar (80%) relative density is also used for the soil pile system. The homogeneity of the sand deposit is controlled with the air pluviation technique and the same controlling parameters. However, the difference with the free-field tests is that this time the piles are embedded in the soil deposit. Thus, some special techniques are required for installing the piles. In the centrifuge tests the methods for installing the piles are different from the engineering practice (where the piles are introduced by drilling holes or punching into the soil). Escoffier et al. [13] discussed the influences of the different ways of pile installation on the final response of inclined piles. One of the proposed methods is adopted in this study. First, all the piles are fixed and maintained to their precise positions in the ESB container [101, 102] at 1g. Then the sand is filled layer-by-layer by air pluviation from the bottom up to the level of the ground surface. A temporary sustaining system is used to maintain the piles during the pluviation, which is mainly composed by a aluminium plate, two steel rods and thin plastic wires, see in Fig. 4.8. All the pieces in the temporary supporting system have to be thin enough to minimize the *"shadowing effect"* during the sand pluviation (shadowing effect: during sand pluviation the presence of piles influence the falling of sand into the container and thus disturbs the homogeneity of the sand deposit).

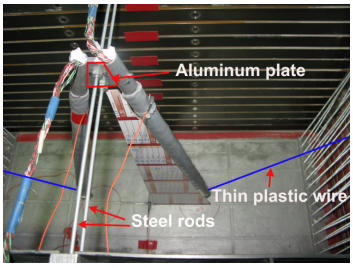

Figure 4.8: Positoining piles in ESB container

The thin aluminium plate (see in Fig. 4.8) is used to maintain precisely the inclination angle of 15°. The two piles are suspended by two steel rods in the container that are temporarily attached. In this way, the piles are floating inside the container. However, due to the falling of sand the impacts influence their exact positions. In order to avoid this, two thin plastic wires are attached on the tips of the two piles to provide additional supports. During the pluviation, when the sand surface is about 5 cm higher than the tips of the piles, the wires are cut to free the pile tips. After the sand surface arrives at the prescribed height, the pluviation stops and the steel rods are removed. Then the pile cap is installed onto the pile heads by tightening the bolts using a dynamic torque screwdriver. Finally, the superstructure is installed onto the top of the pile cap.

As mentioned before, in order to record the movement of the soil pile superstructure, sensors have to be installed into the system. The typical arrangement of the sensors in the centrifuge model is shown in Fig. 4.9. The movement of soil column is followed by a set of accelerometers from CH03∼CH09 and from CH14∼CH19. Comparison of the maximum acceleration and displacement measured during the free field tests showed that the measurements from these accelerometers are representative of the free field acceleration and are not influenced by the pile group Appendix B. Similarly, the movements of the pile cap and the superstructure are monitored by the accelerometers from CH10∼CH13. In addition to the accelerometers, three high speed laser sensors are used on the superstructure. Several accelerometers are also attached on one side of the container in order to capture its behavior.

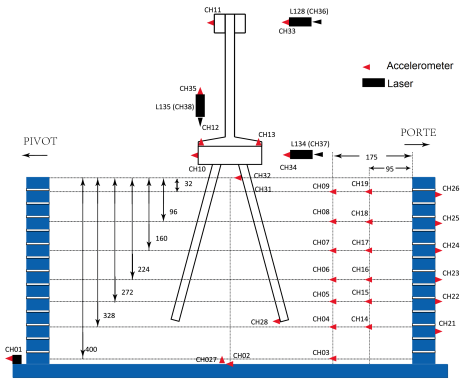

Figure 4.9: Typical sensors arrangement of soil-pile-superstructure system in centrifuge tests

4.1.4 Experimental program

A total of 22 tests have been performed among which 2 free field tests, 2 tests with only the cap and 18 test on piles groups with superstructures. In order to verify the repeatability of the tests, 4 tests have been repeated. Table. 4.1.4 give the tests that have been performed and Tables. 4.6, 4.7 and 4.8 list the input sequences that have been followed for the earthquakes and sinusoidal tests.

For the centrifuge tests using real earthquake signals, the shaking sequence is listed in Table. 4.6

NO.	Seismic signal	Arias Intensity (m/s)
1, 2, 3	Martinique Jara -1 dB	0.2
4, 5, 6	Northridge -20 dB	0.2
7, 8, 9	Northridge -9 dB	2.43
10, 11, 12	Kobe -4 dB	3.51
13, 14, 15	Martinique Jara -1 dB	0.2
16, 17 ,18	Northridge -20 dB	0.2

Table 4.6: Shaking sequence of real earthquake signals

NO.	Sinusoidal signal	Arias Intensity (m/s)
1, 2	2.0 Hz, 0.05 g	0.34
3, 4	2.0 Hz, 0.1 g	1.35
5, 6	2.0 Hz, 0.2 g	5.37
7, 8	2.0 Hz, 0.4 g	21.38

Table 4.7: Shaking sequence of sinusoidal signals, 2.0 Hz

NO.	Sinusoidal signal	Arias Intensity (m/s)
1, 2	3.5 Hz, 0.05 g	0.35
3, 4	3.5 Hz, 0.1 g	1.39
5, 6	3.5 Hz, 0.2 g	5.54
7, 8	3.5 Hz, 0.4 g	22.06

Table 4.8: Shaking sequence of sinusoidal signals, 3.5 Hz

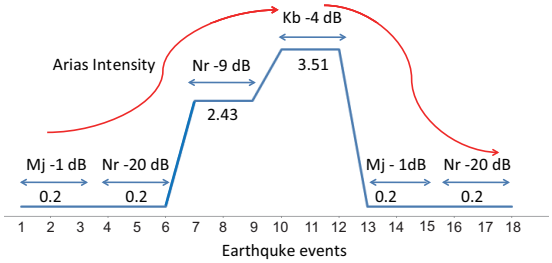

Figure 4.10: Variation of arias intensity, real earthquake excitations

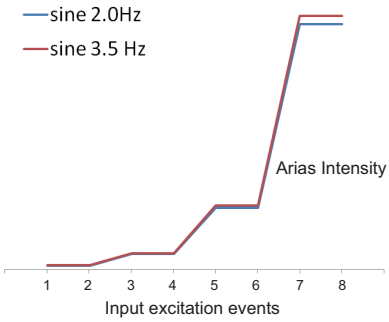

Figure 4.11: Variation of arias intensity, sinusoidal excitations

NO.	Date	Discription
01	2011-01-27	*Free field test (real earthquake)
02	2011-03-09	Vertical pile group (real earthquake)
03	2011-04-22	Inclined pile group (real earthquake)
04	2011-06-24	*Inclined pile group with short building (real earthquake)
05	2011-06-30	*Vertical pile group with short building (real earthquake)
06	2011-12-09	*Inclined pile group with tall building (real earthquake) Superseded, replaced by test 23
07	2012-01-17	Vertical pile group with tall building (real earthquake) Superseded, replaced by test 24
08	2012-03-02	Free field test (sine with tapered parts)
09	2012-04-05	Free field test (sine with constant amplitude)
10	2012-04-11	Inclined pile group with short building (sine 3.5 Hz)
11	2012-05-15	Vertical pile group with short building (sine 3.5 Hz)
12	2012-05-21	Vertical pile group with taller building (sine 3.5 Hz)
13	2012-07-02	Inclined pile group with taller building (sine 3.5 Hz)
14	2012-07-03	Inclined pile group with taller building (sine 2.0 Hz)
15	2012-08-13	Vertical pile group with taller building (sine 2.0 Hz)
16	2012-08-14	Vertical pile group with short building (sine 2.0 Hz)
17	2012-08-24	Inclined pile group with short building (sine 2.0 Hz)
18	2012-12-11	Inclined pile group with tall building (real earthquake)
19	2012-12-13	Vertical pile group with tall building (real earthquake)

Note: * means the test has been repeated.

The examination of the Repeatability of the centrifuge test is presented in Appendix. G.

4.2 Definitions, structure of the analysis and abbreviations

For convenience, several definitions, assumptions and symbols concerning the analysis and interpretation of the experimental results are introduced in this section. The organization of the experimental results, the main structure of the analysis and some abbreviations follow.

4.2.1 Definitions, assumptions and explanations

- **Identities of the piles used in the experiments (P7 and P8)**

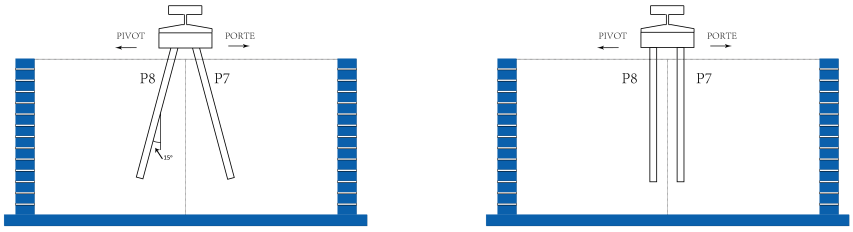

(a) Inclined pile group (b) Vertical pile group

Figure 4.12: Illustration of P7 and P8 in pile groups

The centrifuge tests being dynamics (with changes in the direction of the loading), it is not possible to determine which one is the front or the rear pile. In the following, they are named P7 and P8 according to their positions. The pile close to the "Porte" on the right is called P7 and the other, close to the "Pivot", P8 see in Fig. 4.12. The same rule is adopted for the vertical and the inclined pile group.

- **Residual, dynamic and total bending moment** Due to the permanent deformation of the soil and the influence of the superstructure during an earthquake event, embedded deep pile foundations move from their initial position. Permanent lateral displacements occur at the pile head but also along the pile, see in Fig. 4.13. The residual bending moment can be measured as the difference between the bending moment at the beginning and at the end of the earthquake event, see in Fig. 4.14. As it is shown in this figure, the total bending moment is decomposed into two parts: a dynamic part and a residual part. The dynamic bending moment is obtained by removing the residual bending moment from the total bending moment, as it is shown in Fig. 4.15.

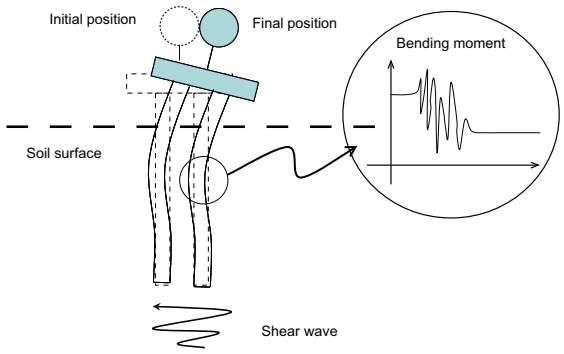

Figure 4.13: Illustration of residual permanent deformation

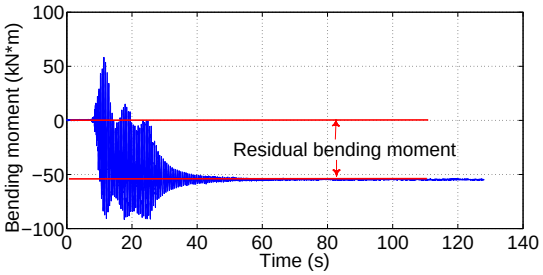

Figure 4.14: Illustration of total bending moment in certain section in pile

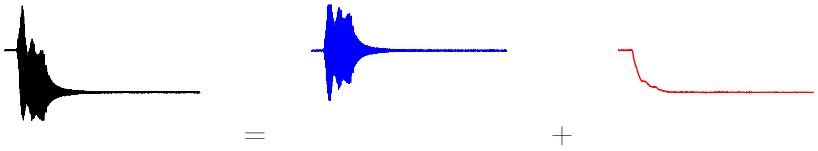

(a) Total bending moment (b) Dynamic bending moment (c) Residual bending moment

Figure 4.15: Decomposition of the total bending moment

- **Accumulation effect of residual bending moment**

  During the experimental campaign it was observed that in successive earthquake events the residual bending moment can evolve. However, if the same earthquake signal is applied 3 times, the evolution or accumulation effect is limited. In addition, for the case of multiple seismic sequences, the accumulation of residual bending moment stops after the strong earthquakes. The last small earthquakes are not capable to induce new residual bending moment in the piles. The maximum residual bending moment depends therefore on the maximum earthquake loading. With the accumulation of residual bending moment the piles are also subjected to an initially prestressed state than can influence the results. This effect is taken into account in the analyses

presented hereafter. Figs. 4.16 and 4.17 show the evolution of the residual bending moment for the vertical pile group with short superstructure under 2.0 Hz sinuisoidal excitations and for the inclined pile group with slender superstructure under seismic excitations.

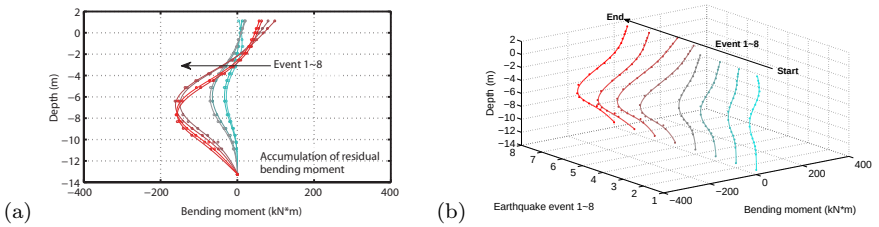

Figure 4.16: Accumulation of residual bending moment – vertical pile group with short superstructure, 2.0 Hz sinusoidal excitations

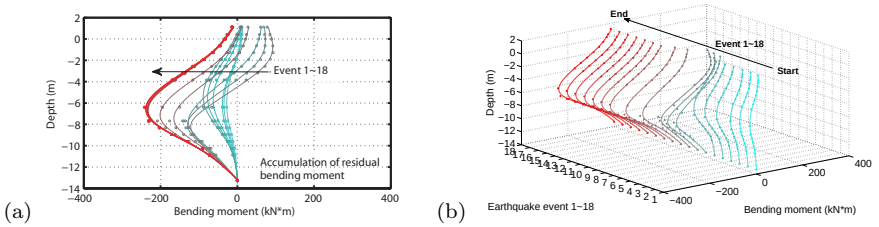

Figure 4.17: Accumulation of residual bending moment – inclined pile group with slender superstructure, real earthquake excitations

- **Rotation (rocking) and horizontal displacement (translation) of the pile cap**

In all the experiments, the responses of the pile cap and the superstructures (when installed) are monitored by sets of accelerometers as shown in Fig. 4.18. The vertical movements of the pile cap are measured by the sensors CH12 and CH13. The horizontal displacements of the pile cap and the superstructure are measured by the sensors CH10 and CH11 respectively. The sensor CH09 near the soil is far enough from the pile foundation and it is used to capture the movement of the soil surface.

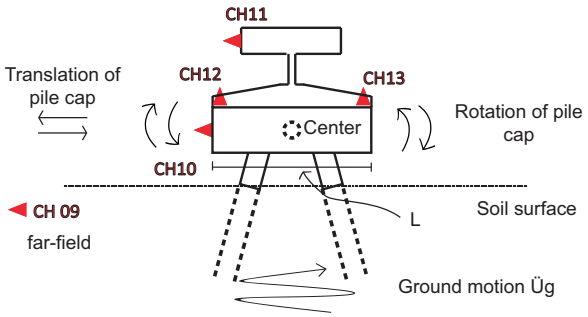

Figure 4.18: Illustration of calculation of rotation of pile cap

Knowing the acceleration time history of pile cap, the displacement time history can be obtained by double integration process [121]. Due to the limitation of the accelerometers, only the dynamic displacement can be obtained by double integration. The rotation of pile cap can be expressed as the ratio between the displacement of pile cap and the length of pile cap. The schematic representation of calculation of pile cap is shown in Fig. 4.19

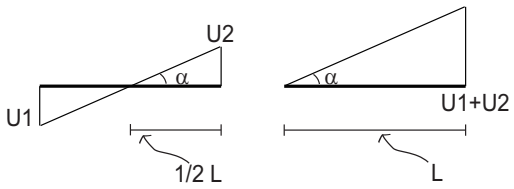

Figure 4.19: Schematic representation of calculation rotation of pile cap

The rotation of pile cap α can be calculated by $\frac{U_1}{(1/2)L}$ or $\frac{U_2}{(1/2)L}$. To be more accurate, the rotation of pile cap is calculated by using Eq. 4.1

$$\alpha \approx \tan(\alpha) = \frac{U_1 + U_2}{L} \tag{4.1}$$

where L is the length of pile cap 140 mm in model scale and 5.6 m in prototype scale.

As shown in Fig. 4.19, the relative translation of the pile cap with respect to the soil surface can be obtained by calculating the differences between the displacement of the pile cap and the displacement of the soil surface.

For both the rotation and displacement components calculated in this way and due to the limited number of accelerometers, the residual part of the measurements can not be preserved. Therefore, the displacements calculated from the measured accelerations represent the dynamic displacements only.

- **Overturning moment and total horizontal force (base shear) acting on the pile foundations**

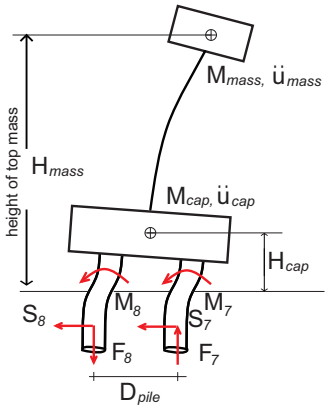

Figure 4.20: Illustration of the movements of pile cap and forces acting on the foundation system

The calculation of the force and moment can either be calculated from the inertia forces generated by the mass of the super-structure or from the base resistance forces, see Fig. 4.20. For example the overturning moment M can be obtained either from Eq. 4.2 or Eq. 4.3:

$$M_{\text{inertial}} = M_{\text{mass}}\ \ddot{u}_{\text{mass}}\ H_{\text{mass}} + M_{\text{cap}}\ \ddot{u}_{\text{cap}}\ H_{\text{cap}} \tag{4.2}$$

$$M_{\text{base}} = M_7 + M_8 + \frac{1}{2} D_{\text{pile}}(F_7 + F_8) \tag{4.3}$$

Since the system is in dynamic equilibrium, the moment M_{inertial} should be identical with the moment M_{base}. Fig. 4.21 shows for example a good agreement between the overturning moment calculated from the inertia forces and the base resistance forces. In all the analyses presented in this document, the inertial forces will be used to calculate the forces on the pile cap.

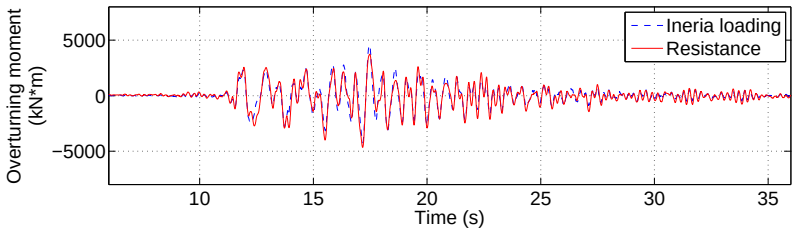

Figure 4.21: Inertial loading induced by superstructure vs. resistance from bending moments and axial forces of piles: Vertical pile group with short building under Kobe -4 dB earthquake

- **Representative values used in the analysis of experimental results**

  This section introduces the method followed to select the representative values for analyzing the experimental results. The representative value means

the typical value that can represent the main phenomena of the tests. This is also a way to reduce the size of the experimental database and select the most valuable data. The determination of the representative values of several experimental terms like peak acceleration, maximum displacement, maximum rotation, total base shear, total overturning moment, residual bending moment, dynamic bending moment, total bending moment and axial force are introduced hereafter.

As mentioned before, in both seismic and sinusoidal tests, each input signal is repeated by 2 or 3 times. It is observed that the results obtained for 2 or 3 successive identical inputs are quite similar. This is may due to the high density sand used in the experiments that restrained the evolution of the behavior of the soil-pile foundation system.

From the engineering point of view, the important parameters are the excessive internal forces and deformation on the structural members.In this study, the maximum values are thus selected as representative. In this way, the size of the database is reduced by 2 or 3 times. Although the method of selecting the representative values seems not conservative, it highlights the most unfavorable loading cases.

Looking at the stresses in the piles, it is observed from the experimental results that the bending moments (residual bending moment, dynamic bending moment and total bending moments) and axial force in the pile P7 are higher than (or equal) to the ones in the pile P8 (this is may due to the fist loading direction in the tests). For detailed information, refer to Appendix. F. The maximum response of the pile P7 is therefore considered as the representative value. For the case of the axial force, since no important residual effects have been observed during the tests, the maximum total axial force within the repeated excitation is directly selected as the representative value.

The residual bending moment, dynamic bending moment, total bending moment and axial force are expressed as maximum envelope curves and therefore only the maximum values during the dynamic excitation history are considered.

- **Data normalization**

  In order to evaluate the different performances, cross comparisons are made between the various pile configurations. In addition, it is of more interest to identify the ratios between the different configurations than the original data. In order to normalize the experimental quantities, the vertical pile group configuration is chosen as the reference configuration. The measured quantities will thus normalized with respect to the vertical pile configuration. An illustration of the referenced configuration is shown in Fig 4.22.

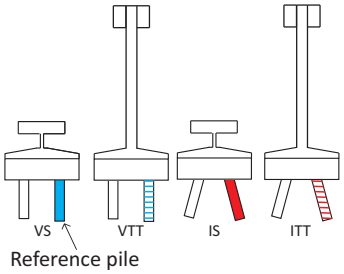

Figure 4.22: Illustration of referenced configurations

- **Zero initial stress state**

  The analyses of the performance of the inclined piles are based on the assumption that all the initial stresses in the piles (bending moments and axial forces) are zero at the beginning. The possible bending moments generated during the air pluviation, the assembling of the pile cap and the in-flight consolidation stages are thus neglected. In addition, since both the short and tall buildings are designed to have approximately the same total weight, the initial states for all the pile configurations with superstructures are assumed identical. Although the inclination of the piles may cause some differences in terms of pile stresses in the initial state, this effect is also not be taken into account.

- **Equivalent rotational, transnational stiffness and associated damping ratio**

  In order to handle the overturning moment-rotation, horizontal force-translation loops, the calculation of the stiffness (rotational and transnational) degradation curves and the associated damping ratio, the method proposed in chapter3 is adopted. A schematic representation is shown in Fig. 4.23, where K_{Rmax} and K_R are the initial rotational and equivalent rotational stiffness, respectively; similarly, K_{Tmax} and K_T are the initial translational and equivalent translational stiffness, respectively.

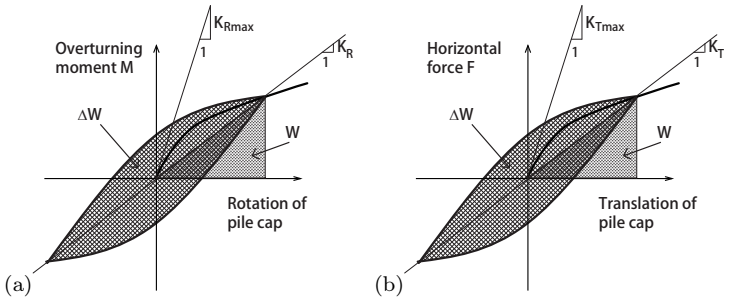

Figure 4.23: Illustration of calculation of equivalent rotational, translational stiffness and associated damping ratio: rotational stiffness and damping ratio: (b) translational stiffness and damping ratio

4.2.2 Main structure and organization of the analysis

One of the primary objectives of the experimental study is to investigate the seismic performance of inclined piles considering the effects of soil pile superstructure interaction. In order to achieve this, several complementary tests have to be carried out. The complementary tests and their objectives are:

- **Free-field tests**:they are performed with real earthquake excitations and they are used to determine the resonant frequency of the soil column. In addition, the results from the free-field tests are used to compare with the far-field responses from other tests. The results indicate a good agreement of the soil column responses, something that ensures that the loading actions for the soil are identical. For more details, refer to Appendix. B.

- **Pile group tests without superstructures**: the tests on pile group (inclined and vertical) without superstructure was used in evaluating the so called "kinematic interaction" under seismic actions. The term "kinematic interaction" used in this dissertation with caution, since it is not a real kinematic interaction. To be more precise, it is more appropriate to call it soil-pile-cap interaction that due to the inertial effect induced by the pile cap. The results indicate poor performance of inclined piles in terms of pure soil-pile-cap responses. For more details, refer to Appendix. C.

In order to be more concise, only the main body of the seismic analyses are presented in the dissertation.

The seismic analysis of the inclined piles is composed of three parts:

- **Performance of inclined piles with Seismic Soil Pile Superstructure Interaction (SSPSI) under real earthquake excitations**: it is shown that using inclined piles and increasing the position of the gravity center of the superstructure play a beneficial role in the performance of foundation system.

- **Performance of inclined piles with Seismic Soil Pile Superstructure Interaction (SSPSI) under sinusoidal excitations**: 2.0 Hz and 3.5 Hz sinusoidal excitations are used. The influence of the height of gravity center is further highlighted.

- **Performance of inclined piles in terms of rocking and horizontal translation behavior**: the behavior of the inclined and vertical pile groups is analyzed in terms of horizontal and rotational stiffness degradation and damping properties.

4.2.3 Abbreviations

The different abbreviations that are used in the analyses of the experimental results are listed in Table. 4.10.

Symbol	Meaning
SSPSI	Seismic soil-pile-superstructure interaction
Mj	Martinique Jara earthquake
Nr	Northridge earthquake
Kb	Kobe earthquake
IS 	Inclined pile group with short building
VS 	Vertical pile group with short building
IT 	Inclined pile group with tall building
VT 	Vertical pile group with tall building
ITT 	Inclined pile group with taller building
VTT 	Vertical pile group with taller building
BS	Base shear force acted on the foundation
OM	Overturning moment acted on the foundation
RBM	Residual bending moment
RSHR	Residual shear stress in pile
DSHR	Dynamic shear stress in pile
SHR	Shear shear stress in pile
RBM_{max}	Maximum residual bending moment along piles
RBM_{P7}	Residual bending moment on pile P7
$RBM_{P7max,VS}$	Maximum residual bending moment on pile P7 in vertical pile group with short building
DM	Dynamic bending moment
DM_{P7}	Dynamic bending moment on pile P7
$DM_{P7max,VS}$	Maximum Dynamic bending moment on pile P7 in vertical pile group with short building
M	Total bending moment
M_{P7}	Total bending moment on pile P7
$M_{P7max,VS}$	Maximum total bending moment on pile P7 in vertical pile group with short building
N	Axial force in the pile
N_{P7}	Axial force in pile P7
$N_{P7max,VS}$	Maximum Axial force in pile P7 in vertical pile group with short building
z	Depth of the pile
D	Diameter of pile (0.72 m)
D_{pile}	Center-to-center distance between piles
K_T	Translational stiffness
K_R	Rotational stiffness
D_T	Translational damping
D_R	Rotational damping

Table 4.10: Symbols used in the analyses of performance of inclined piles

4.3 Performance of inclined piles with seismic soil-pile-superstructure interaction (SSPSI) under real earthquake excitations

Different from the kinematic interaction, when there are superstructures on pile foundations, under seismic excitations, piles were subjected to not only kinematic soil-pile interaction, but also to the soil-pile-structure interaction. The inertial loads transferred from superstructures significantly influence the behavior of pile foundations. And in return, the behavior of the superstructure was also influenced by the motions of the foundations. This process is called seismic soil-pile-superstructure interaction. This section provides insights about the behaviors of inclined and vertical piles under seismic soil-pile-superstructure interaction. The experimental results indicate a significant influence of the presence of superstructure on the performances of both inclined and vertical piles.

4.3.1 Response of superstructures with SSPSI

4.3.1.1 Response of superstructures, analyses in frequency domain

The first 6 small base shaking were used to evaluate the frequency response of the pile groups with short and tall buildings. Transfer functions are calculated between the accelerations measured on the top of the buildings and those measured near the soil surface. The transfer functions of short building on inclined and vertical pile groups are shown in Fig. 4.24. For the tall building on the two pile configurations, the transfer functions are shown in Fig. 4.25. The estimated frequency responses are listed in Table. 4.11. Keep in mind that the frequencies of the buildings (either short or tall) with fixed-base condition is 2.0 Hz (see in section. 4.1.3), when the buildings are installed on the pile cap, due to the soil-foundation interaction, their frequencies decrease.

Configurations	Frequency of top mass (Hz)	Frequency of pile cap (Hz)
IS 	1.94	6.28
VS 	1.80	4.26
IT 	1.70	7.12
VT 	1.62	5.30

Table 4.11: Summary of frequency response of short and tall building on inclined and vertical pile groups

The presence of inclined pile reduces the effect of the SSPSI on the frequency response of the superstructure. For the case of short and slender superstructures, when they are installed on the inclined pile groups, the frequencies are 0.14 Hz and 0.08 Hz higher than they are on the vertical pile groups. In addition, increase of the

gravity center of the superstructure enhances the SSPSI on the frequency response of the superstructure for both pile group configurations (-0.24 Hz and -0.18 Hz for the inclined and the vertical pile group respectively).

The presence of the superstructure also modified the response of the pile cap. According to the analysis of tests of soil-pile-cap system i.e. tests without superstructure, see in Appendix C, section C.1.1.1. The frequency of the inclined and vertical pile group are 10.6 and 6.0 Hz respectively. For short and slender superstructures on inclined pile group, the frequency of pile cap decreased from 10.6 to 6.1 Hz and from 10.6 to 7.0 Hz, respectively.

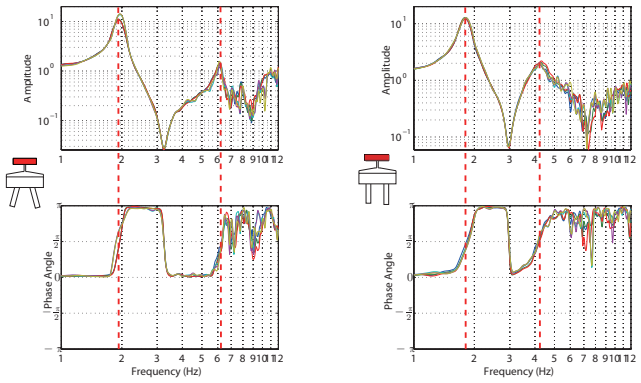

(a) IS (b) VS

Figure 4.24: Transfer function between the horizontal acceleration of the top mass and near the soil surface (z = 1.28 m) under the first 6 small earthquakes: (a) inclined pile group with short building and (b) vertical pile group with short building

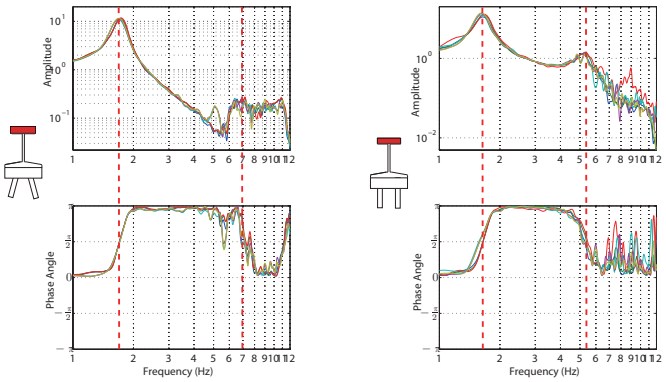

(a) IT (b) VT

Figure 4.25: Transfer function between the horizontal acceleration of the top mass and near the soil surface (z = 1.28 m) under the first 6 small earthquakes: (a) inclined pile group with tall building and (b) vertical pile group with tall building

The presence of inclined pile decreases the effect of SSPSI on the frequency response of both superstructures. For both pile group configurations, the increase of the gravity center increases the SSPSI effect on the response frequency (the effect is more pronounced for inclined pile configuration).

4.3.1.2 Response at the pile cap

The lateral displacement of pile cap is a very important concern in foundation engineering. The maximum lateral displacement should not exceed the allowable displacement. The lateral responses at the pile caps in both inclined and vertical pile group are investigated. In this section, the influences of inclined piles, type of superstructure and base shaking frequency on the lateral response of pile cap are analyzed. The response of pile cap is evaluated in terms of peak acceleration, maximum displacement and maximum rotation, the results are shown in Figs. 4.26, 4.27 and 4.28, respectively.

In terms of peak accelerations, for both short and tall building, pile cap connected with inclined piles has less peak acceleration for all the earthquake events, except for the last two small earthquakes Mj -1 dB and Nr -20 dB.

However, the performances of inclined piles is influenced by both the gravity center of superstructure and the base shaking frequency. For small earthquakes, the effect of inclined piles is limited which is contrary to the slender one. For strong earthquakes, the effect of gravity center of the superstructure is less noticeable. After the strong earthquakes, for the last two small earthquakes, larger acceleration appears at the inclined pile group when a slender superstructure is supported. In addition, the actual values of the last two small earthquakes are higher than those in the first two small earthquakes, this might due to the response of the pile was under a pretressed state due to the residual bending moment after strong earthquakes. This effect is also observed in the following analyses of pile cap displacement and pile cap rotation.

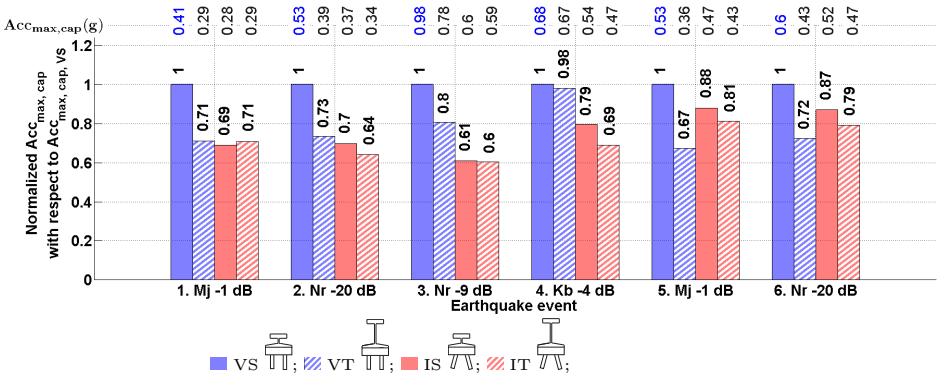

Figure 4.26: Normalized maximum acceleration of pile cap, under real earthquake excitations

Concerning the displacements at the pile cap, for both short and tall buildings

inclined piles induce smaller values.

However, as it is for the maximum acceleration, the effect of inclined piles is influenced by the base shaking and the type of superstructure. Except for the Kb -4 dB earthquake, the performances of inclined piles are more pronounced for short superstructure. This difference may due to the frequency range of the Kobe earthquake which has very low frequency contents.

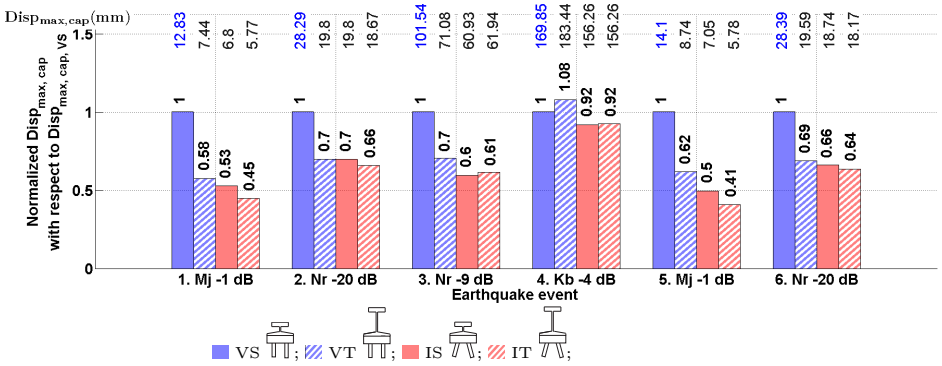

Figure 4.27: Normalized maximum displacement of pile cap

The comparison of pile cap rotation is shown in Fig. 4.28. For short building, inclined pile group configuration increases the rotation of pile cap in the case of small earthquakes and reduced the rotation in strong earthquakes. For slender superstructure, inclined piles always increase the pile cap rotation.

For both the inclined and vertical pile group configurations, higher gravity center induces higher pile cap rotation except for the case Mj -1 dB earthquake. In the case of low level of base shaking, the presence of inclined pile increase the rotation at the pile cap. This effect is more pronounced when a slender superstructure is supported. This result is accordance with that obtained by Giannakou [9] from elastic FEM simulation. However, in the case of strong earthquakes, the presence of inclined piles slightly decreases (or even slightly increase) the rotation for both short and slender superstructures. It seems that the strong earthquakes decrease the effect of inclined piles.

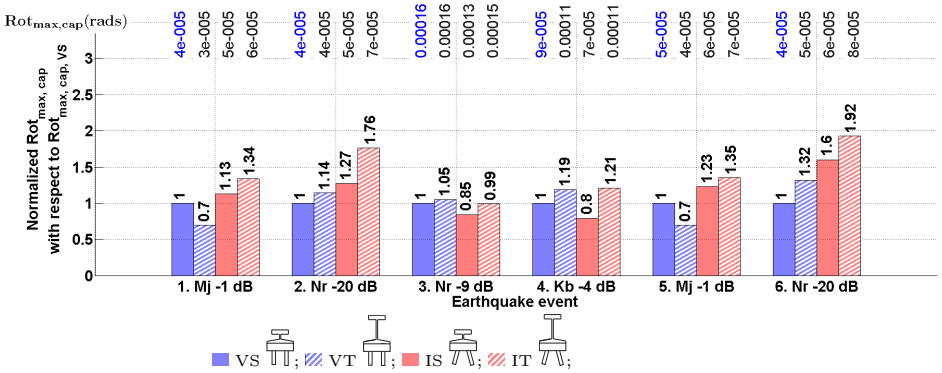

Figure 4.28: Normalized maximum rotation of pile cap, under seismic excitations

4.3.1.3 Total base shear and overturning moment

The total base shear force and overturning moment are important for structural design. The total base shear force for different configurations under earthquake events is given in Fig. 4.29.

For all the base shaking, except for the low earthquake Nr -20 dB, inclined piles reduce the base shear force. However, performance of inclined piles is largely influenced by the gravity center of the superstructure For all the base shaking, except for the Kb -4 dB earthquake the presence of a short superstructure enhances the good performance of inclined piles.

For the Kobe earthquake, the performance of inclined piles seems to be not sensitive to the gravity center of the superstructure. This is an indication that the frequency of the base shaking influences the performance of inclined piles.

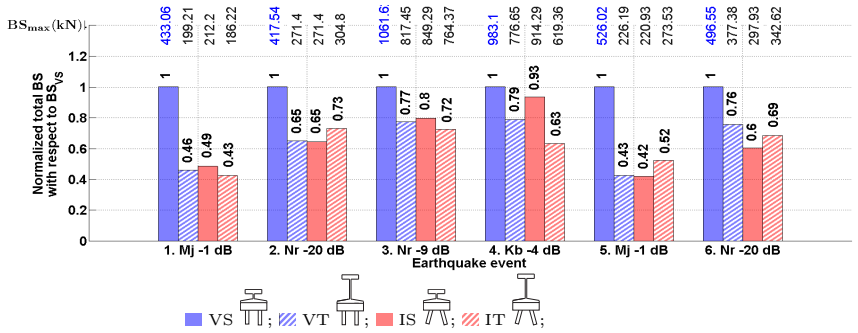

Figure 4.29: Normalized maximum base shear force, under seismic excitations

The results for overturning moment are summarized in Fig. 4.30. Similar as the base shear, inclined piles reduce the overturning moment and this effect is more pronounced for short superstructure.

For the same pile configurations, either inclined or vertical, tall building induces higher overturning moment,except for vertical pile configuration in small earthquakes of Mj -1 dB. However, the values for tall building and short building are are sufficiently close to be regarded as the same.

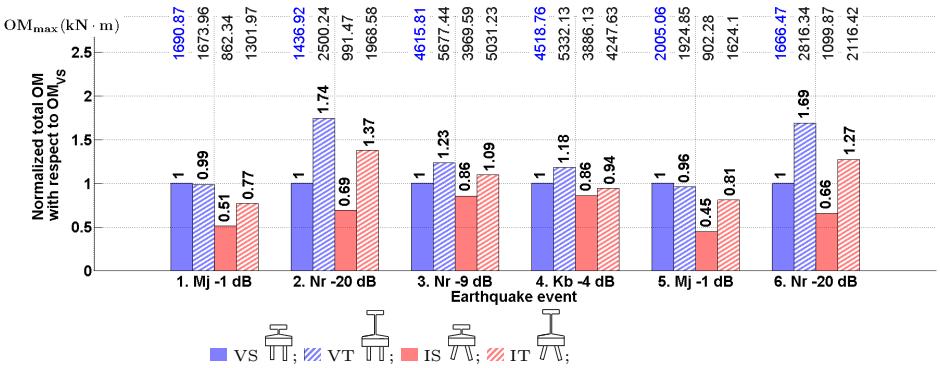

Figure 4.30: Normalized maximum overturning moment, under seismic excitations

Concerning the base shear and overturning moment, inclined piles play a beneficial role. Contrary to vertical pile group, for most of the cases, the inclined pile groups with either short or slender superstructure have a smaller total resultant force acting on the base of the foundation. For strong earthquakes and due to the high nonlinearity that develops in the soil, the effects of inclined piles and of the gravity center of the superstructure are reduced.

4.3.2 Stresses in piles with SSPSI

In this section, the "generalized" stresses in piles (bending moment, shear force and axial force) resulting from the combined kinematic and inertial interactions are analyzed and discussed. The envelope curves of the maximum stresses along the piles and the peak values are compared for different pile group and superstructure configurations.

4.3.2.1 Residual bending moment in piles

Fig. 4.31 shows the accumulated residual bending moment profiles for the successive earthquake events. The peak values alone the profiles are summarized in Fig. 4.32.

The presence of inclined pile influences the shape of the residual bending profiles. Inclined piles induce a "C" shape that differs from the "S" shape obtained for the vertical pile group. For both, the type of superstructure has an effect on the depth of the maximum residual bending moment. For a short superstructure, inclined piles increase the depth of the maximum residual bending moment from $4D$ to $6D$, whereas the depth is almost the same for the strong earthquakes. For a slender superstructure, the tendency seems to be the same even if for the vertical pile group (due to the difficulty in determining the shape of the profiles, the depth of the maximum residual bending moment is not always obvious). For the inclined pile group, the maximum bending moment appears at a depth of around $6D$ for the first two small earthquakes; during and after the strong earthquakes, the depth increases to $10D$ against $5D$ for the vertical pile group.

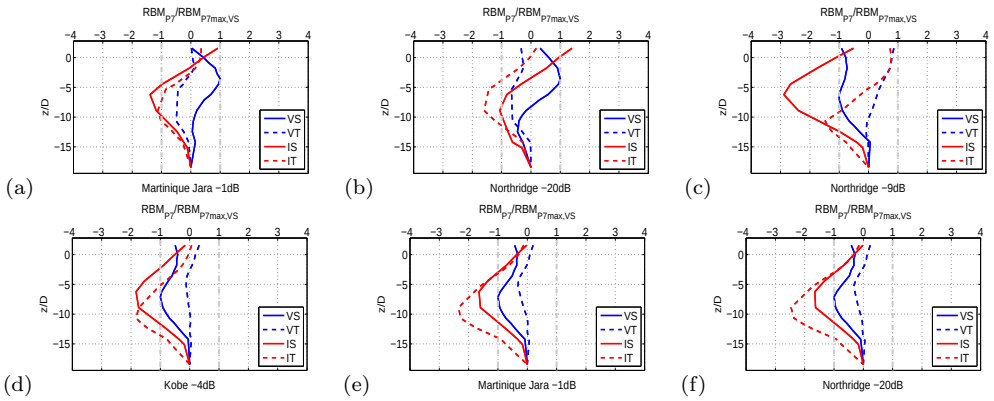

Figure 4.31: Normalized residual bending moment profiles, under real earthquake excitations

The performance of inclined piles depends on the type of superstructure, the base shaking and the loading history. It is can be seen in Fig. 4.32 that for the first two small earthquakes, the influence of inclined piles is almost the same for both type of superstructures; when strong earthquakes are applied, the effect of inclined piles is more pronounced for the case of a short superstructure. For the last two small earthquakes (contrary to the first two small ones), the effect of inclined piles is however more pronounced for a slender superstructure. This is certainly due to the accumulation of residual bending moments from the previous earthquake events. For the accumulation of residual bending moment, refers to section. 4.2.1.

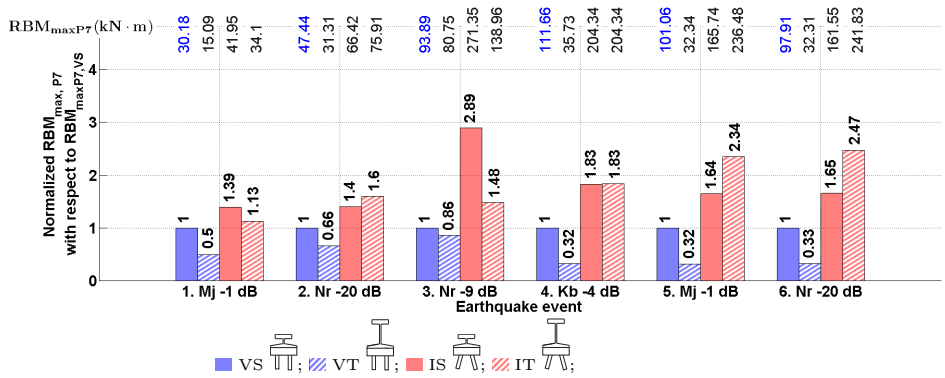

Figure 4.32: Normalized redidual bending moment, under real earthquake excitations

4.3.2.2 Total bending moment in piles

The residual bending moment and the dynamic bending moment are considered hereafter together (as the total bending moment). Fig. 4.33 shows the normalized maximum total bending moment profiles. With the presence of residual bending moment, the curves are dragged and distorted in an asymmetric way. It is very difficult to define the shape of the maximum total bending moment curves. Qualitatively speaking, the response of vertical pile group configuration is more intense than of an inclined one.

Fig. 4.34 shows the ratios between the peak values of the total bending moment. The presence of inclined piles reduces the maximum total bending moment for both short and slender superstructures. However, the good performance of the inclined piles is influenced by the type of superstructure and the base shaking frequency content. The good performance of inclined piles is more pronounced for the short superstructure. Contrary to the slender superstructure, this performance is not influenced by the frequency of the base shaking.

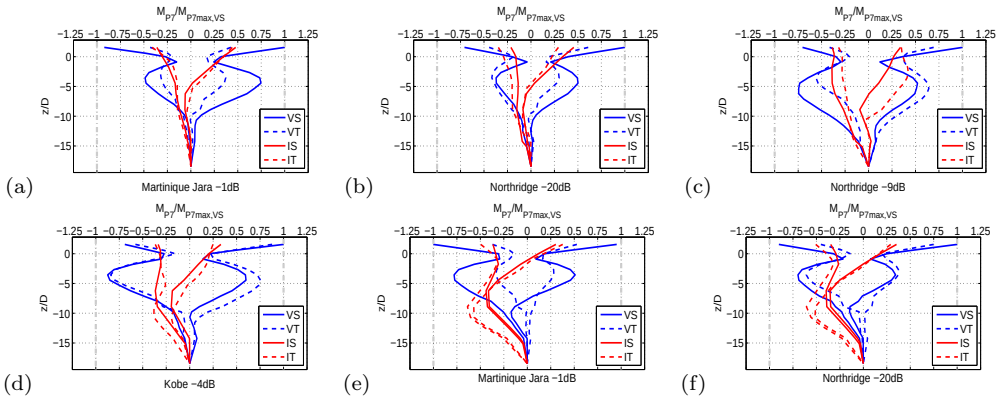

Figure 4.33: Normalized envelop curves of maximum total resultant bending moment, under real earthquake excitations

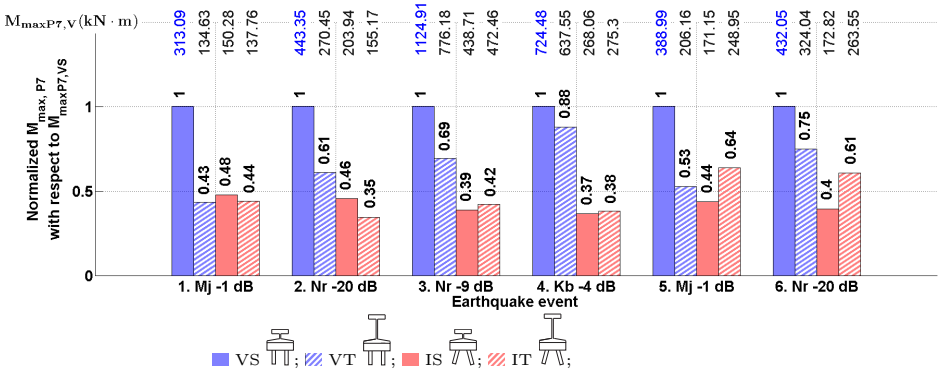

Figure 4.34: Normalized total bending moment under real earthquake excitations

4.3.2.3 Axial forces in piles

As explained previously, the residual effect can be ignored for the axial force. The pile stresses in terms of axial force are thus presented directly in the form of a total axial force. Fig. 4.35 shows the normalized axial force profile for different configurations. For the friction piles, a reduction of the axial force with increasing pile embedded depth is observed, although in some cases the axial force profiles are distorted. Due to small number of instrumented compression strain gauges, it is difficult to determine more precisely the shape of the axial force profiles. Due to these difficulties, the axial force profiles are not discussed hereafter further.

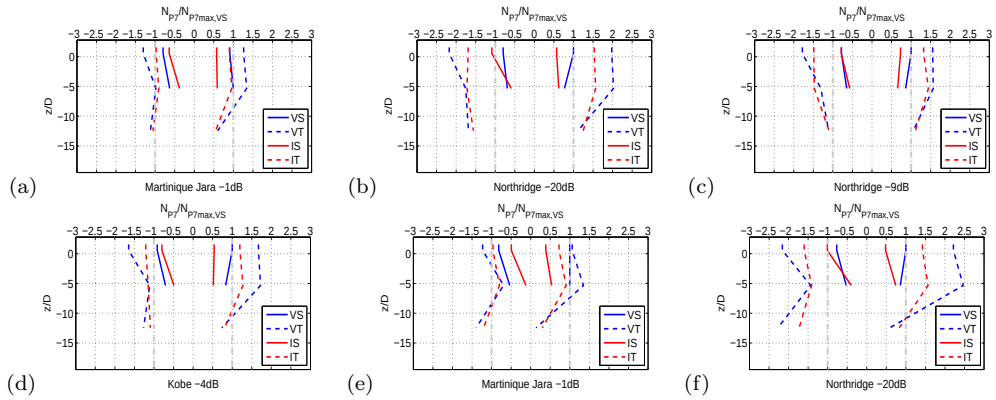

Figure 4.35: Normalized axial forces, under real earthquake excitations

According the results shown in Fig. 4.36, for both short and slender superstructures, inclined pile have less or equal axial force to the vertical one. For both inclined and vertical pile configurations, the increase of gravity center of superstructure results in a increase of axial force in the piles.

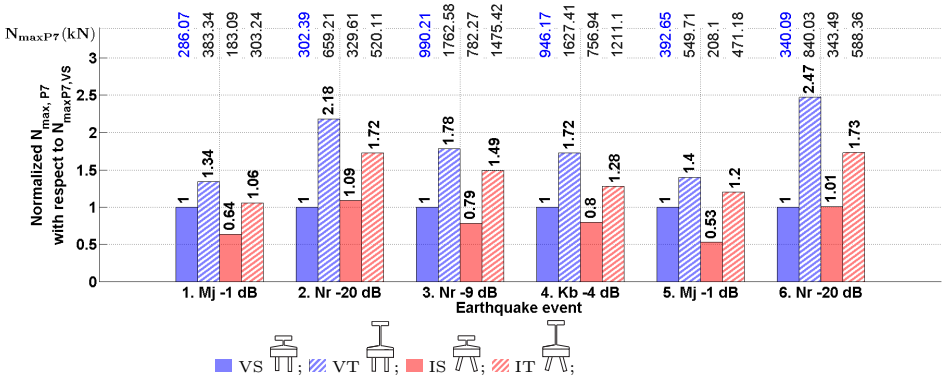

Figure 4.36: Normalized maximum axial force, under real earthquake excitations

4.3.3 Summary

In this section, the performance of inclined piles concerning seismic soil-pile - superstructure interaction (SSPSI) was analyzed and discussed. Cross comparisons were carried out to study the performance of different pile foundations with different superstructures, the presence of inclined piles and the gravity center were regarded as the two parameters. The comparisons were first carried out between different pile configurations which support the same type of building. Then to highlight the influence of the gravity center of the superstructure, comparisons were made between the same pile configuration with different types of superstructures. Main conclusions can be drawn from the results:

1. Compared with the pure soil-pile interaction, the presence of the superstructure (inertial loading) does modified both the responses of inclined and vertical pile group.

2. Superstructures built on inclined piles have higher resonant frequencies. This may be due to the higher horizontal stiffness provided by inclined piles. Regardless the pile group configuration (either inclined or vertical), increase of gravity center of superstructure decrease the resonant frequency.

3. Inclined piles tend to reduces the peak accelerations and maximum displacements on the top of the superstructures. For the same superstructure, inclined piles also help to reduce the pile cap rotation during strong earthquakes.

4. Concerning the base shear and overturning moment, inclined piles play a quite beneficial role in reducing the inertial loading of the superstructures. Contrary to vertical pile group, for most the cases, inclined pile group with either short or tall building, has less total resultant forces acted on base of foundation. Although, in strong earthquakes, with the high nonlinearity that developed in the soil, the effects of inclined piles and gravity center of superstructures are reduced, inclined piles still play beneficial roles.

5. In terms of residual bending moment, inclined piles still have poor performance compared with the vertical piles. However, with the presence of inclined piles, compared with the vertical piles, the performance of inclined piles have been changed from detrimental to beneficial. For the same type of superstructures (either short or slender), inclined piles have less or equal stresses to the vertical piles. It could also be observed that contrary to the vertical piles, inclined piles are less sensitive to the variation of gravity center of the superstructures which they support.

6. Even if the results are not presented in the main text, looking at the pure soil-pile interaction, the presence of superstructures has more influence on vertical piles (especially for the short superstructure).

7. For both inclined and vertical pile configurations, an increase of the gravity center induces higher axial forces in the piles. In terms of bending moments, a higher gravity center may have a beneficial effect on the performance of both inclined and vertical configurations. It is also found that vertical piles are much more sensitive to the variation of the gravity center of the superstructures.

4.4 Performance of inclined piles with seismic soil-pile-superstructure interaction (SSPSI) under sinusoidal excitations

A series of sinusoidal tests are conducted in order to highlight the influence of the base shaking frequency combined with the frequency of the superstructure on the performance of vertical and inclined piles. Two frequencies, 2.0 Hz and 3.5

Hz, are selected. The frequency 2.0 Hz is not far from the resonant frequency of the superstructure with fixed base condition; 3.5 Hz is estimated to be the resonant frequency of the soil column. The slender superstructure used in the previous seismic

tests is replaced by a even taller superstructure in order to emphasize the effect of the height of the gravity center. Cross comparisons are carried out between configurations of inclined piles with short (IS) and slender superstructures (ITT) and a vertical pile group with short (VS) and slender superstructures (VTT).

4.4.1 Response of superstructures with SSPSI

4.4.1.1 Responses of pile caps

Figs. 4.37 and 4.38 show the normalized displacements for each configuration for the 2.0 Hz and 3.5 Hz sinusoidal excitations respectively. The performance of inclined piles regarding the maximum displacements at the pile caps is largely influenced by the base shaking (more effect at 3.5 Hz) and by the type of superstructure. At 2.0

Hz and for the short building, inclined piles reduce the displacement at pile caps of about -9% to -36%. For the slender superstructure, inclined piles have almost no effect (expect for the 2.0 Hz 0.05 g input. Nevertheless, precision is not so good as for the other inputs because the values of the displacements are too small). For

the 3.5 Hz and for the short building, inclined piles greatly reduce the pile cap displacement by around 47∼67%. For the slender superstructure, this reduction is smaller (-21% to -46%), except for 3.5 Hz 0.2 g where an increase of around 75% is found. For the vertical pile configuration, a slender superstructure induces a smaller pile cap displacement. For the inclined pile configuration, except for 3.5 Hz 0.2 g, the displacement is slightly increased. Therefore, as the higher displacement appears when a short building is supported by vertical piles, the beneficial role of inclined piles is higher for the case of a slender superstructure.

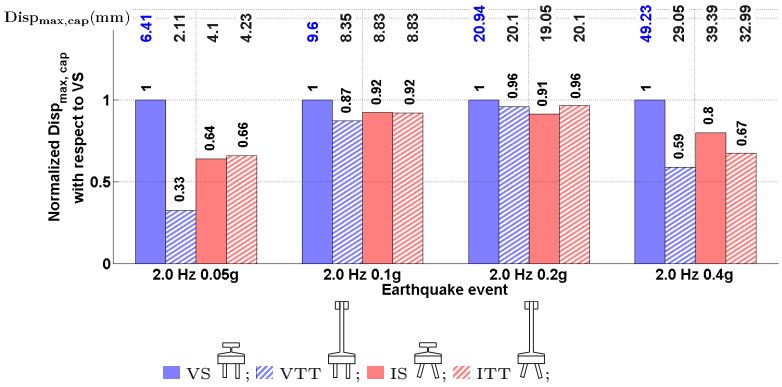

Figure 4.37: Normalized maximum displacement of pile cap, under 2.0 sinusoidal excitations

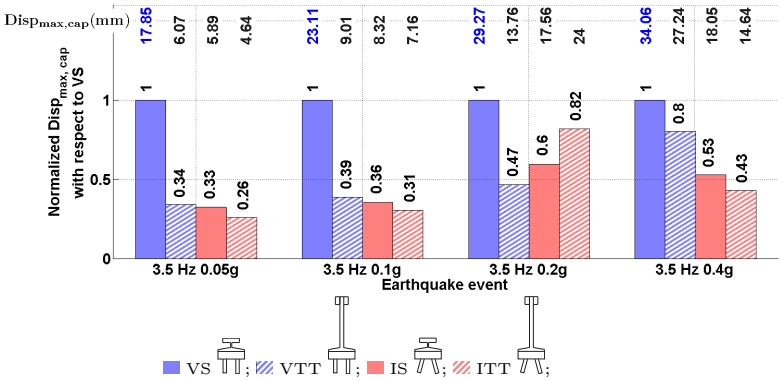

Figure 4.38: Normalized maximum displacement of pile cap, under 3.5 Hz sinusoidal excitations

In terms of rotation of the pile cap, performance of inclined pile is largely influenced by the frequency of the base shaking (beneficial behavior at 3.5 Hz but negative at 2.0 Hz).

At 2.0 Hz, for short building, inclined piles increase the rotation of pile cap, however the effect is limited in case of large earthquake. For slender superstructure, inclined piles almost have no effect on the rotation of pile cap for the last two larger earthquake.

On the contrary, at 3.5 Hz, for both short and slender superstructures, inclined piles reduce the rotation of pile cap, from -19 % to 54% and from -43% to -68% for short and slender superstructures, respectively. In addition, it is noticeable that at 3.5 Hz, the cap rotation is higher when a short building is supported, contrary to the case of 2.0 Hz base shaking.

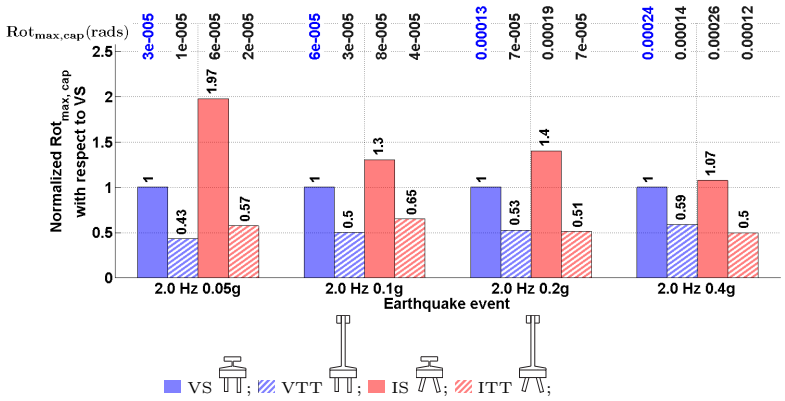

Figure 4.39: Normalized maximum rotation of pile cap, under 2.0 Hz sinusoidal excitations

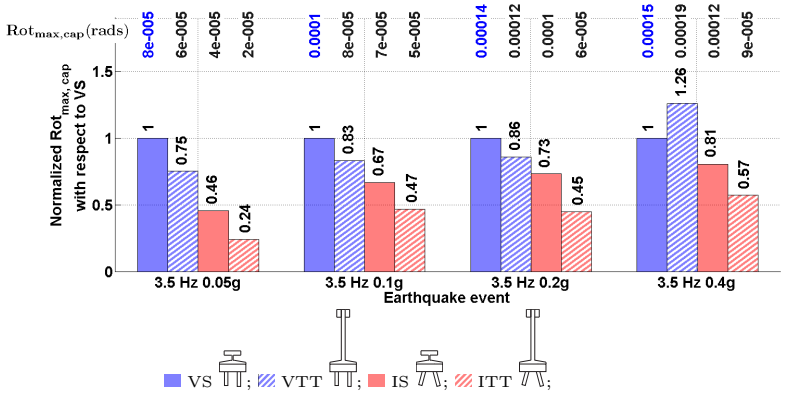

Figure 4.40: Normalized maximum rotation, under 3.5 Hz sinusoidal excitations

4.4.2 Inertial loads induced by superstructures with SSPSI, sinusoidal tests

4.4.2.1 Base shear force

Figs. 4.41 and 4.42 show the results of the total base shear force acting on the foundations under 2.0 Hz and 3.5 Hz sinusoidal excitations respectively. The performance of the inclined piles is largely influenced by the frequency of the base shaking. Furthermore, at 3.5 Hz, the type of superstructure influences also the effects of the inclined piles.

At 2.0 Hz sinusoidal excitation the effect of inclined piles is negligible for both short and slender superstructures. An increase of the gravity center of the superstructure reduces the base shear force.

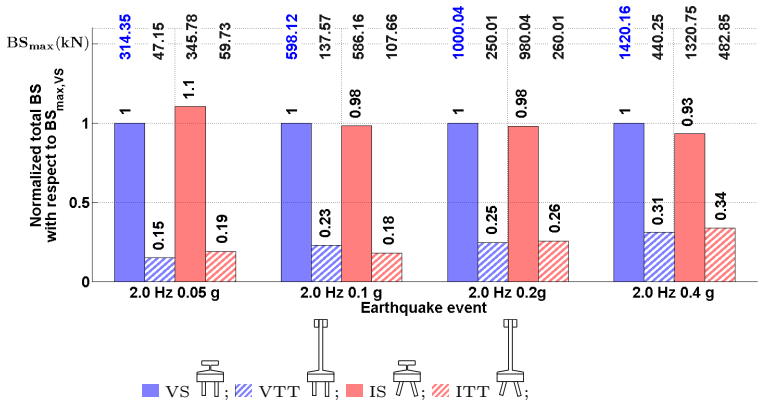

Figure 4.41: Normalized maximum base shear force, under 2.0 Hz sinusoidal excitations

At 3.5 Hz sinusoidal excitation, for the case of inclined piles and the short building the base shear force is significantly reduced (from 68% to 46%). For a slender building, the base shear force is found increased; this effect however vanishes for high intensity excitations.

For vertical piles, a slender superstructure reduces the base shear force. This reduction is much smaller when a short superstructure is supported.

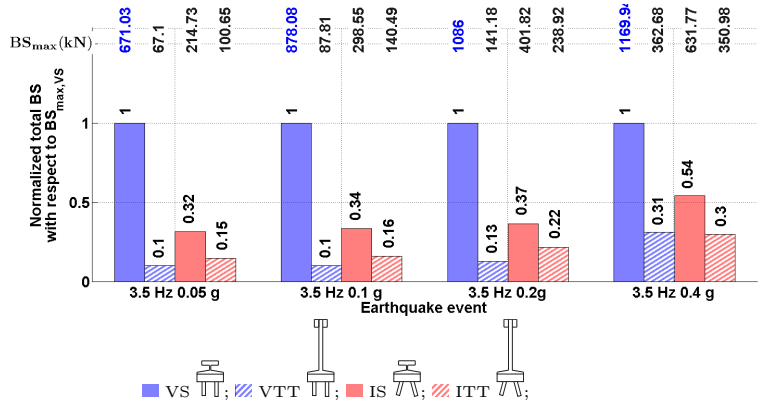

Figure 4.42: Normalized maximum base shear, under 3.5 Hz sinusoidal excitations

4.4.2.2 Overturning moment

Figs. 4.43 and 4.44 show the maximum overturning moment acting on the foundation under 2.0 Hz and 3.5 Hz base shaking respectively. In all cases, the overturning moment is higher at 2.0 Hz (fixed-base frequency). The performance of inclined piles is largely influenced by the type of superstructure. At 2.0 Hz, the base shaking effect is negligible for short building on inclined piles, whereas for slender superstructure it is beneficial (-21% to 44%) (except for 2.0 Hz 0.05g).

In addition for both pile group configurations, a slender superstructure decrease the maximum overturning moment (except in the case of the vertical piles subject to 2.0 Hz 0.4g).

At 3.5 Hz, for both superstructures, inclined piles significantly change the overturning moment. With the increase of the excitation intensity, this effect slows down for the short superstructure (71% to 47%) and goes up for the slender one (-43% to 67%).

For vertical pile configuration, slender superstructure tends to reduce the overturning moment, however, the reduction effect vanishes for the 3.5 Hz 0.4 g excitation, higher overturning moment is observed. For inclined pile configuration, the influence of the height of gravity center is regarded as negligible.

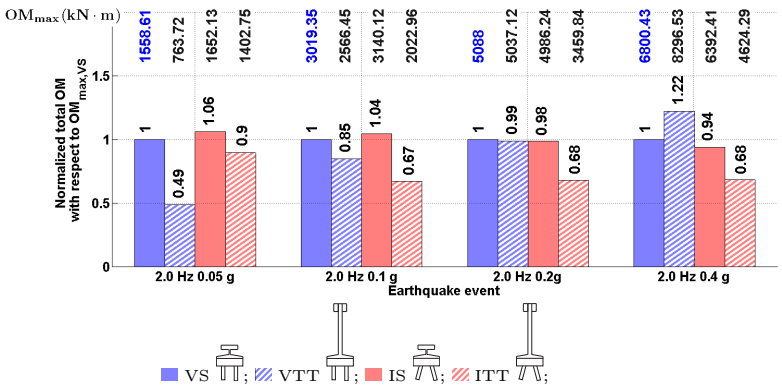

Figure 4.43: Normalized maximum overturning moment, under 2.0 Hz sinusoidal excitations

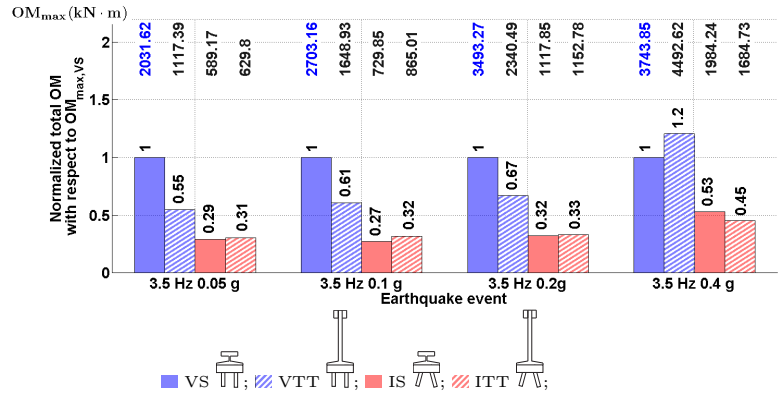

Figure 4.44: Normalized maximum overturning moment, under 3.5 Hz sinusoidal excitations

4.4.2.3 Summary

It can be concluded from this section that, the performance of inclined piles is influenced by both base shaking frequency and the height of the gravity center of superstructure.

- At 2.0 Hz sinusoidal excitations: for short superstructure inclined piles do not influence the base shear and overturning moment. The total inertial loads

(base shear + overturning moment) resulting from short superstructure are identical for both pile groups.

For slender superstructure, inclined piles do not influence the base shear forces and for both pile configurations. In addition, although slender superstructure helps to reduce overturning moment on vertical piles, for inclined piles the reduction is more efficient.

- Under 3.5 Hz sinusoidal excitations: for short superstructure inclined piles have a beneficial behavior by decreasing base shear and overturning moment. In the case of slender superstructure, the situation is much more complicated. Slender superstructure on inclined piles has higher base shear force, however, less overturning moment. It is very difficult to evaluate which configuration (VTT or ITT) is really subjected to a more favorable loading combination of base shear and overturning moment. Generally speaking, with the increase of the position of the gravity center, the inertial loads are reduced.

4.4.3 Stresses in piles with SSPSI, sinusoidal tests

4.4.3.1 Residual bending moment in piles

The performance of inclined piles in terms of residual bending moments is influenced by the frequency of the base shaking especially for the case of short superstructure. Figs. 4.45 and 4.46 show the normalized residual bending moment profiles under 2.0 Hz and 3.5 Hz sinusoidal excitations respectively.

At 2.0 Hz, both inclined and vertical piles have a "C" looked like shape. The peak values for inclined piles are at $7.5D$ depth. For the vertical piles, under small excitations (0.05 g and 0.1 g), the peak values are about $7.5D$ depth. During strong inputs (0.2 g and 0.4 g) the peak values are at $10D$ depth. For all the configurations the maximum residual bending moment is bellow the soil surface.

At 3.5 Hz, the peak values for the configuration IS is at $7.5D$ depth. For the other configurations, peak values are approximately at $10D$ depth. Inclined piles reduce the depth of the maximum residual bending moment when a short building is supported ($7.5D$ depth against $10D$ depth for the other configurations).

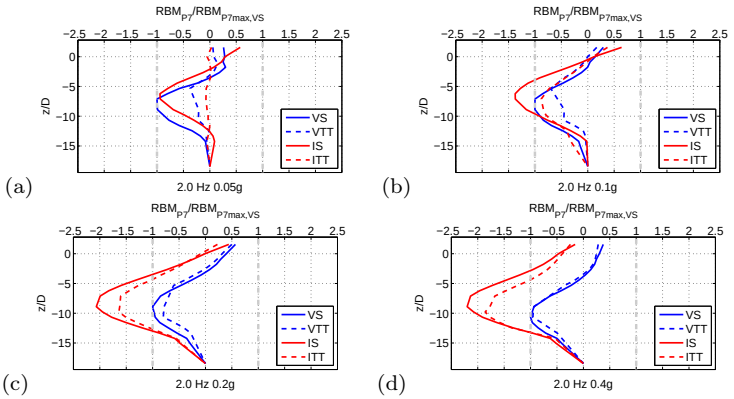

Figure 4.45: Normalized residual bending moment, under sinusoidal excitations

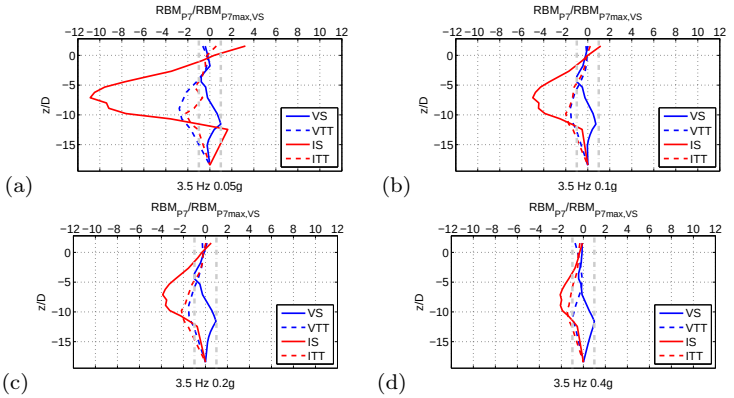

Figure 4.46: Normalized residual bending moment, under sinusoidal excitations

Figs. 4.47 and 4.48 show the normalized peak values of residual bending moment under 2.0 Hz and 3.5 Hz sinusoidal excitations respectively.

At 2.0 Hz, inclined piles have a detrimental behavior by increasing the maximum residual bending moment except for small input (0.05 g). This effect is increased by the accumulation of residual bending moment through successive events.

For both the vertical and inclined pile configurations, slender superstructure induces less residual bending moment. However, this reduction decreases with increasing excitation intensity (from 60 to 4% for the vertical piles and from 90 to 15% for the inclined piles).

At 3.5 Hz, inclined piles induce higher residual bending moment, this effect is more pronounced but decreases with successive input for short superstructure from 1000 to 110%.

The presence of inclined piles changes also the effect of the variation of the gravity center. When inclined piles are used, the increase of the gravity center induces less residual bending moment in comparison with the vertical pile group configuration. However, this effect goes down with the accumulation of residual bending moment for both configurations.

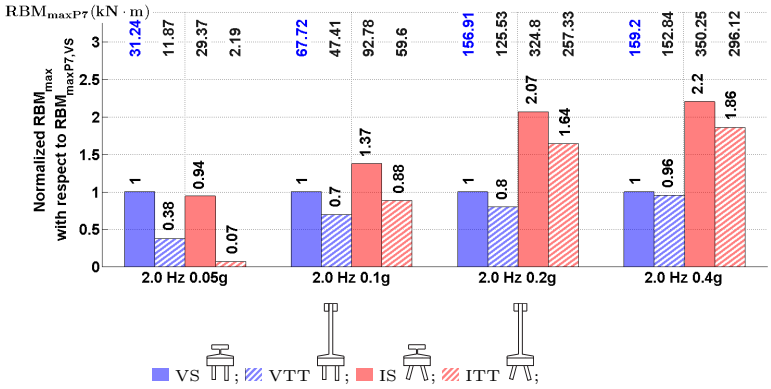

Figure 4.47: Normalized maximum RBM, under 2.0 Hz sinusoidal excitations

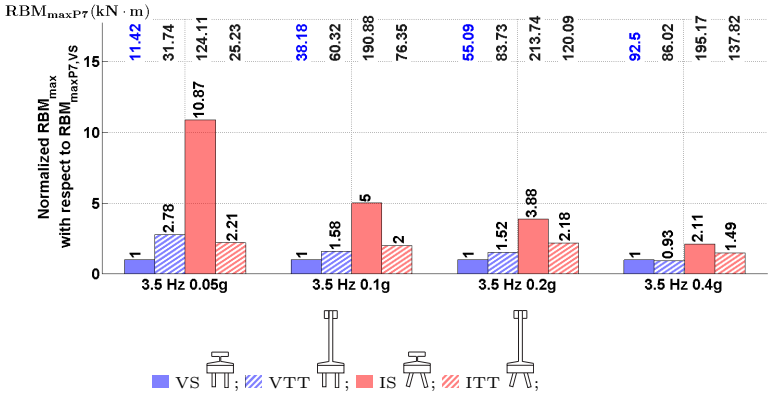

Figure 4.48: Normalized maximum RBM, under 3.5 Hz sinusoidal excitations

4.4.3.2 Total resultant bending moment in piles

Figs. 4.49 and 4.50 show the normalized total bending moment profiles under 2.0 Hz and 3.5 Hz sinusoidal excitations respectively.

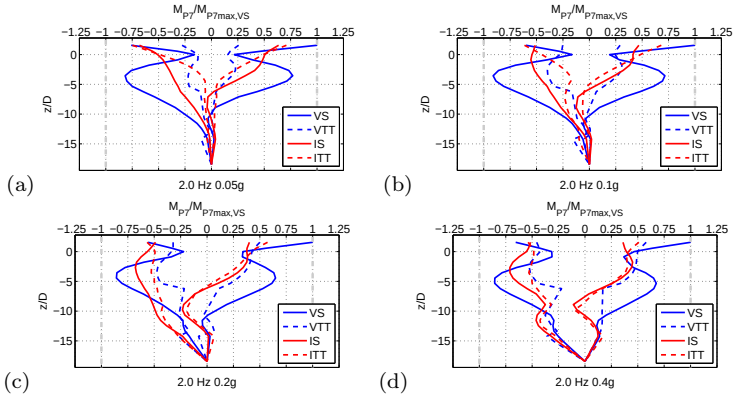

Figure 4.49: Normalized maximum total resultant bending moment, under sinusoidal excitations

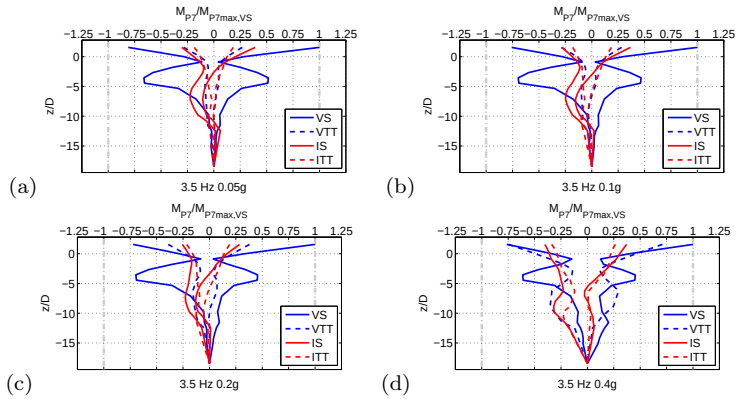

Figure 4.50: Normalized total bending moment, under sinusoidal excitations

The normalized peak values along the profiles are summarized in Figs. 4.51 and 4.52.

At 2.0 Hz, performances of inclined piles are influenced by the type of superstructure. For short superstructure, inclined piles induce less bending moment, this reduction effect is around 30∼40% for all inputs. For slender superstructure, inclined piles have a increase the bending moment, however this effect goes down from -170 to 7%.

For vertical pile configuration, slender superstructure greatly reduces the bending moment, the reduction effect goes down from 70 to 50%. For inclined pile configuration, under small intensity excitations, slender superstructure slightly increase the bending moment. However, during strong intensity input, slender superstructure reduces the bending moment. The reduction effect goes up from -10 to 24%.

At 3.5 Hz, inclined piles reduce the maximum bending moment for both type of superstructure. This effect is more pronounced for short superstructure (-60 % to 71%), for which larger total bending moment are concerned, than for the slender one (-35% to -54%). In addition, the presence of inclined pile reduce the effect of the type of superstructure.

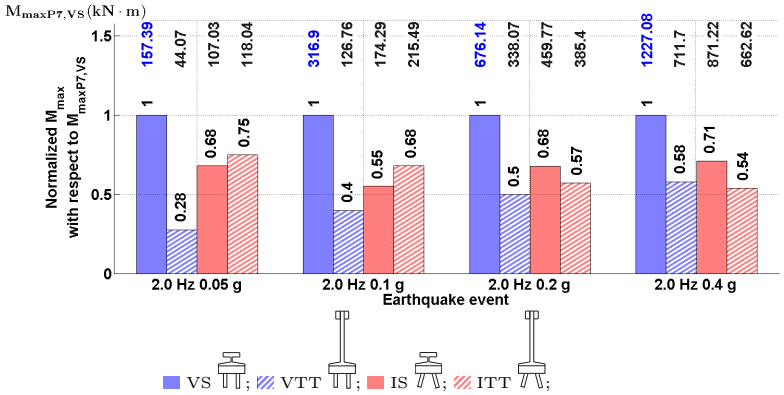

Figure 4.51: Normalized maximum total bending moment, under 2.0 Hz sinusoidal excitations

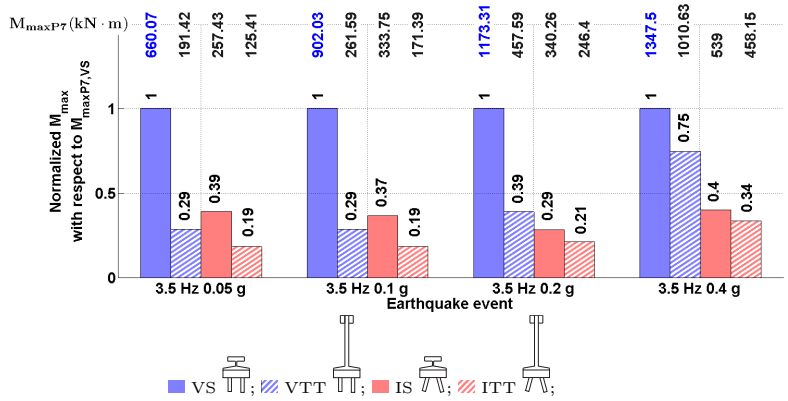

Figure 4.52: Normalized maximum total bending moment, under 3.5 Hz sinusoidal excitations

4.4.3.3 Axial force in piles

Due to less compression strain gauges are instrumented in piles, it is very difficult to evaluate the influence of inclined piles on the axial force profile.

Figs. 4.53 and 4.54 show the normalized maximum axial force of each configuration for 2.0 and 3.5 Hz sinusoidal excitations, respectively.

At 2.0 Hz, inclined piles reduce the axial force by about 20% for short superstructure and 5∼39% for the slender one. In addition, for both pile group configuration, slender superstructure induces less axial force.

At, 3.5 Hz, contrary to the 2.0 Hz tests, the performance of inclined piles are largely influenced by the type of superstructure. When a short superstructure is supported, inclined piles significantly reduce the axial force (-30% to 55%). At the contrary, for slender superstructure, inclined piles increase the axial force (from 105% to 75 % with the increase of excitation intensity).

For both inclined and vertical pile configurations, slender building induces less axial force. However, in the case of inclined piles, the effect of the type of superstructure is less pronounced (-80% to 65% for vertical piles against -12% to 17% for inclined piles, respectively.)

The performance of the inclined piles is largely influenced by the type of the supported superstructure. For the short superstructure, inclined piles have a beneficial behavior contrary to the case when a slender superstructure is supported. However, the maximum total bending moment is higher when the short superstructure is supported (from 185% to 455%). Consequently, inclined piles play a beneficial role for the case of a short superstructure. This is due to the fact that when inclined piles are used, the effect of the type of superstructure is negligible (contrary to the case of vertical piles).

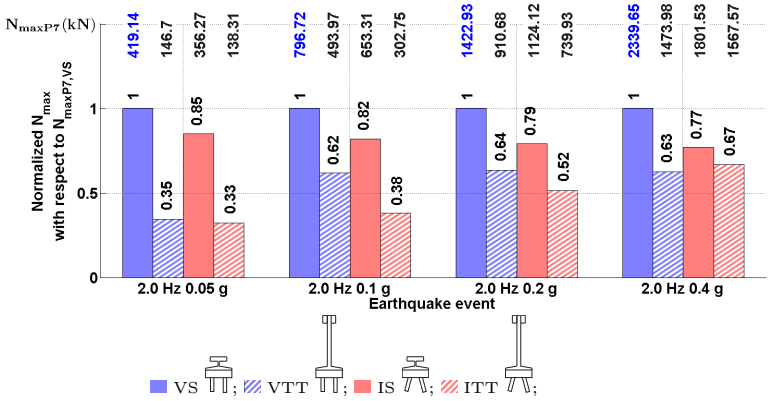

Figure 4.53: Normalized maximum axial force, under 2.0 Hz sinusoidal excitations

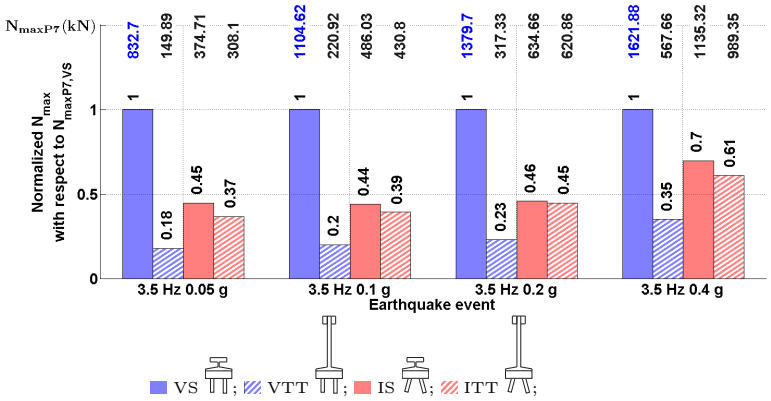

Figure 4.54: Normalized maximum total bending moment, under sinusoidal excitations

4.4.3.4 Summary

In this section, the influences of inclined piles and gravity center on the performance of pile foundations in studied experimentally by series of sinusoidal tests. It is convinced that, the performance of inclined piles is influenced by the frequency of base shaking and also the type of superstructure. The conclusions are as follows:

- **Residual bending moment**: Generally speaking, in terms of residual bending moment, for both short and slender superstructures, the performance of inclined piles is poor.

  Under 2.0 Hz excitation, both for short and slender superstructures, with the increase of excitation intensity the poor performance get even worse. Under 3.5 Hz excitation, for short superstructure (but not for the slender one), with the increase of excitation intensity the poor performance is however mitigated.

  For the vertical pile configuration, under 2.0 Hz excitation, the slender superstructure reduces the residual bending moment. This effect is attenuated

with increase of the excitation intensity. However, under 3.5 Hz excitation, slender superstructure increase the residual bending moment. This effect is also reduced with increasing excitation intensity.

For inclined pile configurations, slender superstructure is always beneficial in reducing the residual bending moment in piles.

- **Total bending moment**: under 2.0 Hz excitation, for the case of inclined piles and a short superstructure the effect on the total bending moment is reduced regardless the excitation intensity. On the contrary, for a slender superstructure inclined piles increase this effect (that is however reduced during strong excitations).

  Under 3.5 Hz excitation, inclined piles decrease the total bending moment both for short and slender superstructures. The reduction effect is not affected by the excitation intensity for the short superstructure. For the slender superstructure, the reduction effect increases for high intensity excitations.

- **Axial force**: under 2.0 Hz excitation, inclined piles play a reduction effect both for short and slender superstructures. For the short superstructure, the reduction effect is not sensitive to the excitation intensity. In the case of the slender structure the reduction effect is reduced for high intensity excitations. The slender superstructure is beneficial both for the vertical and the inclined piles. This beneficial effect is reduced for high intensity excitations.

  Under 3.5 Hz excitation, inclined piles reduce the axial force for the short superstructure. This effect is reduced for high intensity excitations. On the contrary, for slender superstructure the axial force is increased.

4.5 Performance of inclined piles in terms of rocking and horizontal translation behavior

When pile foundations are subjected to seismic loads, foundations move horizontally combined with rocking movements on the pile caps. The translation or rocking behavior of the foundations can be significantly influenced by the presence of inclined piles. In this section, the translation and the rocking behavior of the inclined and vertical pile foundations are compared and analyzed.

4.5.1 Rocking behavior of pile foundations

The results from the tests with 2.0 Hz sinusoidal excitations are first shown in terms of hysteresis loops in Fig. 4.55. The degradation curves of rotational stiffness are shown in Fig. 4.56. Following the hysteresis loops, it is obvious that the inclined pile foundation has more energy dissipation than the vertical pile group. The damping ratio for the inclined pile foundation goes up to 30 % while for the vertical pile foundation is around 10 %, see in Fig. 4.56 (b) and (d). However, the presence of inclined piles does not influence so significantly the rotational stiffness degradation curve, see in Fig. 4.56 (a) and (c). It could also be noticed that for the same foundation (inclined or vertical configuration), the rotational stiffness is not influenced by the type of the superstructure (see in Fig. 4.56, blue data points are for the tall building while red data points are for the short building. The gravity center of the superstructure does not change the behavior of the foundation).

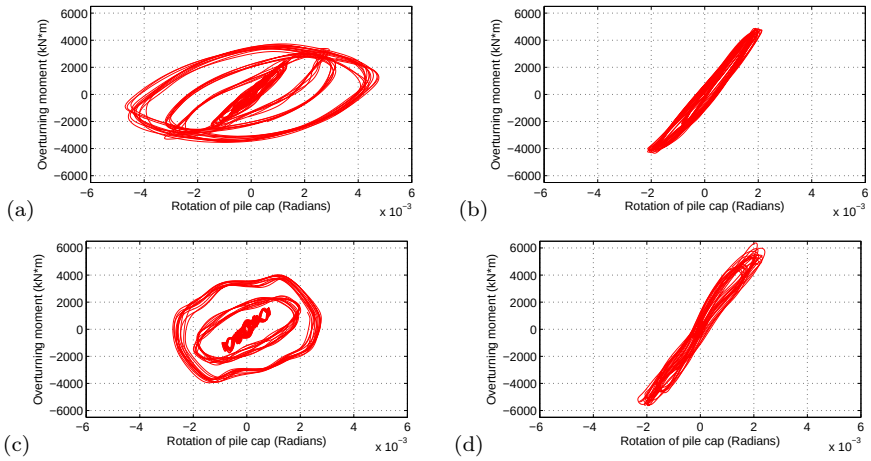

Figure 4.55: Rotation-moment Hysteresis loops, 2.0 Hz sine input: (a) Inclined pile group with short building; (b) Vertical pile group with short building; (c) Inclined pile group with taller building (14.16 m) and (d) Vertical pile group with taller building (14.16 m)

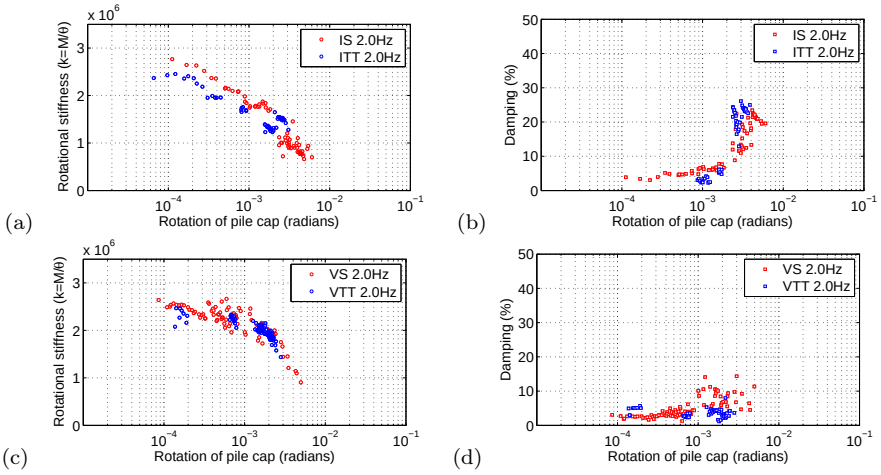

Figure 4.56: Rotational stiffness degradation curve of inclined and vertical pile foundations, 2.0 Hz input: (a) Rotational stiffness degradation curve of inclined pile group with short building and taller building (b) Damping ratio (c) Rotational stiffness degradation curve of vertical pile group with short building and taller building (d) Damping ratio

For the 3.5 Hz and the real earthquake tests, conclusions are similar as for the 2.0 Hz input tests. For the detailed results, refer to Appendix. E. The computed rotational stiffness degradation curve and associated damping ratio for 3.5 Hz and real earthquake tests are shown in Figs. 4.57 and 4.58.

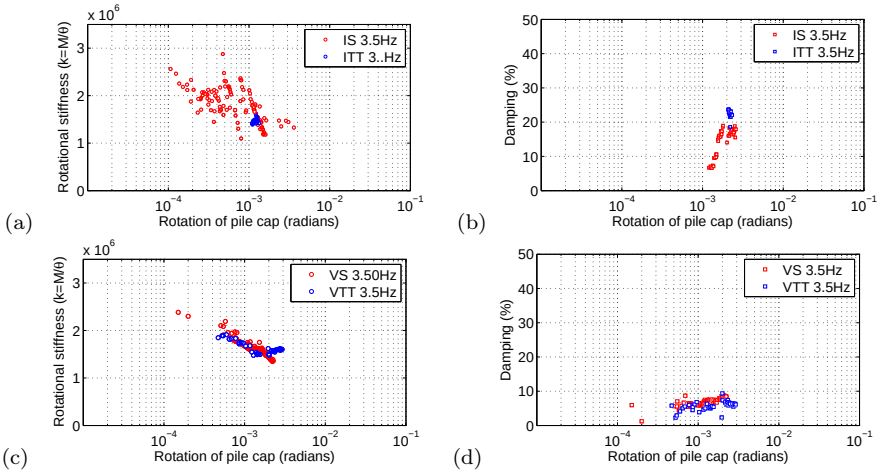

Figure 4.57: Rotational stiffness degradation curve of inclined and vertical pile foundations, 3.5 Hz input: (a) Rotational stiffness degradation curve of inclined pile group with short building and taller building (b) Damping ratio (c) Rotational stiffness degradation curve of vertical pile group with short building and taller building (d) Damping ratio

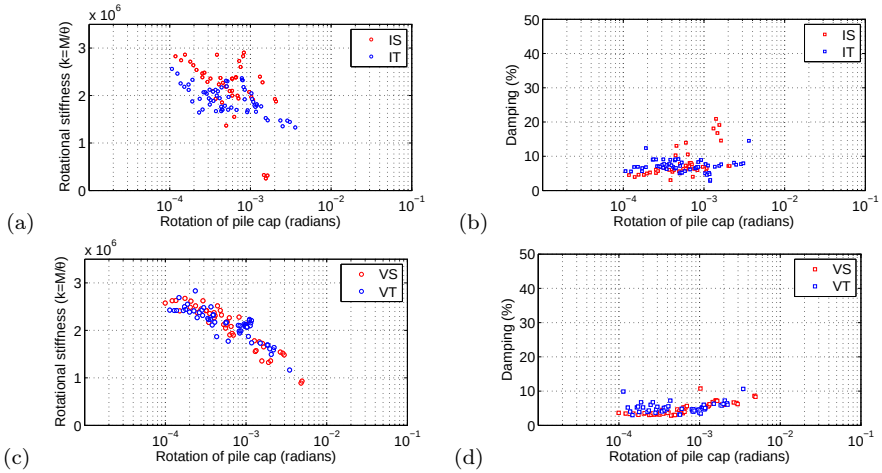

Figure 4.58: Rotational stiffness degradation curves, real earthquake input: Inclined pile group with (a) short and tall building and (b) damping ratio; (d) Vertical pile group with short and tall building and (d) damping ratio

It is observed that the rotational degradation and damping ratio curves follow almost the same trend in all the results, (see in Fig. 4.59). The good agreement between all the tests indicates that the responses of the pile foundations installed in dry sand are frequency independent. Furthermore, the presence of a superstructure does not influence the mechanical behavior of the foundations. The presence of inclined piles has limited effect on the rotational degradation behavior, however it significantly influences the energy dissipation properties of the pile foundation systems. When the rotation of the pile cap is between 1.0×10^{-3} and 5.0×10^{-3}, the damping ratio for the inclined pile foundation is (around) 2.5 times higher than that of the vertical pile foundation.

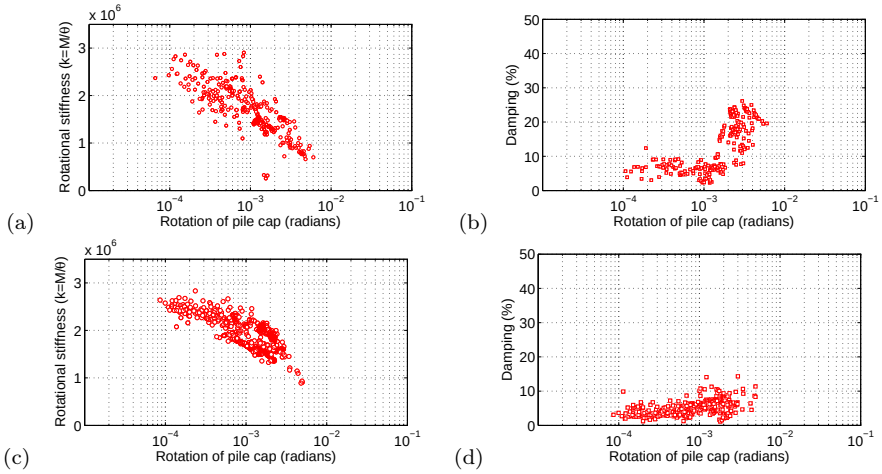

Figure 4.59: Rotational stiffness degradation curves from all input signals: Inclined pile group with (a) short and tall building and (b) damping ratio; (c) Vertical pile group with short and tall building and (d) damping ratio

The data points of the rotational stiffness diagram for the inclined and vertical pile foundations are fitted using the following empirical equation:

$$K_R = \frac{K_{Rmax}}{1 + \alpha\ \gamma_r^{\beta}} \tag{4.4}$$

where K_R is the secant rotational stiffness of the pile foundation; K_{Rmax} the maximum rotational stiffness; and α and β constants. For the inclined pile foundation K_{Rmax} is estimated $2.35{\times}10^6$ kN·m/rad while for the vertical pile foundation K_{Rmax} is $2.50{\times}10^6$ kN·m/rad. For both configurations α and β are $5.0{\times}10^3$ and 1.4 respectively. The maximum rotational stiffness for the inclined pile foundation is a little lower than that of the vertical pile foundation due to the inclined piles. The fitting curves together with all the data points are plotted in Fig. 4.60.

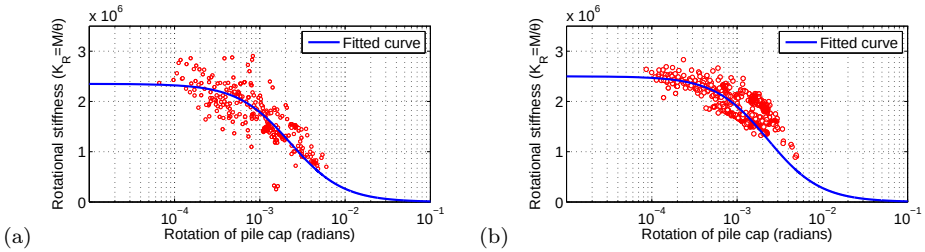

Figure 4.60: Fitted Rotational stiffness degradation curves: (a) Inclined pile foundation and (b) Vertical pile foundation

Following the same procedure in Chapter 2, the damping ratio curves for inclined foundation and vertical foundation are linked with the rotational degradation curve. The proposed form for the fitting equation is the following:

$$D_R = D_{Rmax}\left(m\left(\frac{K_R}{K_{Rmax}}\right)^2 - n\left(\frac{K_R}{K_{Rmax}}\right) + 1\right) \tag{4.5}$$

where D_R is the rotational damping ratio; D_{Rmax} is the maximum rotational damping ratio; m and n are fitting parameters. For the inclined pile foundation, D_{max} is estimated around 35 while for the vertical pile foundation D_{max} is 22. For both cases m and n are 0.63 and 1.5 respectively. The relationships between rotational stiffness and damping ratio for the inclined and vertical foundations together with the fitting curves are plotted in Fig. 4.61

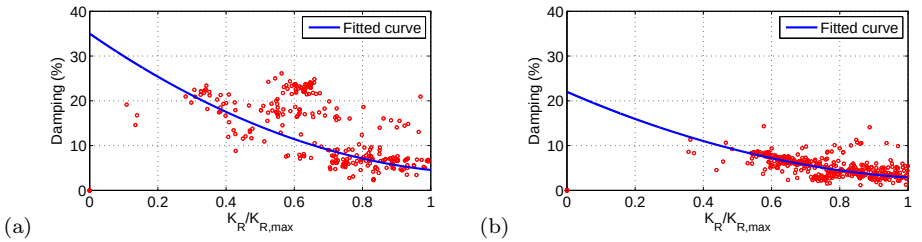

Figure 4.61: Damping ratio in function of normalized rotational stiffness: (a) Inclined pile foundation and (b) Vertical pile foundation

Finally the damping ratio diagrams for inclined foundation and vertical foundation with fitting curves are shown in Fig. 4.62

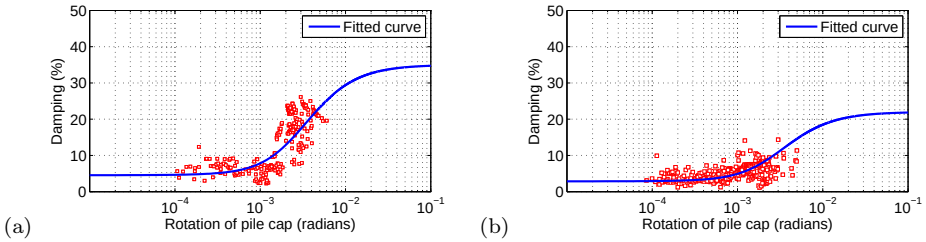

Figure 4.62: Damping ratio in function of normalized rotational stiffness: (a) Inclined pile foundation and (b) Vertical pile foundation

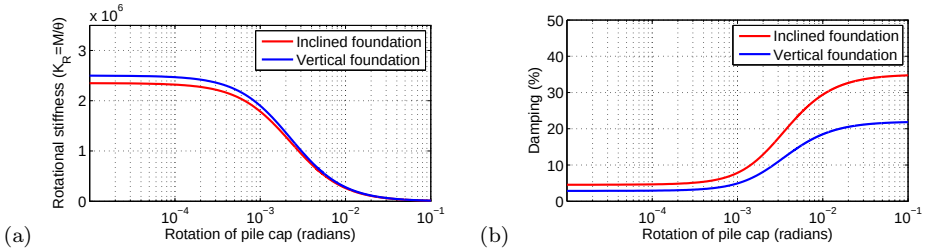

Figure 4.63: Comparison of rocking behavior of Inclined pile foundation and vertical foundation: (a) degradation of rotational stiffness and (b) damping ratio

It can be seen in Fig. 4.63 that the rotational stiffness is not significantly influenced by the presence of the inclined piles. However, the maximum damping ratio is increased approximately by 60 %.

4.5.2 Horizontal translation behavior of pile foundations

The hysteresis loops concerning the horizontal translation of pile foundations under 2.0 Hz sinusoidal excitation are shown in Fig. 4.64. Both inclined and vertical pile foundations present energy dissipation. However, it is interesting to notice from the translational stiffness degradation curves shown in Fig. 4.65(a) and (c),

that the horizontal stiffness is significantly increased (around 2.5 times) due to the inclined piles. The same conclusions are also obtained analyzing the results for 3.5 Hz and real earthquake excitations. For detailed results, refer to Appendix. E. The translational degradation curves and the associated damping ratio are shown in Figs. 4.65, 4.66 and 4.67.

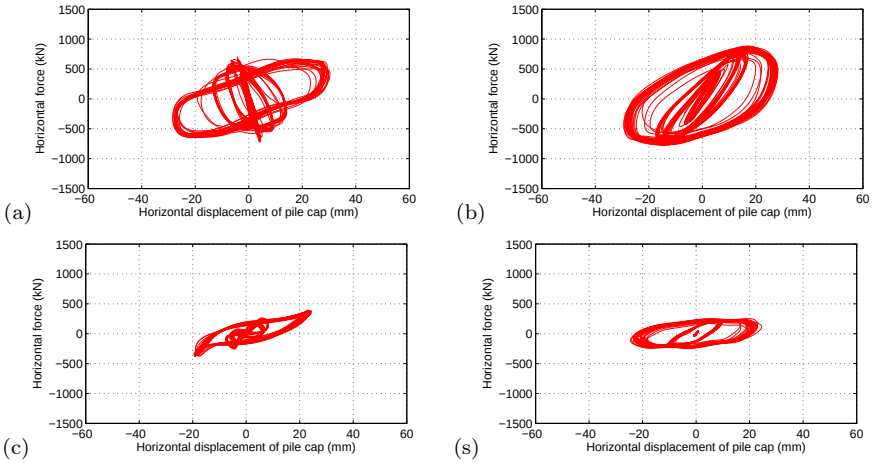

Figure 4.64: Translation-force Hysteresis loops, 2.0 Hz sine input: (a) Inclined pile group with short building; (b) Vertical pile group with short building; (c) Inclined pile group with taller building (14.16 m) and (d) Vertical pile group with taller building (14.16 m)

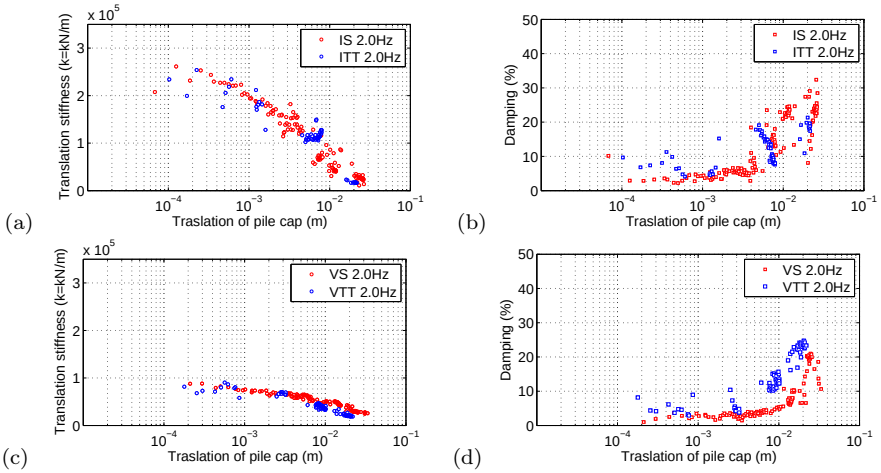

Figure 4.65: Translational stiffness degradation curve of inclined and vertical pile foundations, 2.0 Hz input: (a) Rotational stiffness degradation curve of inclined pile group with short building and taller building (b) Damping ratio (c) Rotational stiffness degradation curve of vertical pile group with short building and taller building (d) Damping ratio

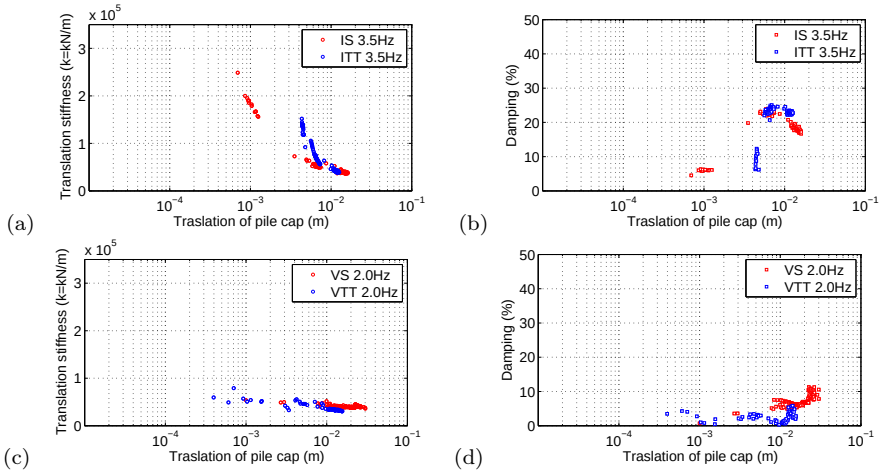

Figure 4.66: Translational stiffness degradation curve of inclined and vertical pile foundations, 3.5 Hz input: (a) Rotational stiffness degradation curve of inclined pile group with short building and taller building (b) Damping ratio (c) Rotational stiffness degradation curve of vertical pile group with short building and taller building (d) Damping ratio

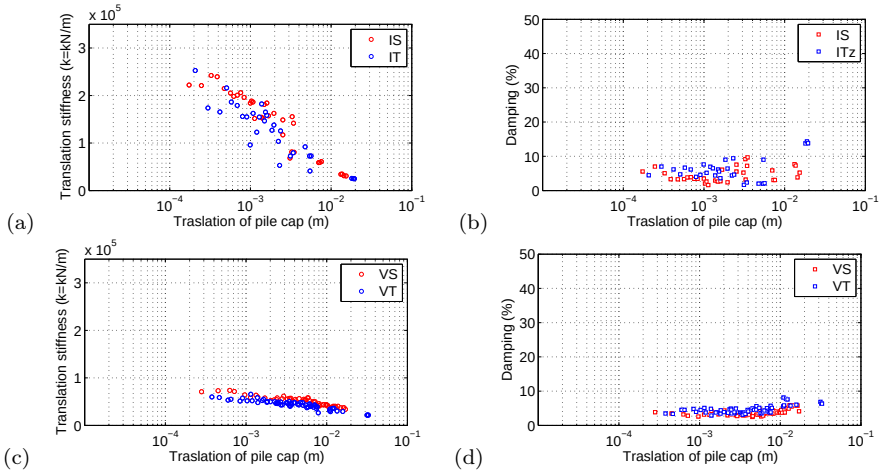

Figure 4.67: Translational stiffness degradation curves, real earthquake input: (a) Inclined pile group with short and tall building and (b) damping ratio; (d) Vertical pile group with short and tall building and (d) damping ratio

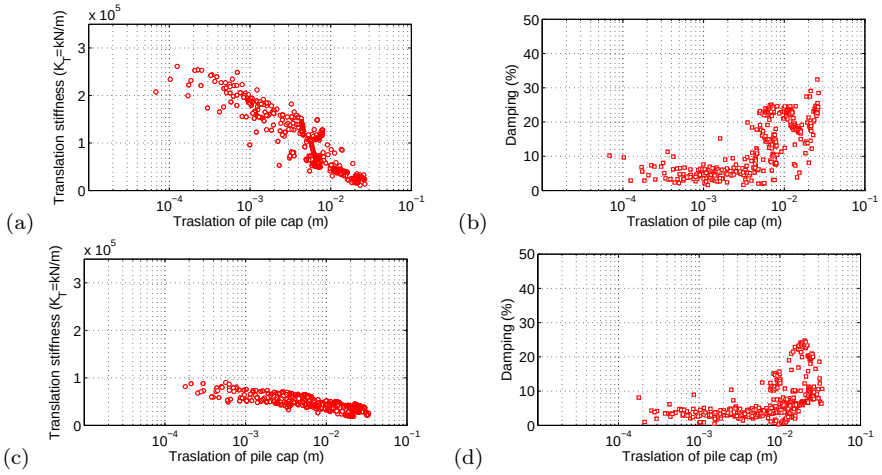

Figure 4.68: Translational stiffness degradation curves, all input signals: (a) Inclined pile group with short and tall building and (b) damping ratio; (c) Vertical pile group with short and tall building and (d) damping ratio

Plotting the results from all the different input signals together, see in Fig. 4.68, it is obvious that they have all a very similar and strong tendency. This confirms the former conclusion that the behavior of pile foundations is frequency independent. Following the same procedure as in the previous sections, the horizontal translation stiffness degradation diagrams are fitted by empirical equations:

$$K_T = \frac{K_{Tmax}}{1 + \alpha\ \gamma_t^{\beta}} \tag{4.6}$$

where K_T is the damping ratio; K_{Tmax} is the maximum horizontal translation stiffness; γ_t is the horizontal translation; α and β are fitting parameters. For the inclined pile foundation K_T is estimated around $2.3{\times}10^5$ kN/m, while for the vertical pile foundation K_T is $0.75{\times}10^5$ kN/m. α and β for both cases are 200 and 1.05 respectively. For the damping ratio associated with the horizontal translation, a similar fitting equation is used as previously that takes the following form:

$$D_T = D_{Tmax}\left(m\left(\frac{K_T}{K_{Tmax}}\right)^2 - n\left(\frac{K_T}{K_{Tmax}}\right) + 1\right) \tag{4.7}$$

where D_T is the damping ratio associated with the translation of the pile cap; D_{Tmax} is the maximum damping ratio; m and n are two fitting parameters. For the inclined pile foundation D_{Tmax} is estimated around 33% while for vertical pile foundation, D_{Tmax} is around 35 %. m and n for both cases are 0.88 and 1.8 respectively. Figs.4.69, 4.70 and 4.71 show the comparisons of the fitting curves with the all the data points shown in Fig. 4.68.

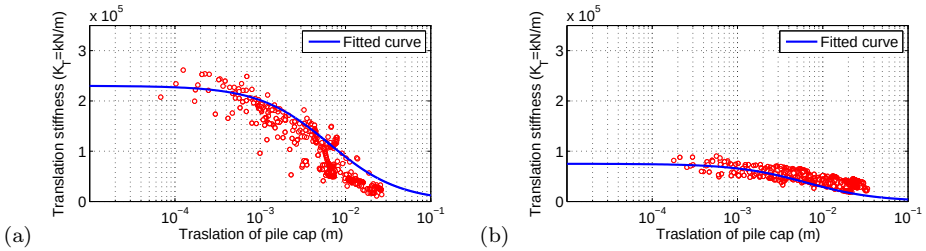

Figure 4.69: Fitted horizontal translation stiffness degradation curves: (a) Inclined pile foundation and (b) Vertical pile foundation

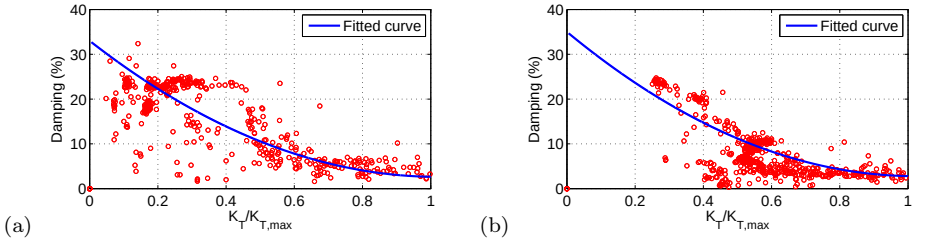

Figure 4.70: Damping ratio in function of normalized rotational stiffness: (a) Inclined pile foundation and (b) Vertical pile foundation

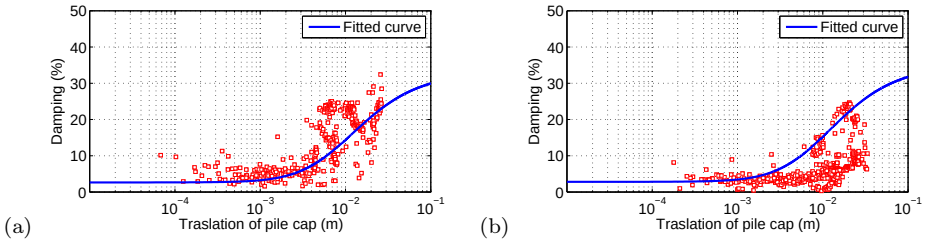

Figure 4.71: Fitted horizontal translation stiffness degradation curves: (a) Inclined pile foundation and (v) Vertical pile foundation

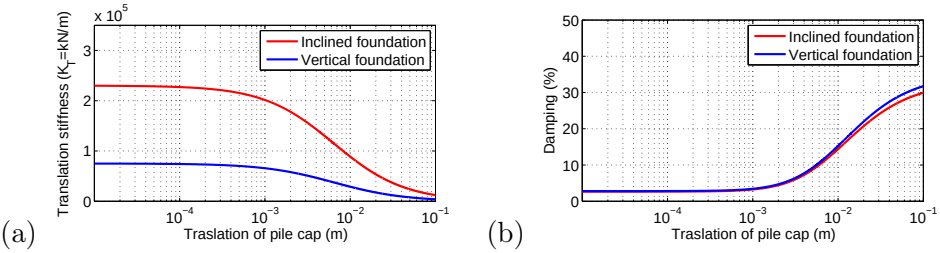

Figure 4.72: Comparison of translation behavior of Inclined pile foundation and vertical foundation: (a) degradation of rotational stiffness and (b) damping ratio

Finally, it can be concluded from Fig. 4.72 that: inclined piles greatly increase

the horizontal stiffness of foundation system by around 2.5 times; while the damping ratio of inclined pile group keeps almost the same as that of the vertical pile group.

4.5.3 Summary

In this section, a comprehensive comparison of the performance between inclined and vertical pile foundations is carried out. The behavior of the inclined pile foundation is found beneficial with respect to different parameters. For the rocking behavior, the presence of the inclined piles increases the rotational damping ratio without losing so much rotational stiffness; for the horizontal translation behavior, inclined piles have a more important horizontal stiffness than the vertical configuration, with almost the same dissipation ability. The results from a relative large number of tests show that the behavior of the pile foundation system is frequency independent and the influence of the position of the gravity center could be ignored.

4.6 Conclusions

In this Chapter, a comprehensive experimental study of performance of inclined piles is presented. The conclusions are following:

1. Compared with the pure soil pile kinematic interaction, the presence of a superstructure (inertial loading) modifies both the responses of inclined and vertical pile groups.

2. Superstructures built on inclined piles have higher resonant frequencies. This is probably due to the higher horizontal stiffness provided by the inclined piles. Regardless the pile group configuration (inclined or vertical), an increase of the gravity center of the superstructure decreases the resonant frequency.

3. Inclined piles tend to decrease the peak accelerations and maximum displacements on the top of the superstructures. For the same superstructure, inclined piles reduce also the pile cap rotation during strong earthquakes.

4. Inclined piles play also a beneficial role by reducing the inertial loading on the superstructures (base shear and overturning moments). Comparing to a vertical pile group, in most of the cases, incline pile groups with either short or tall buildings have a smaller total resultant force acting on the base of the foundation. For strong earthquakes however, due to the high non linearity developed in the soil, the effects of inclined piles or of the gravity center are reduced.

5. In terms of residual bending moments, inclined piles tend to have a worse performance compared with vertical piles.

6. Inclined piles seem to be less sensitive to the variation of the gravity center of the superstructures.

7. Looking at the pure soil pile kinematic interaction, the presence of superstructures has more influence on vertical piles (especially for the short superstructure).

8. Superstructures on vertical piles attract higher inertial loads compared with superstructures on inclined piles.

9. For both inclined and vertical pile configurations, an increase of the gravity center induces higher axial forces in the piles. In terms of bending moments, a higher gravity center may have a beneficial effect on the performance of both inclined and vertical configurations. It is also found that vertical piles are much more sensitive to the variation of the gravity center of the superstructures.

10. For the rocking behavior, the presence of the inclined piles increases the rotational damping ratio without losing so much the rotational stiffness; for the horizontal translation behavior, compared with vertical pile foundation, the inclined one have greatly larger horizontal stiffness than the vertical one, while keeps almost the same dissipation ability as the vertical pile foundation. The results from a relative a large number of tests show that, the behavior of the pile foundation system is frequency in-dependent, and the influences from the gravity center could be ignored.

Chapter 5

Finite element modeling of Soil Structure Interaction

With the increasing computer power and the development of commercial finite element codes, the numerical modeling of Soil Structure Interaction using classical 2D or 3D finite elements attracts the attention of both researchers and engineers [9,15,27,62–64]. In this chapter, a Drucker-Prager type constitutive law based on the hypoplasticity theory is introduced. Although having a relatively small number of material parameters, comparison with experimental results proves the performance of the model. In Chapter 6 it will be extensively used to develop a new macro-element for pile foundations.

5.1 A Drucker-Prager model based on hypoplasticity

5.1.1 Formulation

The performance of a soil pile interaction numerical strategy greatly depends on the adopted soil constitutive law. The Mohr-Coulomb [122] and the Drucker-Prager [123] elastoplastic laws are the most commonly used constitutive relations in geotechnical engineering. In this section, the choice is made to introduce a Drucker-Prager type model based on the hypoplasticity theory. The term hypoplasticity was introduced by Dafalias [124] to designate a particular type of bounding surface plasticity with a vanishing elastic domain [125]. In comparison with elastoplastic models, hypoplasticity can provide a more smooth numerical response [125], (see also Fig. 5.3). An outline of the hypoplasticity theory was presented by Kolymbas in 1991 [126].

In the following, a constitutive law similar to an elastic perfectly plastic Drucker-Prager model is formulated according to the hypoplasticity theory and it is used to numerically reproduce the behavior of the sand. The basic framework of the hypoplastic formulation is provided with the following equation [127] [31] (in the following the **bold** letters define tensors and vectors $\|\|$ the norm of a tensor):

$$\dot{\mathbf{T}} = \mathcal{L}\mathbf{D} + \mathbf{N}\|\mathbf{D}\| \tag{5.1}$$

where $\dot{\mathbf{T}}$ and $\mathbf{D}$ are the stress rate and stretching rate (6x6) tensors respectively. In contrast with elastoplasticity, in hypoplasticity the tangent stiffness matrix varies continuously with the direction of the velocity, a property known as incremental

nonlinearity [128] [129]. The nonlinear behaviour of the material results thus from the interaction between the matrix $\mathcal{L}$ and vector $\mathbf{N}$.

It is considered hereafter that the initial value $\mathcal{L}^{\mathrm{e}}$ of the matrix $\mathcal{L}$ depends on the bulk modulus K and the shear modulus $G_{\max}$ in the elastic range. It has the following form (the Lamé coefficient $\mu = G_{\max}$ according to Hooke's law):

$$\mathcal{L}^{\mathrm{e}} = \begin{bmatrix} K+4\mu/3 & K-2\mu/3 & K-2\mu/3 & 0 & 0 & 0 \\ K-2\mu/3 & K+4\mu/3 & K-2\mu/3 & 0 & 0 & 0 \\ K-2\mu/3 & K-2\mu/3 & K+4\mu/3 & 0 & 0 & 0 \\ 0 & 0 & 0 & \mu & 0 & 0 \\ 0 & 0 & 0 & 0 & \mu & 0 \\ 0 & 0 & 0 & 0 & 0 & \mu \end{bmatrix} \tag{5.2}$$

For a frictional material like sand, $G_{\max}$ is influenced by the mean effective confining pressure p and the void ratio e [130, 131]:

$$G_{\max} = f_n(e, p) \tag{5.3}$$

It is usually considered that proposed by Delfosse-Riday et al. [103]:

$$G_{\max} = A\,\frac{(B-e)^2}{(1+e)}\,p^C \tag{5.4}$$

where A, B, C are material constants. For the basis form of hypoplastic constitutive model, at this stage, $\mathcal{L}$ equals to $\mathcal{L}^{\mathrm{e}}$.

The constitutive vector $\mathbf{N}$ is defined following the approach proposed by Niemunis [31]:

$$\mathbf{N}(\mathbf{T}) = -y(\mathbf{T})\mathcal{L}\mathbf{m}(\mathbf{T}) \tag{5.5}$$

where $\mathbf{T}$ the stress tensor, $y(\mathbf{T})$ is a scalar function named degree of non linearity and $\mathbf{m}(\mathbf{T})$ defines the plastic flow direction.

The scalar function $0 \leq y(\mathbf{T}) \leq 1$ is chosen here as a function of the current stress $q(\mathbf{T}) = \sqrt{3J_2}$ and a predefined limit stress $\sigma_{\mathrm{y}}(\mathbf{T})$ as follows:

$$y(\mathbf{T}) = \left(\frac{q(\mathbf{T})}{\sigma_{\mathrm{y}}(\mathbf{T})}\right)^{n_c} \tag{5.6}$$

with n_c being a constant that controls the isotropic evolution of $y(\mathbf{T})$ (see also Fig. 5.4) and J_2 the second invariant of the deviatoric stress tensor. The ratio $q(\mathbf{T})/\sigma_y(\mathbf{T})$ measures the distance between the current stress surface (which expands isotropically) and the predefined yield surface, see Fig. 5.1(a). It is considered hereafter that the predefined yield stress $\sigma_y(\mathbf{T})$ can not be surpassed, meaning that once the yield surface reached $q(\mathbf{T}) - \sigma_y(\mathbf{T}) = 0$.

The objective being to use an hypoplastic constitutive law similar to the elastic perfectly plastic Drucker-Prager model, the chosen $\sigma_y(\mathbf{T})$ has to lie on the classical Drucker-Prager yield surface. Furthermore, the Drucker-Prager yield surface can be matched with the Mohr-Coulomb yield surface on the compression corners (see

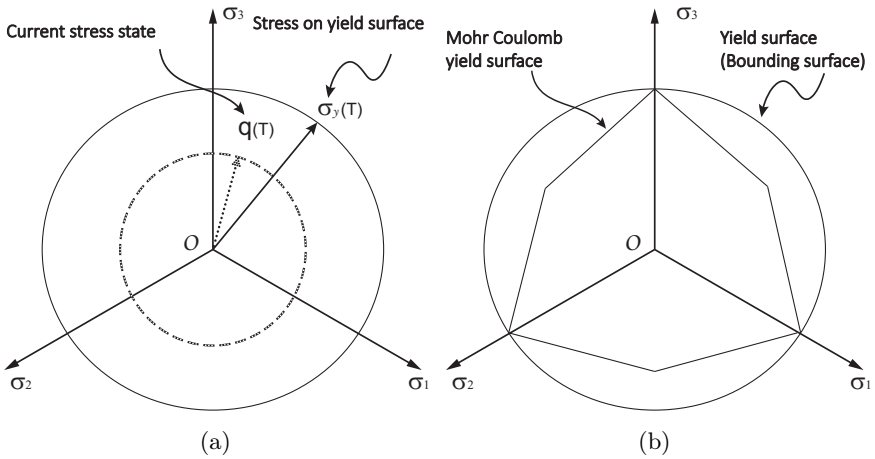

Figure 5.1: (a) Cross-sections of the current stress and yield surfaces (b) matching the predefined yield surface with the Mohr-Coulomb criterion

Fig. 5.1(b)). The way to do this, function of the mean effective confining pressure $p(\mathbf{T})$ and the material frictional angle ϕ, is explained hereafter, [132].

The Drucker Prager yield criterion has the following general form:

$$F = q(\mathbf{T}) - M_c\, p(\mathbf{T}) - k_c = 0 \tag{5.7}$$

where M_c and k_c are material constants expressed in terms of the friction angle ϕ and the cohesive strength c:

$$M_c = \frac{6sin\phi}{3 - sin\phi} \tag{5.8}$$

$$k_c = 6c\frac{cos\phi}{3 - sin\phi} \tag{5.9}$$

Assuming a dry sand and thus a zero cohesive strength ($c = 0$), $k_c = 0$ and the yield function reads:

$$F = q(\mathbf{T}) - M_c\, p(\mathbf{T}) = 0 \tag{5.10}$$

From Eq. (5.10) it is obvious that the constant parameter M_c defines the slope of the yield surface (see Fig. 5.2). According to Eq. (5.10) it can also be assumed that $\sigma_y(\mathbf{T}) = M_c\, p(\mathbf{T})$ and thus the scalar function of Eq. (5.6) reads:

$$y(\mathbf{T}) = \left(\frac{q(\mathbf{T})}{\sigma_y(\mathbf{T})}\right)^{n_c} = \left(\frac{q(\mathbf{T})}{M_c\, p(\mathbf{T})}\right)^{n_c} \tag{5.11}$$

The plastic flow direction $\mathbf{m}(\mathbf{T})$ is defined according to the bounding surface model [124] [133] [134]. The current stress $q(\mathbf{T})$ is assumed to lie on a *loading surface* f which has a similar shape with the yield surface F (*bounding surface*), see Fig. 5.2. The expression of the loading surface can be thus defined as:

$$f = q(\mathbf{T}) - M_c\,(p(\mathbf{T}) - p_0) = 0 \tag{5.12a}$$

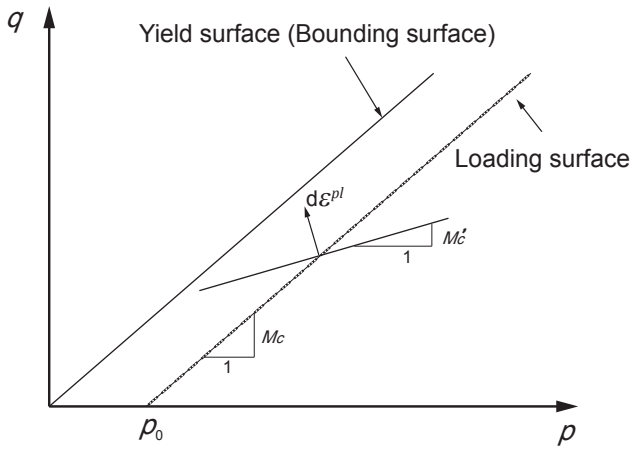

Figure 5.2: Plastic flow direction

with

$$p_0 = \frac{1}{M_c}(\sigma_y(\mathbf{T}) - q(\mathbf{T})) = \frac{1}{M_c}(M_c\, p(\mathbf{T}) - q(\mathbf{T})) \tag{5.12b}$$

When $q(\mathbf{T})$ reaches the limit stress $\sigma_y(\mathbf{T}) = M_c\, p(\mathbf{T})$, $p_0 = 0$ and the loading surface coincides with the bounding surface.

Due to the similar shapes of the yield and loading surfaces, for given stress state $(p(\mathbf{T}), q(\mathbf{T}))$, the directions normal to the two surfaces are identical. In order to determine the direction of the plastic strain increment $d\varepsilon^{pl}$ (see Fig. 5.2), one can thus only refer to the yield surface. As usually done for soils, a non-associated flow rule is chosen:

$$G = q(\mathbf{T}) - M_c^{'}\, p(\mathbf{T}) \tag{5.13a}$$

with

$$M_c^{'} = \frac{6sin\psi}{3 - sin\psi} \tag{5.13b}$$

and ψ is the sand dilation angle. The parameter $M_c^{'}$ defines the direction of the plastic strain increment (see Fig. 5.2). The direction of plastic strain is given by Eq. 5.14:

$$\mathbf{m}(\mathbf{T}) = \frac{\partial G/\partial \mathbf{T}}{\|\partial G/\partial \mathbf{T}\|} \tag{5.14}$$

The comparison of the results on a simple shear test using the Drucker-Prager model and the proposed hypoplastic model is shown in Fig. 5.3. In this example, the friction and dilation angles of the sand are assumed equal to 33° and 0° respectively and the mean confining pressure 149 kPa. The hypoplastic model provides the same ultimate strength as the Drucker-Prager model but follows a more smooth transition curve.

The influence of the coefficient n_c on the response of model is shown in Fig. 5.4. Increasing values of n_c provide responses close to the Drucker-Prager model.

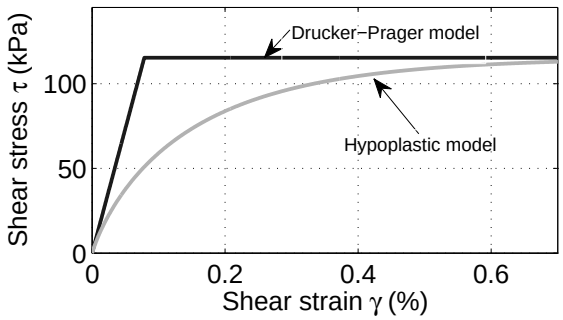

Figure 5.3: Comparison of the Drucker-Prager model with the proposed hypoplastic model

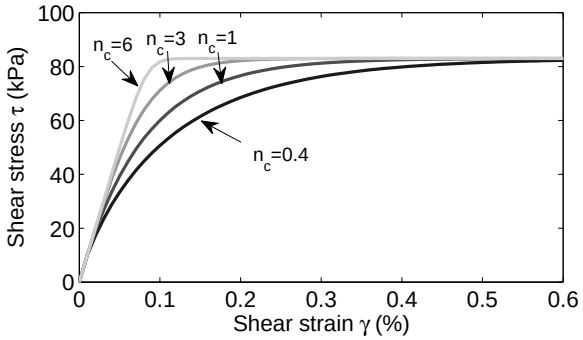

Figure 5.4: Influence of the coefficient n_c on the hypoplastic model behavior

The hypoplastic model yield surface in the principal stress space is shown in Fig. 5.5.

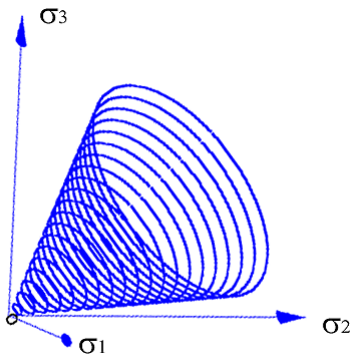

Figure 5.5: Yield surface of the hypoplastic model in the principal stress space

The hypoplastic model presented in this section provides good results for monotonic loading. The extension to cyclic loading is introduced hereafter.

5.1.2 Intergranular strain concept

The previous formulation can not distinguish between loading and reloading which causes ratcheting [31] and therefore has a poor performance at small strain amplitudes. To overcome this problem, Niemunis and Herle [30] introduced the concept of intergranular strain $\mathbf{h}$, which can be seen as an internal state variable. The evolution rate of the intergranular strain is defined as follows (the symbol $\dot{()}$ defines the derivative with respect to time):

$$\dot{\mathbf{h}} = \begin{cases} (\mathcal{I} - \hat{\mathbf{h}}\hat{\mathbf{h}})\rho^{\beta_r} : \mathbf{D} & (\hat{\mathbf{h}} : \mathbf{D} > 0) \\ \mathbf{D} & (\hat{\mathbf{h}} : \mathbf{D} \leq 0) \end{cases} \tag{5.15}$$

where $\rho = \frac{\|\mathbf{h}\|}{R}$ the normalized magnitude of $\mathbf{h}$ ($0 \leq \rho \leq 1$) (scalar), β_r and R constants, $\mathcal{I}$ the identity matrix and $\hat{\mathbf{h}}$ a unit vector defined as:

$$\hat{\mathbf{h}} = \begin{cases} \mathbf{h}/\|\mathbf{h}\| & (\mathbf{h} \neq 0) \\ 0 & (\mathbf{h} = 0) \end{cases} \tag{5.16}$$

Introducing the concept of intergranular strain the hypoplastic formulation of the law is rewritten as [30]:

$$\dot{\mathbf{T}} = \mathbf{M} : \mathbf{D} \tag{5.17}$$

with

$$\mathbf{M} = [\rho^{\chi} m_T + (1 - \rho^{\chi}) m_R]\mathcal{L} + \begin{cases} \rho^{\chi}(1 - m_T)\mathcal{L} : \hat{\mathbf{h}}\hat{\mathbf{h}} + \rho^{\chi}\mathbf{N}\hat{\mathbf{h}} & (\hat{\mathbf{h}} : \mathbf{D} > 0) \\ \rho^{\chi}(m_R - m_T)\mathcal{L} : \hat{\mathbf{h}}\hat{\mathbf{h}} & (\hat{\mathbf{h}} : \mathbf{D} \leq 0) \end{cases} \tag{5.18}$$

where χ, m_T, m_R constants. The constitutive matrix $\mathcal{L}$ is now different from the one used in the previous formulation (see Eq. 5.2). It is redefined according to Eq. 5.19 to ensure that at $\rho = 0$ the initial stiffness $\mathcal{L}^{\mathrm{e}}$ of the material is retrieved:

$$\mathcal{L} = \frac{\mathcal{L}^{\mathrm{e}}}{m_R} \tag{5.19}$$

5.2 Model calibration and validation

The different material parameters for the Fontainebleau sand are summarized:

ϕ	ψ	n	R	m_R	m_T	β_r	χ
39° (peak) and 33° (critical)	11°	0.4	$1.5e^{-4}$	3.0	2.0	0.1	1.02

Table 5.1: Hypoplastic model with intergranular strain: calibrated parameters used for the simulation

For the basic parameters, the friction angle ϕ is taken as 39° ($\phi = 39°$ is the peak friction angle, and $\phi = 33°$ is the critical friction angle for Fontainebleau sand), while the dilation angle is set to be 11° [1]. For the other material parameters, the

calibration procedure can be divided into two steps. First, the calibration of parameter n is done by comparing the G/G_{max} response of basic hypoplastic equations with that from the G/G_{max} properties obtained for Fontainebleau sand, see chapter. 3. (when the intergranular strain is considered, the response of hypoplastic model in terms shear modulus degradation is not so realistic, to avoid this effect, the calibration of n is done by removing the intergranular strain temporarily). It can be seen in Fig. 5.6 that, with n equals to 0.4, the numerical response is in good agreement with the experimental data and this for different confining pressures.

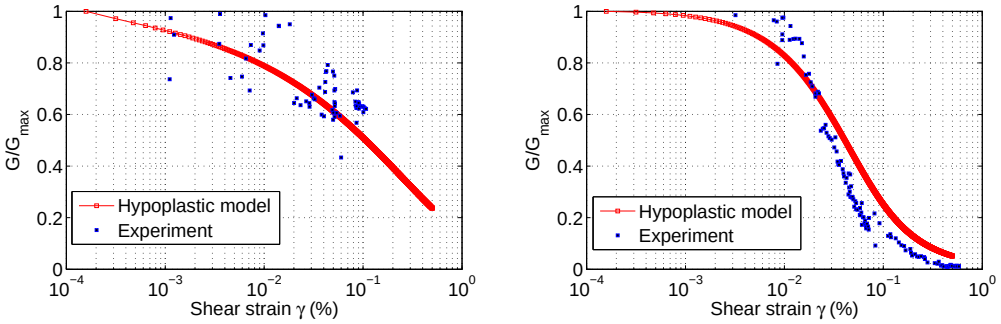

Figure 5.6: Comparison of the G/G_{max} curve with the experimental data (a) confining pressure 149 kPa and (b) confining pressure 21 kPa

Then basic hypoplastic model is equipped with intergranular strain again, and the calibration of the parameters related to the intergranular strain (χ, m_T, m_R,ξ and β_r) is done by a trial-error process by comparing the cyclic response of the model with the hysteresis loops obtained from chapter. 3. The results are shown in the following section, see Fig. 5.13.

The validation of the proposed hypoplastic model is done hereafter considering three different cases (i) a single element (ii) a monotonic loading (iii) a dynamic loading.

5.2.1 Single element performance

The responses of the proposed constitutive laws are tested on a single element subjected to pure shear (which is the general loading situation in dynamic centrifuge tests), see in Fig. 5.7(a). A specific loading is divided in three parts (see in Fig. 5.7(b)): the first part with increasing loading cycles, followed by a one way cyclic loadings and an unloading part. Calculations are done considering three constitutive laws, the elastic perfectly plastic Drucker-Prager model, the hypoplastic model without intergranular strain and the hypoplastic model with intergranular strain. For all the calculations the confining pressure is assumed 150 kPa.

As expected, the elastic perfectly plastic Drucker-Prager model is not able to reproduce any energy dissipation in the small one-way cyclic loading part and before

yielding of the material, see in Fig. 5.8(a). On the contrary, the hypoplastic model without the intergranular strain concept produces excessive accumulation of stress in the small one-way cyclic loading part, see in Fig. 5.8(b). Only the extended hypoplastic model with the intergranular strain concept is able to reproduce a realistic behavior, see in Fig. 5.8(c).

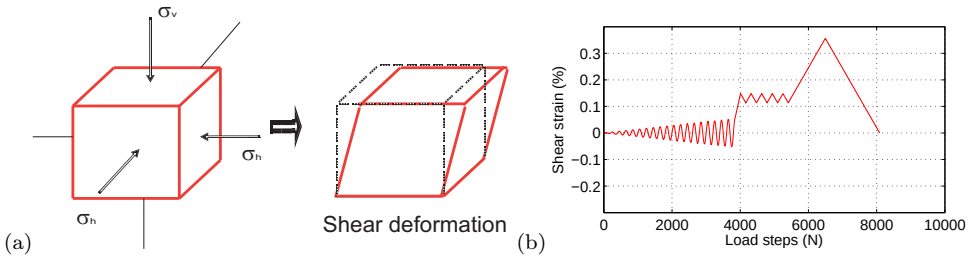

Figure 5.7: Pure shear deformation (a) loading (b)

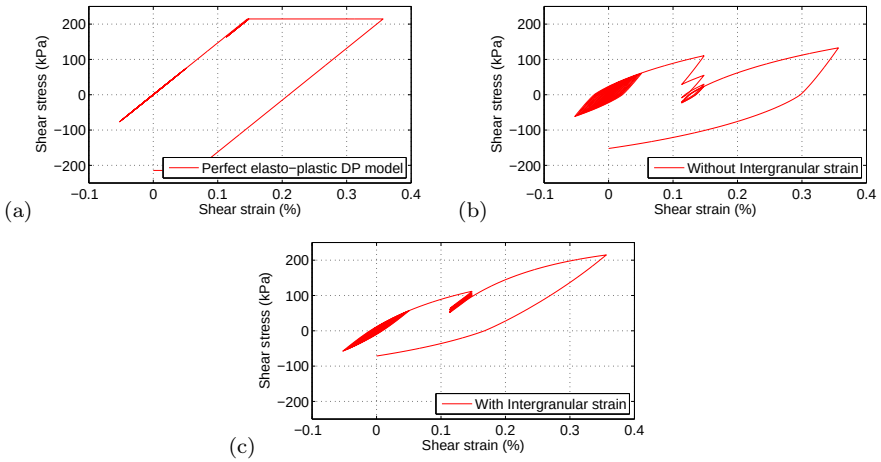

Figure 5.8: Response of a single element under pure shear (a) Elastic perfectly plastic Drucker-Prager model; (b) hypoplastic model without intergranular strain and (c) hypoplastic model with intergranular strain

The validation was also carried out by using laboratory triaxial element test data. Simulations were carried out on confining pressure at 50 kPa, 100 kPa and 200 kPa [19] respectively. The parameters used for the simulations of triaxial tests are summarized in Table. 5.2

ϕ	ψ	n	R	m_R	m_T	β_r	χ
33° (critical)	11° (Dense) and 3° (Loose)	0.4	$1.5e^{-4}$	3.0	2.0	0.1	1.02

Table 5.2: Hypoplastic model with intergranular strain: calibrated parameters used for the simulation

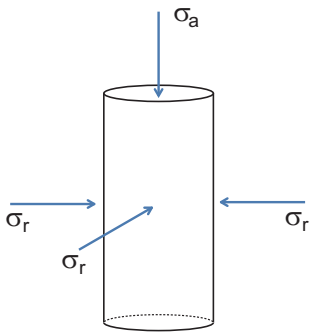

Figure 5.9: Triaxial compression tests on Fontainebleau sand [19]

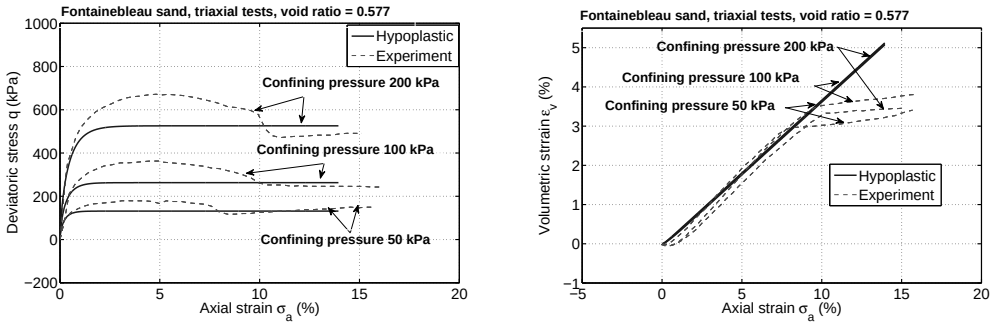

Figure 5.10: Triaxial compression tests on dense Fontainebleau sand, void ratio = 0.577, simulation vs. experiments

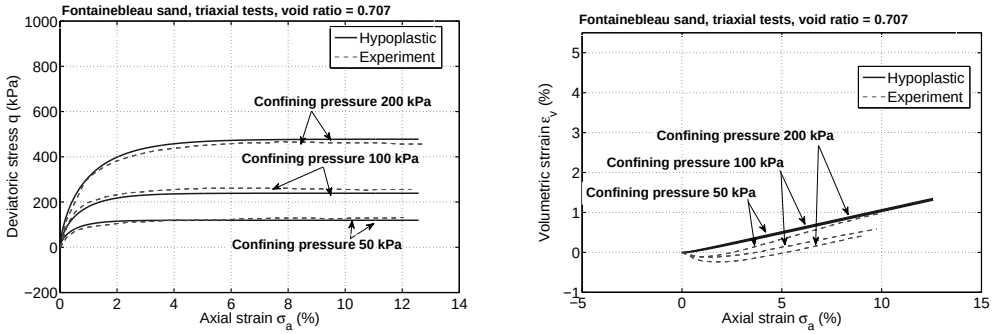

Figure 5.11: Triaxial compression tests on loose Fontainebleau sand, void ratio = 0.707, simulation vs. experiments

It can be seen from the results that the proposed constitutive soil model can well capture the behavior of Fontainebleau sand in loose condition. In the case of dense sand, the soil model can not well predict the peak strength of the sand. However, if the critical state friction angle is used, the ultimate mobilized strength of sand can be well captured.

5.2.2 Simulation of free-filed response

The validation of the constitutive law for dynamic loadings is presented hereafter using the experimental results of the free-field tests. The material parameters are listed in Table. 5.1. Fig. 5.13 shows the comparison of the results with the hysteresis loops obtained from the sinusoidal tests while Fig. 5.14 the results from the free-field test with a real earthquake excitation (Kobe -4 dB). Numerical results are in very good agreement with the experimental data.

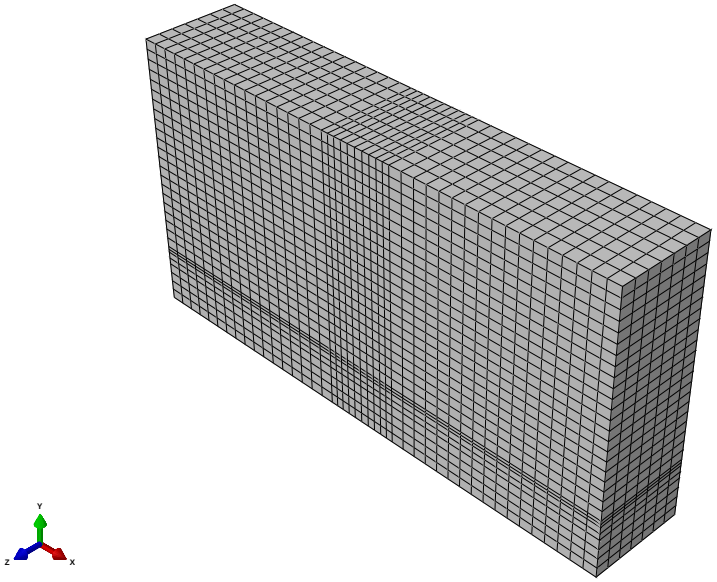

Figure 5.12: FEM mesh for simulation of free-filed

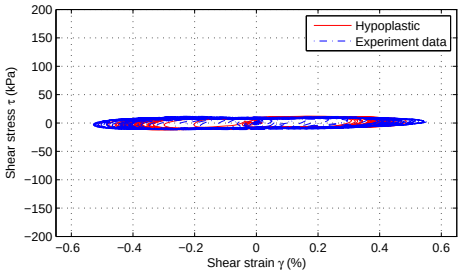

(a) Depth 1.2m, confining pressure 21 kPa

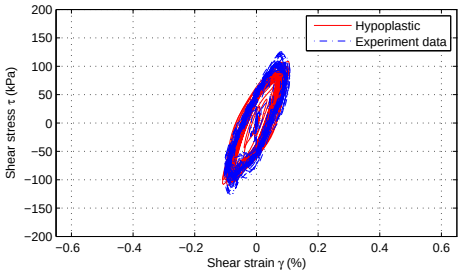

(b) Depth 14.4m, confining pressure 128 kPa

Figure 5.13: Hypoplastic model with intergranular strain: Numerical Vs. experimental results, free-filed tests using a sinusoidal signal - shear stress vs. shear strain: (a) depth 1.2 m and depth (b) 14.4 m

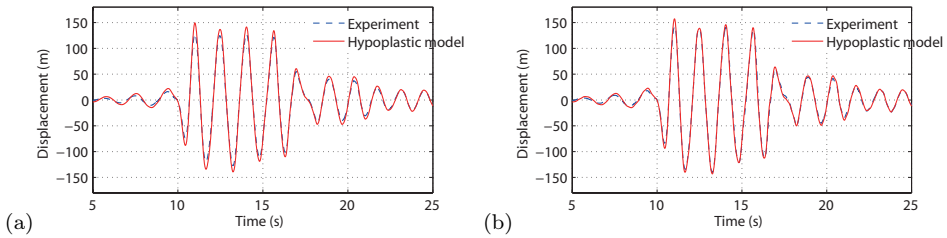

Figure 5.14: Hypoplastic model with intergranular strain: Numerical Vs. experimental results, free-filed tests using the Kobe earthquake signal - displacement time histories: (a) depth 1.28 m (CH-05) and (b) depth 10.88 m (CH-09)

5.2.3 Monotonic loading

Analyses are carried out using the finite-element code ABAQUS standard analyzer [135]. Taking the advantages of symmetry, only half of the soil-pile system was modeled. Both the sand and pile are modeled by 3-D solid elements. In the finite element model, pile was assumed to have linear material properties and sand was modeled using the simple hypoplastic model. FEM model for single vertical pile in soil is shown in Fig. 5.15. The boundary conditions applied at the bottom of the model restrict the nodal displacement in Y and Z directions. While, for the lateral boundaries, the nodal displacements are restricted in the normal direction. There is no load eccentricity on the pile head i.e. the pile head has the same height with the ground surface. Fig. 5.15 presents the FEM model mesh in general case, when it is used in simulate the centrifuge tests, the necessary modification of the geometry of the model is required.

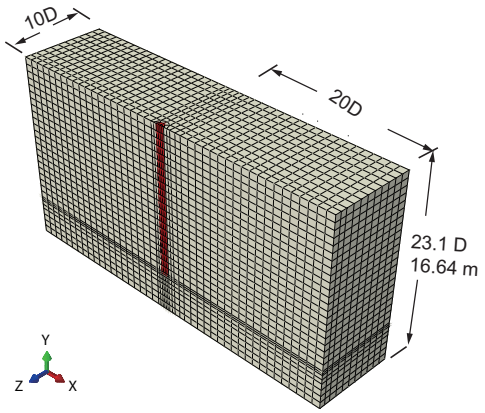

Figure 5.15: FEM model for single vertical pile in soil

In order to validate the constitutive law for a Soil Pile Interaction problem the results from two centrifuge tests are reproduced hereafter. The first is the one performed by Rosquoët [1] to investigate the lateral resistance of a pile; the second refers to the work of Guefrech et al. [136] on the vertical bearing capacity of a pile.

Rosquoët [1] performed monotonic loading tests on a single vertical pile embedded in Fontainebleau sand at the centrifuge facility of IFSTTAR Nantes. The homogeneous dry Fontainebleau sand sample had a density $\gamma = 1630$ kg/m^3 and a relative density $D_r = 86\%$. The comparison of the numerical results with the experimental data is shown in Fig. 5.16. The numerical model fits well the experimental data and the lateral ultimate strength of the single vertical pile is well predicted around 5000 kN.

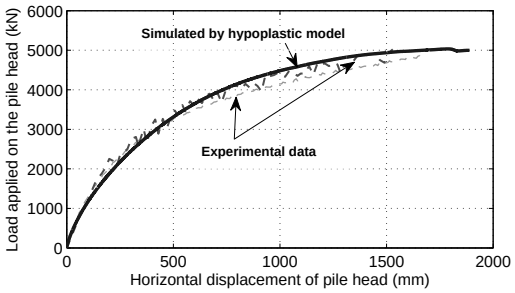

Figure 5.16: Hypoplastic model with intergranular strain: Numerical Vs. experimental results for a single pile submitted to lateral loading

Guefrech et al. [136] studied the vertical bearing capacity of a pile embedded in Fontainebleau Sand with a density $\gamma = 1686$ kg/m^3 and a relative density $D_r = 88\%$. The comparison of the numerical results with the experimental data is shown in Fig. 5.17. Although the numerical model slightly overestimates the vertical bearing capacity, the differences between the numerical results and experimental data are acceptable.

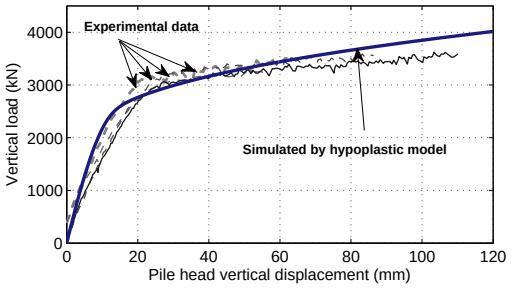

Figure 5.17: Hypoplastic model with intergranular strain: Numerical Vs. experimental results for a single pile submitted to vertical compression

5.2.4 Soil Structure Interaction

Finally in this section, the performance of the finite element model to reproduce Soil Pile Structure Interaction problems under real earthquake signals is studied. The same modeling procedure was adopted as it has been explained in section. 5.2.3. Note that, in the simulation of seismic responses of soil-pile-superstructure system,

the acceleration history is imposed at the base of the FEM models. The typical configurations (vertical pile group and inclined pile group with superstructures) are presented in Figs. 5.18, considering vertical or inclined piles, short or tall buildings, some selected results are presented.

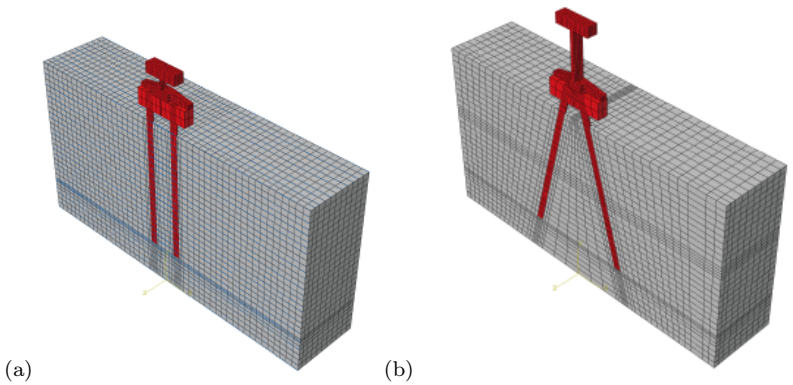

(a) (b)

Figure 5.18: Selected configurations: (a) vertical pile group with short superstructure (b) inclined pile group with slender superstructure

The results of the simulation of soil-pile-superstructure system under seismic excitations are shown in Figs.5.19, 5.20 and 5.21. The comparisons are based on the maximum dynamic bending moments envelops of piles, the residual bending moments are not taken into account. It is a limitation that the model can not well capture the residual bending moment results from the complex soil-pile interactions. However, in terms of the dynamic bending moment, the FEM model has good agreement with the experimental data.

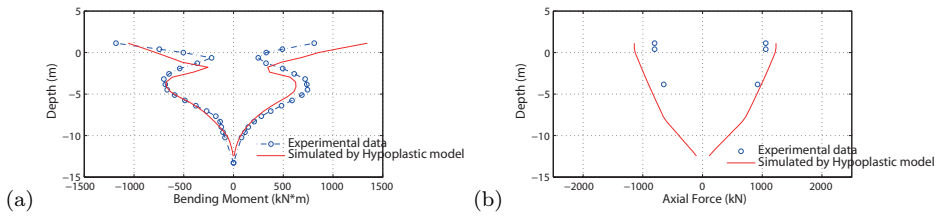

(a) (b)

Figure 5.19: Comparison of numerical results of vertical pile group with short superstructure, real earthquak excitation (Northridge -9 dB): (a) Bending moment and (b) axial force

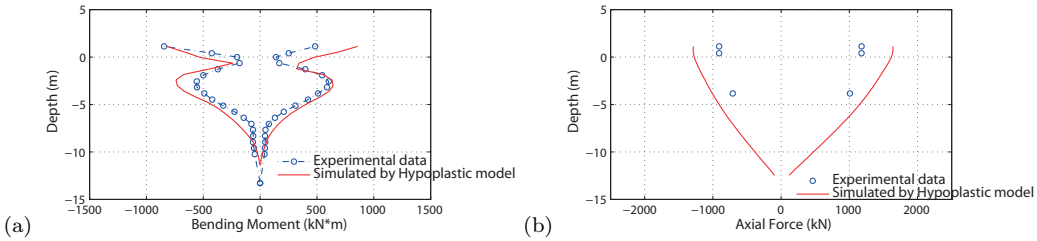

Figure 5.20: Comparison of numerical results of vertical pile group with short superstructure, real earthquak excitation (Kobe -4 dB): (a) Bending moment and (b) axial force

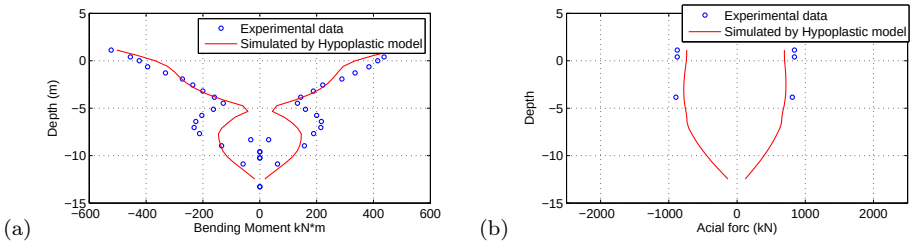

Figure 5.21: Comparison of numerical results of vertical pile group with slender superstructure, real earthquak excitation (Kobe -4 dB): (a) Bending moment and (b) axial force

5.3 Conclusions

In the chapter, 3D FEM modeling of the soil-pile-superstructure system is presented. A simple constitutive of sand which incorporates the concept of hypoplastic was introduced. The proposed constitutive model has very less material parameters and the calibration of these parameters are relatively easy. By comparing the results from numerical simulations with various experimental data, it can be concluded that, the FEM model can successfully capture the behavior of the soil-pile-superstructure system, which provide strong support in developing macro-element in the next Chapter.

Chapter 6

A macro-element for pile foundations in sand

A new macro-element for pile foundations in sand is presented in this chapter. The development follows the key issues already highlighted in the recent studies on macro-elements for shallow foundations [76, 78, 79, 83, 137–139], (i.e. definition of yield surface, plastic flow rule and hardening laws) and it is done within the framework of hypoplasticity, as proposed by Salciarini and Tamagnini [83]. Starting from the yield surface for a single vertical pile and a vertical pile group the details of the macro-element formulation are presented. Special considerations for inclined piles are discussed and a compromising solution for inclined pile foundations is proposed. Validation is provided through comparison with the experimental results.

6.1 Macro-element model for vertical piles

In this section, the method to develop a macro-element for a single vertical pile or a vertical pile group is introduced. The general steps are the following:

1. Define the yield surface using numerical calculations;
2. Propose an analytical equation to describe the yield surface;
3. Choose an adequate plastic flow rule;
4. Define the relevant hardening laws.

6.1.1 3D numerical yield surface for a single vertical pile

The way to find the 3D yield surface (or failure envelop) for a single vertical pile is presented hereafter. The adopted sign conventions are shown in Fig. 6.1.

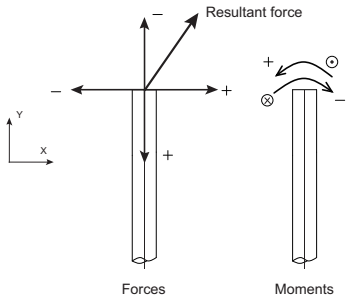

Figure 6.1: Adopted sign conventions

In order to find the 3D failure envelope, swipe tests and radial displacement tests are numerically performed (as proposed by Gottardi et al. [29] for circular footings):

- Swipe tests: a vertical displacement is first applied on the pile until the vertical force reaches a certain level. Then, an increasing horizontal displacement is imposed while the vertical displacement is kept constant.
- Radial displacement tests: the ratio between the applied displacements or the combined rotation-displacement increments is kept constant.

The numerical radial displacement tests were carried out based on the FEM mesh shown in Fig. 6.2. Analyses are carried out using the finite-element code ABAQUS standard analyzer [135]. Taking the advantages of symmetry, only half of the soil-pile system was modeled. Both the sand and pile are modeled by 3-D solid elements. In the finite element model, pile was assumed to have linear material properties and sand was modeled using the simple hypoplastic model discussed in Chapter. 5. Different from the modeling technique used in Chapter 5, interface elements were used for the radial displacement tests, since in order to obtain the ultimate yield strength of the soil-pile system, the FEM model has difficulties to converge. The interface elements can help to overcome these difficulties. Interface between pile and soil was approximately modeled by defining contact properties using friction factor which is close to the friction angle of the soil. For applying the friction behavior, penalty algorithm was used [135]. In addition, in order to avoid the excessive distortion of elements and to enhance the simulation of large deformation, adaptive meshing technique (ALE) was also adopted [135]. The boundary conditions applied at the bottom of the model restrict the nodal displacement in Y and Z directions. While, for the lateral boundaries, the nodal displacements are restricted in the normal direction. There is no load eccentricity on the pile head i.e. the pile head has the same height with the ground surface.

Note that, the same sand properties were assumed to the soil deposit, accordingly, same material parameters were used, see Chapter 5. Also for the pile, exactly the same geometry and properties were assumed in the FEM model. Such considerations ensure that the failure surfaces found for piles and pile groups are consistent with the experiments.

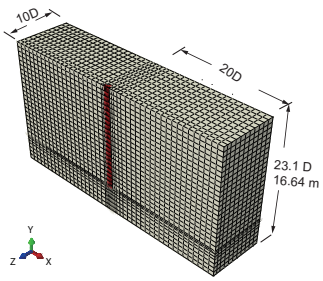

Figure 6.2: FEM model for single vertical pile in soil

6.1.1.1 $H - V$ plane

To investigate the form of the failure surface in the $H - V$ plane, free pile head conditions ($M = 0$) are considered. As shown in Fig. 6.3, a prescribed displacement is numerically applied on the top of the pile head (that can rotate freely) in a certain direction angle δ. The angle δ varies from $0 \sim 360°$ to scan the failure surface in all directions. The value of the prescribed displacement is relatively large to ensure that the ultimate strength is reached. By connecting the peak values in all directions (see Fig. 6.4) the complete yield surface is obtained. In practice, calculations are stopped when numerical convergence problems appear. The objective being to capture the 3D failure envelope, large deformations have to be considered in the finite element calculations and a re-meshing technique is necessary. Softening parts are not taken into account, only the peak values are used to reproduce the failure surface.

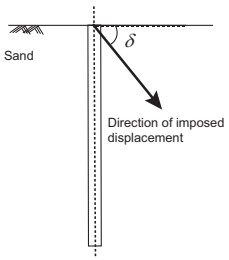

Figure 6.3: Radial displacements tests in the H-V plane

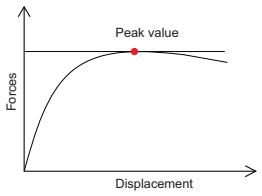

Figure 6.4: Determination of the peak values

Different selected loading paths in the $H - V$ plane for the numerical radial displacement tests are shown in Fig. 6.5(a). Numerical swipe tests are also performed

and the applied loading paths are plotted in Fig. 6.5(b). It can be seen that the load is first increased in the vertical axis up to a certain level. Then, a horizontal displacement is applied and the forces follow a path until the ultimate strength is reached. In this way, the swipe tests follow approximately the surface of the failure envelope [29]. The arrows in Fig. 6.5(b) denote the directions of the corresponding loading paths.

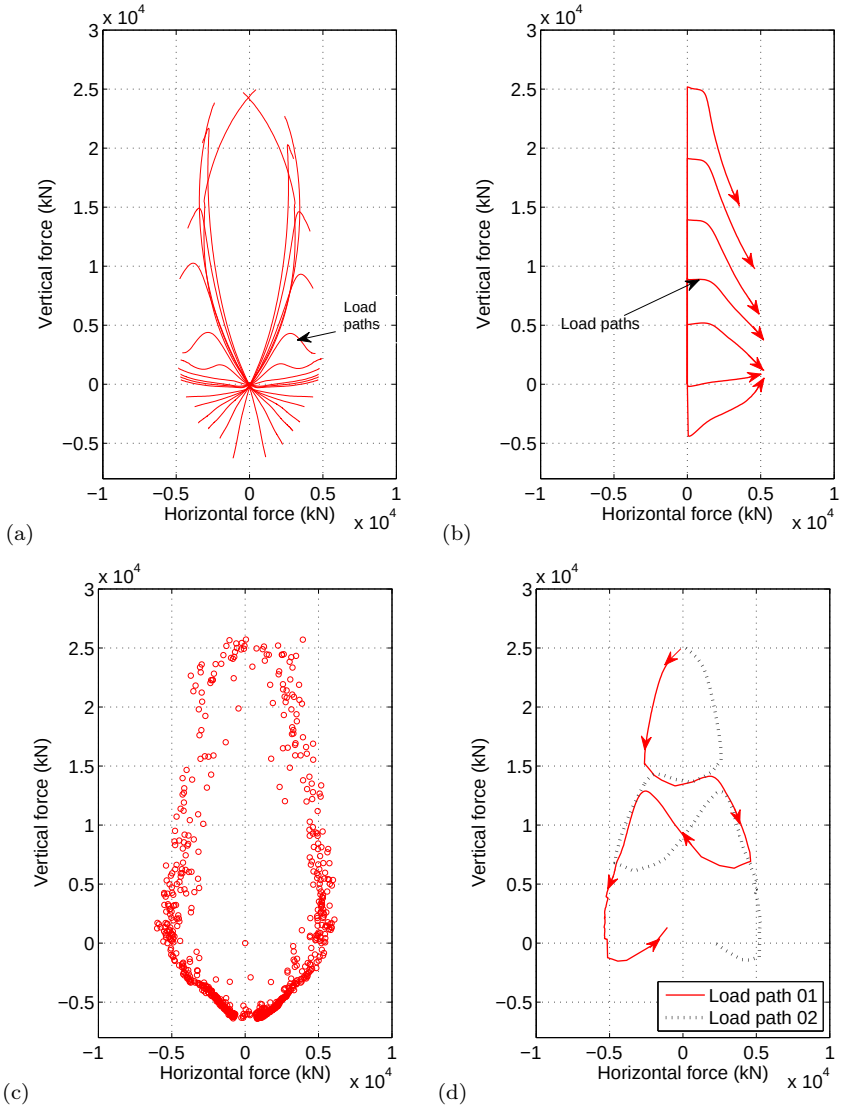

Figure 6.5: Selected load paths for the numerical radial displacement tests (a), for the numerical swipe tests (b), complete results from the numerical radial displacement tests (c) and the numerical swipe tests with more complex load paths (d) in the H-V plane (M=0)

The numerical results from both the radial displacement tests and swipe tests provide similar failure envelopes, see in Figs. 6.5(c) and (d). The failure envelope is

thus load path independent and has a fixed shape and position in the $H-V$ space. In the following, the radial displacement method is preferentially chosen to derive the failure envelope.

A large number (around 500) of numerical radial displacement tests are performed and the ultimate strength (or failure locus) of each test is plotted in Fig. 6.5(c). The data points form a unsmoothed curve, due to the high non-linearity. The main results are summarized hereafter:

- The cross-section of the failure envelope is (almost) symmetric about the vertical force axis but not about the horizontal force axis.
- A single vertical pile has a larger bearing capacity in compression than in tension.
- The presence of a vertical load (compression or tension) reduces the horizontal bearing capacity.

The obtained failure envelope is similar to the experimental data from Meyerhof and Ranjan [37] corresponding to a single vertical pile in dense sand with a length to diameter ratio L/D equal to 15. The authors indicated that the ultimate resultant load for vertical piles in compact and dense sand decreases when the resultant force varies from a standalone vertical load to a standalone horizontal load (i.e. the horizontal component of the resultant force decreases with increasing vertical load). According to the results shown in Fig. 6.5(c), when $V = 0$ the horizontal bearing capacity H_0 is estimated around 5000 kN; when the vertical load increases at V =20000 kN (i.e. 80% of the ultimate vertical bearing capacity), the horizontal bearing capacity is estimated around 2700 kN (considering the average value of the scatter data points). The horizontal bearing capacity is thus found reduced by 48%.

6.1.1.2 $H-M$ plane

The failure envelope is hereafter investigated in the $H-M$ plane and this for different vertical loading levels. The procedure is divided in two steps: first, the pile is loaded until a certain vertical force V_i. Then, radial displacement loadings are applied considering a constant ratio between the combined rotation-displacements increments, see Fig. 6.6.

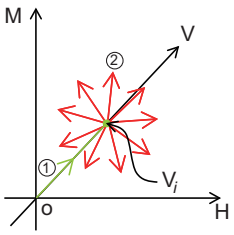

Figure 6.6: Radial displacements in the $H-M$ plane at the vertical load level V_i

In analogy with the $H-V$ plane, load paths in the $H-M$ plane start from the origin and stop at the failure envelope, see Fig. 6.7(a). The main results are summarized hereafter (Fig. 6.7(b) and Fig. 6.8 for different vertical load levels):

- The failure envelopes present a remarkable inclined elliptical shape.
- The presence of bending moment has a significant influence on the horizontal bearing capacity of the pile. The contribution depends on the loading direction (or the respective signs of the horizontal force and bending moment).
- The influence of the vertical load on the inclination of the bearing capacity diagrams is negligible.
- The increase of the vertical load decreases the size of the bearing capacity diagram (similar trends have been found in compression and in tension).

The shape and inclination of the failure envelope can be explained as follows: The presence of a positive bending moment on the pile head increases the horizontal force bearing capacity (see the area with the arrow 1 in Fig. 6.7(b)). It can be seen in Fig. 6.1 that a positive horizontal force drives the pile head in the x-axis positive direction while a positive bending moment in the x-axis negative direction. A positive bending moment will thus restrain the pile deformations caused by a positive horizontal force. To overcome the counterbalance effect of the bending moment, an increased horizontal force is required in order to reach the ultimate state. Therefore, the required horizontal loading in part 1 (arrow 1) is higher than in point A (corresponding to the horizontal bearing capacity with $M = 0$). Part 1 can thus be seen as the horizontal force dominated failure part.

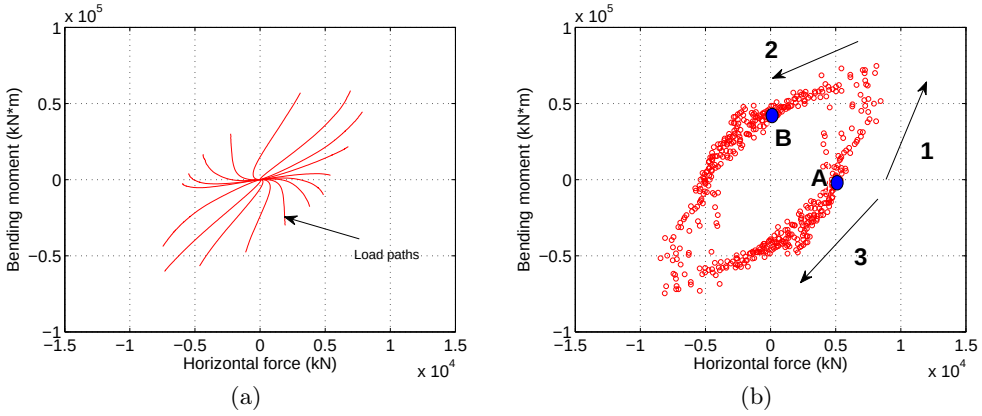

Figure 6.7: (a) Load paths (b) numerical radial displacement tests in the $H-M$ plane at $V = 0$

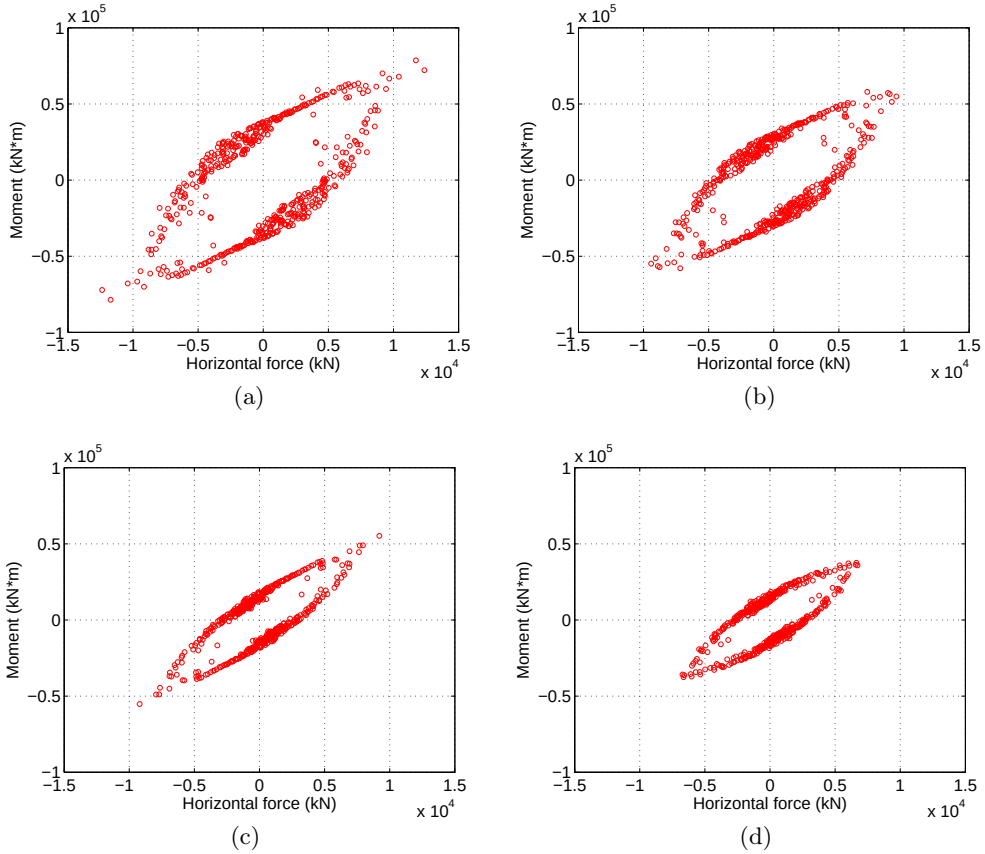

Figure 6.8: Failure envelopes at different vertical load levels in the H-M plane: (a) V=1.0×10^4 kN (b) V=1.5×10^4 kN (c) V=2.0×10^4 kN (d) and V=2.25×10^4 kN

For the same reason, and in order this time to overcome the presence of an horizontal force, a greater bending moment is needed in part 2. The required bending moments are larger that the failure moment at point B. Part 2 can be seen as the bending moment dominated part. If now the sign of the horizontal force and bending moment are opposite, both actions drive the pile in the x-axis positive direction. The presence of bending moment accelerates the failure of the pile soil system and the horizontal forces are reduced, Fig. 6.7(b) part 3.

6.1.1.3 $H-M-V$ space

By combining the results in the $H-V$ plane (Fig. 6.5(c)) and in the $H-M$ plane for different vertical load levels (Fig. 6.7(b) and Fig. 6.8), the complete failure envelope in the $H-M-V$ space is plotted in Fig. 6.9. All the numerical data points belong to a 3D surface that has inclined elliptical cross-sections along the vertical force axis.

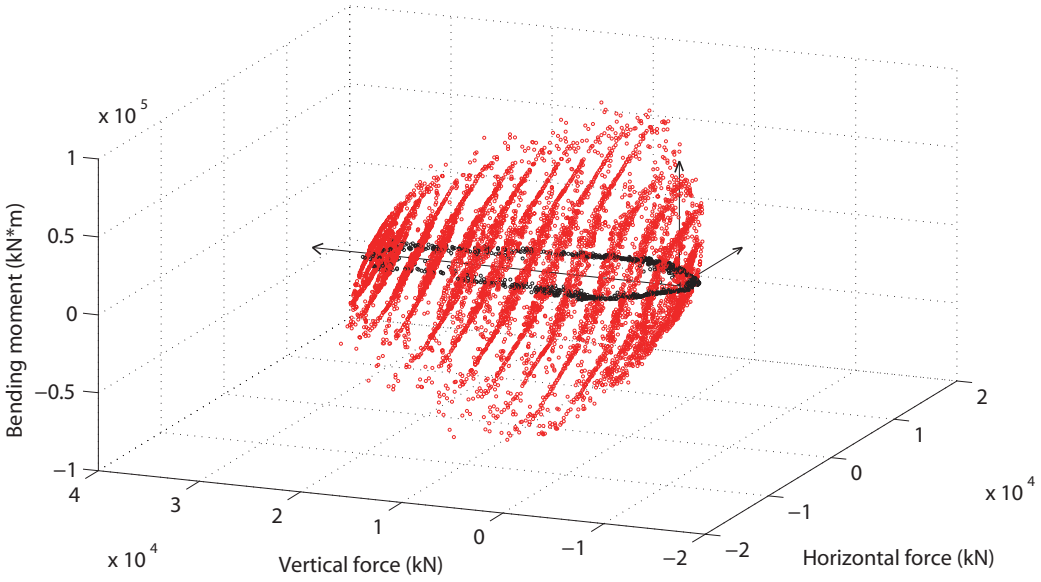

Figure 6.9: Numerical failure envelope in the H-M-V space

From the numerical radial tests in Fig. 6.9 the horizontal bearing capacity ($V = 0$ and $M = 0$) is estimated at H_0 =5000 kN, the vertical compression bearing capacity ($H = 0$ and $M = 0$) V_{c0} =25000 kN, the vertical tension bearing capacity ($H = 0$ and $M = 0$) V_{t0} = 5100 kN and the ultimate bending resistance (H=0 and V=0) $M_0 = 0.42{\times}10^5$ kN·m. These values play an important role in the construction of the analytical relationship of the 3D failure envelope for a single vertical pile in sand presented in the following section.

6.1.2 3D analytical yield surface for a single vertical pile

6.1.2.1 $H - V$ plane

In the H-V plane there is no bending moment and thus a pinned connection can be considered between the pile head and the pile cap (no moments are transmitted). Meyerhof and Ranjan [37] proposed a semi-empirical formula to evaluate the interaction between the horizontal and vertical forces that reads:

$$\left(\frac{H}{H_0}\right)^2 + \left(\frac{V}{V_0}\right)^2 = 1 \tag{6.1}$$

where H_0 and V_0 are the horizontal and vertical bearing capacities of the pile. Eq. (6.1) can be written in a normalized form as follows:

$$f = m^2 + v^2 - 1 \tag{6.2}$$

where $m = H/H_0$ and $\upsilon = V/V_{c0}$ in compression or $\upsilon = V/V_{t0}$ in tension. V_{c0} and V_{t0} are the vertical compression and tension bearing capacity respectively, m and υ are dimensionless quantities.

The comparison of the semi-empirical Eq. (6.2) with the numerical results is shown in Fig. 6.10. The agreement is satisfactory although some small discrepancies are identified in the tension part (dash line, see in Fig. 6.10(a)). A small amplification of the differences is also seen in the normalized curve (see in Fig. 6.10(b)) that is often used in the macro-element technology [76, 80, 138]. Nevertheless, the agreement is considered acceptable and Eq. (6.2) is used hereafter for the tension and compression parts. Therefore, and in order to determine the failure envelope of a single pile is sand in the $H - V$ plane three parameters are necessary: the horizontal bearing capacity H_0, the vertical compression bearing capacity V_{c0} and the vertical tension bearing capacity V_{t0}.

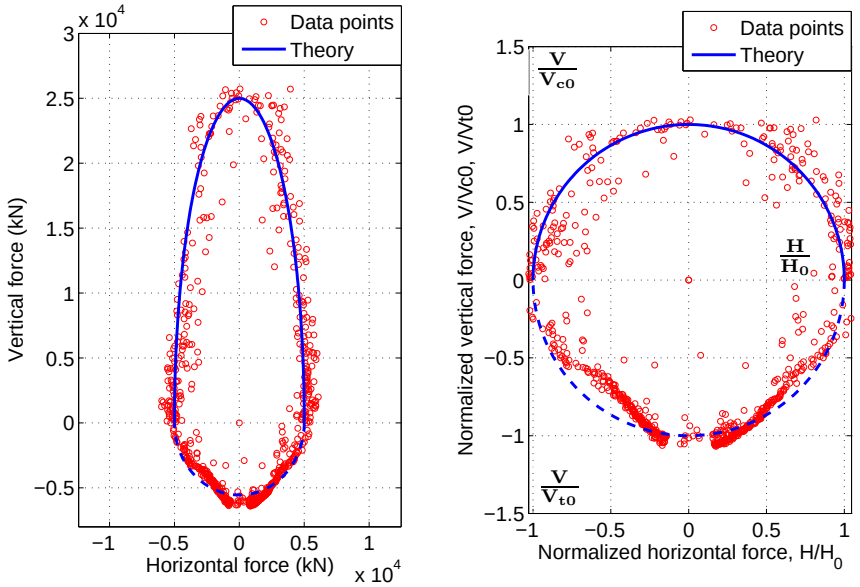

(a) (b)

Figure 6.10: Comparison of Eq. (6.2) with the numerical results (a) in the $H - V$ plane and (b) in the normalized $\frac{H}{H_0}$ - $\frac{V}{V_{c0}}$ - $\frac{V}{V_{t0}}$ space

6.1.2.2 $H - M - V$ space

As shown in section 6.1.1.2, the failure envelope in the $H - M$ plane has an inclined elliptical shape. Inspired from the article of Gottardi et al. [29], where the authors proposed a formula to reproduce an inclined elliptical failure envelope valid for circular footings, a similar equation is proposed hereafter for a single pile in sand:

$$f = \alpha m^2 + \xi n^2 - \beta mn - \rho(\upsilon) = 0 \tag{6.3}$$

where $m = H/H_0$ the normalized horizontal force, $n = M/M_0$ the normalized bending moment and $\upsilon = V/V_{c0}$ or $\upsilon = V/V_{t0}$ the normalized vertical force (dependent on the sign of the vertical load). α, ξ, β and ρ are constants that control the shape of the ellipse. Eq. (6.3) is an inclined ellipse in the $H - M$ plane where the parameter α controls the intersections of the curve with the H axis, β with the M axis and ρ the isotropic expansion or contraction of the ellipse; the combination of α, ξ and β controls the inclination of the ellipse.

The parameters are first fitted using the normalized numerical data in the $H-M$ plane at zero vertical force. They are found equal to $\alpha = 1.0$, $\xi = 1.0$, $\beta = 1.5$ and $\rho = 1.0$, Eq. (6.3) thus becomes:

$$f = 1.0m^2 + 1.0n^2 - 1.5mn - 1.0 = 0 \tag{6.4}$$

The fitted curves are plotted in Fig. 6.11 (a) and (b) and show a good agreement with the numerical data both in the H-M and in the normalized H/H_0 - M/M_0 plane.

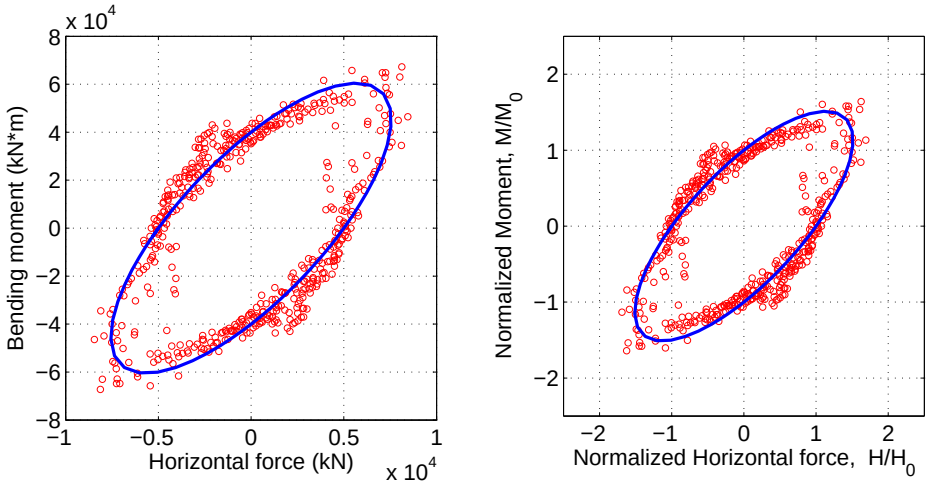

(a) (b)

Figure 6.11: Comparison of Eq. (6.4) with the numerical results (a) in the $H - M$ plane and (b) in the normalized $\frac{H}{H_0}$ - $\frac{M}{M_0}$ plane

As discussed in section 6.1.1.2, the vertical load influences the size of the elliptical cross-sections but not their inclinations, see Fig. 6.8. In order to introduce this behaviour, it is proposed hereafter to link the parameter ρ in Eq. (6.3) and Eq. (6.4) with the vertical load as follows:

$$f = 1.0m^2 + 1.0n^2 - 1.5mn - (1 - \upsilon^2) = 0 \tag{6.5}$$

Fig. 6.12 shows the comparison of the numerical results with Eq. (6.5) in the normalized H/H_0 - M/M_0 plane and this at different vertical force levels. Although the proposed equation can not accurately fit all the data points, especially for important vertical force levels (see for example Fig. 6.12(c) and (d)), it captures the main

features of the behaviour. The proposed equation is therefore considered hereafter satisfactory.

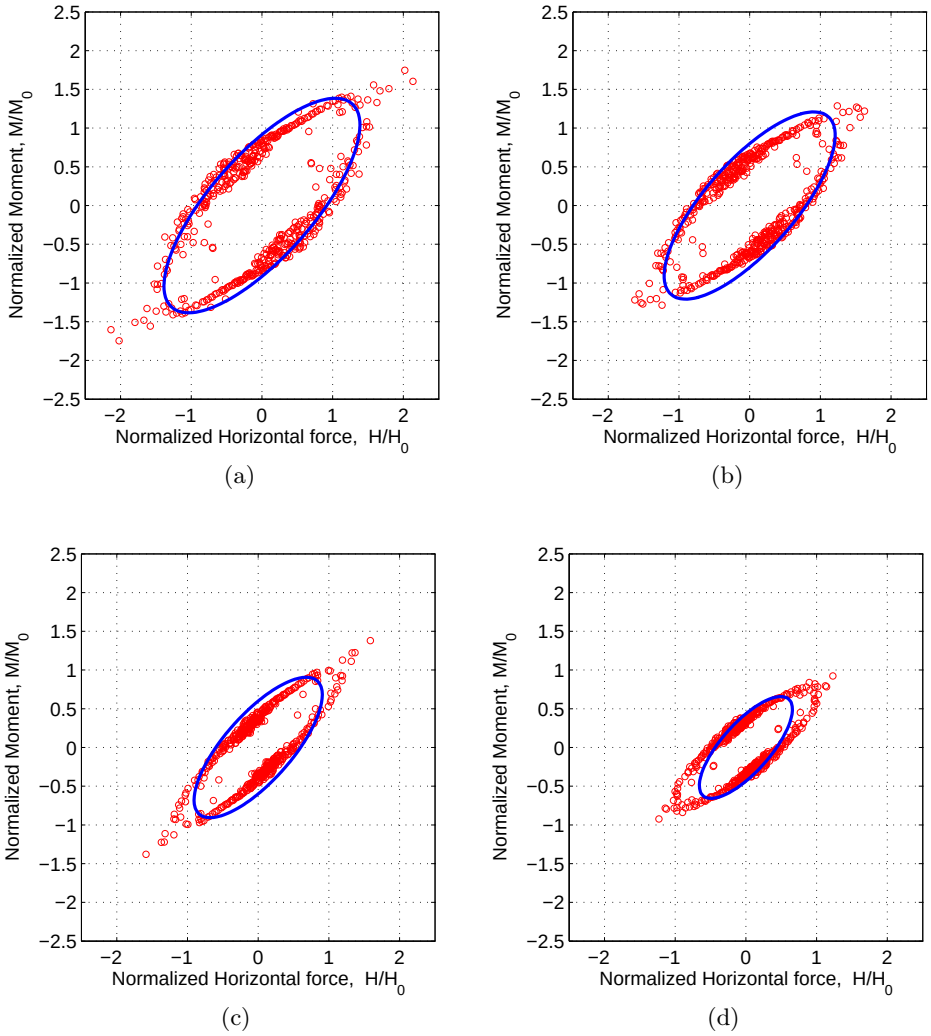

Figure 6.12: Comparison of Eq. (6.5) with the numerical results in the normalized $\frac{H}{H_0}$ - $\frac{M}{M_0}$ plane at different vertical force levels: (a) V/V_0=0.4 (b) V/V_0=0.6 (c) V/V_0=0.8 and (d) V/V_0=0.9

When $n = 0$ (corresponding to zero moment at the pile head) Eq. (6.5) becomes equal to Eq. (6.2). In other words, the proposed equation is applicable for both pinned pile-head conditions in the $H-V$ plane and constrained pile-head conditions in the $H - M - V$ space.

The 3D failure envelope provided by Eq. (6.5) is plotted from different view points in Fig. 6.13(a) and (b). Fig. 6.13(c) contains the 3D failure enveloppe in the normalized H/H_0, M/M_0, V/V_{c0}, and V/V_{t0} space. The tension part of the failure envelope is marked with a dark color.

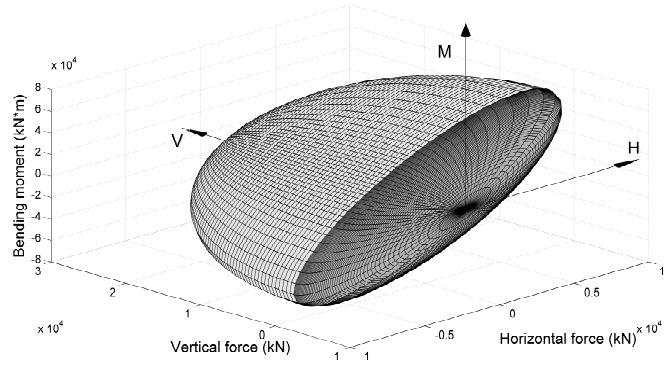

(a)

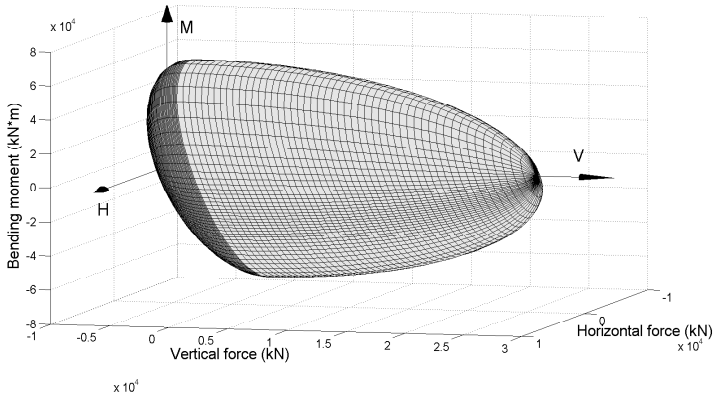

(b)

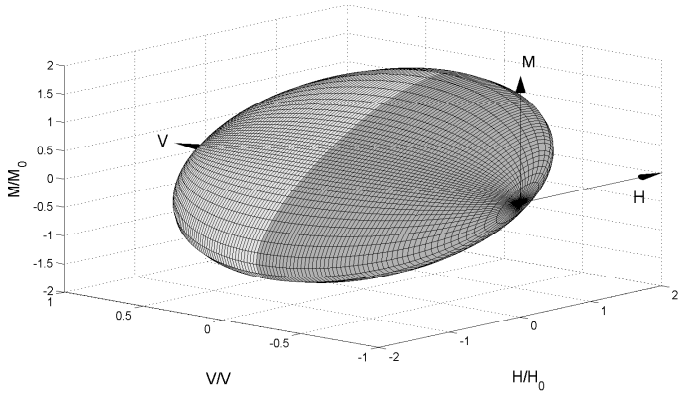

(c)

Figure 6.13: 3D failure envelope provided by Eq. (6.5) from (a) view point 1 (b) view point 2 and (c) in the normalized $\frac{H}{H_0}$ - $\frac{M}{M_0}$ - $\frac{V}{V_{c0}}$ - $\frac{V}{V_{t0}}$ space

Finally, the 3D failure envelope for a single vertical pile in sand defined by Eq. (6.5) is plotted in Fig. 6.14 together with all the numerical data points. The

proposed surface reproduces the 3D distribution of the numerical data with a correlation factor R^2 estimated around 0.89. Key parameters for the 3D failure envelope are: the horizontal bearing capacity H_0, the vertical compression bearing capacity V_{c0}, the vertical tension bearing capacity V_{t0} and the bending bearing capacity M_0.

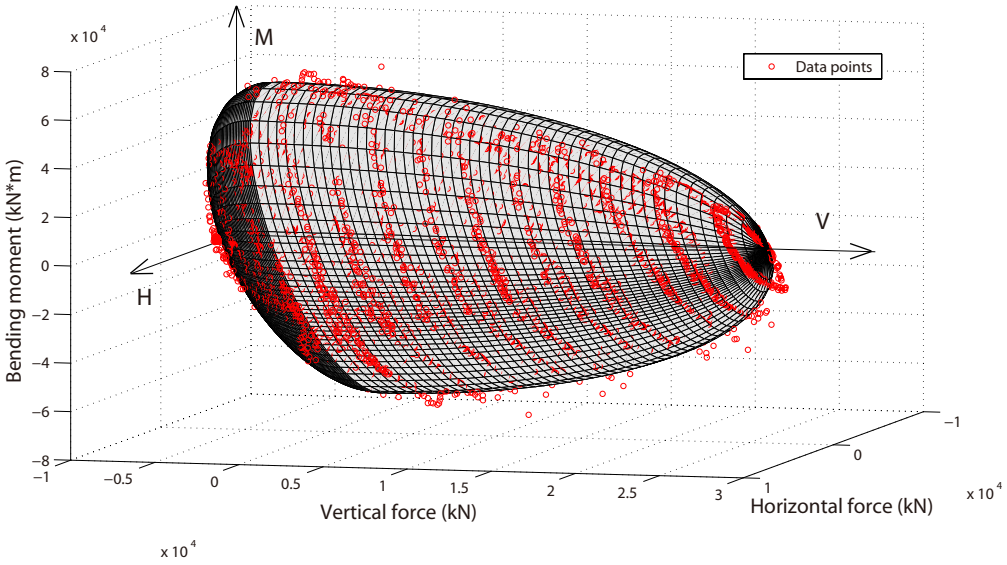

Figure 6.14: 3D failure envelope for a single vertical pile in sand: yield surface provided by Eq. (6.5) Vs. numerical data points

6.1.3 3D yield surface for a vertical pile group

In the case of pile groups, the same numerical radial tests were performed based on the FEM meshes shown in Fig. 6.15. Using the same numerical approach as in the previous sections, the failure envelopes for vertical pile groups with different pile spacing are investigated hereafter. Note that the pile group with $4D$ pile spacing is the one that has been used in the centrifuge tests, see in chapter 4.

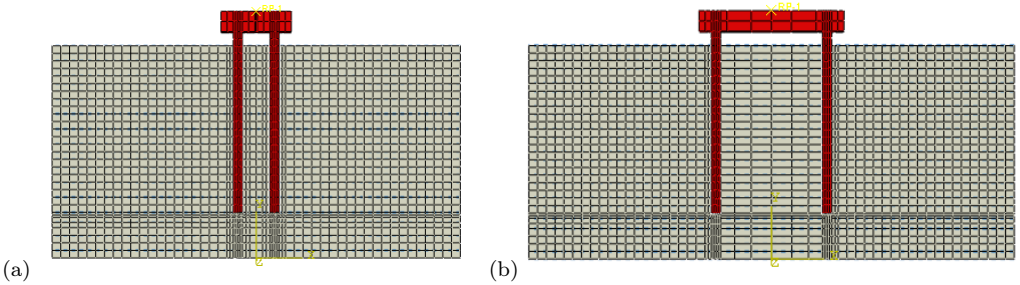

Figure 6.15: FEM meshes for pile groups: (a) pile group with pile spacing $4D$; (b) pile group with pile spacing 8D

Using the same numerical approach as in the previous sections, the failure envelopes for vertical pile groups with different pile spacing are investigated hereafter. It is found that the shapes of the failure envelopes are similar with the ones of a single vertical pile. However, with increasing pile spacing the failure envelope increases. For example, Fig. 6.16 shows the results from numerical radial displacement tests on a foundation with two vertical piles at $4D$ pile distance (the actual configuration of the vertical pile group used in the centrifuge tests see chapter 4, D is the pile's diameter). Looking at the cross section of the failure envelope, see in Fig. 6.16(b) and comparing with the one of a single pile (see in Fig. 6.7(b)), the yield surface for the vertical pile group is found enlarged.

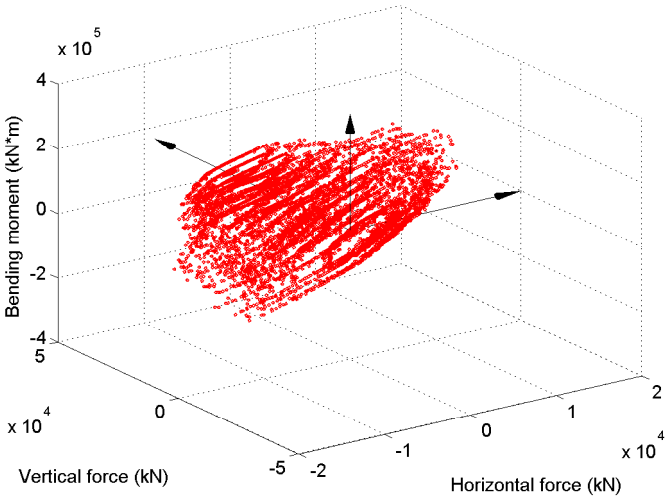

(a)

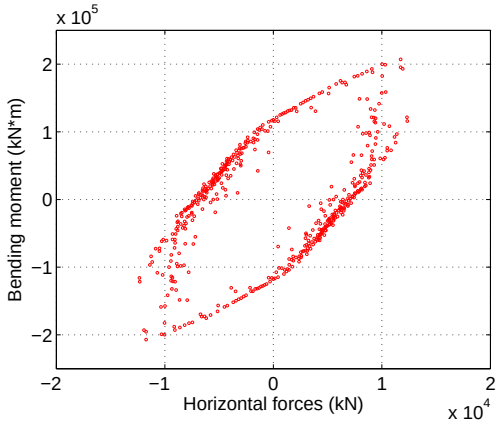

(b)

Figure 6.16: Numerical failure envelope of a vertical pile group with a $4D$ pile spacing: (a) 3D failure envelop in the $H - M - V$ space; (b) cross-section in the $H - M$ plane at $V = 0$ kN

Similar results can be found for a pile group with two piles at $8D$ spacing. Fig. 6.17 shows the cross sections of the failure surfaces of a single vertical pile, a vertical pile group with $4D$ pile spacing and a vertical pile group with $8D$ pile spacing in the $H - M$ plane. With increasing pile spacing, the bearing capacity of the pile group increases. According to the results shown in Fig. 6.17, with more piles in the foundation, the failure surface of the pile foundation is influenced by both the number of piles and the pile spacing. In addition, rotation of the failure surface could be observed. However, this effect is not considered in this dissertation.

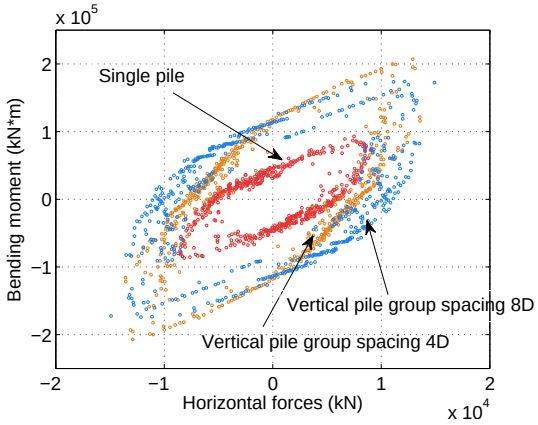

Figure 6.17: Cross sections of the failure envelope surfaces for pile groups with different pile spacing: single vertical pile, vertical pile group with $4D$ pile spacing and vertical pile group with $8D$ pile spacing

From the previous analyses, the failure envelope of pile group is linked with the bearing capacity of a single pile by number of piles N and the pile spacing. With given numbers of pile, when pile spacing increase, the bearing capacity of pile group increase as well. The influence of pile spacing is known as group effect. By introducing the pile group effect factor μ, the failure envelop of pile group could be obtained based on that of a single pile. When group effect is negligible, the bearing capacity of pile group is N times higher than that of a single pile; when the group effect acts, the bearing capacity of pile group is μN times of a single pile. In this dissertation, the group effect factor μ is roughly estimated. For example, the horizontal bearing capacities of a single pile, a pile group with a $4D$ spacing and a pile group with a $8D$ pile spacing are estimated 0.5×10^4 kN, 0.75×10^4 kN and 1.0×10^4 kN respectively. For a vertical pile group with fixed pile-cap connection conditions the pile group effect can thus be ignored when the pile spacing is greater than $8D$, because the failure surface of the pile group with 8D pile spacing is approximately 2 times of the size of the single vertical pile. In the case of the vertical pile group studied in the centrifuge tests ($4D$ pile spacing), the pile group effect factor is estimated to be 0.75.

Following the previous remarks, the analytical equation of the failure surface of a pile foundation with vertical piles can be easily obtained from the failure surface

of a single vertical pile (see Eq. 6.5) that is rewritten as:

$$f = \left(\frac{H}{H_0}\right)^2 + \left(\frac{M}{M_0}\right)^2 - 1.5\left(\frac{H}{H_0}\right)\left(\frac{M}{M_0}\right) - \left(1 - \left(\frac{V}{V_0}\right)^2\right) = 0 \tag{6.6}$$

where, H_0, M_0 and V_0 are the ultimate bearing capacity of a single vertical pile in terms of horizontal force, overturning moment and vertical force. The effects of the pile spacing and the number of piles can be introduced as follows:

$$f = \left(\frac{H}{N\mu H_0}\right)^2 + \left(\frac{M}{N\mu M_0}\right)^2 - 1.5\left(\frac{H}{N\mu H_0}\right)\left(\frac{M}{N\mu M_0}\right) - \left(1 - \left(\frac{V}{N\mu V_0}\right)^2\right) = 0 \tag{6.7}$$

where, H_0, M_0 and V_0 are again the ultimate bearing capacities for a single vertical pile, N is the number of piles and μ is the pile group effect. According to the results from the numerical radial displacement tests the factor μ for a pile group with two piles at $4D$ pile spacing is around 0.75; for a $8D$ pile spacing μ approximately equals 1.0. In other words the pile group effect can be ignored when the pile spacing is greater than $8D$. The failure surfaces for different vertical pile configurations are drown in Fig. 6.18.

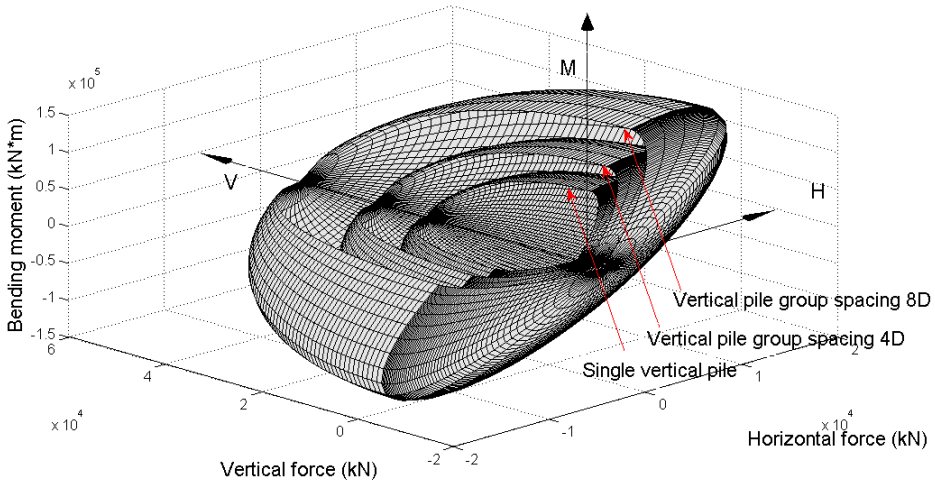

Figure 6.18: 3D failure envelope surfaces for pile groups with different pile spacing: single vertical pile, vertical pile group with $4D$ pile spacing and vertical pile group with $8D$ pile spacing

6.1.4 Macro-element formulation

The macro-element formulation follows the theory of hypoplasticity as proposed by Salciarini and Tamagnini [83] for the case of shallow foundations (see also chapter 5, [30] and [31]). In the macro-element approach, the mechanical response of the pile foundation system is described by means of generalized load vector $\boldsymbol{t}$ (see Eq. 6.8)

and a generalized displacement vector $\boldsymbol{u}$ (see Eq. 6.9) (in the following the **bold** letters define tensors and vectors $\|\|$ the norm of a tensor):

$$\boldsymbol{t} := \{V, H, M\}^T \tag{6.8}$$

$$\boldsymbol{u} := \{w, u, \theta\}^T \tag{6.9}$$

where H, M and V are the resultant forces (horizontal and vertical) and moments acting on the top of foundation; w, u and θ are the respective displacements and rotations. The generalized velocity vector $\boldsymbol{d}$ is then introduced (where the $\dot{()}$ symbol expresses the derivative with respect to time):

$$\boldsymbol{d} := \dot{\boldsymbol{u}} \tag{6.10}$$

and the basic structure of the hypoplastic macro-element in rate-form reads (see also chapter 5, [30] and [31]):

$$\dot{\boldsymbol{t}} = \mathcal{K}(\boldsymbol{t}, \boldsymbol{q}, \boldsymbol{d}) \tag{6.11a}$$

$$\mathcal{K} = \mathcal{L}(\boldsymbol{t}, \boldsymbol{q}) + \boldsymbol{N}(\boldsymbol{t}, \boldsymbol{q})\boldsymbol{\eta}^T \tag{6.11b}$$

$$\boldsymbol{\eta} = \frac{\boldsymbol{d}}{\|\boldsymbol{d}\|} \tag{6.11c}$$

where $\boldsymbol{d}$ is the generalized velocity vector, $\boldsymbol{q}$ is a pseudo-vector of internal variables accounting for the effects of the previous loading history and $\|\|$ the symbol of the norm.

Different from elastoplasticity, the tangent stiffness $\mathcal{K}(\boldsymbol{t}, \boldsymbol{q}, \boldsymbol{\eta})$ varies continuously with the direction of $\boldsymbol{\eta}$ of the generalized deformation velocity. This property is known as incremental nonlinearity [128] [129]. The tangent stiffness plays an important role in modeling the irreversible behavior of the model. $\mathcal{K}(\boldsymbol{t}, \boldsymbol{q}, \boldsymbol{\eta})$ consists of two parts: a "*linear*" part $\mathcal{L}(\boldsymbol{t}, \boldsymbol{q})$ and a "*nonlinear*" part $\boldsymbol{N}(\boldsymbol{t}, \boldsymbol{q})$. The "*linear*" part defines the initial linear constitutive relationship of the macro-element. With the variation of stress state, the "*linear*" part is modified continuously by the "*nonlinear*" part. Both parts play an important role in the modeling of the macro-behavior of the foundation system.

However, with the basic form of hypoplasticity presented by Eq. 6.11, the model is suitable only for monotonic loading cases (this issue was addressed in chapter 5). As a remedy, the "intergranular strain" $\boldsymbol{\delta}$ is introduced as an internal variable following the work of Niemunis and Herle [30]. The constitutive equation of the hypoplastic model is modified as:

$$\dot{\boldsymbol{t}} = \mathcal{K}(\boldsymbol{t}, \boldsymbol{q}, \boldsymbol{\delta})\boldsymbol{d} \tag{6.12}$$

$$\mathcal{K} = [\rho^{\chi} m_T + (1 - \rho^{\chi}) m_R]\mathcal{L} + \begin{cases} \rho^{\chi}(1 - m_T)(\mathcal{L}\boldsymbol{\eta}_{\delta})\boldsymbol{\eta}_{\delta}^{\mathrm{T}} + \rho^{\chi}\boldsymbol{N}\boldsymbol{\eta}_{\delta} & (\boldsymbol{\eta}_{\delta} \cdot \boldsymbol{\eta} > 0) \\ \rho^{\chi}(m_R - m_T)(\mathcal{L}\boldsymbol{\eta}_{\delta})\boldsymbol{\eta}_{\delta}^{\mathrm{T}} & (\boldsymbol{\eta}_{\delta} \cdot \boldsymbol{\eta} \leq 0) \end{cases} \tag{6.13}$$

where χ, m_T, m_R are constants.

The evolution rate of the intergranular strain is defined as:

$$\dot{\boldsymbol{\delta}} = \begin{cases} (\mathcal{I} - \rho^{\beta_r}\boldsymbol{\eta}_{\delta}\boldsymbol{\eta}_{\delta}^{\mathrm{T}})\boldsymbol{d} & (\boldsymbol{\eta}_{\delta} \cdot \boldsymbol{\eta} > 0) \\ \boldsymbol{d} & (\boldsymbol{\eta}_{\delta} \cdot \boldsymbol{\eta} \leq 0) \end{cases} \tag{6.14}$$

where the scalar $0 \leq \rho \leq 1$ is the normalized magnitude of $\boldsymbol{\eta}_\delta$, $\rho = \left(\frac{\|\boldsymbol{\eta}_\delta\|}{R}\right)$, β_r and R constants and

$$\boldsymbol{\eta}_\delta = \begin{cases} \boldsymbol{\delta}/\|\boldsymbol{\delta}\| & (\delta \neq 0) \\ 0 & (\delta = 0) \end{cases} \tag{6.15}$$

where $\mathcal{I}$ is an identity matrix.

By comparing the tangential stiffness matrix in the basic form of the hypoplastic macro-element model (see in Eq. 6.11(b)) and the one which incorporates the intergranular strain (see in Eq. 6.13), it can be seen that both the "linear" and "nonlinear" parts of the constitutive relationship are modified in order to reproduce cyclic loadings. The constitutive matrix $\mathcal{L}$ and the vector $\boldsymbol{N}$ in the "*linear*" and "*nonlinear*" parts respectively are both of great importance for the performance of the hypoplastic macro-element.

The matrix $\mathcal{L}$ that accounts for the stiffness at a load reversal point is defined as:

$$\mathcal{L} = \frac{1}{m_R}\mathcal{K}^e \tag{6.16}$$

$$\mathcal{K}^e := \begin{bmatrix} k_v & 0 & 0 \\ 0 & k_{hh} & k_{hm} \\ 0 & k_{hm} & k_{mm} \end{bmatrix} \tag{6.17}$$

where $\mathcal{K}^e$ is the elastic stiffness matrix and k_v, k_{hh}, k_{mm} and k_{hm} define the vertical, horizontal, rotational and coupled horizontal-rotational stiffness of the foundation system. Different from the macro-element for shallow foundations, the coupled effect between horizontal forces and moments has to be considered, the off-diagonal coupling terms can not be considered negligible.

The nonlinear function $\boldsymbol{N}$ can be expressed as:

$$\boldsymbol{N}(\boldsymbol{t}) = -Y(t)\mathcal{L}\boldsymbol{m}(t) \tag{6.18}$$

Similar to the constitutive law defined in chapter 5, the scalar function $Y(\boldsymbol{t}) \in [0, 1]$ accounts for the degree of nonlinearity, measures the distance from the current stress state to the final yield surface and is defined as:

$$Y(\boldsymbol{t}) = \xi^\kappa \tag{6.19}$$

where $\xi \in [0, 1]$ stands for the measure of the distance and κ is a material constant that controls the evolution of the scalar function.

$\boldsymbol{m}(t)$ defines the direction of plastic flow (it points out the normal direction of the loading surface at the current stress state point). An associate plastic flow role is adopted and finally, the direction of the plastic flow $\boldsymbol{m}(\boldsymbol{t})$ is given by the unit vector:

$$\boldsymbol{m}(\boldsymbol{t}) = \frac{\partial f/\partial \boldsymbol{t}}{||\partial f/\partial \boldsymbol{t}||} \tag{6.20}$$

where, f is the function of the predefined yield surface.

A geometrical interpretation is shown in Fig. 6.19. Suppose the current stress point A $(H^{'}, M^{'}, V^{'})$ that lays on an loading surface described by Eq. 6.21. This

surface has a similar shape with the final yield surface where the point B lays (H^*, M^*, V^*) (Eq. 6.22).

$$\text{Point A}: \left(\frac{H^{'}}{\xi N\mu H_0}\right)^2 + \left(\frac{M^{'}}{\xi N\mu M_0}\right)^2 - 1.5\frac{H^{'}}{(\xi N\mu H_0)}\frac{M^{'}}{(\xi N\mu M_0)} - \left[1 - \left(\frac{V^{'}}{\xi N\mu V_0}\right)^2\right] = 0 \tag{6.21}$$

$$\text{Point B}: \left(\frac{H^{*}}{N\mu H_0}\right)^2 + \left(\frac{M^{*}}{N\mu M_0}\right)^2 - 1.5\frac{H^{*}}{N\mu H_0}\frac{M^{*}}{N\mu M_0} - \left[1 - \left(\frac{V^{*}}{N\mu V_0}\right)^2\right] = 0 \tag{6.22}$$

It is assumed that the loading surface expands isotropically with the development of the stresses, (i.e. the shape remains the same, only the size changes). At last, when the loading surface coincides with the final yield surface (i.e. $H^{'} = H^*$, $M^{'} = M^*$ and $V^{'} = V^*$), $\xi = 1$; at the origin of the stress, $\xi = 0$. For an arbitrary stress state $(H^{'}, M^{'}, V^{'})$ ξ can be determined by substituting the stresses into Eq. 6.21.

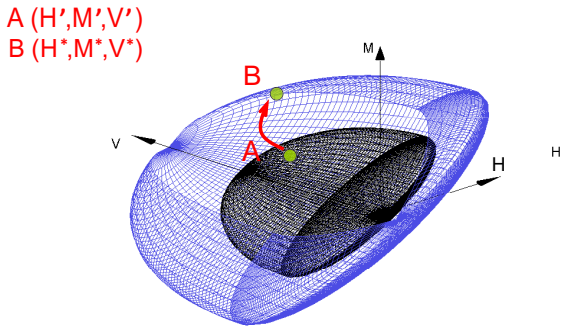

Figure 6.19: Evolution of the loading surfaces in the $H - M - V$ space

6.1.5 Calibration of the macro-element parameters

The macro-element is implemented into the finite element code (a Matlab toolbox) FEDEASLab [140], developed at the University of California, Berkeley. The different parameters are summarized in Table. 6.1:

Parameter	Role	Function
H_0	Horizontal bearing capacity	Failure surface
M_0	Bending bearing capacity	
V_0	Vertical bearing capacity	
k_v	Vertical stiffness	Elastic stiffness
k_{hh}	Horizontal stiffness	
k_{mm}	Rotational stiffness	
k_{hm}	Coupled translation-rotation stiffness	
κ	Evolution of yield surface	Hardening parameter
m_R	Stiffness at load reversal point	Cyclic behavior of hypoplastic model (intergranular strain)
m_R	Stiffness when neutral loading	
R	Range of linearity	
β^r	Rate of evolution of IS	
χ	Transition of stiffness	

Table 6.1: Parameters for the hypoplastic macro-element

The calibration of macro-element parameters was first carried out on single vertical pile. It this dissertation, the elastic stiffness k_v, k_{hh}, k_{mm} and k_{hm} are determined numerically by FEM model. Fig. 6.20 shows the general case of vertical pile foundations, but the procedures for determining the initial stiffness are also applicable for single piles. First, In order to obtain the initial horizontal stiffness of piles or pile groups, a unit displacement was applied on the pile head or pile cap, at the same time, the rotation of the pile head or pile cap is fixed. In this way, the horizontal stiffness k_{hh} together with the coupling stiffness k_{hm}. Secondly, following the same procedures, rotational stiffness k_{mm} could be obtained. In addition, the coupling stiffness k_{hm} obtained from the two steps are identical, which means the determination of the initial stiffness parameters is valid and accurate.

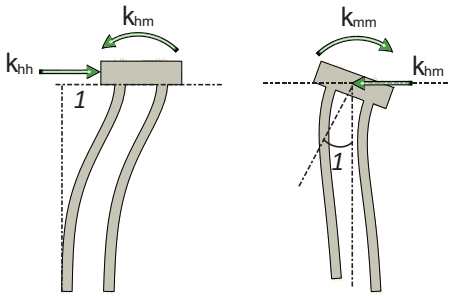

Figure 6.20: Determination of initial stiffness of macro-element

To find the rest of the macro-element parameters, calibration is mainly based on the experimental results from the one-way cyclic load tests [1] that are very useful to find the parameters linked with the intergranular concept. Rosquët [1] performed a series of centrifuge tests to investigate the behavior of a free-head pile in Fontainebleau sand (around 86% in relative density) under monotonic and lateral cyclic loading. The load pattern followed during the centrifuge tests is shown in Fig. 6.21(a). The pile was first charged horizontally to certain stress level followed by one-way cyclic steps; finally, the pile was unloaded. Since the load process was force-controlled, the accumulation of the permanent displacements could be observed, see in Fig. 6.21(b).

The hardening parameter can be calibrated from the loading and unloading part; what is more important, the parameters for the cyclic behavior of the macro-element model can be calibrated from the one-way cyclic part. The well calibrated parameter will give good stiffness at the loading reversal points and at the same time restrain the excessive accumulation of deformation.

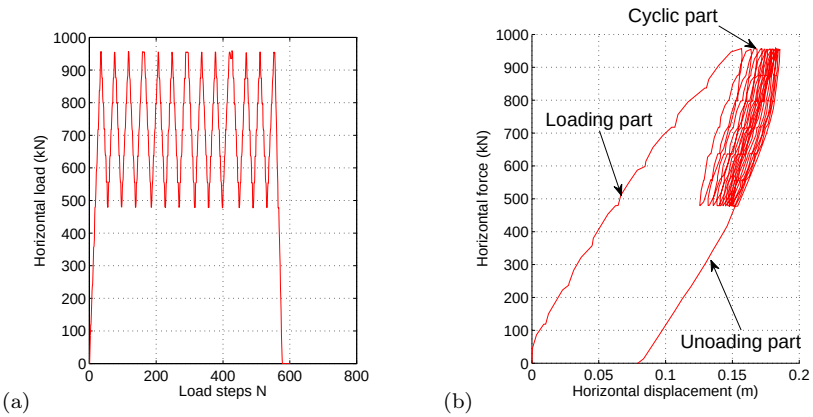

Figure 6.21: Experimental data (from Rosquët [1]) used to calibrate the hypoplastic macro-element: (a) loading; (b) pile head response

The calibrated values in macro-element for single vertical pile is shown in Table. 6.2.

Parameter	Value
H0	0.5×10^4 kN
M0	0.45×10^5 kN·m
V0	2.5×10^4 kN
k_v	8.4×10^5 kN/m
k_{hh}	4.4×10^4 kN/m
k_{mm}	3.3×10^5 kN·m/rads
k_{hm}	1.6×10^4 kN/m
κ	1.2
m_R	5.0
m_T	2.0
R	6.0×10^{-3}
β_r	0.5
χ	0.5

Table 6.2: Parameters of hypoplastic macro-element for single vertical pile

Due to the scarcity of data of the cyclic behavior of pile group in sand, the calibration of the hardening parameter for vertical pile group has to turn to the FEM model. However, the calibration is not directly based on the FEM model, since the FEM model is also an approximation of the real physical problem. FEM model was only used for making qualitative comparisons. The parameters used for single vertical pile was tested on vertical pile group then the results were compared with the results from FEM model.

For the hardening parameter κ. Prescribed monotonic horizontal displacement and rotation were applied simultaneously on the macro-element and the stress paths were plotted in H-V plane. In this way, the horizontal and rotational hardening behavior of the macro-element can be examined at the same time. The stress paths computed by macro-element and by FEM model were compared and shown in Fig. 6.22. The hardening rule defined in the Macro-element agrees well with the FEM model.

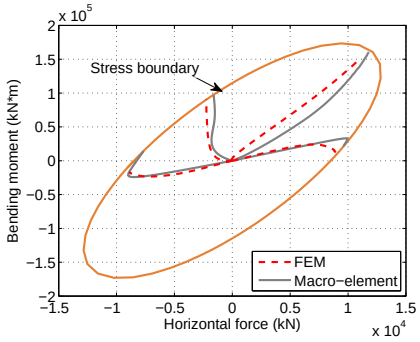

Figure 6.22: Comparison of different loading paths computed by Macro-element and FEM model

For the parameters of intergranular strain, the parameters calibrated for single vertical pile are adopted for the vertical pile group. The cyclic behavior of the macro-element of vertical pile group is compared again with the FEM model, see in Fig. 6.23. It is difficult to judge the accuracy of the parameters, however, the macro-element has the same trend compared with the FEM mode. It is shown that the accumulation of horizontal displacement under one-way cyclic load for macro-element is smaller than those of the FEM model. The calibrated parameters for vertical pile group with $4D$ pile spacing are listed in Table. 6.3:

Parameter	Value
H0	0.75×10^{4} kN
M0	1.01×10^{5} kN·m
V0	3.75×10^{4} kN
k_v	33.6×10^{5} kN/m
k_{hh}	17.6×10^{4} kN/m
k_{mm}	13.2×10^{5} kN·m/rads
k_{hm}	6.4×10^{4} kN/m
κ	1.2
m_R	5.0
m_T	2.0
R	6.0×10^{-3}
β_r	0.5
χ	0.5

Table 6.3: Parameters of hypoplastic macro-element for vertical pile group ($4D$ pile spacing)

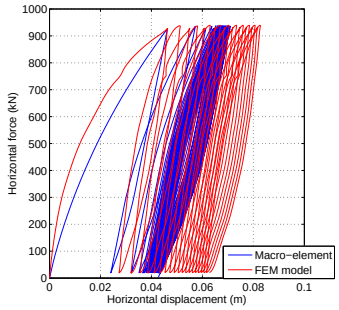

Figure 6.23: Comparison of the cyclic responses of pile head computed by Macro-element and FEM model

Finally, the responses of both the calibrated vertical pile and pile group under horizontal force are shown in Fig. 6.24. The horizontal resistance of vertical pile group is higher than that of the single vertical pile.

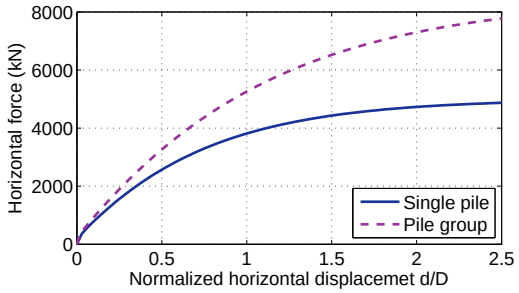

Figure 6.24: Lateral reponses of single vertical pile and vertical pile group ($4D$ pile spacing) computed by Macro-element

6.2 Macro-element for Single Inclined Pile and Inclined Pile Foundation

6.2.1 Considerations of failure envelopes for single inclined pile and inclined pile group

By following the same procedures explained in Section. 6.1.1, the failure envelop surface was first investigated on single inclined pile. The results are shown and compared with the failure envelop of a single vertical pile in Fig. 6.25. Apparently, the failure envelop for single inclined pile (15°) is not symmetric. Compared with the failure envelop of single vertical pile, the failure envelop rotates with respect to the origin by about 15°. The similar results were also reported by Meyerhof [37] and Mroueh [62] in their experimental and numerical results respectively.

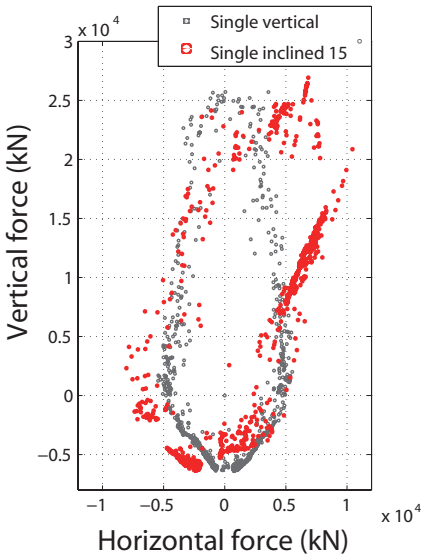

Figure 6.25: Numerical failure envelope of single inclined pile in the H-V plane

The asymmetric failure envelope is due to the loading direction dependent response of single inclined pile. As it is shown in Fig. 6.26, different loading direction results different responses. This agrees well with Zhang et al. [12] that loading direction influences the horizontal response of single inclined pile., see in in Chapter 2.

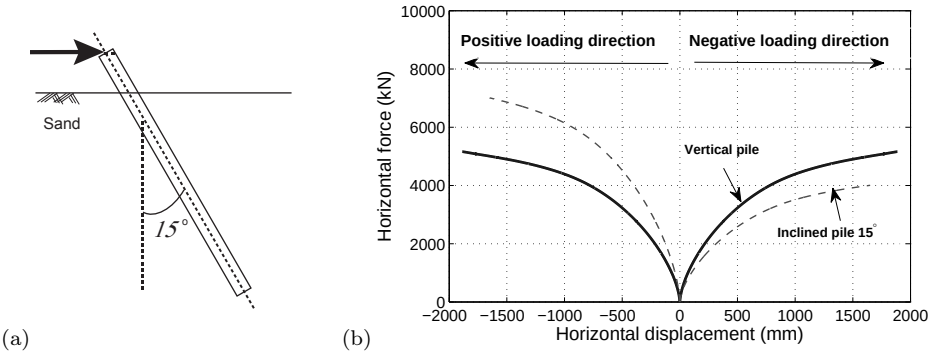

Figure 6.26: Influence of loading direction on the response of inclined pile: (a) a positive inclined pile (b) loading direction dependent response

The complete 3D failure envelop surface for single inclined pile and inclined pile group ($4D$ pile spacing) are shown in Fig. 6.27 and Fig. 6.28 respectively. It can be seen from Fig. 6.27 (b) that for single inclined pile, the failure envelope surface in H-V plane has an ellipse liked shape, however, shifts in the negative axis direction. The intersections of the failure envelope with the horizontal axis indicate different horizontal bearing capacities result from the different loading directions. The whole 3D failure surface is also asymmetric in H-V-M space.

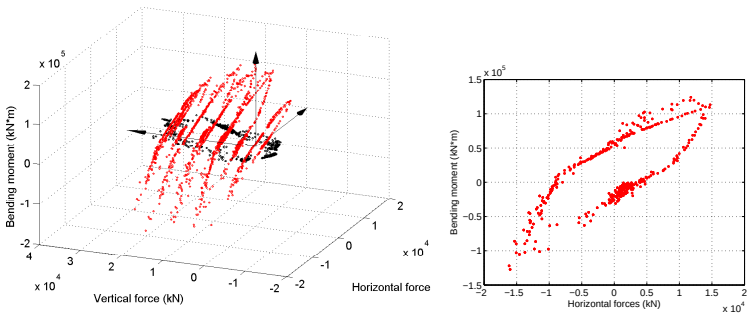

(a) (b)

Figure 6.27: Numerical failure envelope of single inclined pile in the H-V plane

For the 3D failure envelop surface for inclined pile group ($4D$ pile spacing), see in Fig. 6.28, in the H-M plane, the failure envelop manifests a shape that looked like a complicated inclined and "squeezed ellipse". Due to the symmetric configuration of the two inclined piles, despite the inclination, the failure envelop is symmetric.

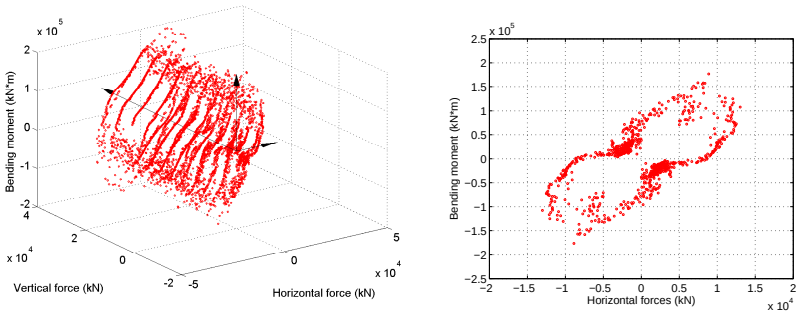

(a) (b)

Figure 6.28: Numerical failure envelope of single inclined pile in the H-V plane

Due to the complex shape of the yield surfaces of single inclined pile and inclined pile foundation, it is very difficult to find mathematical equations that can well capture their features in H-M-V 3D space. In addition, the so complicated geometry of the yield surfaces, may cause numerical difficulties for computing the norm direction of the surface. For example, the geometry cross-section of inclined pile group (Fig. 6.28 (b)) is not convex, even if there exists a function can fit it.

The macro-elements for inclined piles and inclined pile foundations are considered alternatively, due to the difficulties encountered as they were mentioned above. From the view of engineering practice, the usage of single inclined pile for supporting structures are very rare and it is of less engineering interests to consider a single

inclined pile particularly. For this reason, the macro-element for single inclined pile will not be considered in this study. For the inclined pile group, the failure envelop of vertical pile group is roughly close to that of the single vertical pile in terms of the shape. Instead using the complicated surface shown in Fig. 6.28 (b), the failure surface of the vertical pile group will be used for a compromising solution temporarily. For for inclined pile group, the macro-element that developed for vertical pile group was also adopted with necessary modifications on the parameters.

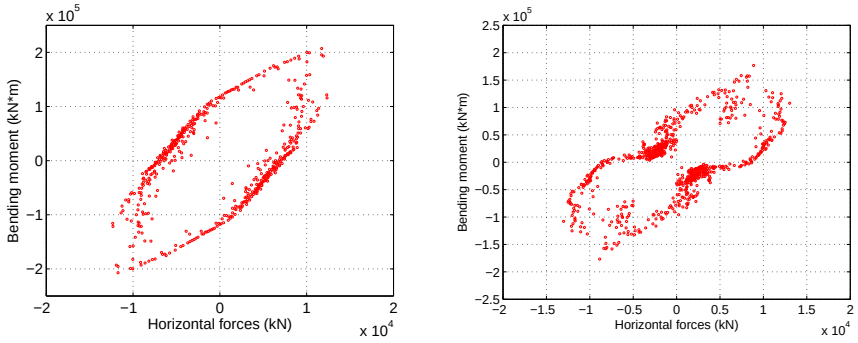

(a) (b)

Figure 6.29: Numerical failure envelopes for: (a) vertical pile group; (b) inclined pile group, in H-M plane with V=0 kN

Recall that in Chapter 4, in the analysis of horizontal and rotational stiffness of inclined and vertical pile group, inclined pile group has significant higher horizontal stiffness than the vertical pile group; however, for the rotational stiffness, the differences are small. For the macro-element of inclined pile group, the parameters that estimated in for the vertical pile group are adopted for inclined pile group, but with a higher horizontal stiffness.

The parameters for macro-element of inclined pile group are listed in Table. 6.4

Parameter	Value
H0	0.75×10^4 kN
M0	1.01×10^5 kN·m
V0	3.75×10^4 kN
k_v	134.4×10^5 kN/m
k_{hh}	17.6×10^4 kN/m
k_{mm}	13.2×10^5 kN·m/rads
k_{hm}	25.6×10^4 kN/m
κ	1.2
m_R	5.0
m_T	2.0
R	6.0×10^{-3}
β_r	0.5
χ	0.5

Table 6.4: Parameters of hypoplastic macro-element for inclined pile group

6.3 Damping in the proposed hypoplastic Macro-element

The damping of macro-element refers to the radiation damping induces by the vibration of structures. Since the macro-element proposed in this dissertation is based on hypoplasticity theory and inherently, hypoplasticity induces hysteresis energy dissipation even in very small strain range. The damping in the constitutive level of the macro-element is not considered. For solving the dynamic problem, slight damping in the Rayleigh damping (damping ratio about 0.2%) in the structural level was used.

6.4 Validation of Macro-element

6.4.1 Validation of Macro-element for Single Vertical Pile under cyclic loading

The experiments performed by Rosquët [1] to investigate the cyclic behavior of single vertical pile are used to validate the macro-element under static cyclic loading. Rosquoët [1] performed monotonic loading tests on a single vertical pile embedded in Fontainebleau sand at the centrifuge facility of IFSTTAR Nantes. The homogeneous dry Fontainebleau sand sample had a density $\gamma = 1630$ kg/m^3 and a relative density $D_r = 86\%$. The experiment is illustrated in Fig. 6.30:

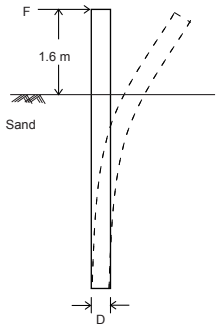

Figure 6.30: Cyclic loading test on single vertical pile (Rosquët [1])

Both one-way, two-way cyclic loading tests with different cyclic loading amplitudes were simulated by macro-element and the results are compared with the experimental data (Figs. 6.31, 6.32 and 6.33). It is convinced that the calibration of model parameters and the macro-element can successfully capture the behavior of single vertical pile under various cyclic loading.

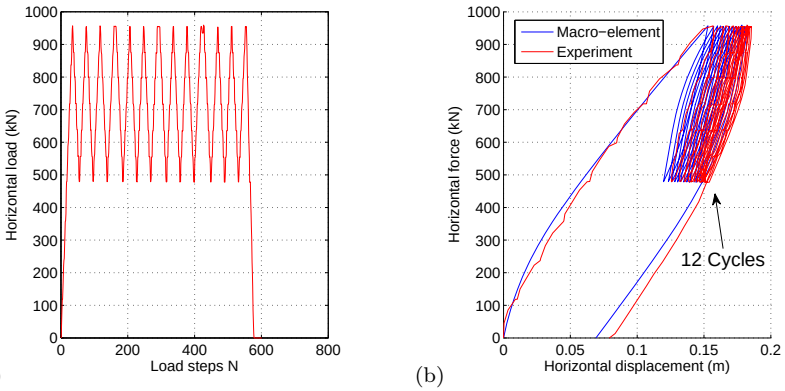

(a) (b)

Figure 6.31: Validation of macro-element for single vertical pile: one-way cyclic loading, 12 cycles amplitude = 480 kN (experimental data from Rosquët [1]): (a) loading; (b) pile head response

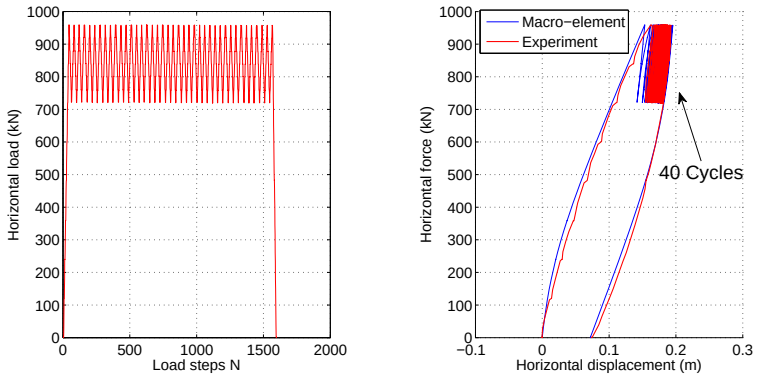

(a) (b)

Figure 6.32: Validation of macro-element for single vertical pile: one-way cyclic loading, 12 cycles amplitude = 240 kN (experimental data from Rosquët [1]): (a) loading; (b) pile head response

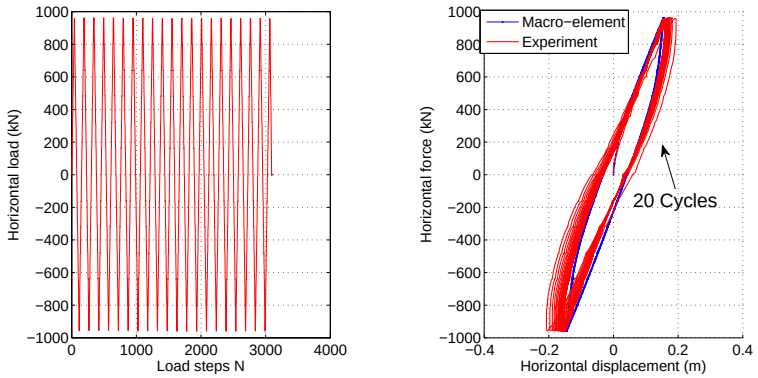

(a) (b)

Figure 6.33: Validation of macro-element for single vertical pile: two-way cyclic loading, 20 cycles amplitude = 1920 kN (experimental data from Rosquët [1]): (a) loading; (b) pile head response

6.4.2 Validation of Macro-element for Vertical Pile Group under dynamic excitations

The validation of macro-element for vertical pile groups is based on the dynamic centrifuge tests that were introduced in chapter 4. However, the excitation signal is taken at the measured acceleration history at the soil surface, which means the far-field response of the soil is input as the excitation signal. Fig. 6.34 shows the configurations of pile groups that were simulated by macro-element.

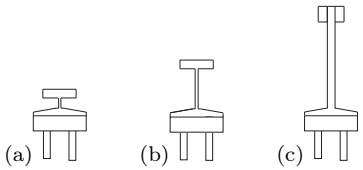

Figure 6.34: Validation of macro-element for vertical pile groups with: (a) short (b) slender and (c) very slender superstructures

Results indicate very good performance of macro-element for vertical pile groups under various dynamic loading conditions. The influence of the superstructure can also be captured by the macro-element.

However, for the short and the very slender superstructures under 3.5 Hz sinusoidal excitations, the response of pile cap simulated by macro-element is very poor, see Figs. 6.38(b) and 6.42(b).

6.4.2.1 Vertical pile group with short superstructure

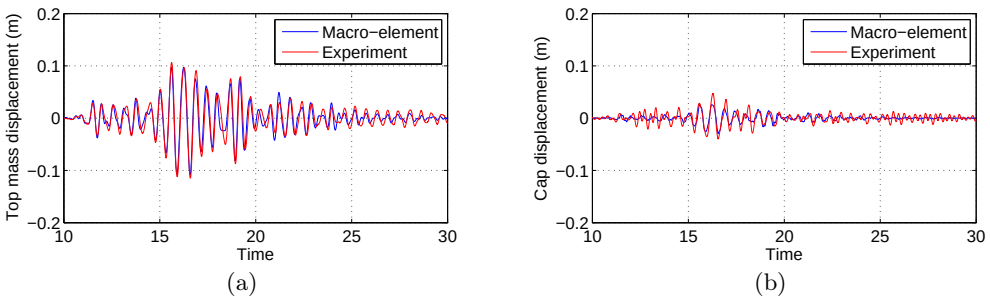

Figure 6.35: Validation of macro-element for vertical pile group: vertical pile group with short building under Northridge -9 dB earthquake: (a) response of top mass; (b) response of pile cap

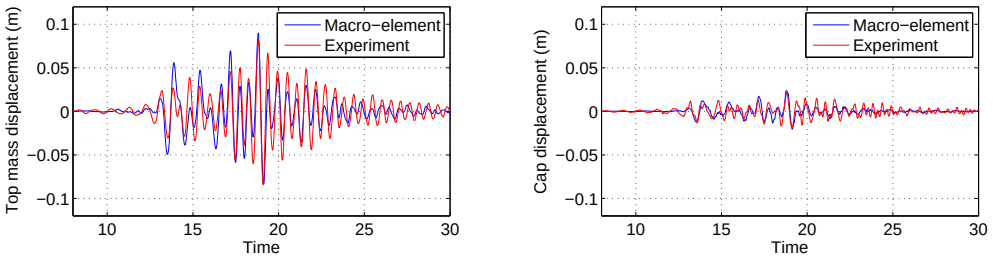

(a) (b)

Figure 6.36: Validation of macro-element for vertical pile group: vertical pile group with short building under Kobe -4 dB earthquake: (a) response of top mass; (b) response of pile cap

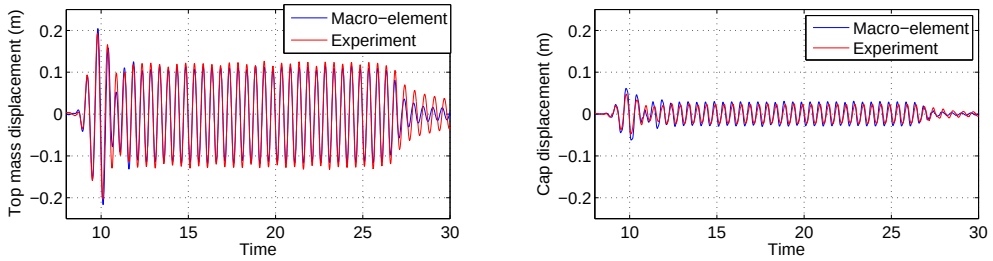

(a) (b)

Figure 6.37: Validation of macro-element for vertical pile group: vertical pile group with short building under sine 2.0 Hz 0.4 g input: (a) response of top mass; (b) response of pile cap

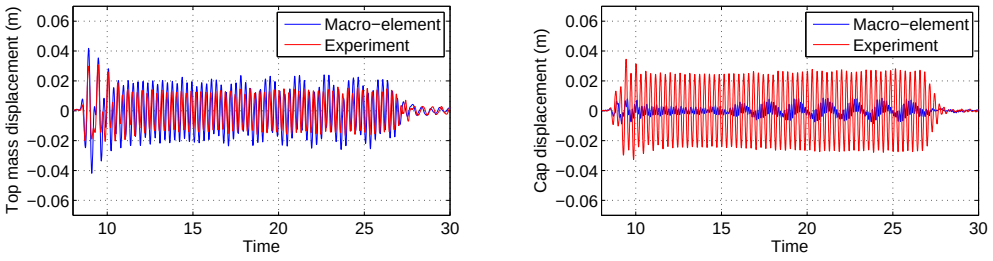

(a) (b)

Figure 6.38: Validation of macro-element for vertical pile group: vertical pile group with short building under sine 3.5 Hz 0.4 g input: (a) response of top mass; (b) response of pile cap

6.4.2.2 Vertical pile group with slender superstructure

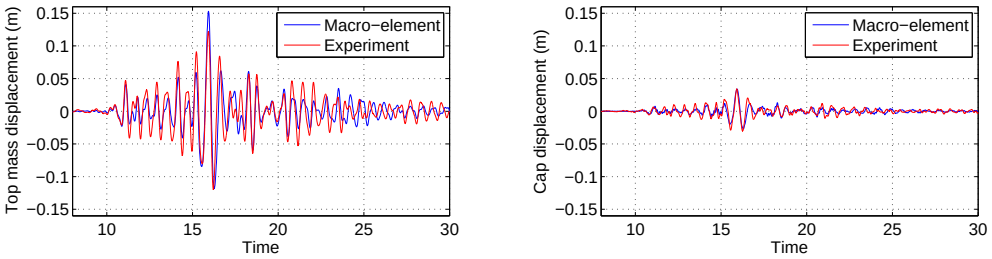

(a) (b)

Figure 6.39: Validation of macro-element for vertical pile group: vertical pile group with tall building under Northridge -9 dB earthquake: (a) response of top mass; (b) response of pile cap

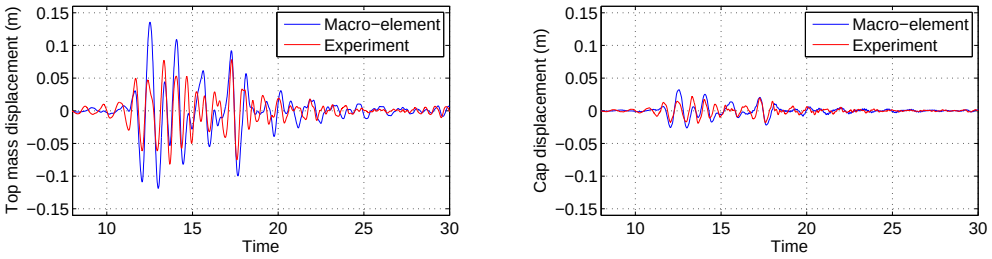

(a) (b)

Figure 6.40: Validation of macro-element for vertical pile group: vertical pile group with tall building under Kobe -4 dB earthquake: (a) response of top mass; (b) response of pile cap

6.4.2.3 Vertical pile group with very slender superstructure superstructure

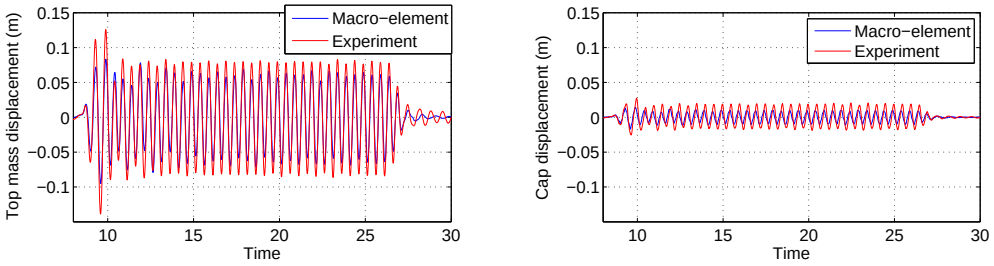

(a) (b)

Figure 6.41: Validation of macro-element for vertical pile group: vertical pile group with taller building under sine 2.0 Hz 0.4 g input: (a) response of top mass; (b) response of pile cap

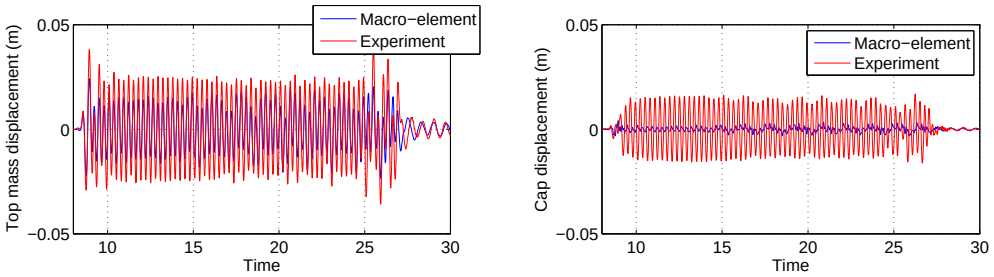

(a) (b)

Figure 6.42: Validation of macro-element for vertical pile group: vertical pile group with taller building under sine 3.5 Hz 0.4 g input: (a) response of top mass; (b) response of pile cap

6.4.3 Validation of Macro-element for Inclined Pile Group under dynamic excitations

The validation of macro-element for inclined pile groups were carried out based on the centrifuge tests, the inclined pile groups configurations are shown in Fig. 6.43. The simulation results are shown in Figs. 6.44 and 6.45. The performances are only just passable. Although the trend of the displacement history can be approximately captured, there are big differences between the response amplitudes and frequencies. The poor performances of the macro-element for inclined pile groups are mainly due to the failure surface and the hardening law that adopted from the vertical pile groups can not represent the true behavior of the soil-pile-superstructure interaction mechanism. The macro-element for inclined pile groups should be improved in the future.

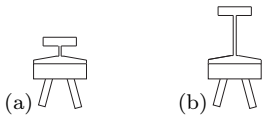

Figure 6.43: Validation of macro-element for inclined pile groups with: (a) short (b) slender superstructures

6.4.3.1 Inclined pile group with short building

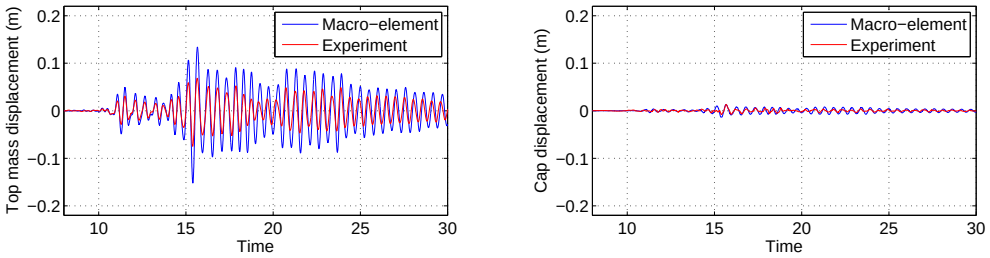

Figure 6.44: Validation of macro-element for inclined pile group: inclined pile group with short building under Northridge -9 dB earthquake: (a) response of top mass; (b) response of pile cap

6.4.3.2 Inclined pile group with tall building

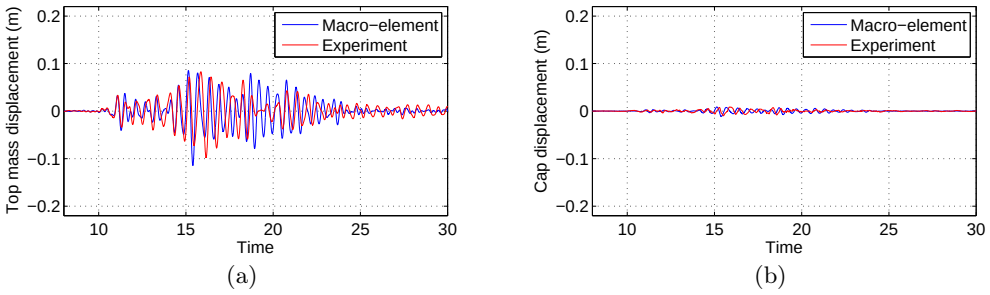

Figure 6.45: Validation of macro-element for inclined pile group: inclined pile group with tall building under Northridge -9 dB earthquake: (a) response of top mass; (b) response of pile cap

6.5 Conclusions

In this chapter, the procedures for developing the macro-element for deep foundations were introduced. The general method using numerical radial displacement tests for finding failures surface of piles and pile foundations is introduced. Analytical equation is proposed for failure surface of single vertical pile, then the equation

is extended to pile groups by introducing the influence of group effect. Relative simple isotropic evolution of failure surface and hardening rules were employed in developing the macro-element. Due to the difficulties encountered for inclined piles and inclined pile groups, the developing of macro-element for inclined pile groups are alternatively considered.

The results from macro-element were compared with the dynamic centrifuge data, the performance of the proposed macro-element for vertical pile groups is satisfactory. For the inclined pile groups, due to the difficulties to find the suitable failure surface and the associated hardening law, the performance of macro-element for inclined pile groups are not so satisfactory.

Chapter 7

Perspectives

In this Ph.D dissertation, an experimental study on the performance of vertical and inclined pile groups and the development of a new macro-element for deep foundations are presented in detail. Future work could be focused on the following aspects:

7.1 Experimental part

1. In this work, the pile to cap connection is assumed fixed. However, as reported by Sadek and Shahrour [141], the pile connection condition significantly influences the response of the pile group. Therefore, the response of both inclined and vertical pile groups with pinned pile to cap connection should be studied in the near future. Other aspects related to the pile group configuration should be addressed as the behavior of a foundation with multiple rows of piles or with different pile inclination angles etc.

2. The influence of the sand density on the behavior of the pile groups needs to be further investigated. In addition, the behavior of inclined piles with soil liquefaction should be studied, since as mentioned in chapter 2 it is the main reason behind different structural failures. Another interesting subject could be the behavior of inclined piles in clay.

7.2 Numerical part

1. More advanced constitutive soil models should be used to capture the complex response of both soil and soil pile interaction under dynamic excitations. Due to the difficulties to perform tests on the response of pile groups considering soil liquefaction, finite element simulations for saturated porous media should be performed.

7.3 Macro-element

1. Asymmetric configurations of inclined pile foundations should be considered (e.g. foundation with both vertical and inclined piles). The pile configuration will certainly influence the failure surface used in the macro-element.

2. As proposed by di Prisco et al. [142], a challenging task for future research in this field consists in introducing either a time factor or a frequency variable into the macro-element constitutive relationship. It is probably better to adopt a rate-dependent form for the constitutive law. A more challenging task is to introduce a liquefaction factor to take into account the pore pressure built-up during dynamic excitations.

Appendix A

Experimental program, base shaking signals and design of superstructures

A.1 List of experiments

A.1.1 List of experiments by Chronological order

NO.	Date	Discription
01	2011-01-27	Free field test (real earthquake input)
02	2011-03-09	Vertical pile group (real earthquake input)
03	2011-03-11	*Repeat test of 01
04	2011-04-22	Inclined pile group (real earthquake input)
05	2011-06-24	Inclined pile group with short building (real earthquake input)
06	2011-06-28	*Repeat test of 05
07	2011-06-30	Vertical pile group with short building (real earthquake input)
08	2011-10-20	*Repeat test of 05
09	2011-11-10	*Repeat test of 07
10	2011-12-09	Inclined pile group with tall building (real earthquake input) Superseded, replaced by test 23
11	2011-12-13	*Repeat test of 10
12	2012-01-17	Vertical pile group with tall building (real earthquake input) Superseded, replaced by test 24
13	2012-03-02	Free field test (sine input with tapered parts)
14	2012-04-05	Free field test (sine input with constant amplitude)
15	2012-04-11	Inclined pile group with short building (sine input 3.5 Hz)
16	2012-05-15	Vertical pile group with short building (sine input 3.5 Hz)
17	2012-05-21	Vertical pile group with taller building (sine input 3.5 Hz)
18	2012-07-02	Inclined pile group with taller building (sine input 3.5 Hz)
19	2012-07-03	Inclined pile group with taller building (sine input 2.0 Hz)
20	2012-08-13	Vertical pile group with taller building (sine input 2.0 Hz)
21	2012-08-14	Vertical pile group with short building (sine input 2.0 Hz)
22	2012-08-24	Inclined pile group with short building (sine input 2.0 Hz)
23	2012-12-11	Inclined pile group with tall building (Real earthquake input)
24	2012-12-13	Vertical pile group with tall building (Real earthquake input)

A.2 Details of experiments

01. Free field test – real earthquake input

Experiment ID	Experiment date
2011_01_27_free_field	2011-01-27

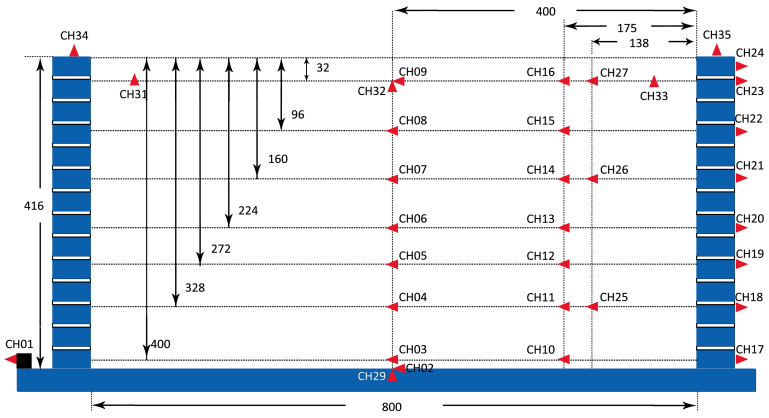

Figure A.1: Sensors planning of free field test – real earthquake

02. Free field test – sine input

A. Sine input with tapered parts

Experiment ID	Experiment date
2012_03_02_free_filed	2012-03-02

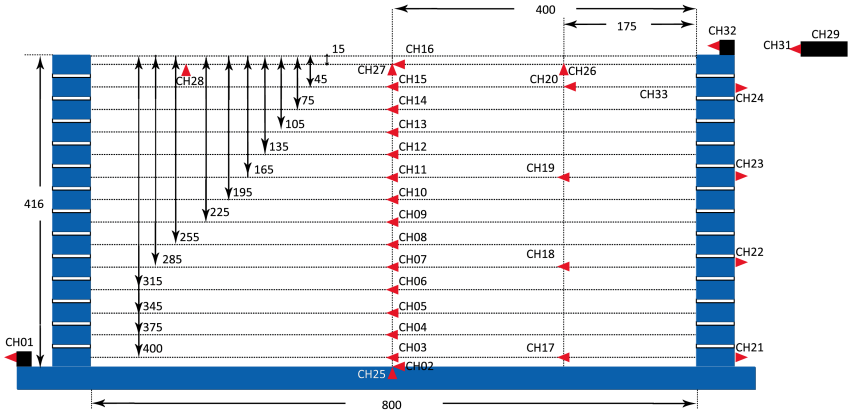

Figure A.2: Sensors planning of free field test – sinusoidal test, tappered signal

B. Sine input with constant amplitude

Experiment ID	Experiment date
2012_04_05_free_filed	2012-04-05

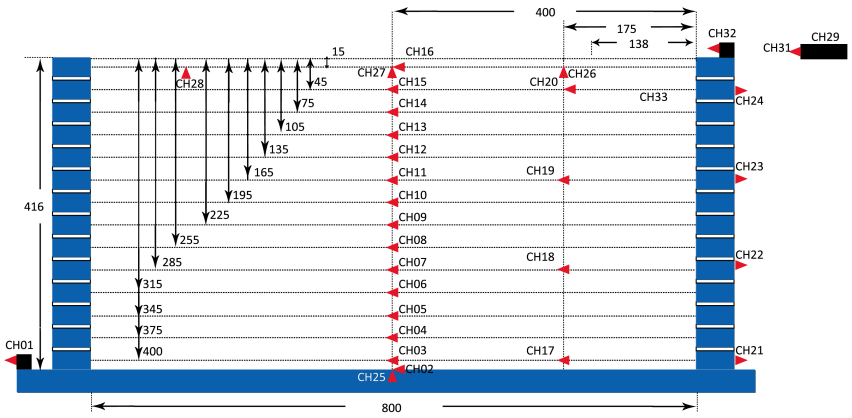

Figure A.3: Sensors planning of free field test – sinusoidal test, signal with constant amplitude

03. Inclined pile group test

Experiment ID	Experiment date
2011_04_22_inclined_pile_Group	2011-04-22

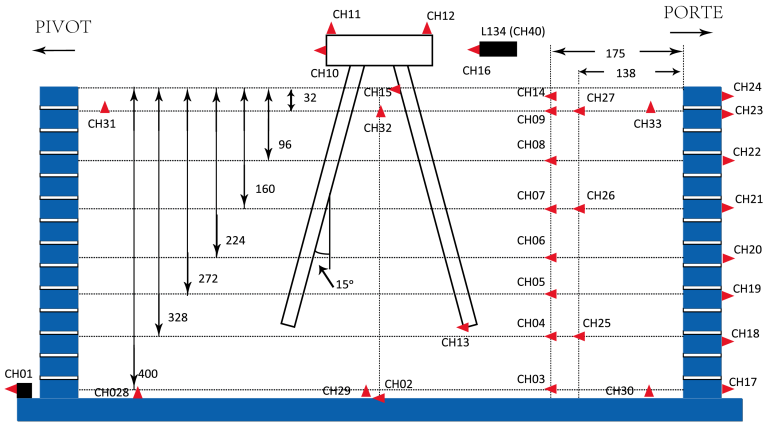

Figure A.4: Sensors planning – inclined pile group

04. Vertical pile group test

Experiment ID	Experiment date
2011_03_09_vertical_pile_Group	2011-03-09

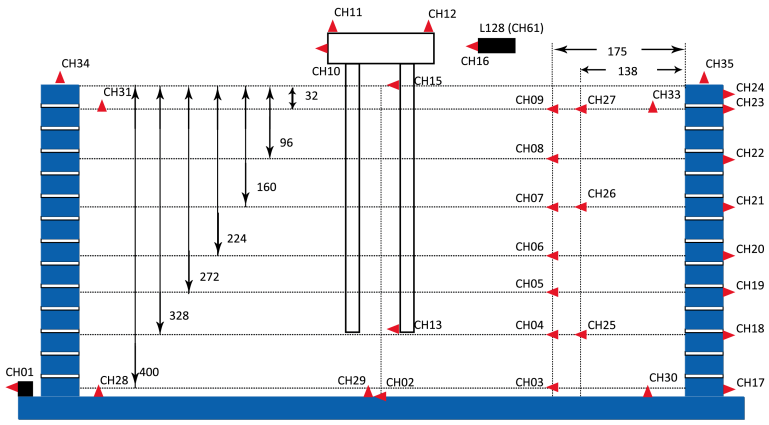

Figure A.5: Sensors planning – vertical pile group

05. Inclined pile group with short building – real earthquake input

Experiment ID	Experiment date
2011_06_24_inclined_short	2011-06-24

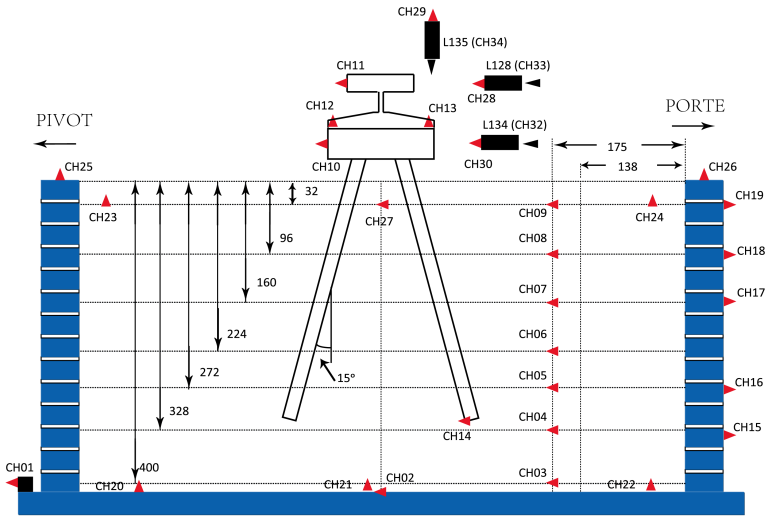

Figure A.6: Sensors planning – inclined pile group with short building, real earthquake

06. Vertical pile group with short building – real earthquake input

Experiment ID	Experiment date
2011_06_30_vertical_short	2011-06-30

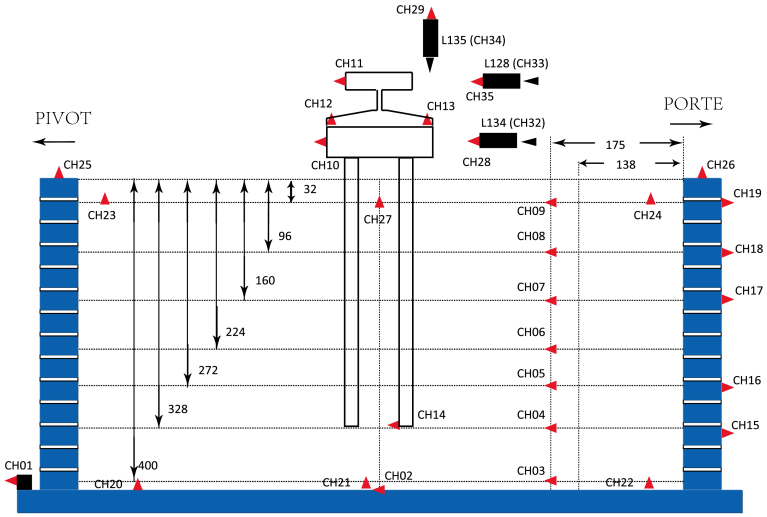

Figure A.7: Sensors planning – vertical pile group with short building, real earthquake

07. Inclined pile group with tall building – real earthquake input

Experiment ID	Experiment date
2012_12_11_inclined_tall	2012-12-11

08. Vertical pile group with tall building – real earthquake input

Experiment ID	Experiment date
2012_12_13_vertical_tall	2012-12-13

09. Inclined pile group with short building – sine input 2.0 Hz

Experiment ID	Experiment date
2012_08_24_inclined_short_sine_80Hz	2012-08-24

10. Vertical pile group with short building – sine input 2.0 Hz

Experiment ID	Experiment date
2012_08_14_vertical_short_sine_80Hz	2012-08-14

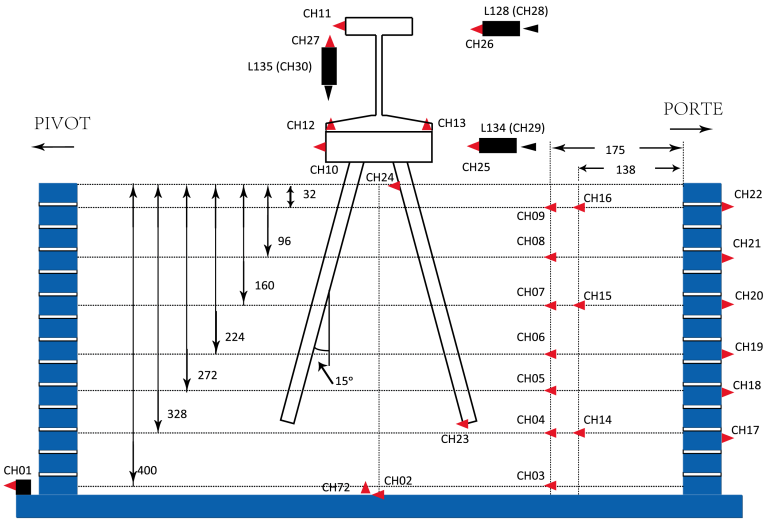

Figure A.8: Sensors planning – inclined pile group with tall building, real earthquake

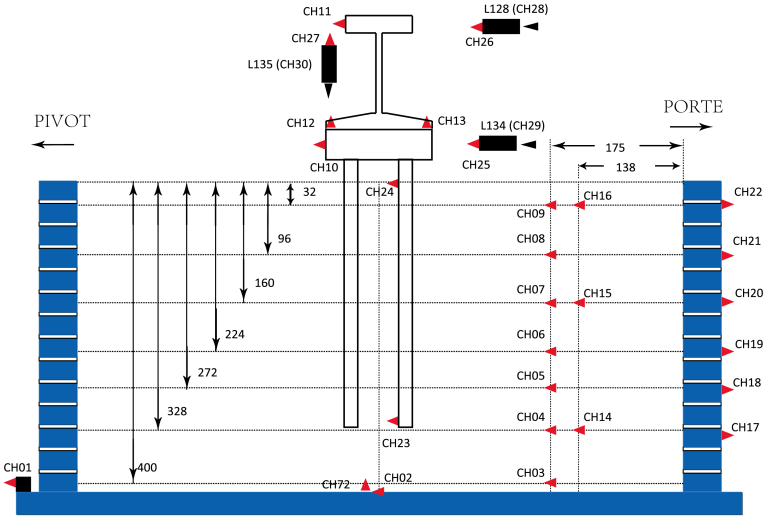

Figure A.9: Sensors planning – vertical pile group with tall building, real earthquake

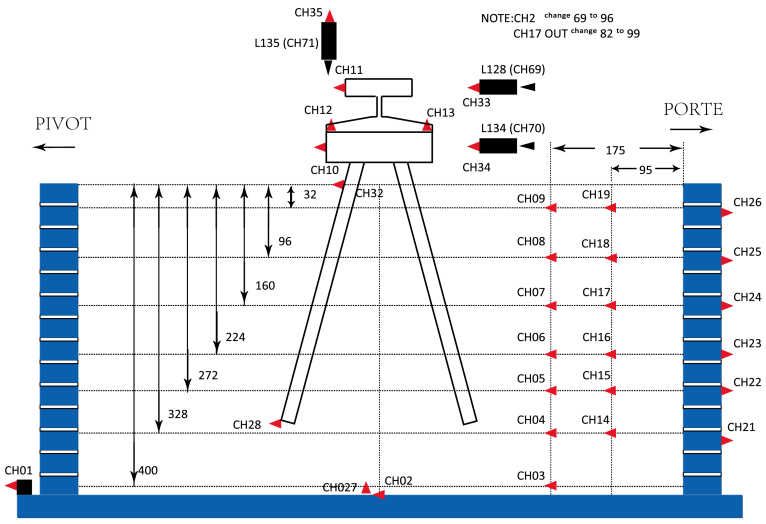

Figure A.10: Sensors planning – inclined pile group with short building, sine 2.0 Hz

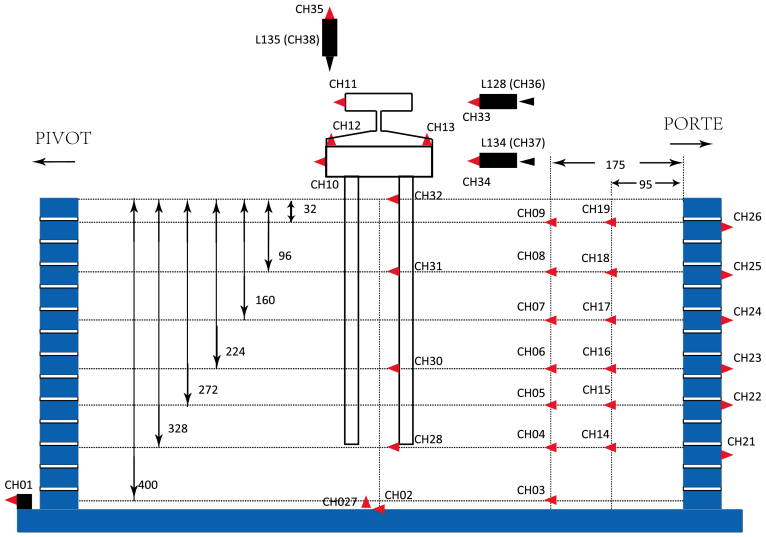

Figure A.11: Sensors planning – vertical pile group with short building, sine 2.0 Hz

11. Inclined pile group with taller building – sine input 2.0 Hz

Experiment ID	Experiment date
2012_07_03_inlcined_tall_sine_80Hz	2012-07-03

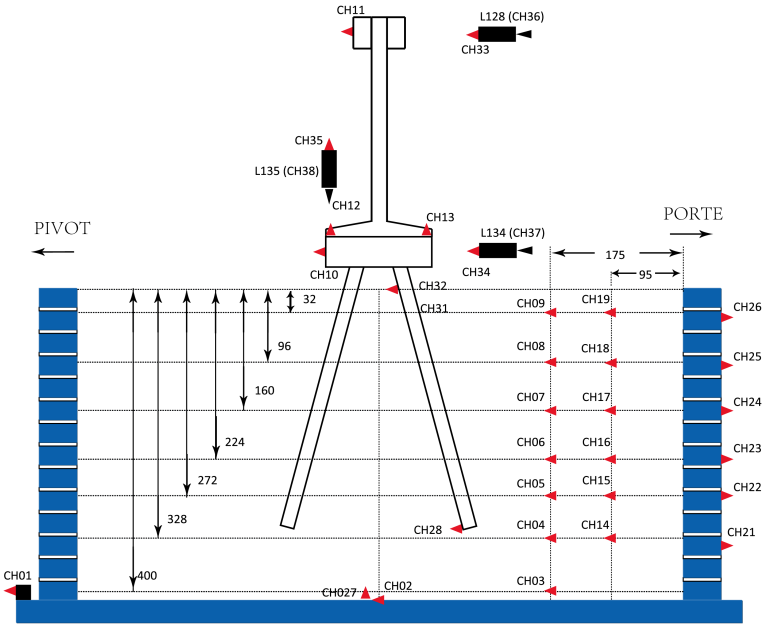

Figure A.12: Sensors planning – inclined pile group with taller building, sine 2.0 Hz

12. Vertical pile group with taller building – sine input 2.0 Hz

Experiment ID	Experiment date
2012_08_13_vertical_tall_sine_80Hz	2012-08-13

13. Inclined pile group with short building – sine input 3.5 Hz

Experiment ID	Experiment date
2012_04_11_inclined_short_sine	2012-04-11

14. Vertical pile group with short building – sine input 3.5 Hz

Experiment ID	Experiment date
2012_05_15_vertical_short_sine	2012-05-15

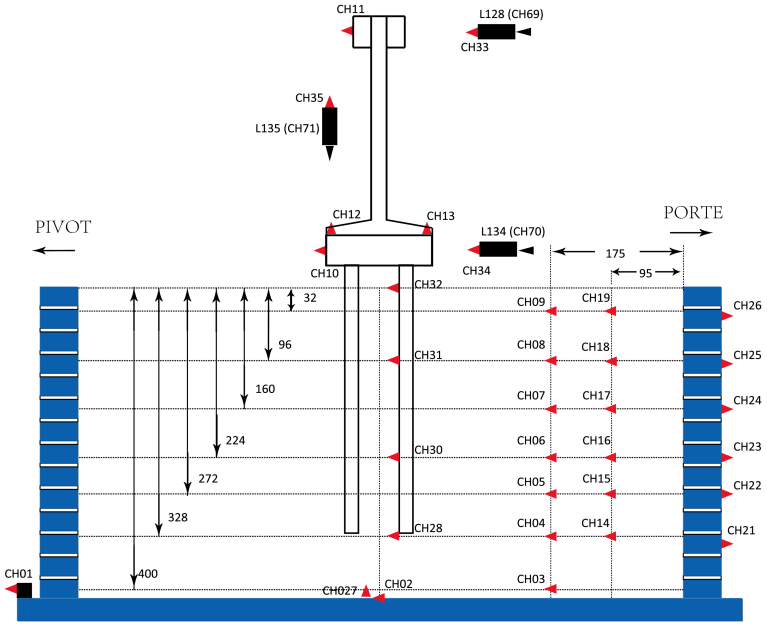

Figure A.13: Sensors planning – vertical pile group with taller building, sine 2.0 Hz

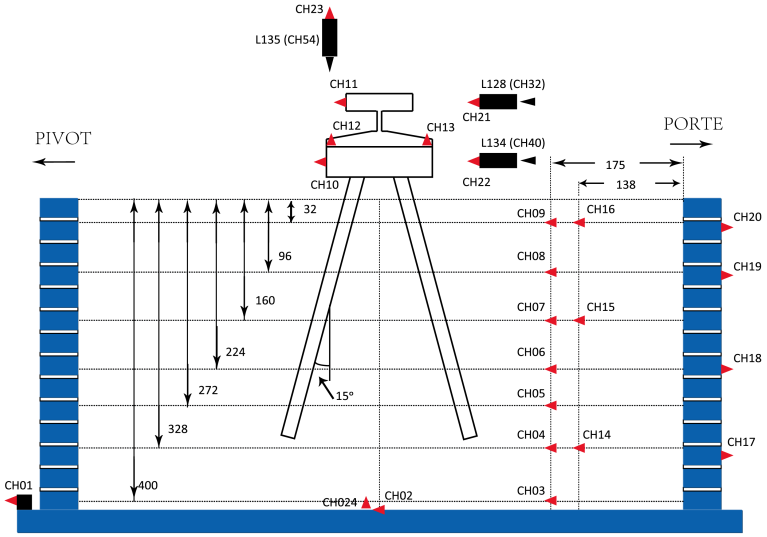

Figure A.14: Sensors planning – inclined pile group with short building, sine 3.5 Hz

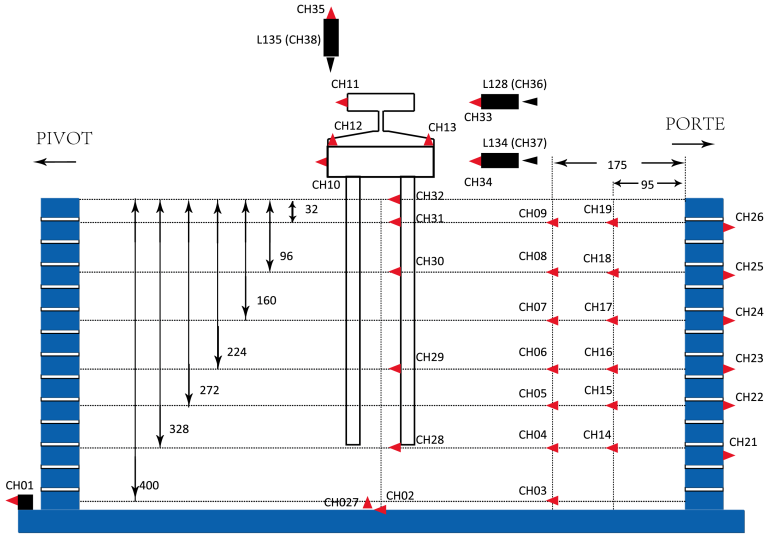

Figure A.15: Sensors planning – vertical pile group with short building, sine 3.5 Hz

15. Inclined pile group with taller building – sine input 3.5 Hz

Experiment ID	Experiment date
2012_07_02_Inclined_tall_sine	2012-07-02

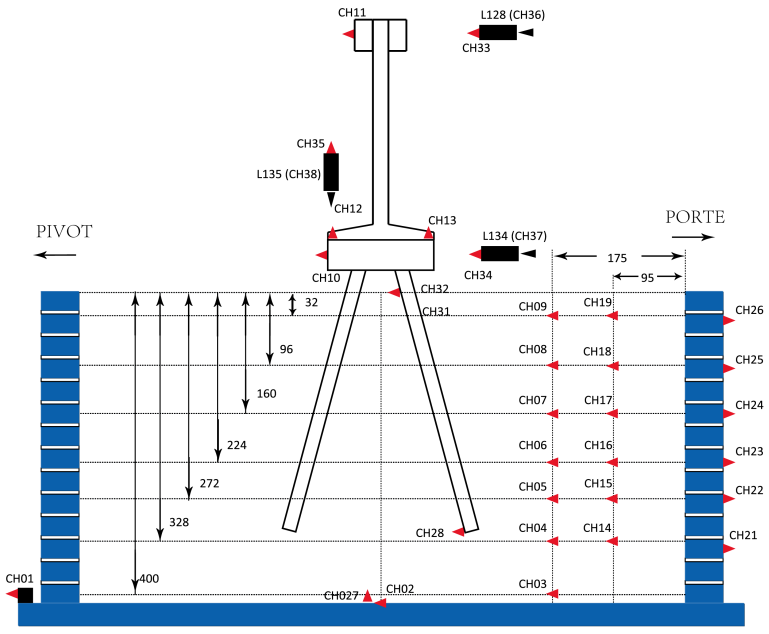

Figure A.16: Sensors planning – inclined pile group with taller building, sine 3.5 Hz

16. Vertical pile group with taller building – sine input 3.5 Hz

Experiment ID	Experiment date
2012_05_21_vertical_tall_sine	2012-07-02

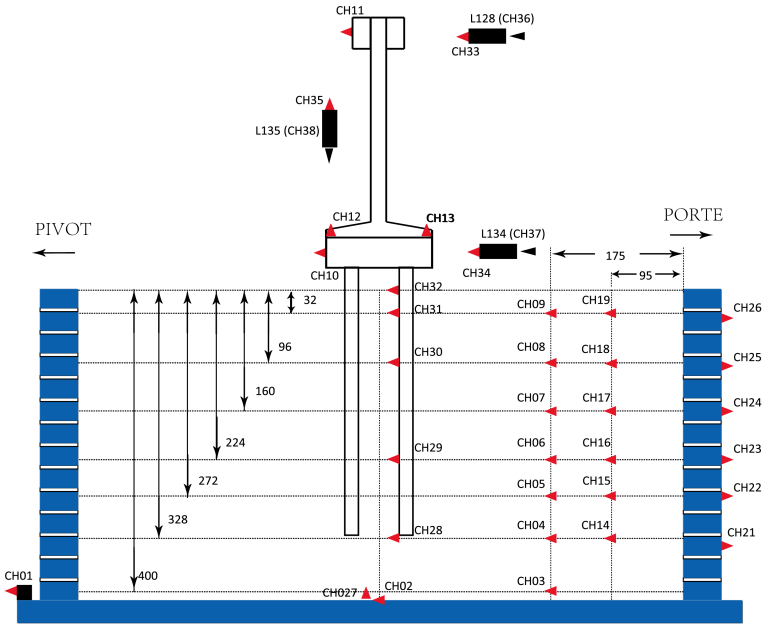

Figure A.17: Sensors planning – vertical pile group with taller building, sine 3.5 Hz

A.3 Characterizations of input signals

Input seismic signal	PGA (m/s^2)	PGV (m/s)	Arias Intensity (m/s)	Significant duration (s)
Martinique Jara -1dB	0.90	0.06	0.2	27.9
Northridge -20dB	1.35	0.09	0.2	11.7
Northridge -9dB	4.79	0.33	2.43	11.7
Kobe -4dB	3.83	0.67	3.51	7.72
sine 2.0 Hz - 2g	0.49	0.04	0.34	15.58
sine 2.0 Hz - 4g	0.98	0.08	1.35	15.58
sine 2.0 Hz - 8g	1.96	0.16	5.37	15.58
sine 2.0 Hz - 16g	3.92	0.31	21.38	15.58
sine 3.5 Hz - 2g	0.49	0.02	0.35	16.10
sine 3.5 Hz - 4g	0.98	0.04	1.39	16.10
sine 3.5 Hz - 8g	1.96	0.09	5.54	16.10
sine 3.5 Hz - 16g	3.92	0.18	22.06	16.10
sine 2.0 Hz - 2g with tapered parts	0.49	0.04	0.34	18.54
sine 2.0 Hz - 4g with tapered parts	0.98	0.08	1.36	18.54
sine 3.5 Hz - 4g with tapered parts	0.98	0.04	1.38	18.71
sine 3.5 Hz - 8g with tapered parts	1.95	0.09	5.53	18.71
sine 12.0 Hz - 8g with tapered parts	1.95	0.07	5.57	18.61
sine 12.0 Hz - 16g with tapered parts	3.89	0.14	21.76	18.61

Table A.2: Characterizations of input signals

A.4 Representation of signal in time and frequency domain

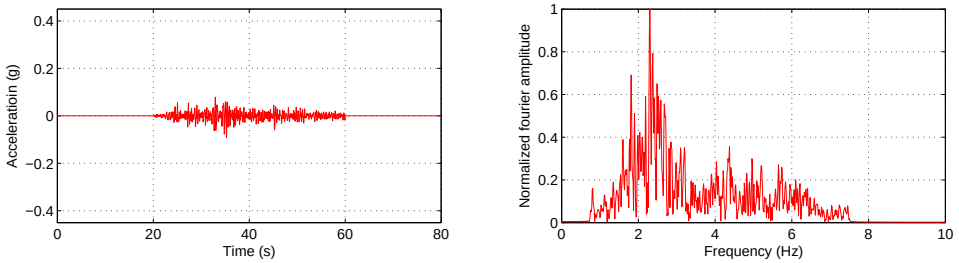

(a) (b)

Figure A.18: Time (a) and frequency (b) representation of Martinique Jara -1 dB earthquake

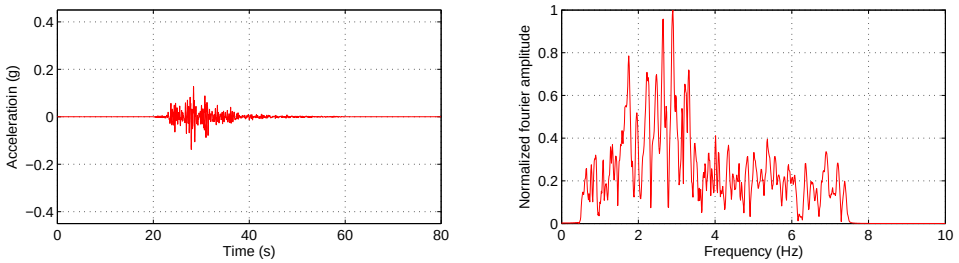

(a) (b)

Figure A.19: Time (a) and frequency (b) representation of Northridge -20 dB earthquake

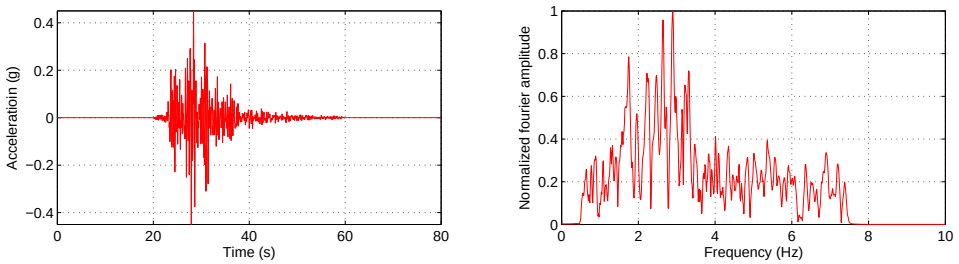

(a) (b)

Figure A.20: Time (a) and frequency (b) representation of Northridge -9 dB earthquake

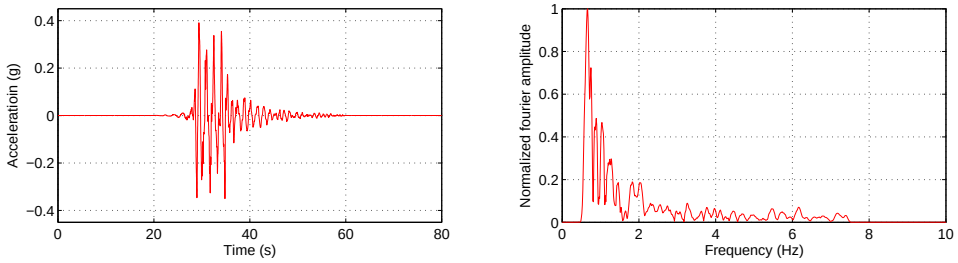

(a) (b)

Figure A.21: Time (a) and frequency (b) representation of Kobe -4 dB earthquake

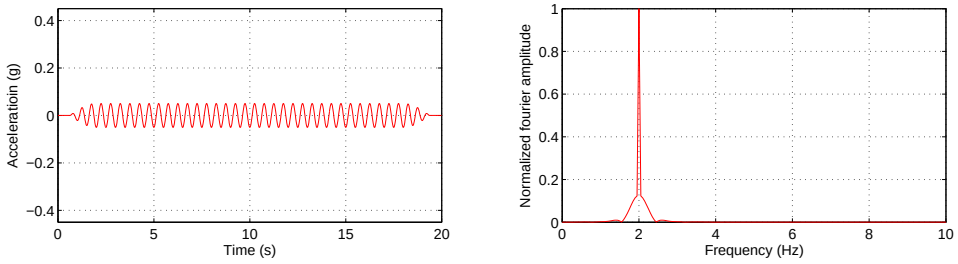

(a) (b)

Figure A.22: Time (a) and frequency (b) representation of sine input 2.0 Hz 2g earthquake

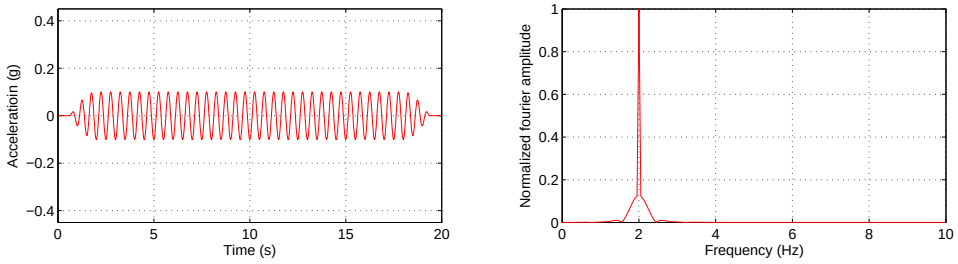

(a) (b)

Figure A.23: Time (a) and frequency (b) representation of sine input 2.0 Hz 4g earthquake

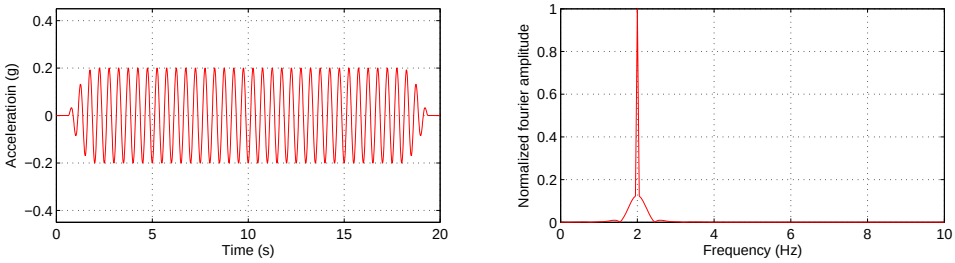

(a) (b)

Figure A.24: Time (a) and frequency (b) representation of sine input 2.0 Hz 8g earthquake

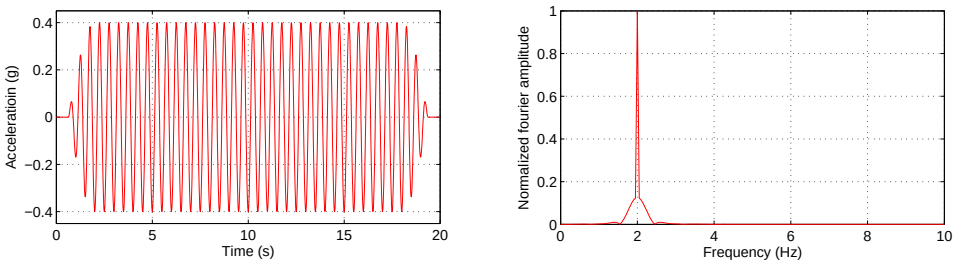

(a) (b)

Figure A.25: Time (a) and frequency (b) representation of sine input 80 Hz 16g earthquake

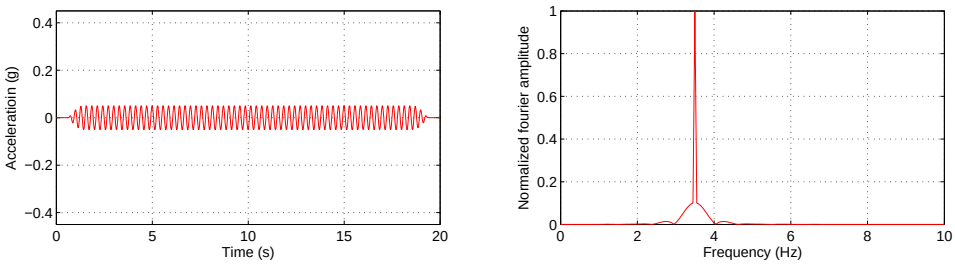

(a) (b)

Figure A.26: Time (a) and frequency (b) representation of sine input 3.5 Hz 2g earthquake

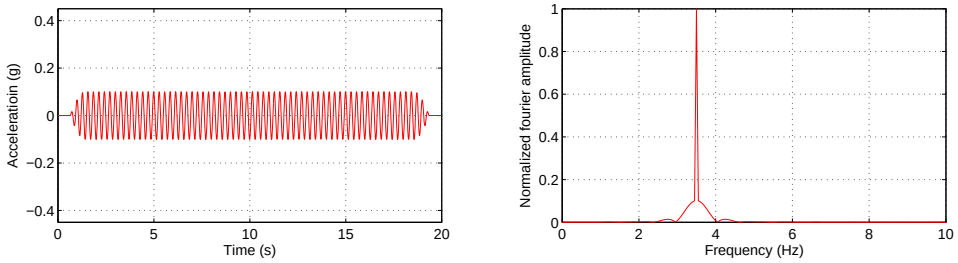

(a) (b)

Figure A.27: Time (a) and frequency (b) representation of sine input 3.5 Hz 4g earthquake

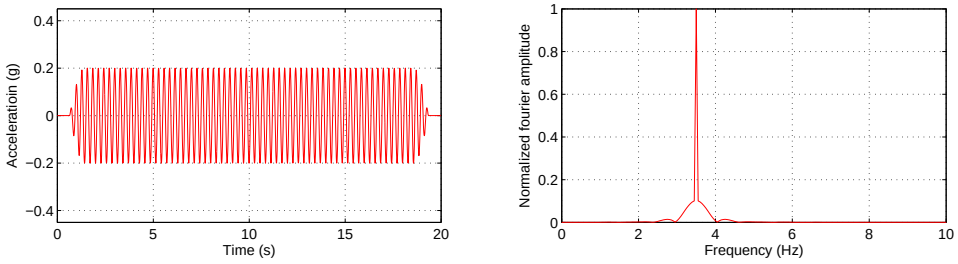

(a) (b)

Figure A.28: Time (a) and frequency (b) representation of sine input 3.5 Hz 8g earthquake

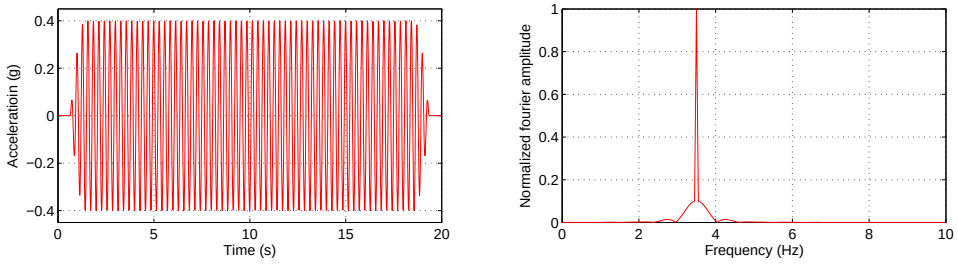

(a) (b)

Figure A.29: Time (a) and frequency (b) representation of sine input 3.5 Hz 16g earthquake

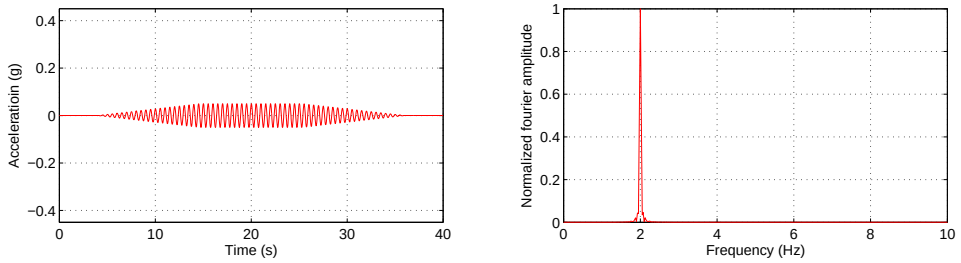

(a) (b)

Figure A.30: Time (a) and frequency (b) representation of sine input 2.0 Hz 2g with tapered parts

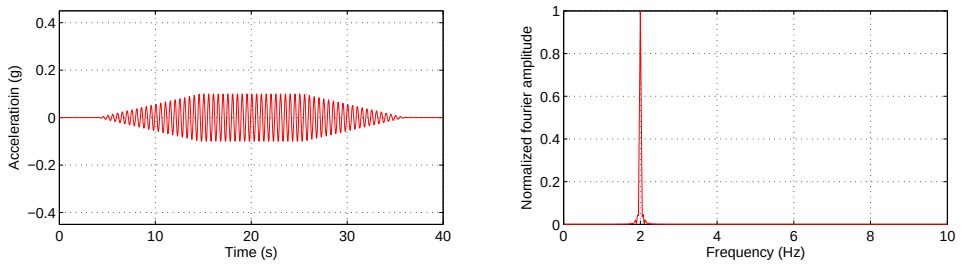

(a) (b)

Figure A.31: Time (a) and frequency (b) representation of sine input 2.0 Hz 4g with tapered parts

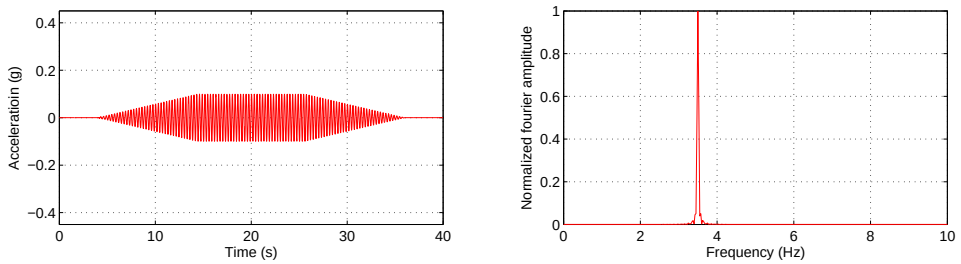

(a) (b)

Figure A.32: Time (a) and frequency (b) representation of sine input 3.5 Hz 4g with tapered parts

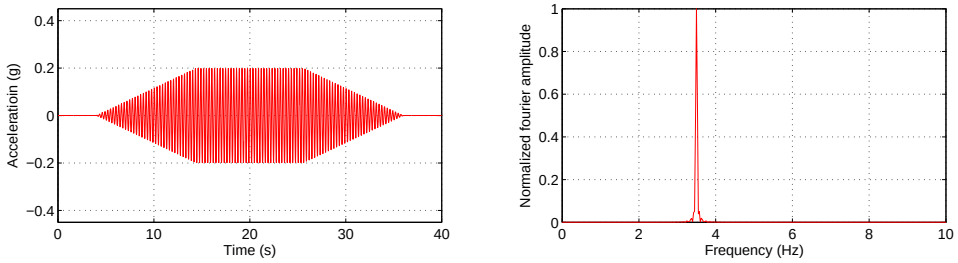

(a) (b)

Figure A.33: Time (a) and frequency (b) representation of sine input 3.5 Hz 8g with tapered parts

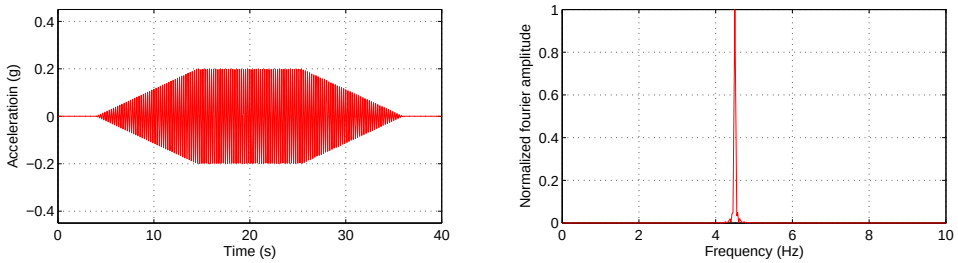

(a) (b)

Figure A.34: Time (a) and frequency (b) representation of sine input 180 Hz 8g with tapered parts

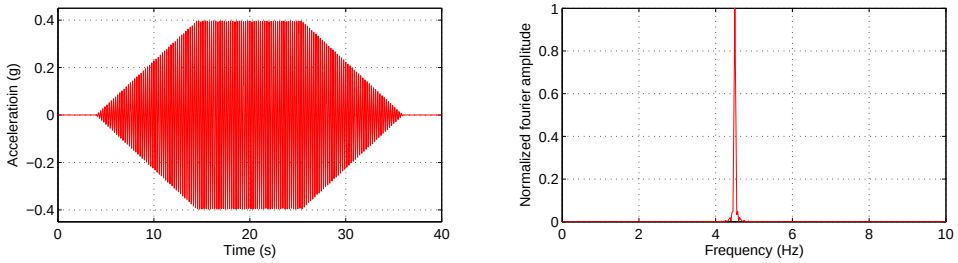

(a) (b)

Figure A.35: Time (a) and frequency (b) representation of sine input 180 Hz 16g with tapered parts

A.5 Super-structure design

A.5.1 Short building

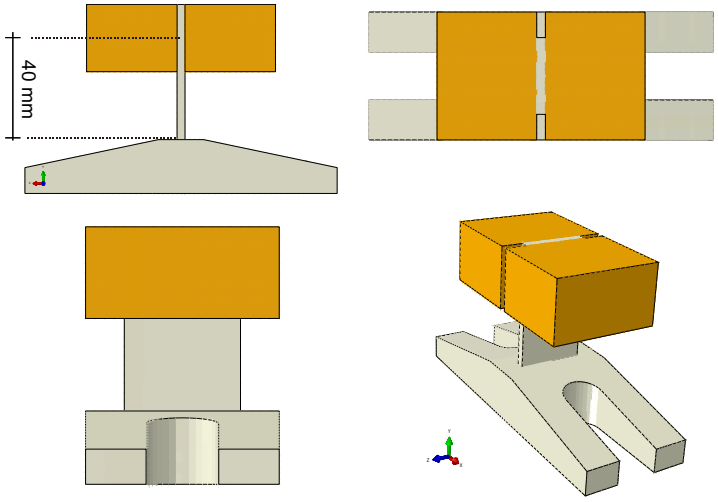

Figure A.36: Sketch drawing of short short building

	Top mass + 0.23×Web column	0.77×Web column + Base
Material	Brass	Aluminum
Weight	0.85 kg	0.056 (kg)
Total weight (model)	0.906 kg	
Height	40 mm	
Frequency	81.0 Hz	

Table A.3: Parameters of short buildingin model scale

A.5.2 Tall building

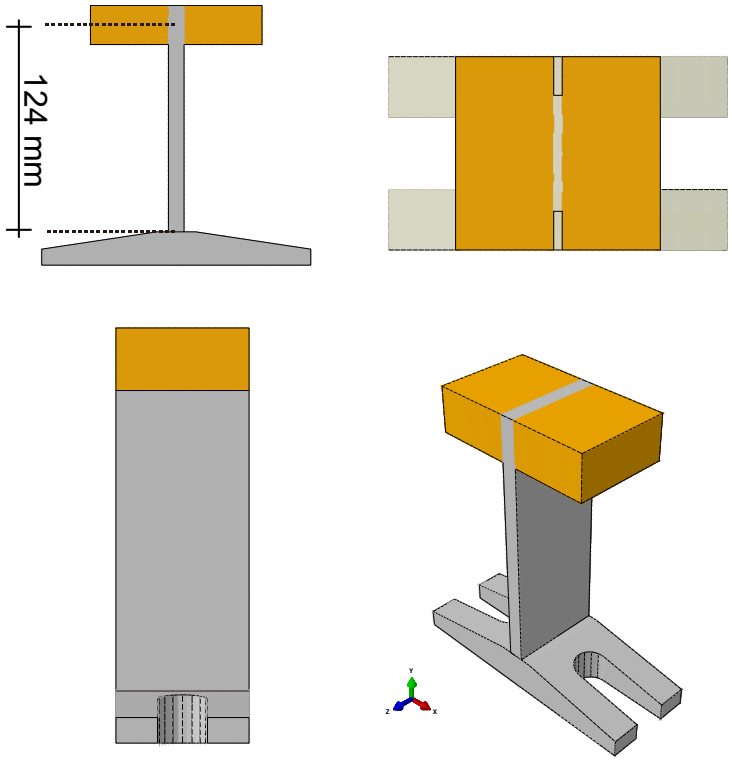

Figure A.37: Sketch drawing of tall building

	Top mass + 0.23×Web column	0.77×Web column + Base
Material	Brass	Aluminum
Weight	0.814 kg	0.223 kg
Total weight (model)	1.037 kg	
Height	124 mm	
Frequency	80.4 Hz	

Table A.4: Parameters of tall building in model scale

A.5.3 Taller building

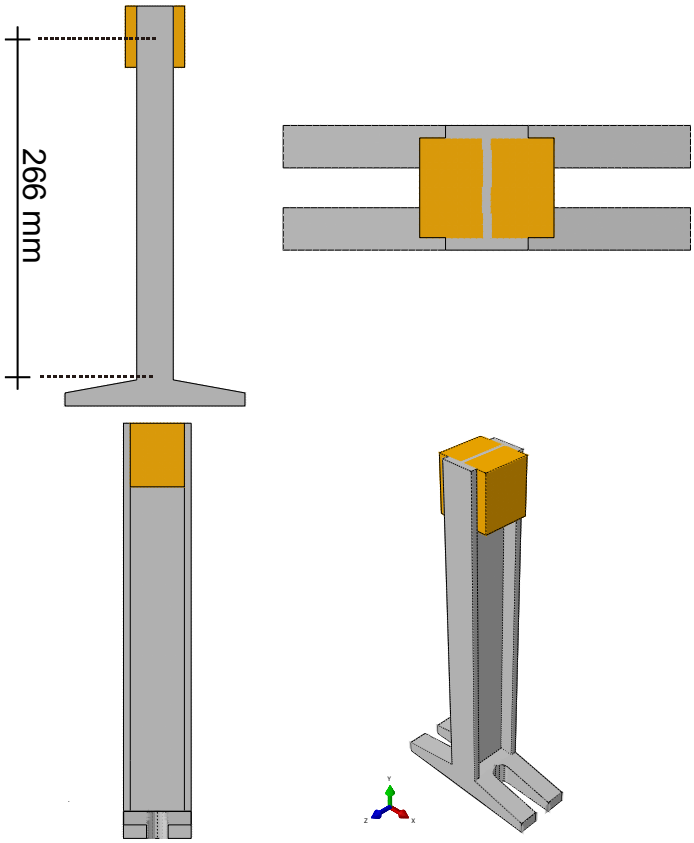

Figure A.38: Sketch drawing of taller building

	Top mass + 0.23×Web column	0.77×Web column + Base
Material	Brass	Aluminum
Weight	0.81 kg	0.387 kg
Total weight (model)	1.197 kg	
Height	248 mm	
Frequency	79.0 Hz	

Table A.5: Parameters of taller building in model scale

Appendix B

Soil column response

B.1 Soil column response under seismic and sinusoidal excitations

In the dynamic centrifuge tests, piles were embedded into the soil. With the exciting motions acted at the base, shear waves and the associated shear deformation of soil column were generated. The deformation of soil column is of great importance for the interactions between soil and piles. In this section, the responses of soil column in the dynamic centrifuge tests are analyzed and discussed.

B.1.1 Soil column responses in free-field tests, real earthquake excitations

The soil column response in the free-field test under real earthquake excitations are discussed at the beginning, since the free-field soil column response is selected as the reference with which the responses from other tests will be compared. The response of soil column in free-filed test is measured by sets of accelerometers in the center of container, see Fig. B.1.

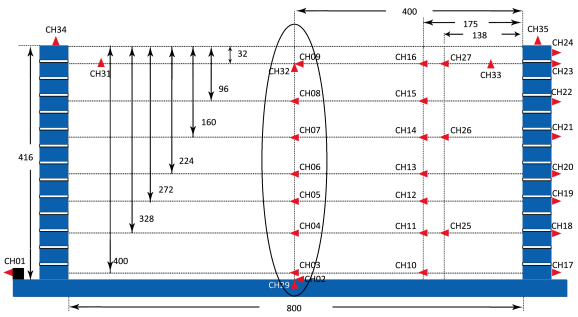

Figure B.1: Accelerometers in free-filed tests

According to the experimental program, several real-earthquake signals with different frequency contents and intensities were used in the free-field tests. The resonant frequency of soil column is identified by the first 6 small earthquakes that are Martinique Jara -1 dB (3 times) and Northridge -20 dB (3 times). The transfer functions that determined between the sensors at the soil surface and bottom are shown in Fig. B.2. By checking the peaks of the amplitude curve and the phase angle

of the transfer functions, the resonant frequency of the soil column is estimated to be 3.5∼3.7 Hz.

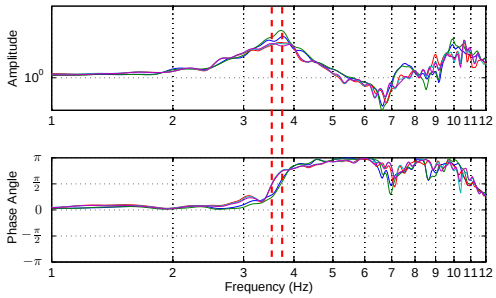

Figure B.2: Resonant frequency of soil column in free-field condition

Fig. B.3 shows the normalized maximum acceleration profile of soil column under different earthquakes. The normalization takes the reference with respect to the maximum acceleration measured acceleration at the bottom of the soil column. The referenced maximum measured accelerations at the bottom of the soil surface are listed in Table. B.1. The soil amplification phenomena could be observed by looking at the normalized acceleration profiles. For the first two small earthquakes, the responses of the soil surface are amplified by around 2.0 and 1.5 times. During the strong earthquake (Fig. B.3 (a) and (b)), with the significant nonlinearity of soil deformation, the amplification decreased. The response of the soil column in the middle depth is even smaller than the input motions, see in Fig. B.3(c) and (d). Finally, during the last two small earthquakes after the strong earthquake, the amplification of the soil column returns back. From the results, it can be seen that the surface motion of the soil could be amplified more in small earthquakes, the higher intensity of the earthquake does not mean a higher soil amplification.

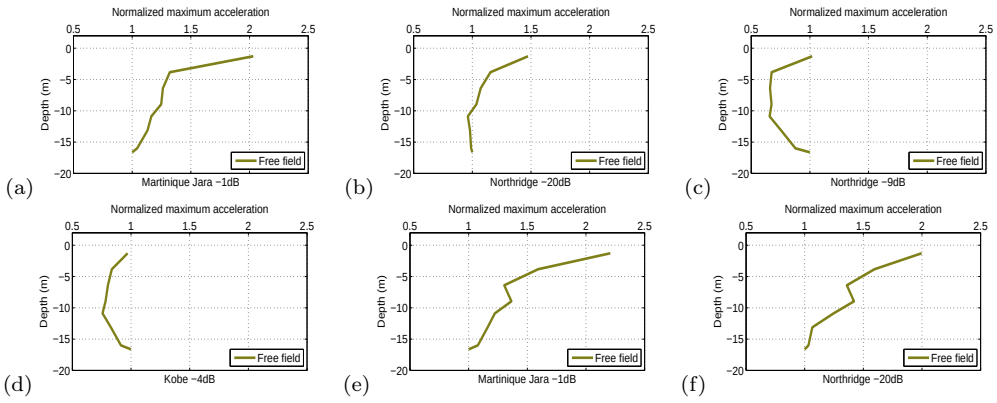

Figure B.3: Soil column response in terms of maximum acceleraion profile in free-field test

	Mj -1 dB	Nr -20 dB	Nr -9 dB	Kb -4 dB	Mj -1 dB	Nr -20 dB
Max. Acc_{base} (g)	0.12	0.19	0.65	0.48	0.13	0.18

Table B.1: Maximum peak accelerations measured of base shaking signal, in free-field tests

Following the same way, the response of soil column are continued to be investigated in the form of maximum displacement profiles. Fig. B.4 shows the normalized maximum displacement profiles of soil column under different earthquake motions. The calculation of displacement from measured accelerations used the double integration process that was introduced in the previous section. The referenced values of the maximum displacement at the bottom of the soil column are listed in Table. B.2. The displacements of the surface of soil column are around 1.4∼1.6 for Martinique Jara -1dB, Northridge -20 dB and Northridge -9 dB respectively. For Kobe -4 dB earthquake, the value is around 1.1.

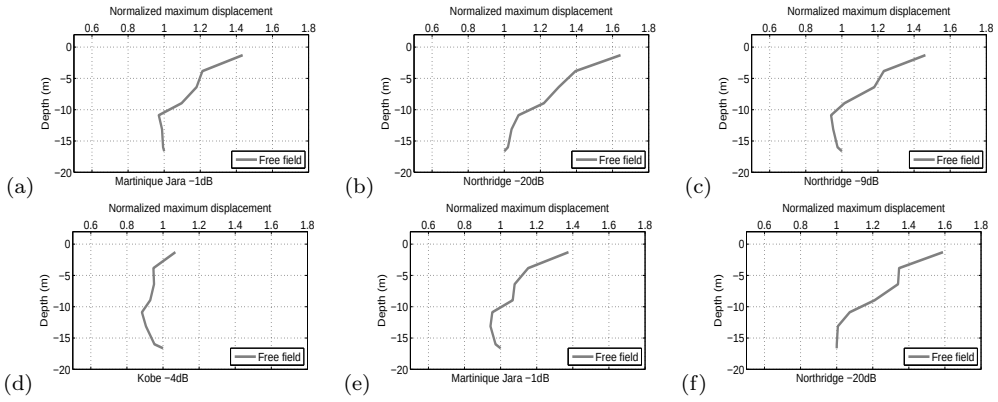

Figure B.4: Soil column response in terms of maximum displacement profile in free-field tests

	Mj -1 dB	Nr -20 dB	Nr -9 dB	Kb -4 dB	Mj -1 dB	Nr -20 dB
Max. $Disp_{base}$ (mm)	4.39	11.24	38.97	145.09	4.75	10.96

Table B.2: Maximum dispalcement of bottom of soil column, in free-field tests

B.1.2 Soil column response with foundations - real earthquake excitations

For the dynamic centrifuge tests of inclined and vertical pile groups. The response of soil column is followed by sets of accelerators that in the middle between piles and container boundary. The sets of accelerometers keep a large distance between the piles and the container boundary. An example is shown in Fig. B.5.

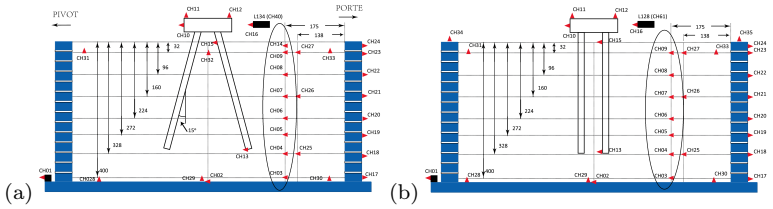

Figure B.5: (a) Accelerometers in test with Inclined pile foundation and with (b) vertical pile foundation

The response of soil column is evaluated by maximum acceleration profiles and compared with the response of the free-field test. The comparision is shown in Fig. B.6. It can be seen from the results that, the soil responses in terms of maximum acceleration profile of the tests with presence of piles are almost the same as that of the free-field test. The free-field response of soil column is not influenced by the presence of piles. When look at the comparison of maximum displacement profiles with the free-field test. Fig. B.7, the conclusions obtained from acceleration profiles are still valid.

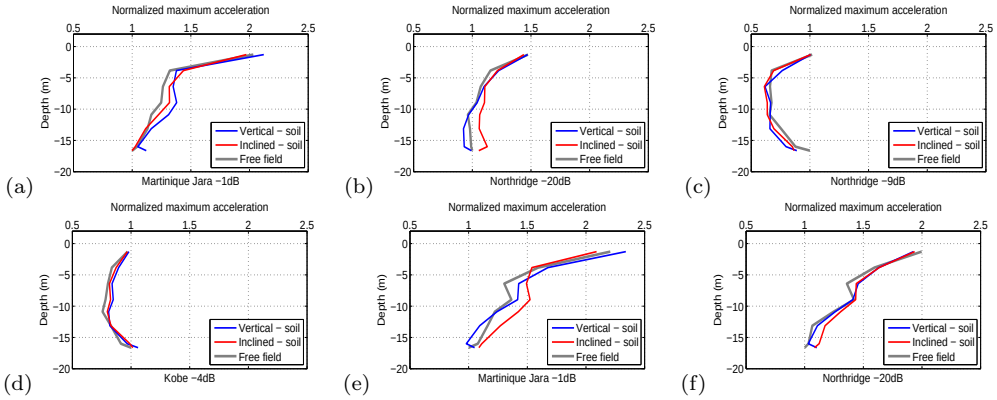

Figure B.6: Soil column response in terms of maximum acceleration profile in tests with presence of inclined and vertical pile group

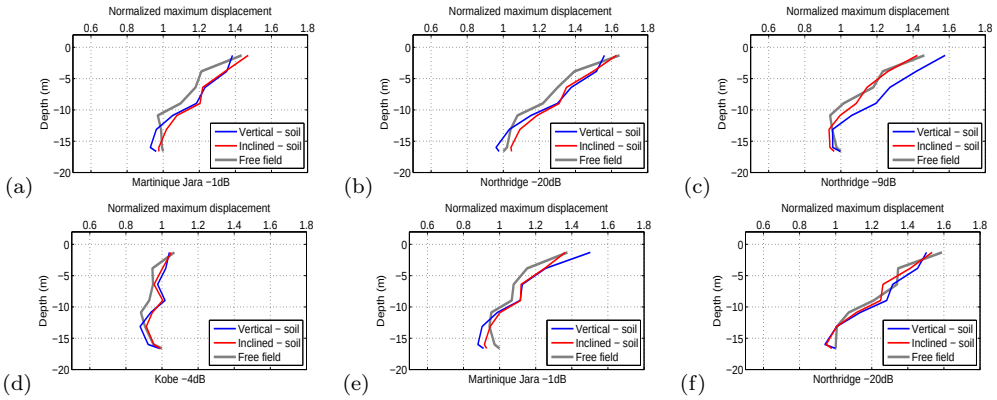

Figure B.7: Soil column response in terms of maximum displacement profile in test with presence of inclined and vertical pile group

The comparison of soil column response then is extended to other tests, where both piles and superstructures were presented. Fig. B.8 and Fig. B.9 show the comparison of maximum acceleration profiles and maximum displacement profiles respectively. Even with the presence of both piles (inclined or vertical) and superstructures (short or tall), the soil column (far enough from piles and boundary) behaved in the same way as the free-field tests.

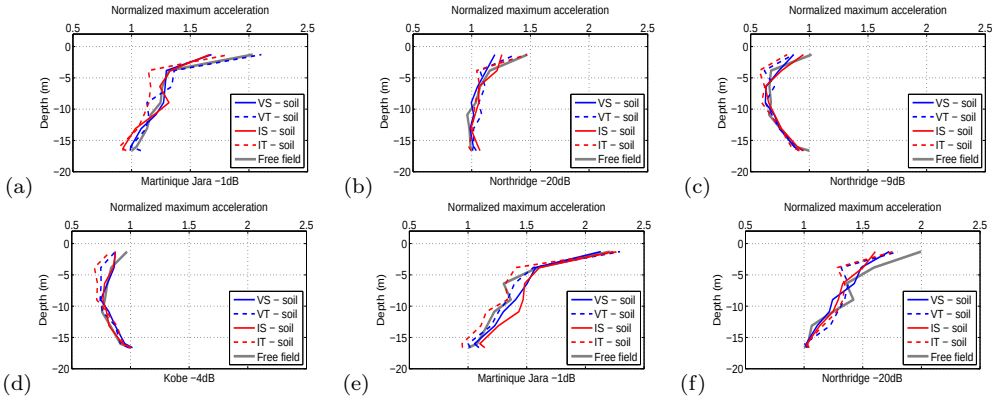

Figure B.8: Soil column response in terms of maximum acceleration profile in test with presence of pile group and superstructures

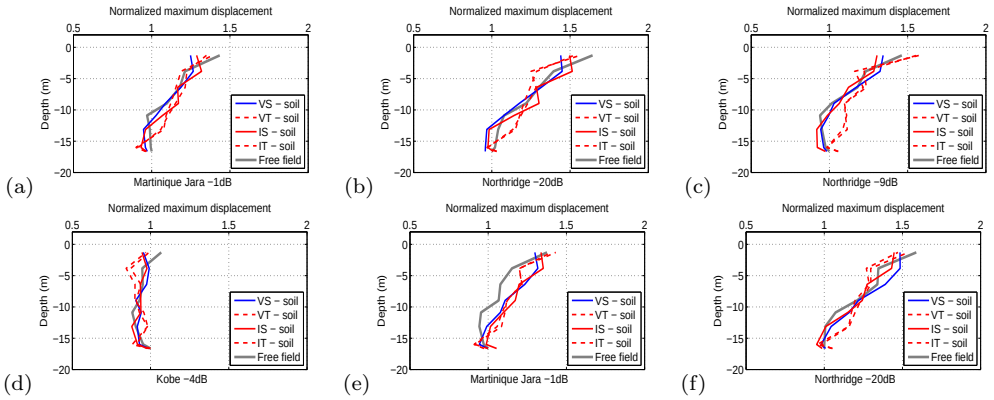

Figure B.9: Soil column response in terms of maximum displacement profile in test with presence of pile group and superstructures

B.1.3 Soil column response with foundations - sinusoidal input

For the tests using sinusoidal excitation signals, since there is no free-field test based on this kind of signal, so the response of the soil column in the tests with vertical pile group and short building was selected to be the reference. Figs. B.10 and B.11 show the response of soil column in the series of tests using 2.0 Hz sinusoidal signals. Both the acceleration and displacement profiles show good agreements and consistent variation trends. At low level of intensity input, 2.0 Hz 0.05 g (peak acceleration of input signal), the acceleration at soil surface was amplified by about 2.25∼2.4 times of the peak base acceleration, Fig. B.10 (a). With the increasing of input intensity, the amplification decreased. For strong input 2.0 Hz 0.4 g, the amplification is about 1.1 times. However, for the maximum displacement profiles, the surface displacement increases with the increasing of input intensity, see Fig. B.11.

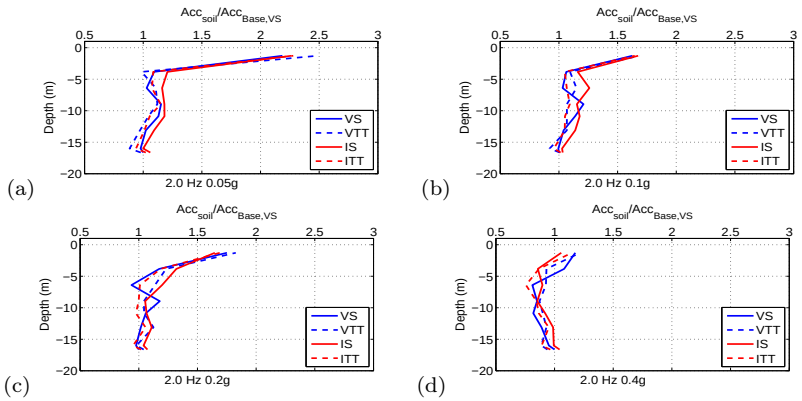

Figure B.10: Soil column response in terms of maximum acceleration profile in test with presence of pile group and superstructures

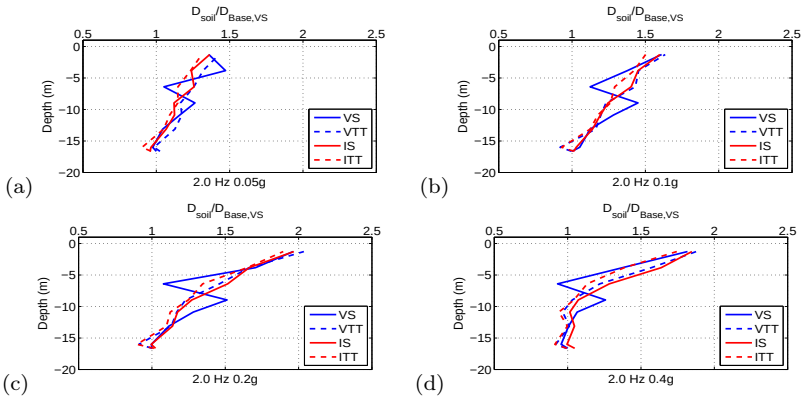

Figure B.11: Soil column response in terms of maximum acceleration profile in test with presence of pile group and superstructures

For the case of tests using sinusoidal signals at 3.5 Hz, the amplification of acceleration decreases with the increase of input intensity. For 3.5 Hz 0.05 g input, see in Fig. B.12 (a), the amplification is around 3.3 time of the base acceleration. For 3.5 Hz 0.05 g input, see in Fig. B.12 (d), the amplification decreased to 0.8. From the results of maximum displacement profiles in Fig. B.13, the decrease of amplification of soil with increase of input intensity could also be observed.

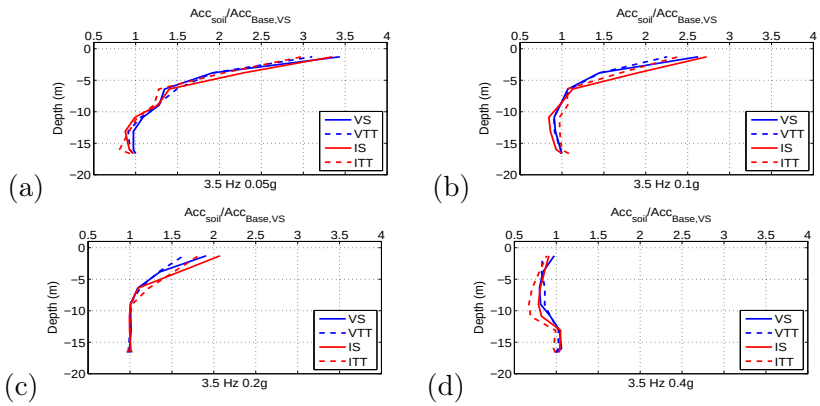

Figure B.12: Soil column response in terms of maximum acceleration profile in test with presence of pile group and superstructures

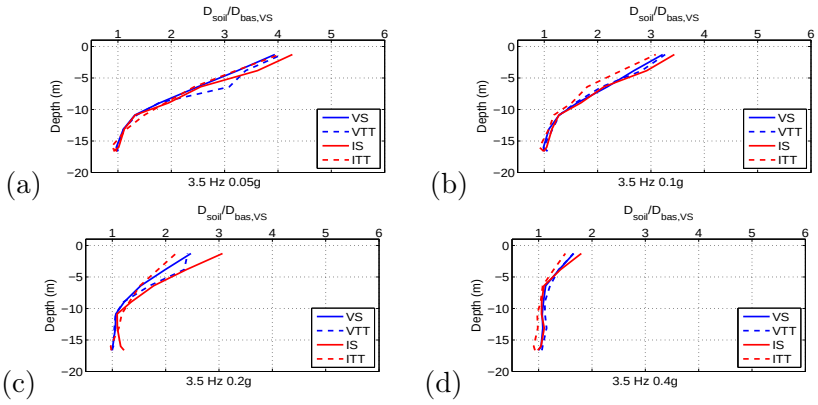

Figure B.13: Soil column response in terms of maximum acceleration profile in test with presence of pile group and superstructures

B.1.4 Summary

In this section, the soil responses in different tests were analyzed. For free-field test using real earthquake excitations, big amplification of acceleration at the soil surface occurred for small earthquakes. During strong earthquakes, the amplification decreased. For sinusoidal test, the amplification of acceleration decreased with the increasing of intensities of input signals. The far-field soil responses in other tests with the presence of piles and superstructures are consistent with the free-field tests, which ensures that for each test using different pile and superstructure configurations, they were subjected to the same soil actions.

Appendix C

Performance of inclined piles with seismic soil-pile-cap under seismic excitations

C.1 Seismic soil-pile-cap "kinematic interaction" under seismic excitations

Earthquake ground motion causes soil displacement known as free-field motion. However, the foundation embedded into the soil will not follow the free field motion. Due to the incompatibility of the stiffness between soil and piles, the interaction between the soil and piles is called as kinematic interaction. Eurocode8 part5 [22] emphasizes the importance of kinematic interaction:

"Piles and piers shall be designed to resist the Kinematic forces arising from the deformation of the surrounding soil due to the passage of seismic waves".

Field observations confirm the importance of the interaction between piles and the surrounding soils. During the Hyogoken-Nambu earthquake in Japan, it is found that even in the absence of super-structures, piles failed because of the deformation of the surrounding ground [66]. Many studies could be found addressing the kinematic interaction about vertical piles and vertical pile groups [143–147]. However, few studies have been carried out on the kinematic response of pile groups with inclined piles. Sadek and Shahrour [141] studied the behavior of micropiles under sinusoidal excitations numerically. it found that inclined micropiles have lower horizontal acceleration on on the pile cap, there were larger internal forces developed, however. Deng et al. [148] performed kinematic analysis for a large pile group containing inclined piles and found that kinematic loading can have a major impact on the magnitude of the maximum axial force that develops in the batter piles. On the experimental part, few studies have been carried out, the very recent studied can be referred to Tazoh et al. [14].

The basic assumption of kinematic interaction is that the pile and pile cap should be light enough to be regarded as weight-less. However, in practice, it is very difficult to meet the requirement of the idealized kinematic interaction, certain inertial effects from the pile cap can not be avoid. The kinematic interaction in the centrifuge tests may not be regarded as perfect in which, the inertial effect of the pile cap is included. To be more accurate, the "kinematic interaction" called in this dissertation should be more appropriate to be regarded as kind of soil-pile-cap interaction. Both of the

piles and pile caps are made from aluminum alloy, the material has high stiffness and very light self-weight. It is assumed that this kind of soil-pile-cap interaction is very close to the true kinematic interaction. Real earthquake input signals were used in the tests and are listed in Table. 4.6 in Chapter 4. The two configurations studied are the inclined pile group and vertical pile groups without superstructures on the pile caps.

C.1.1 Response of pile cap with soil-pile kinematic interaction

C.1.1.1 Frequency response of pile caps

According to the experimental program, the first 6 earthquakes (Martinique Jara -1 dB 3 times and Nothridge -20 dB 3 times) are small earthquakes with wide range of frequency contents, they were used to determine the responses of pile caps in frequency domain. The frequency representation is shown in Fig. 4.2 (a) and (b) in section. 4.1.2. It is assumed that under such small earthquakes, the responses of pile groups are approximately elastic. The responses of inclined and vertical pile groups are presented in terms of transfer functions between the accelerations measured on the pile caps and those measured near the soil surface. For example, see in Fig. C.1 (a) and (b), CH10 measures the acceleration of pile cap; CH09 measures the acceleration near the soil surface.

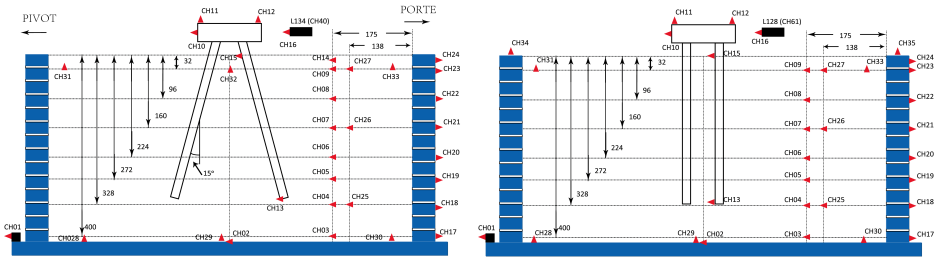

(a) (b)

Figure C.1: (a) Inclined pile foundation and (b) vertical pile foundation

Thanks to the presence of the high frequency components (frequency higher than 8.0 Hz) that are out of the range of input signals, the frequency response of inclined pile cap is estimated to be 10.6 Hz, see in Fig. C.2 (a). In the case of vertical pile group, the response of the translation rocking mode of the pile cap is estimated to be 6.0 Hz, see in Fig. C.2 (b). This frequency is within the frequency ranges of the two small earthquakes. The presence of the inclined piles increased the frequency response of the pile group, which indicates an increasing of the horizontal stiffness of the pile group.

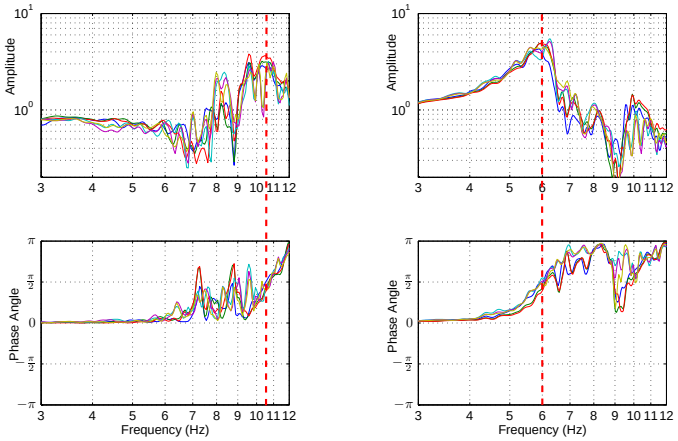

Figure C.2: Transfer functions between horizontal acceleration of the pile cap and horizontal acceleration near the soil surface (z = 1.28 m) under the first 6 small earthquakes: (a) inclined pile group and (b) vertical pile group

C.1.1.2 Responses of pile caps in terms of maximum displacement and rotation

The responses of pile cap under different earthquakes in terms of peak acceleration, maximum horizontal displacement and maximum rotation of pile cap are summarized in Figs. C.3, C.4 and C.5, respectively. All the results are normalized with respect to the responses of vertical pile group. The actual values are also summarized and listed on the top of the figure and the referenced value is marked in blue. For example, in Fig. C.3, in the case of first Martinique Jara -1 dB earthquake (Mj-1dB), the maximum acceleration of pile cap for vertical pile group is 0.26 g which is the referenced value in the current earthquake event. The response of inclined pile group in terms of peak acceleration in the current earthquake event is 0.25 g. After the normalization with respect to the referenced value, the ratio 0.99 is obtained and plotted on the top of the red bar. In this dissertation, this kind of bar plot figures are often used in comparing responses between different configurations. In this way, the readers can have not only the information about the ratios but also the actual values.

In terms of peak accelerations at pile cap, see in Fig. C.3, for small earthquake, Mj -1 dB and Nr -20 dB (group 1, group 2, group 5 and group 6), inclined piles have very limited effect in reducing the peak accelerations. However, during strong earthquakes, Nr -9 dB and Kb -4 dB (group 3 and group 4), inclined piles greatly reduce the peak accelerations, especially for the Nr -9 dB earthquake, the reduction is around 40%.

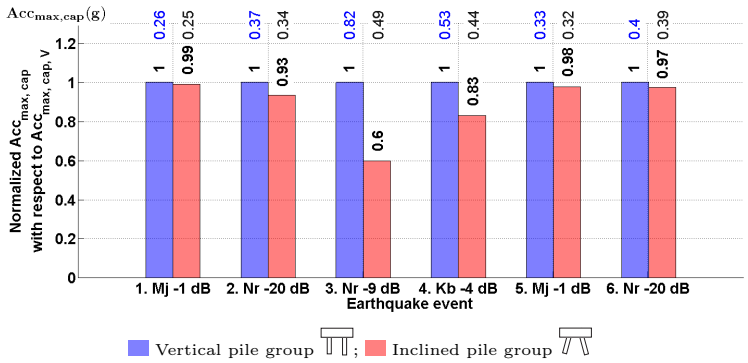

Figure C.3: Normalized peak acceleration of pile cap with respect to vertical pile group under real earthquake excitations

Fig. C.4 shows the normalized displacement at pile caps. the response of inclined pile group in terms of maximum displacement is around 80% of the vertical pile group, except the strong earthquake Kobe -4 dB, the response of the inclined pile group is almost the same as the vertical one, the difference is about 5%. This agrees with the conclusions from Giannakou [9] that for inclined angles between 5° and 15°, which are most commonly used in practice, the response of the foundation in terms of displacement is almost the same as that of the vertical pile group; a significant reduction in the peak acceleration at the pile cap for fixed pile-to-cap connection could be observed.

In addition, according to the normalized rotation of pile cap shown in Fig. C.5, inclined piles induce higher rotation at pile cap. For small earthquakes Mj -1 dB, Nr -20 dB (group 1, group 2, group 5 and group 6), inclined piles results about 1.5∼2.0 times higher cap rotation. However, the effect of inclined piles is reduced in strong earthquakes that during earthquake Kb -4 dB (group 4), pile cap connected with inclined piles has even less rotations.

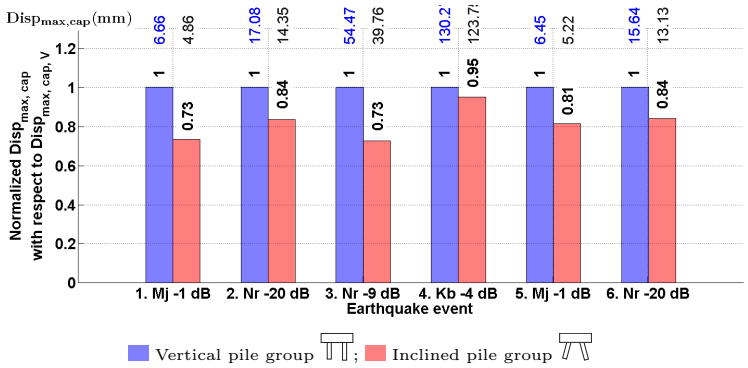

Figure C.4: Normalized maximum displacement of pile cap with respect to vertical pile group under real earthquake excitations

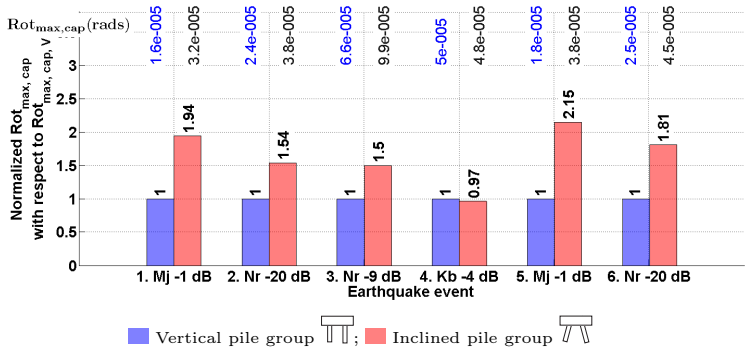

Figure C.5: Normalized maximum rotation of pile cap with respect to vertical pile group under real earthquake excitations

C.1.2 Stresses in piles with soil-pile-cap interaction

In this dissertation, the pile stresses refer to the section forces in pile, such as bending moment, shear force and axial force distributed a along the pile. The decomposition of the total bending moment into residual bending moment and dynamic bending moment was introduced in the previous section, see in section. 4.2.1. The same rule can be also applied to shear force in pile. In this section the bending moment (or shear force) was first decomposed into residual and dynamic parts, and analyzed individually to highlight their own roles in the pile performance. Then the two parts were considered together as the total resultant bending moment (or shear force) to evaluate pile performance under dynamic excitations. For axial force in pile, there was no important residual effect had been observed in the experiments, the analysis of axial force is directly based on the final total axial force.

C.1.2.1 Residual, dynamic and total bending moment in piles

The response of the pile groups in terms of residual bending moment is shown in Fig. C.6, it can be seen from the results that inclined piles induce significant residual bending moment than that of the vertical pile group. The inclined pile group is very sensitive to the dynamic excitations, even very small earthquake with low intensity can induce high residual bending moment in the inclined piles. Fig. C.6 (a) shows the residual bending moments from the first three small Martinique Jara -1 dB earthquake inputs. During the first three small earthquakes, there was almost no residual bending moment developed in the vertical pile group, however, relatively large residual bending moment was found in the inclined piles. That is why such big difference appeared at the beginning of the test with small earthquake input signals. The inclined pile group have about 12.5 times higher residual bending moment than that of the vertical one. With the increasing of the input intensity, the residual bending moment developed gradually in the vertical pile group and the ratio of the residual bending moment between the inclined and vertical pile group tends to be mobilized. After the strong earthquake Nothridge -9 dB and Kobe -4

dB earthquakes, the residual bending moment in the inclined piles were found to be around 4.0 times higher than that of the vertical pile group.

A *'C'* shape liked profile of the residual bending moment was found for the inclined pile group , while a *'S'* shape liked profile was found for the vertical pile group. For the inclined pile group, the peak value of the residual bending moment is located at the depth of $7.5D$ in depth, for the vertical pile group, there are two apparent peaks can be found the locations are about $5D$ and $15D$ in depth.

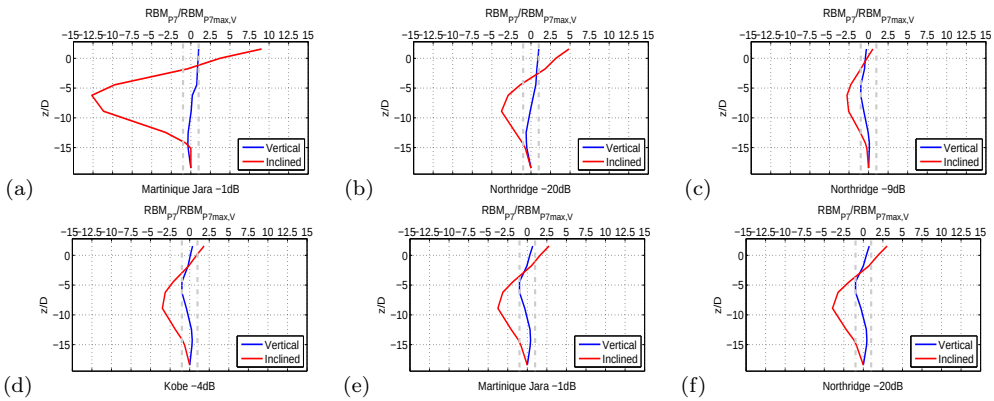

Figure C.6: Normalized residual bending moment, under real earthquake excitations

Fig. C.7 shows the ratio of the maximum residual bending moment between inclined pile group and vertical pile group. It could be regarded as another way to intemperate the results shown in Fig. C.6, only the peak values of the residual bending moment profiles and their ratios are considered. The ratio shown in Fig. C.7 for the first Mj -1 dB does not mean a high residual bending moment, the actual value is 4.52 kN·m×12.66 = 57.2 kN·m. The maximum residual bending moment for both inclined and vertical pile appeared in Nr -9 dB earthquake, they are 307.40 kN·m and 111.38 kN·m respectively. For another strong earthquake, Kobe -4 dB earthquake, big residual bending moments for both inclined and vertical pile are also observed but not as higher as those in Nr -9 dB. This may due to the frequency contents for Northridge earthquake has energy around 3.5 Hz (the resonant frequency of soil column), soil column was extensively excited, the soil-pile-cap interaction is more pronounced; while the frequency contents for Kobe earthquake is in the low frequency range, the soil column can be excited as much as the Northridg earthquake. The residual bending moment for both inclined and vertical pile increased and mobilized after the strong earthquake. Inclined piles induce higher residual bending moment for all the earthquakes (all intensities and all frequency contents).

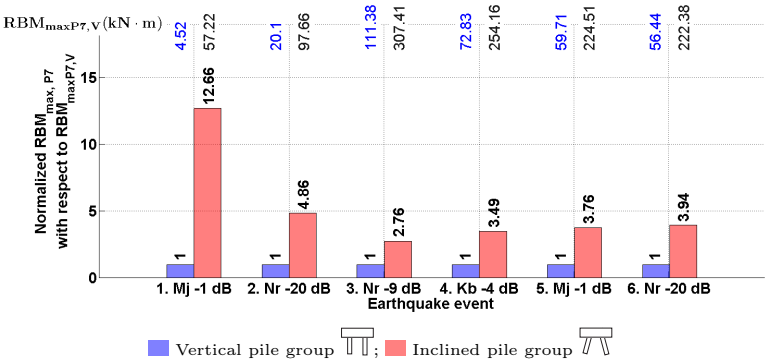

Figure C.7: Normalized maximum residual bending moment of inclined pile group and vertical pile group under seismic excitations

As it was mentioned before, the total response of piles in terms of bending moment can be decomposed into residual bending moment and dynamic bending moment, the summation of the two parts gives the total final response. The dynamic bending moment is obtained by removing the effect of residual bending moment from the previous tests and the accumulation of residual bending moment during the earthquake is also removed. The results of dynamic bending moment of inclined and vertical pile group are shown in Figs. C.8 and C.9.

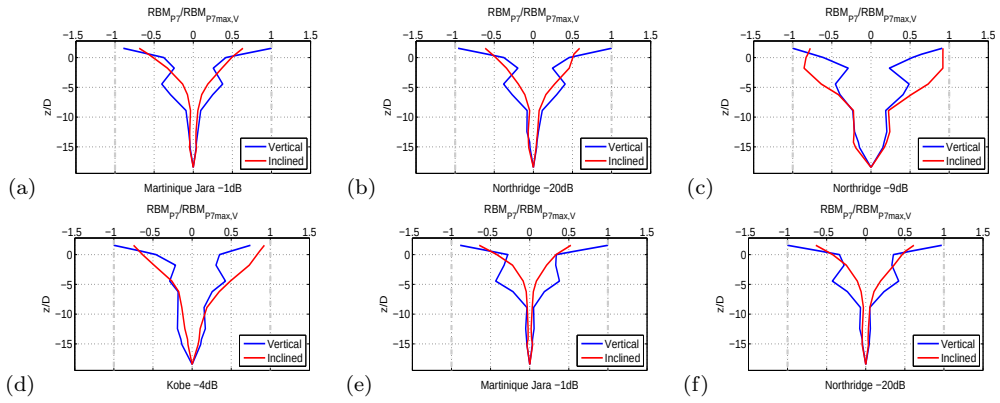

Figure C.8: Normalized dynamic bending moment, under real earthquake excitations

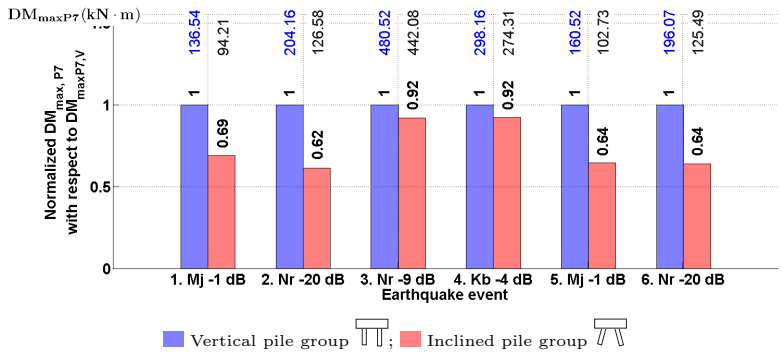

Figure C.9: Normalized maximum dynamic moment of inclined pile group and vertical pile group under seismic excitations

In terms of dynamic bending moment, the results are quite positive for the performance of inclined pile group, because the envelop curves of inclined pile group under all the earthquake events are smaller than the vertical group. The bending moment profile for inclined pile group are totally different for that of the vertical one. The peak values of of both the inclined pile group and vertical group always locate at the pile cap, although there are small peaks could be found under soil surface for the vertical pile group (about $5D$ in depth, see in Fig. C.8). However, for the correct evaluation of the performance of inclined pile group, it is of the first importance to take into account the residual bending moments induced by previous events and the accumulation effects, according to the study of Escoffier in 2012 [47]. The correct interpenetration of the bending moment of inclined and vertical pile group relay on the total bending moment which the evolution of the residual bending moment has to be included.

The response of the pile groups in terms of total resultant residual bending moment is shown in Fig. C.10. It can be seen from the results that for the smaller earthquakes at the beginning i.e. 3 times Maratinique Jara -1dB and Northridge -20 dB earthquakes, see in Fig. C.10 (a) and (b). Although significant residual bending moments developed in the inclined piles, the overall resultant total bending moment of inclined piles are smaller than that of the vertical pile group. For big earthquakes Fig. C.10 (c) and (d), the larger bending moment can be found both on the pile head and below the soil surface. The bending moment on the pile head is about 1.25 times higher than the vertical pile group and the bending moment developed below soil surface is about 2 times higher than the vertical one. The maximum bending moment is always found at the pile cap for the vertical pile group; for the inclined pile group, besides the big value found at the pile cap, the bending moment below the soil surface, around $8D$ in depth is found to be also significant. Compared with the results of the dynamic bending moment, the peak value below soil surface is largely underestimated, which gives wrong evaluation of the performance of inclined pile foundation.

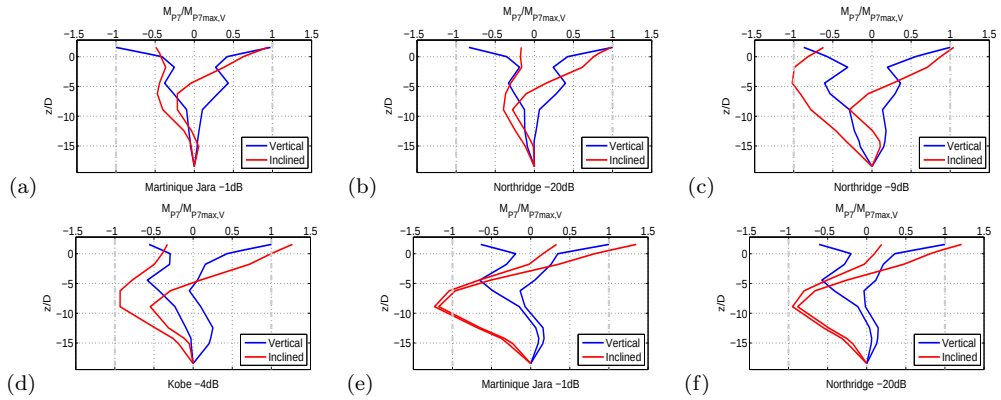

Figure C.10: Normalized total bending moment, under real earthquake excitations

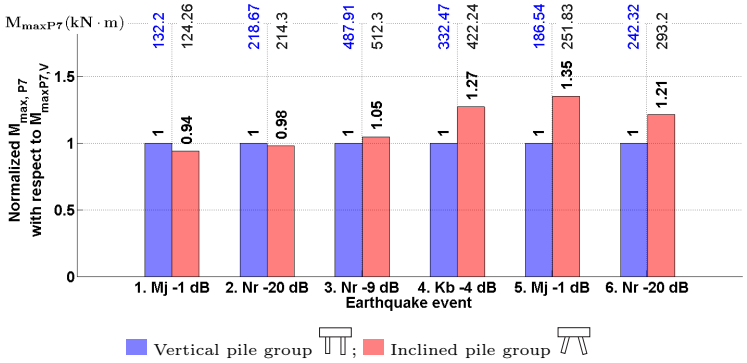

Figure C.11: Normalized maximum total bending moment of inclined pile group and vertical pile group under seismic excitations

C.1.2.2 Shear force in piles

Figs. C.12 and C.13 show the results for the comparison of total shear force. As it can be seen from the results, although high residual shear stress was developed in the inclined piles, the dynamic shear stress remedied the poor performance of inclined pile in terms of shear force. The total shear stress for inclined pile in found to be smaller than that of the vertical pile. In the case of strong earthquake with important soil-pile interaction, Nr -9 dB earthquake, the shear stress is approximate the same as the vertical pile, which is just 4% less. For the other earthquakes, the it is more evident that inclined pile induces less shear force.

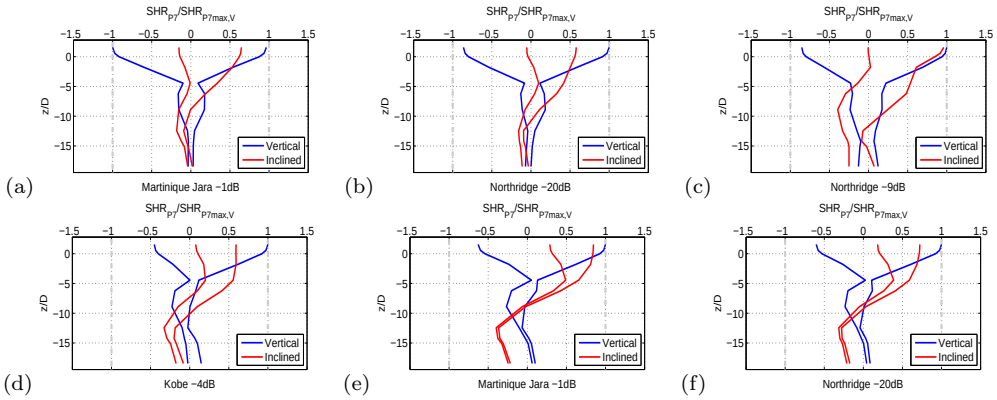

Figure C.12: Normalized total shear stress, under seismic excitation

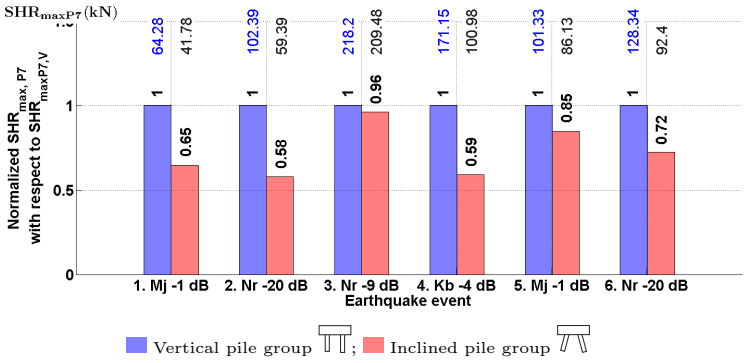

Figure C.13: Normalized maximum total shear stress with respect to vertical pile under seismic excitations

C.1.2.3 Axial force in piles

For the axial force in the piles, since no significant accumulation of residual effects were observed during the test, only the results of total resultant axial force will be discussed hereafter. Fig. C.14 shows the normalized axial force with respect to the pile in vertical pile group. Firstly, it can be seen from the results that the response of inclined pile group in terms of axial force is detrimental. From small intensity earthquake input up to high intensity earthquake input, for all the cases, larger axial force was developed in the inclined pile group. The axial forces at the inclined piles are found to be 1.2 $\sim$ 1.5 times higher than that of the vertical pile group. Secondly, the inclination of 15° does not change the axial force distribution profile, for a friction pile group (or floating pile group), the axial force decreases with the increasing of pile embedded depth.

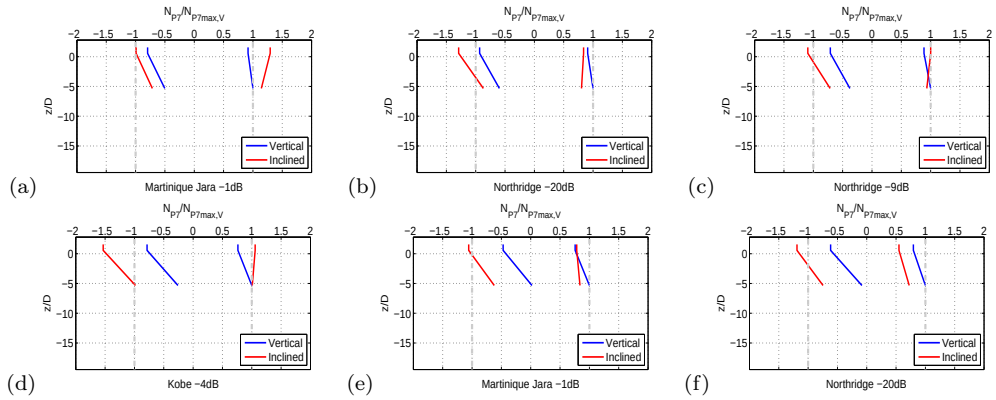

Figure C.14: Normalized total axial force, under seismic excitations

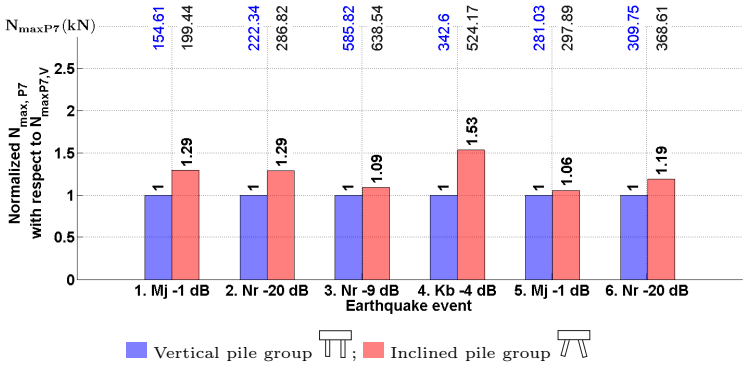

Figure C.15: Normalized maximum total axial force with respect to vertical pile under seismic excitations

C.1.3 Summary

In this section, the responses of inclined and vertical pile group are discussed. The performance of the inclined pile group is evaluated according to the residual bending moment, dynamic bending moment, total bending moment and axial force. The conclusions are following:

1. Due to the constrains of physical modeling, the response of the inclined pile group was studied. The soil-pile-cap "kinematic" response of battered piles tends to confirm their detrimental effects. The conclusions obtained in this section are consistent with that from the study from Giannakou et al. [9, 27].

2. The inclined piles are very sensitive to the soil movement so as to induce largely higher residual bending moment. The residual bending moment profiles are totally different for the inclined and vertical pile group. The effects of the residual bending moment must not be ignored.

3. The results of the total bending moment also indicate the negative performance

of inclined pile group. The total bending moment profile of inclined pile group are different from that of the vertical pile group.

4. Inclined piles exhibit larger axial forces than vertical piles.

5. The rotation of the inclined pile group is found to be higher than the vertical pile group.

6. However, positive aspects of inclined piles can be found that the lateral displacement and peak acceleration of inclined pile group are smaller than that of the vertical pile group. The inclined piles induce less shear force than the vertical pile.

7. The frequency analysis indicates higher horizontal stiffness of the inclined pile group.

Appendix D

Discussion about the influence of superstructures on the responses of pile groups

It has been observed in the experiments that the presence of superstructure does influence the response of both inclined and vertical piles significantly. According to the experimental results, the presence of the superstructure does improved the performance of inclined pile groups. The presence of superstructure saves the poor performance of inclined piles in the pure soil-pile-cap interaction (Appendix C). In this section, the influence of the superstructures will be discussed with more details. The responses of piles under seismic soil-pile-superstructure interaction will be studied by comparing the responses under seismic soil-pile-superstructure interaction with those under soil-pile-cap interaction conditions.

For vertical pile configuration, the cross comparisons were carried out between vertical pile group (V), vertical pile group with short building (VS) and vertical pile group with slender building (VT) by taking the vertical pile group without building (V) as the referenced configuration.

For inclined pile configuration, the cross comparisons were carried out between inclined pile group (I), inclined pile group with short building (IS) and inclined pile group with slender building (IT) by taking the vertical pile group without building (I) as the referenced configuration.

D.0.4 Influence of superstructure on responses of vertical piles

Fig. D.1 shows the comparison of residual bending moments of configuration of V, VS and VT with respect to vertical pile group (V). It can be seen from the results that will the presence of superstructures, residual bending moment has been easily developed in vertical piles, even during small earthquakes, Fig D.1 (a) and (b). It is difficult to describe the shapes of the profiles in the first two small earthquaks, however, the profiles of residual bending moment manifest "S" shapes, after strong earthquakes. The maximum value on the profiles for vertical pile group and vertical pile group with slender building are close to each other, about $5D$ below the soil surface. For vertical pile group with short building, the depth of the maximum value increases to around $7.5D$.

Fig. D.2 shows the ratios of the maximum residual bending moment along piles between different configurations. The presence of short building induces larger resid-

ual bending moment during all the earthquakes, except the earthquake Nr -9 dB. In earthquake Nr -9 dB, the residual bending moment is just a little bit lower than the vertical pile configuration without building. In the case of slender building, in the first two small earthquakes, Mj -1 dB and Nr -20 dB, slender building induces higher values, however, during and after strong earthquakes, slender building reduces the residual bending moment. It also could be observed that compared with the short building, slender building always induces less residual bending moment in piles.

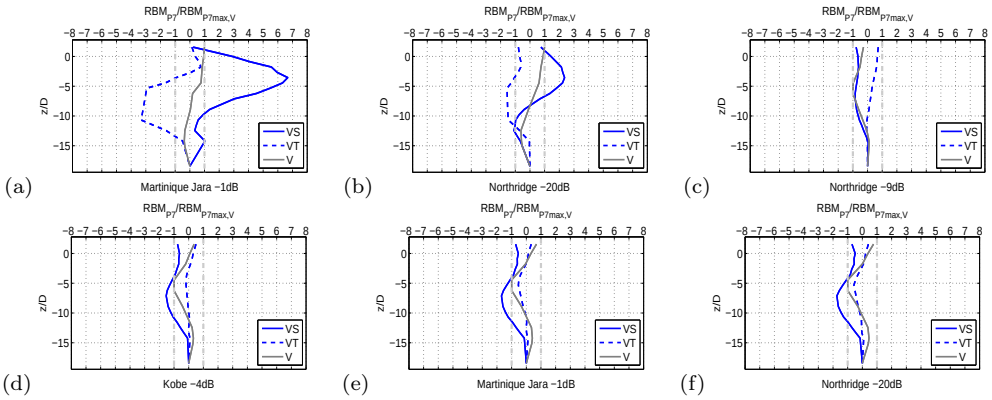

Figure D.1: Normalized residual bending moment, under real earthquakes excitations

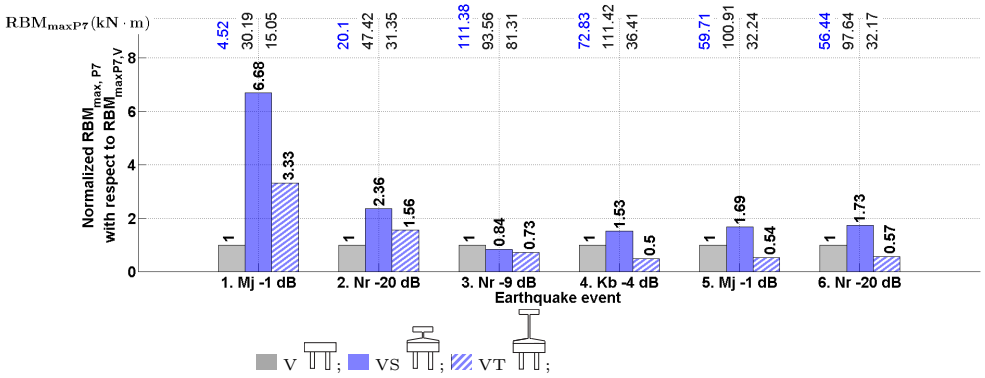

Figure D.2: Normalized maximum residual bending moment, under real earthquake excitations

In the aspect of dynamic bending moment, the normalized profiles are shown in Fig. D.4. As it can be expected that the presence of the superstructures increases the dynamic bending moment both below the soil surface and at pile heads. However, the superstructure does not change the shape of the dynamic bending profiles, the peaks below the soil surface are more pronounced. The dynamic bending moment profiles for all the configurations below the depth $10D$ are almost the same regardless the presence of the superstructures.

The ratios between different configurations are shown in Fig. D.4. It is clear

that superstructures induce higher dynamic bending moments in piles. For short building the increase is around 1.∼2.5 times for all the earthquakes; for slender building is around 1.0∼1.5 times. One can see that short building induces more dynamic bending moment.

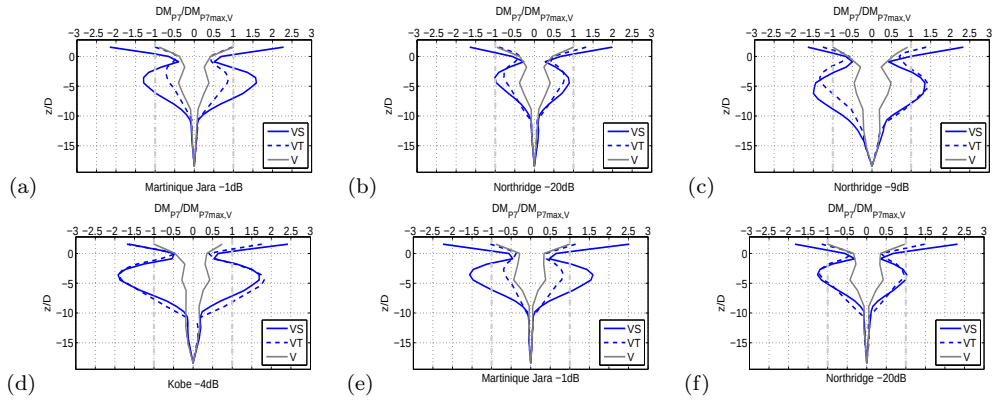

Figure D.3: Normalized dynamic bending moment, under real earthquake excitations

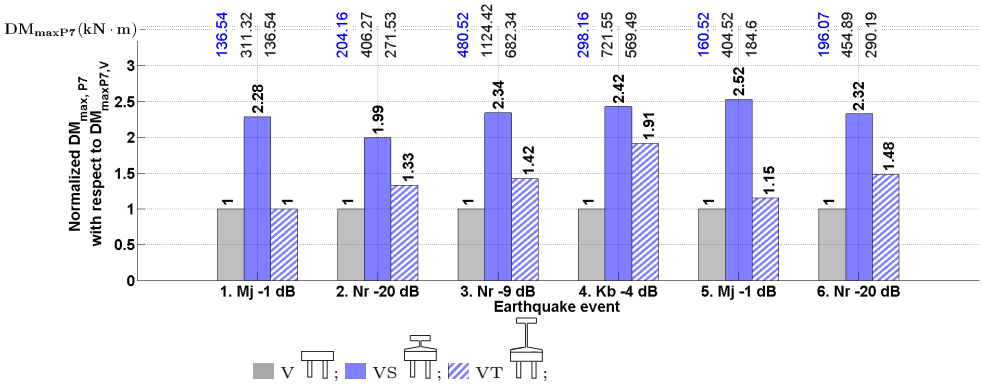

Figure D.4: Normalized maximum dynamic bending moment of of configurations V, VS, and VT with respect to V, under real earthquake excitations

Results for the normalized total bending moment profiles are shown in Fig D.5. The presence of superstructures play role in increasing the magnitude of the bending moment profiles for vertical pile group without building; however, the shape of the profiles are kept.

According to the ratios listed in Fig. D.6, regardless the intensities of exciting earthquakes, short superstructure on vertical pile group induces an average of 2.0 times higher bending moment in piles. For slender building, the increase is about 1.3 times. However, the influence of the gravity center to the responses piles is reduced in strong earthquakes, Nr -9 dB and Kb -4 dB, with the highly developed nonlinearity in soil. For example, in the earthquake Kb -4 dB, the ratios of the vertical pile foundation with short and slender building to the referenced vertical

pile group are 2.18 and 1.91, respectively.

The comparisons of the configuration of VS and VT with the referenced configuration V are based on the assumption that the weight of superstructure did not induce differences in the initial bending moment in vertical piles. So the equal zero initial stress states in terms of bending moment were assumed for all the pile configurations. However, regarding the axial forces, the configurations of V, VS and VT are not comparable, due to their different initial state induced by the superstructure. Naturally, adding more mass results higher axial forces in piles. Due to the differences of the initial axial force state, the comparison on the axial forces are not considered among the configurations, V, VS, and VT.

As it was introduced before, shear stresses are linked with the bending moments in piles, similar conclusions can also obtained for comparison of shear forces, which will not be repeated in this section.

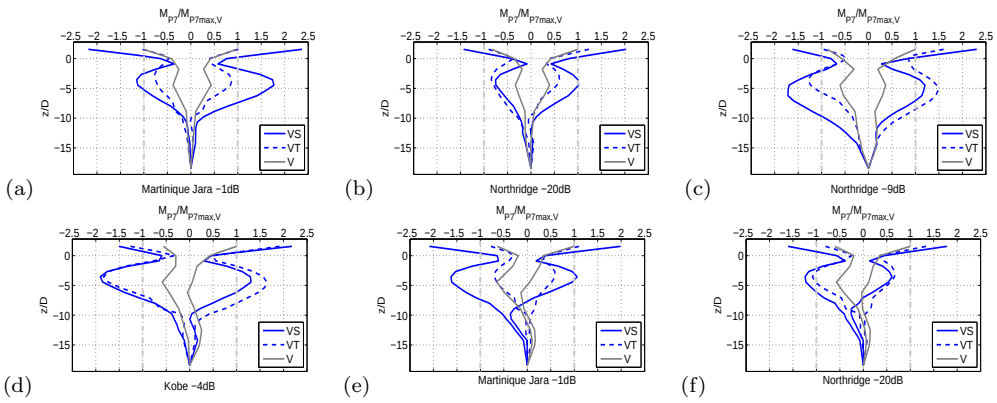

Figure D.5: Normalized total bending moment, under real earthquake excitations

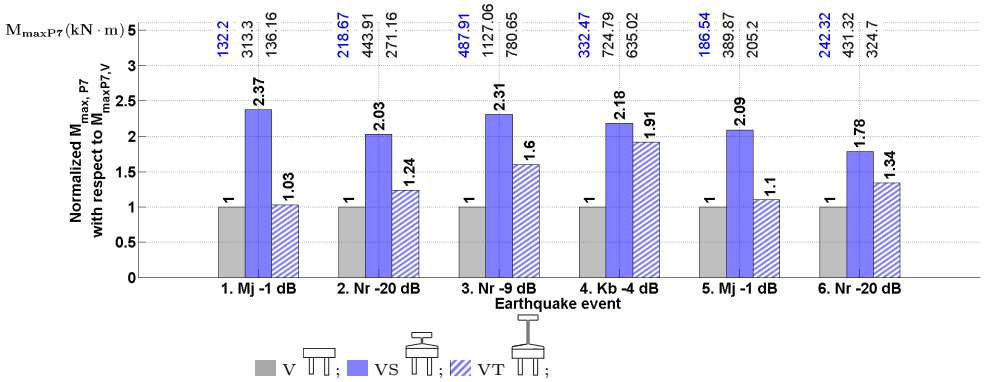

Figure D.6: Normalized maximum total bending moment, under real earthquake excitation

D.0.5 Influence of superstructure on response of inclined piles

Following the same procedures, the influence of superstructures on the responses of inclined piles are investigate by the cross comparison between the configurations inclined pile group (I), inclined pile group with short building (IS) and inclined pile group with slender building (IT). The referenced configuration is inclined pile group without superstructure (I).

Fig. D.7 shows the maximum residual bending moment profiles of different inclined pile configurations. Regardless the presence of the type of superstructures, a apparent "'C" shape could be found for all the configurations. The peak values below soil surface appear at the depth $7.5D$ for configuration I and IS. For inclined pile group with slender building, the depth is about $10D$.

The ratios of the peak values along the profiles between different configurations are shown in Fig D.8. The presence of superstructures reduce the residual bending moment in piles that formed in the soil-pile kinematic interaction. Except inclined pile group with slender building under earthquake Mj -1 dB and Nr -20 dB, the residual bending moment is a little higher, but the values are close that could be regarded as the same.

The higher gravity center of the superstructure could reduces the residual bending moment further in small earthquake Mj -1dB and strong earthquakes Nr -9 dB. In the earthquake kb -4 dB earthquake, short building and slender building have the same effect on the residual bending moment. For the other earthquakes, the presence of tall superstructure increase the residual bending moment.

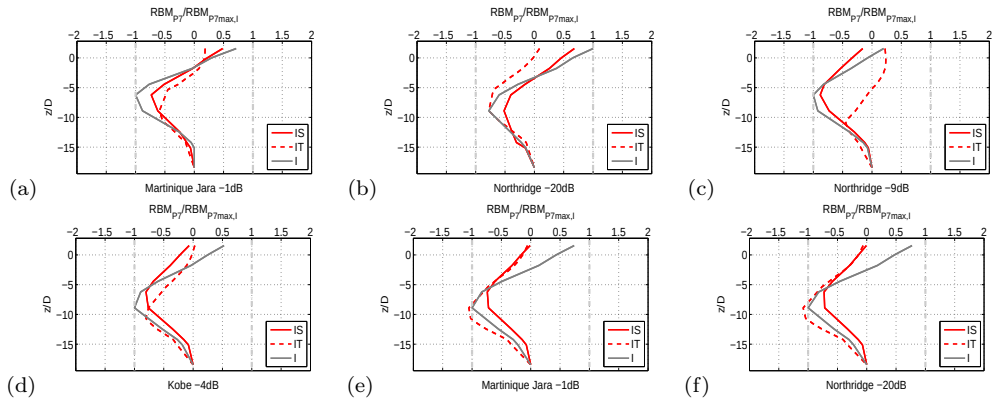

Figure D.7: Normalized residual bending moment, under real earthquake excitations

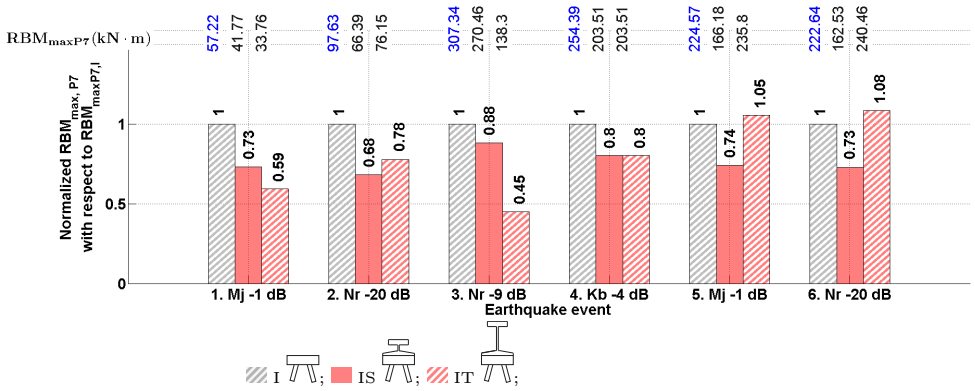

Figure D.8: Normalized maximum residual bending moment, under real earthquake excitations

The normalized dynamic bending moment profiles of different configurations are shown in Fig. D.9. Regardless the types of superstructures, the shapes of dynamic bending moment profiles are all most the same. For small earthquakes, the presence of superstructure induces higher dynamic bending moment at pile heads as it could be expected. However, during strong earthquakes Nr -9 dB and Kb -4 dB, with the high nonlinearity developed in soil, the influence of the superstructures on the dynamic bending moment in piles is very limited.

The ratios of the peak values between different configurations are summarized in Fig. D.10 also confirm the above conclusions. In addition, compared with the short superstructure, slender building induces less or equal dynamic bending moment to the short one in the first two small earthquakes and strong earthquakes. However, in the last two small earthquakesm Mj -1 dB and Nr -20 dB, tall superstructure slightly increase the dynamic bending moment.

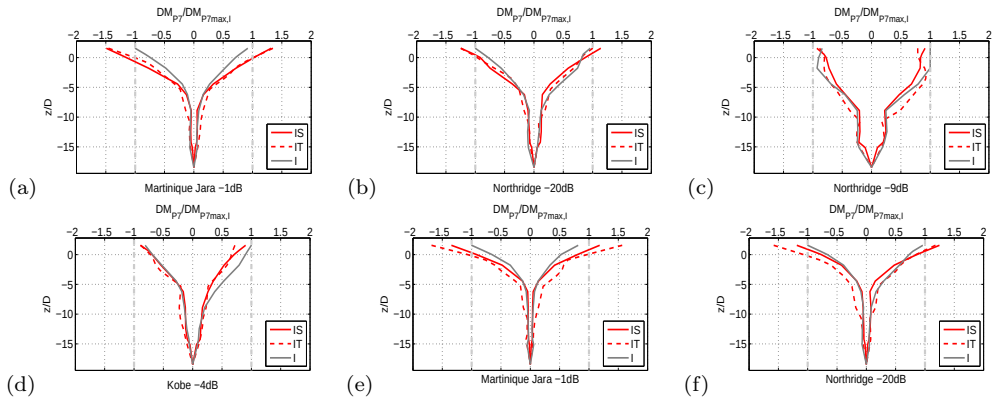

Figure D.9: Normalized dynamic bending moment, under real earthquake excitations

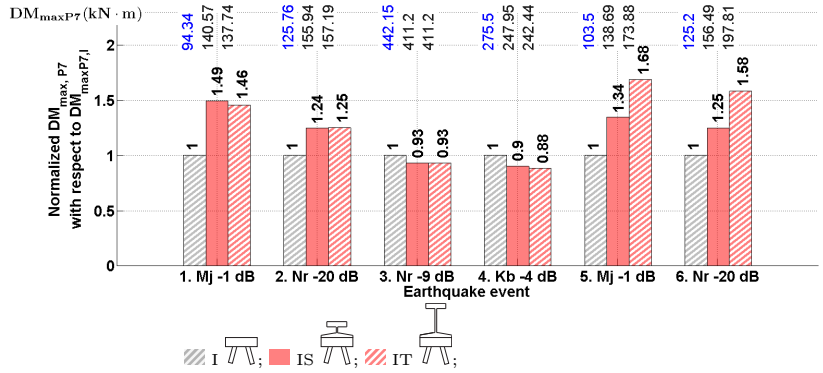

Figure D.10: Normalized maximum dynamic bending moment, under real earthquake excitations

Fig. D.11 shows the normalized total bending moment profiles of different configurations. The shapes of total bending moment for all the configurations are similar. With the "'superposition" of residual bending moment and dynamic bending moment, the total bending moment profiles are dragged away in one side results asymmetric distributions of bending moment. Qualitatively speaking, the presence of superstructures does not have important influence the behavior of inclined piles.

Fig. D.11 shows the ratios of peak values along the normalized total bending moment curves between different pile configurations. Except for the first small earthquake Mj -1 dB, regardless the type of superstructures, the total bending moment is reduced by the presence of superstructures. Although in the first small earthquake, superstructures induce slightly higher bending moments, the actual values for the bending moments are small compared with the other earthquakes.

For short building, except for the first small earthquake, the reduction of total bending moment is around 5∼37%; in the case of slender building, except for the fist small earthquake, the reduction of total bending moment is around 1∼35%. The short superstructure reduces the total bending moment more efficiently than the tall superstructure, except for the first two small earthquake, Mj -1 dB and Nr -20 dB earthquakes.

Due to the different initial stress state in piles in terms of axial forces, the comparisons are not considered. Since shear forces are linked with bending moments in piles, superstructures play the similar reduction effect.

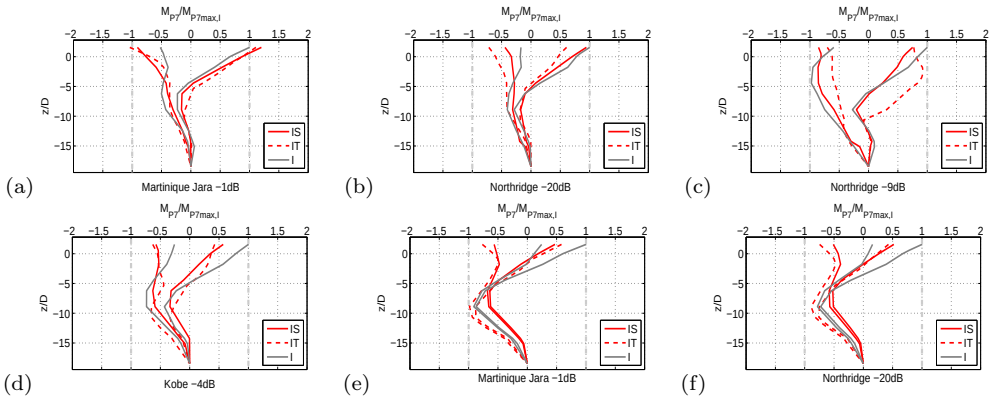

Figure D.11: Normalized total bending moment, under real earthquake excitations

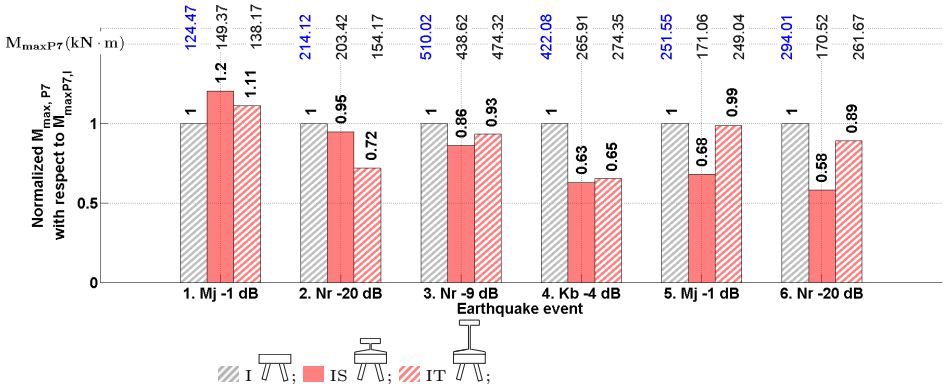

Figure D.12: Normalized maximum total bending moment, under real earthquake excitations

D.0.6 Summary

From the above analyses it seems that when superstructures are placed on an inclined group the response is attenuated comparing with a vertical pile group. Results are also consistent when looking at the base shear force and the overturning moment. Looking at the responses obtained for soil pile cap interaction, the presence of a superstructure has more influence for the vertical piles (especially for the short building). Superstructures on vertical piles attract higher inertial loads compared with superstructures on inclined piles. Although the presence of superstructures improves slightly the performance of inclined piles, it is probably more accurate to say that vertical piles with superstructures attract so important forces that their performance is poor.

Appendix E

Hysteresis loops for rotation and translation behavior of pile groups

The foundations configurations used in sinusoidal excitations and seismic excitations are shown in Tables. E.1 and E.2, respectively. The hysteresis loops for each configuration are shown in the same order in the figures hereafter.

2.0 Hz and 3.5Hz	
Inclined	Vertical
 = 5.12 m	 = 5.12 m
 = 14.16 m	 = 14.16 m

Table E.1: Foundation configurations for sinusoidal excitations

Real earthquake input	
Inclined	Vertical
 = 5.12 m	 = 5.12 m
 = 8.48 m	 = 8.48 m

Table E.2: Foundation configurations for real earthquake excitations

E.1 Experimental results of Rocking behavior of pile foundations

Rotation-moment hysteresis loops, 2.0 Hz sinusoidal excitations

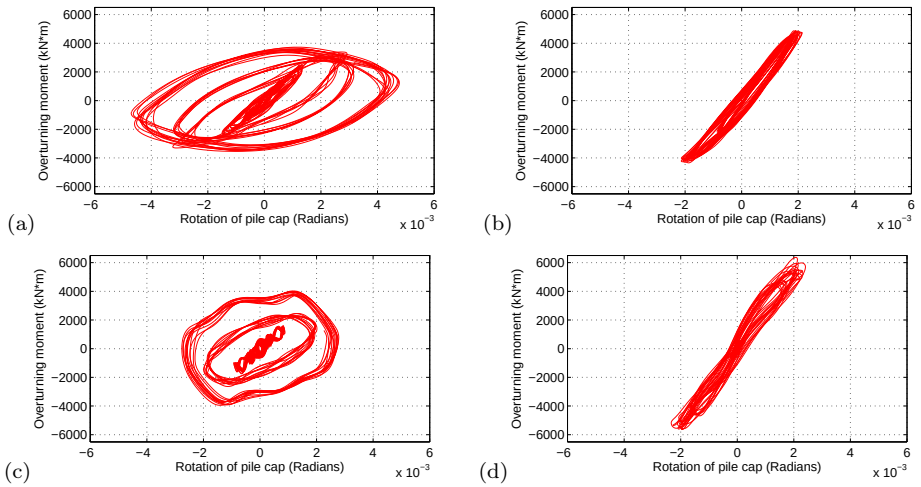

Figure E.1: Rotation-moment Hysteresis loops, 2.0 Hz sine input: (a) Inclined pile group with short building; (b) Vertical pile group with short building; (c) Inclined pile group with taller building (14.16 m) and (d) Vertical pile group with taller building (14.16 m)

Rotation-moment hysteresis loops, 3.5 Hz sinusoidal excitations

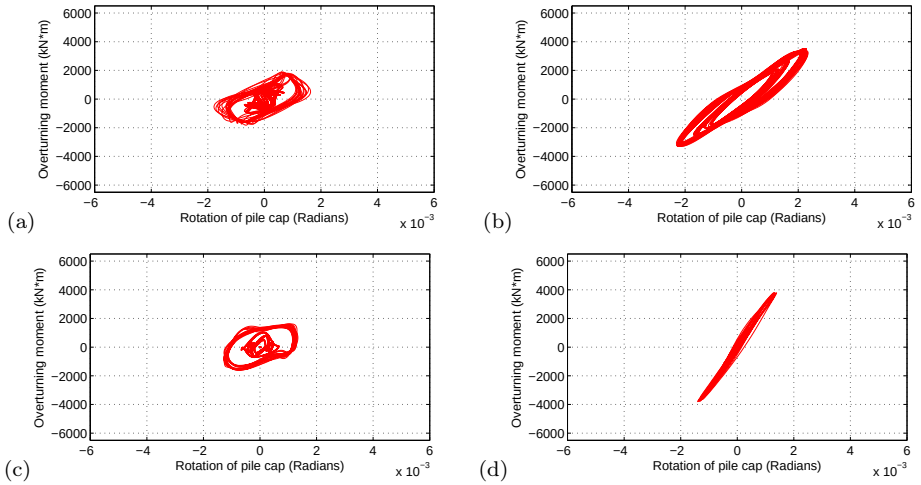

Figure E.2: Rotation-moment Hysteresis loops, 3.5 Hz sine input: (a) Inclined pile group with short building; (b) Vertical pile group with short building; (c) Inclined pile group with tall building (14.16 m) and (d) Vertical pile group with tall building (14.16 m)

Rotation-moment hysteresis loops, real earthquake excitations

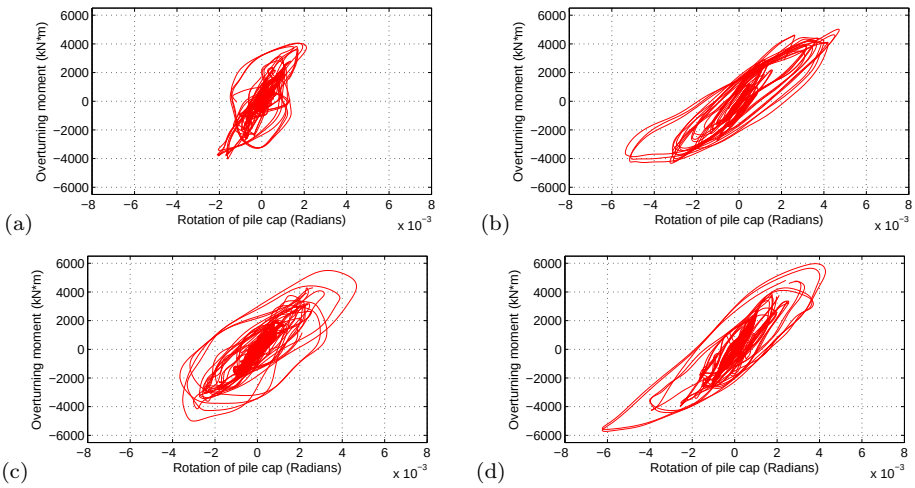

Figure E.3: Rotation-moment Hysteresis loops, real earthquake input: (a) Inclined pile group with short building; (b) Vertical pile group with short building; (c) Inclined pile group with tall building (8.48 m) and (d) Vertical pile group with tall building (8.48 m)

E.2 Experimental results of translation behavior of pile foundations

Translation-force hysteresis loops, 2.0 Hz sinusoidal excitations

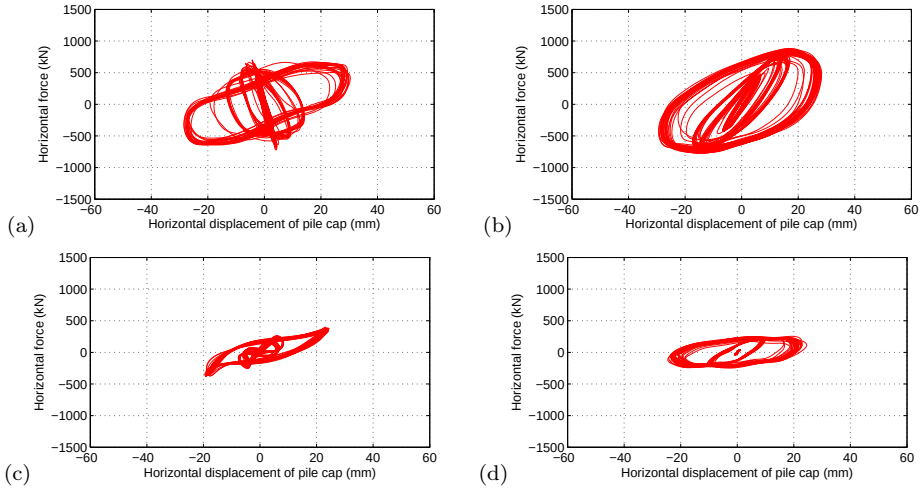

Figure E.4: Translation-force Hysteresis loops, 2.0 Hz sine input: (a) Inclined pile group with short building; (b) Vertical pile group with short building; (c) Inclined pile group with taller building (14.16 m) and (d) Vertical pile group with taller building (14.16 m)

Translation-force hysteresis loops, 3.5 Hz sinusoidal excitations

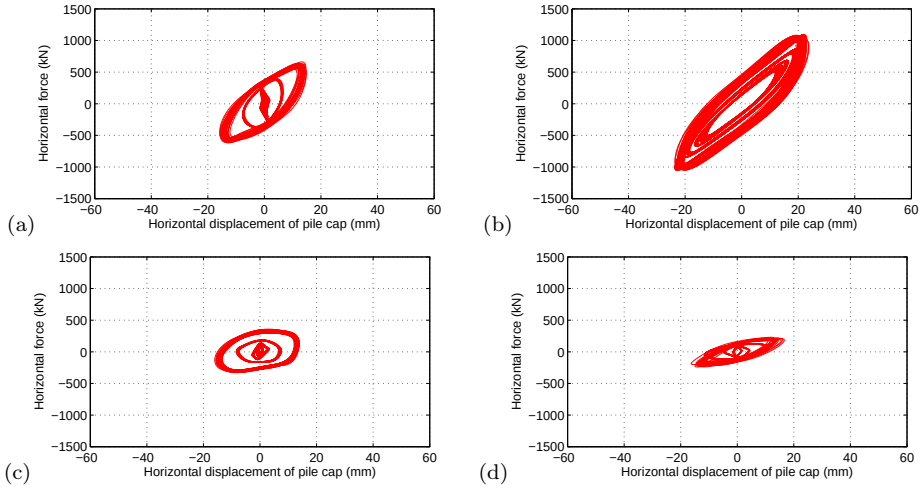

Figure E.5: Translation-force Hysteresis loops, 3.5 Hz sine input: (a) Inclined pile group with short building; (b) Vertical pile group with short building; (c) Inclined pile group with taller building (14.16 m) and (d) Vertical pile group with taller building (14.16 m)

Translation-force hysteresis loops, real earthquake excitations

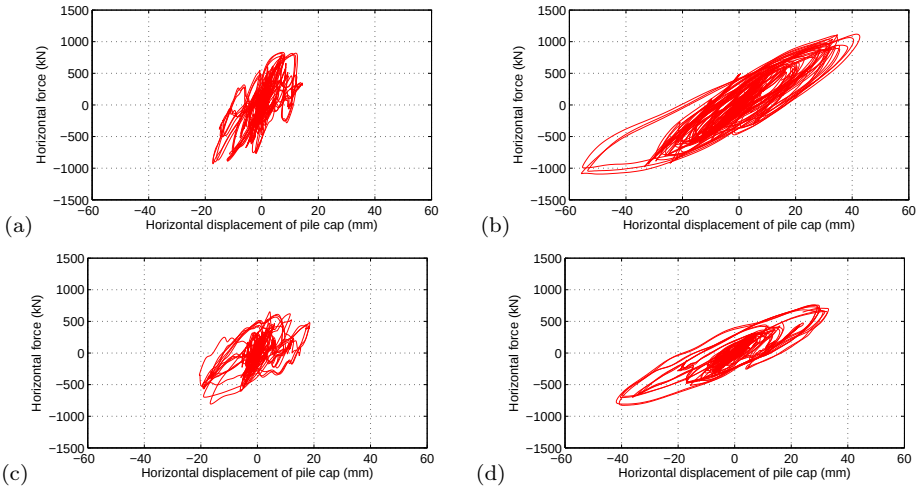

Figure E.6: Translation-force Hysteresis loops: (a) Inclined pile group with short building; (b) Vertical pile group with short building; (c) Inclined pile group with tall building (8.48 m) and (d) Vertical pile group with tall building (8.48 m)

Appendix F

Summary of redisual bending moment and total bending moment

F.1 Residual Bending moment

F.1.1 Residual Bending moment – sine input

F.1.1.1 Inclined pile group with short superstructure under 2.0 Hz sine input

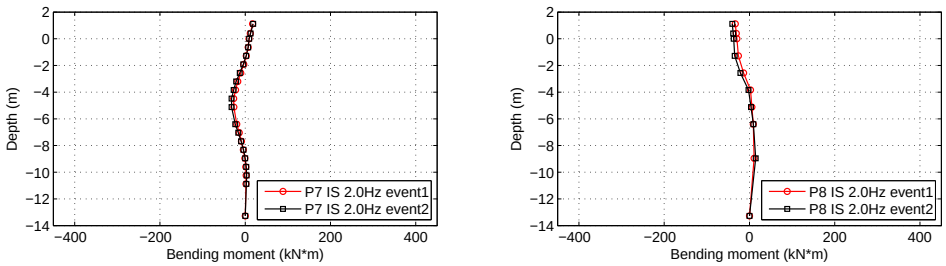

(a) (b)

Figure F.1: Inclined pile group with short building – Event 1 and 2

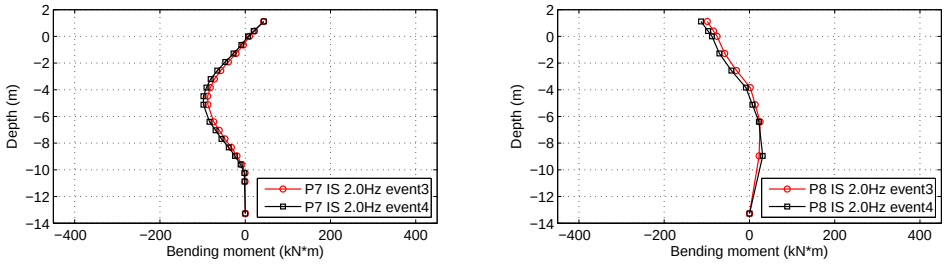

(a) (b)

Figure F.2: Inclined pile group with short building – Event 3 and 4

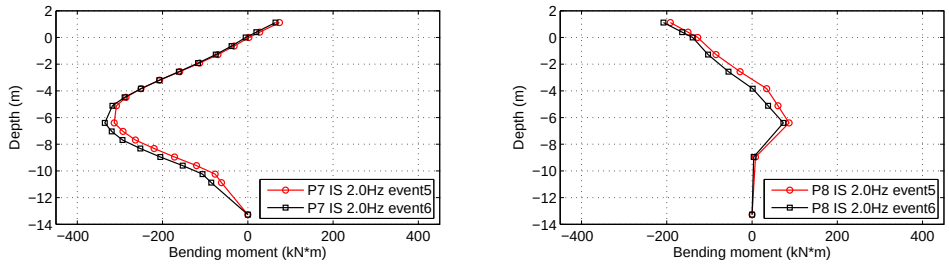

(a) (b)

Figure F.3: Inclined pile group with short building – Event 5 and 6

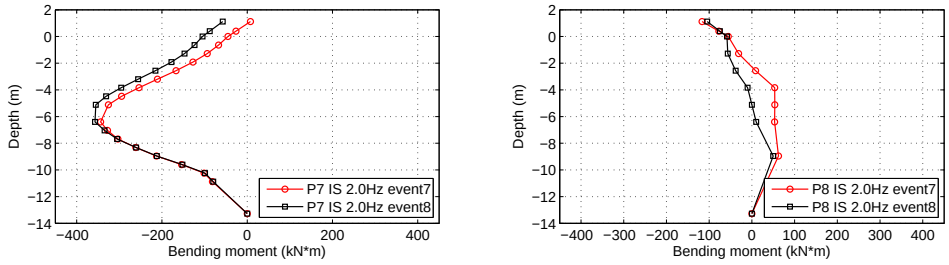

(a) (b)

Figure F.4: Inclined pile group with short building – Event 7 and 8

F.1.2 Residual bending moment – real earthquake input

F.1.2.1 Inclined pile group with tall building under real earthquake input

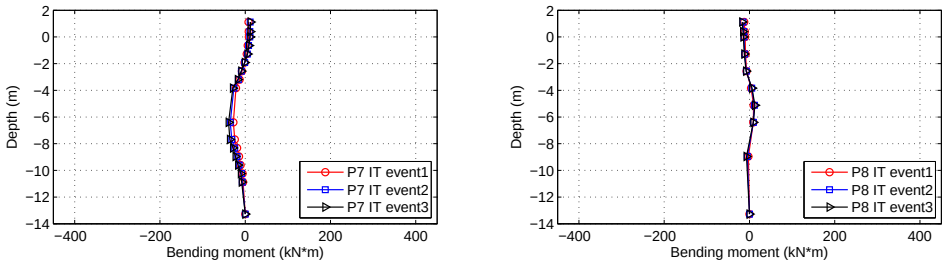

(a) (b)

Figure F.5: Inclined pile group with tall building – Martinique Jara -1dB, event 1, 2 and 3

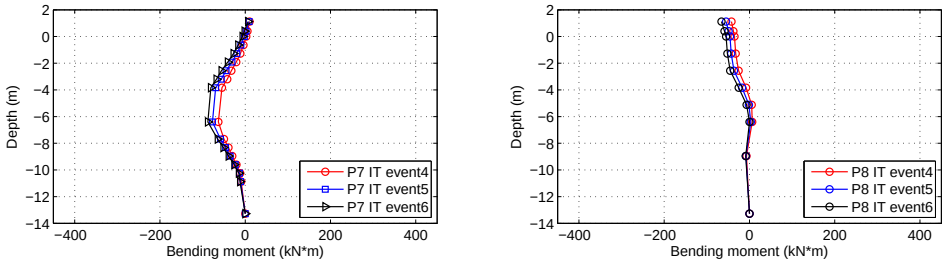

(a) (b)

Figure F.6: Inclined pile group with tall building – Northridge -20dB, event 4, 5 and 6

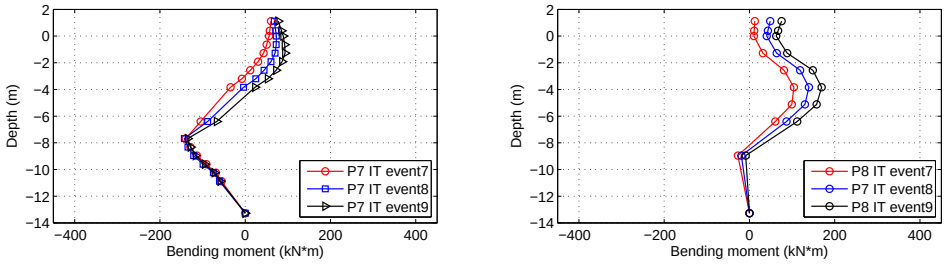

(a) (b)

Figure F.7: Inclined pile group with tall building – Northridge -9dB, event 7, 8 and 9

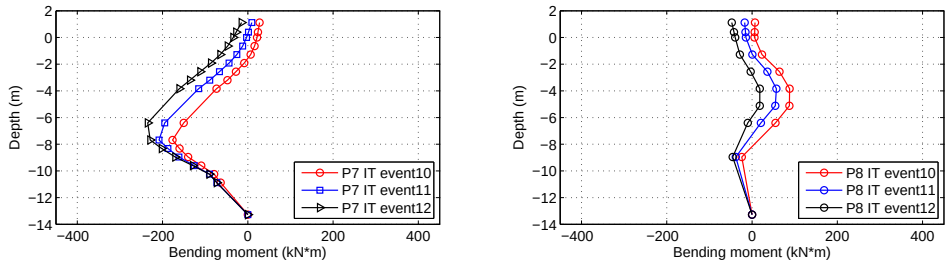

(a) (b)

Figure F.8: Inclined pile group with tall building – Kobe -4dB, event 10, 11 and 12

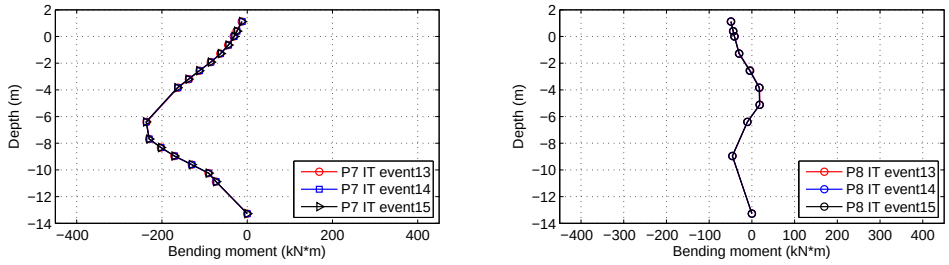

(a) (b)

Figure F.9: Inclined pile group with tall building – Martinique Jara -1dB, event 13, 14 and 15

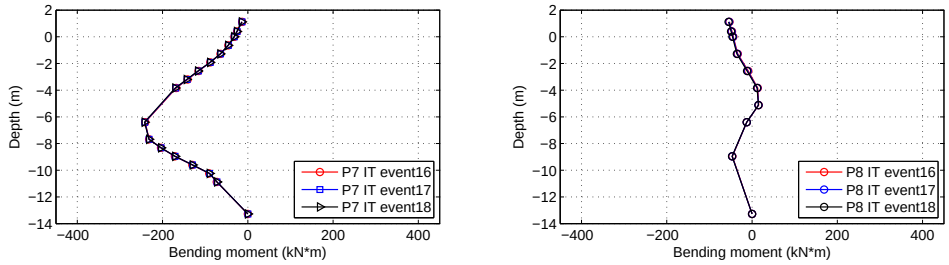

(a) (b)

Figure F.10: Inclined pile group with tall building – Northridge -20dB, event 16, 17 and 18

F.2 Total Bending moment

F.2.1 Total Bending moment – sine input

F.2.1.1 Inclined pile group with short superstructure under 2.0 Hz sine input

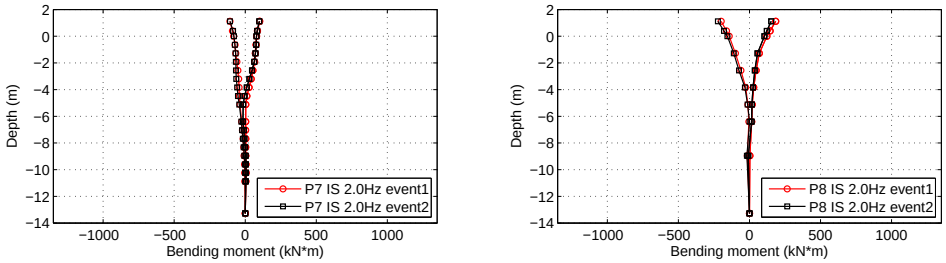

(a) (b)

Figure F.11: Inclined pile group with short building – Event 1 and 2

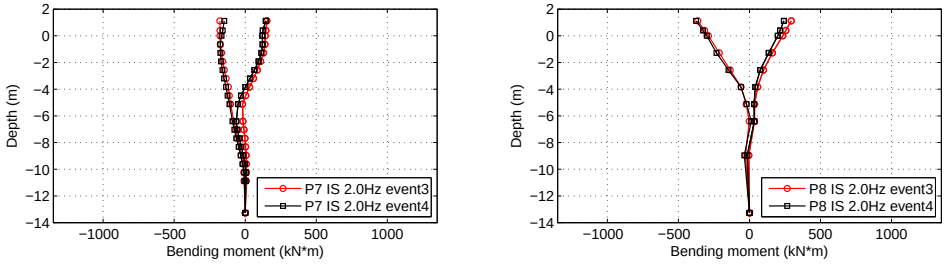

(a) (b)

Figure F.12: Inclined pile group with short building – Event 3 and 4

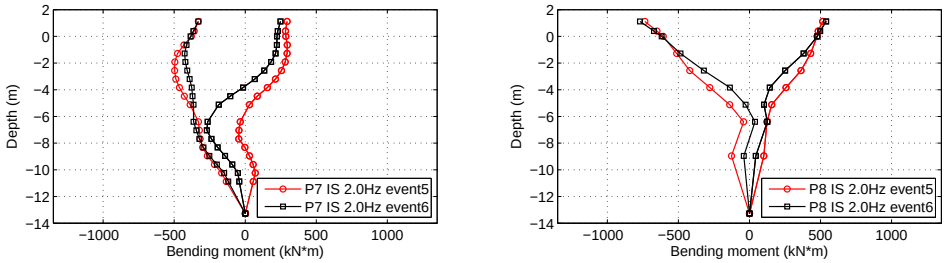

(a) (b)

Figure F.13: Inclined pile group with short building – Event 5 and 6

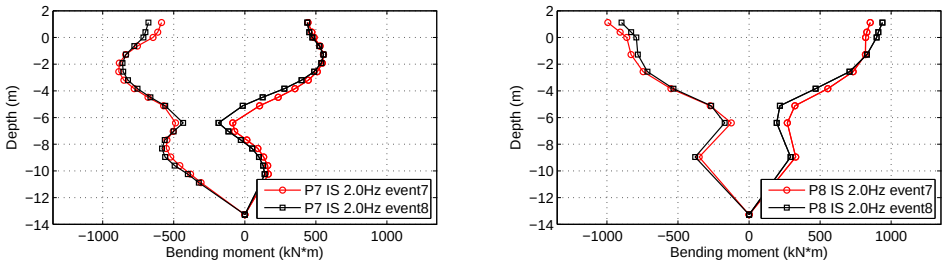

(a) (b)

Figure F.14: Inclined pile group with short building – Event 7 and 8

F.2.2 Total bending moment – real earthquake input

F.2.2.1 Inclined pile group with tall building under real earthquake input

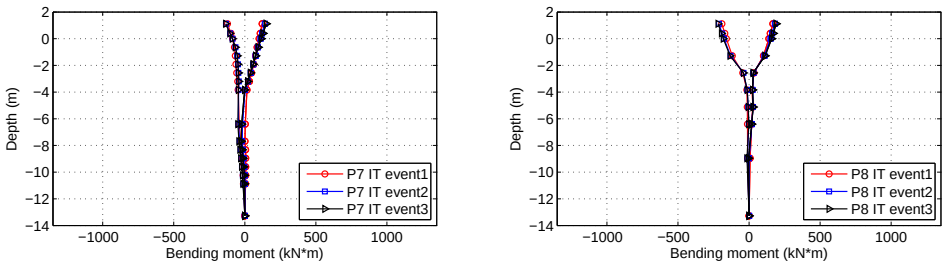

(a) (b)

Figure F.15: Inclined pile group with tall building – Martinique Jara -1dB, event 1, 2 and 3

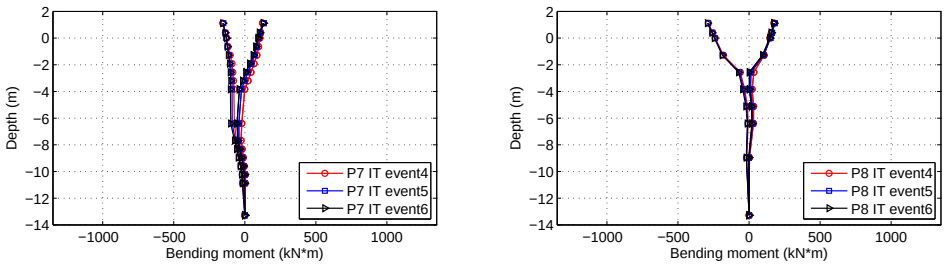

(a) (b)

Figure F.16: Inclined pile group with tall building – Northridge -20dB, event 4, 5 and 6

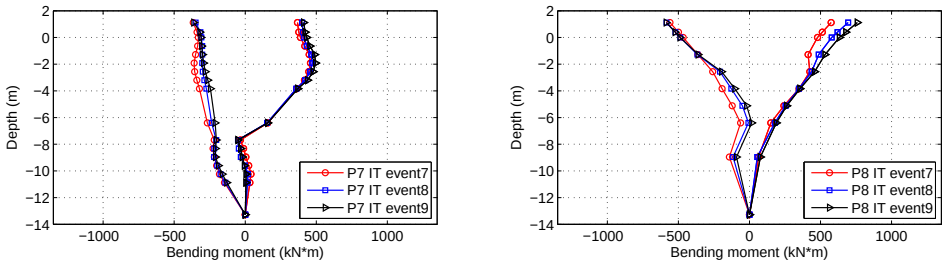

(a) (b)

Figure F.17: Inclined pile group with tall building – Northridge -9dB, event 7, 8 and 9

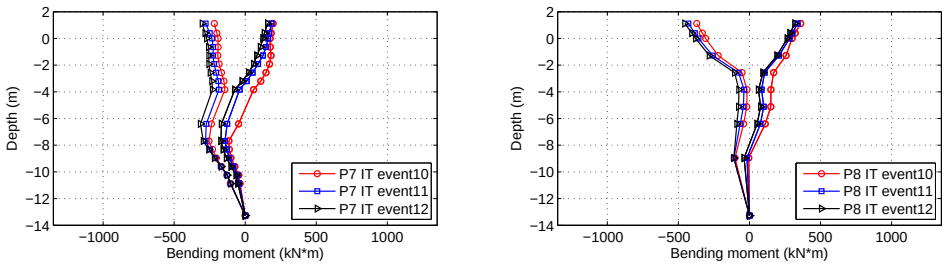

(a) (b)

Figure F.18: Inclined pile group with tall building – Kobe -4dB, event 10, 11 and 12

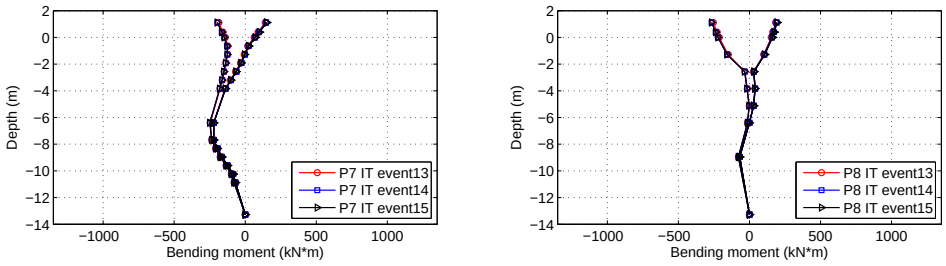

(a) (b)

Figure F.19: Inclined pile group with tall building – Martinique Jara -1dB, event 13, 14 and 15

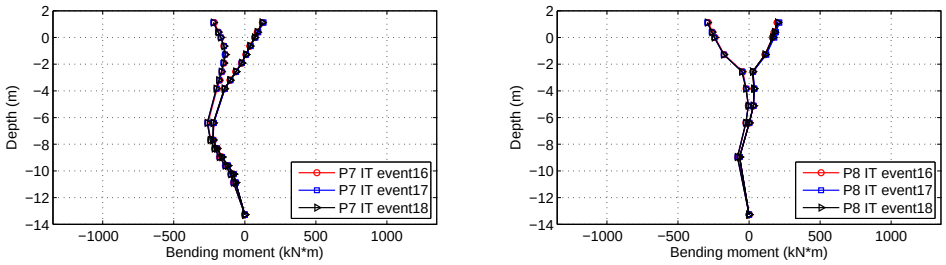

(a) (b)

Figure F.20: Inclined pile group with tall building – Northridge -20dB, event 16, 17 and 18

Appendix G

Analysis of Repeatability of Experiments

Several centrifuge tests were repeated the check the reliability of the experimental data. Several measured quantities such as input base shaking signals, response of soil column, response of superstructures, residual bending moment, dynamic bending moment, total bending moment of pile and CPT test were compared with the original test.

G.1 Free field tests

1. Comparison of input signal in terms of acceleration (small earthquake – Northridge -20 dB)

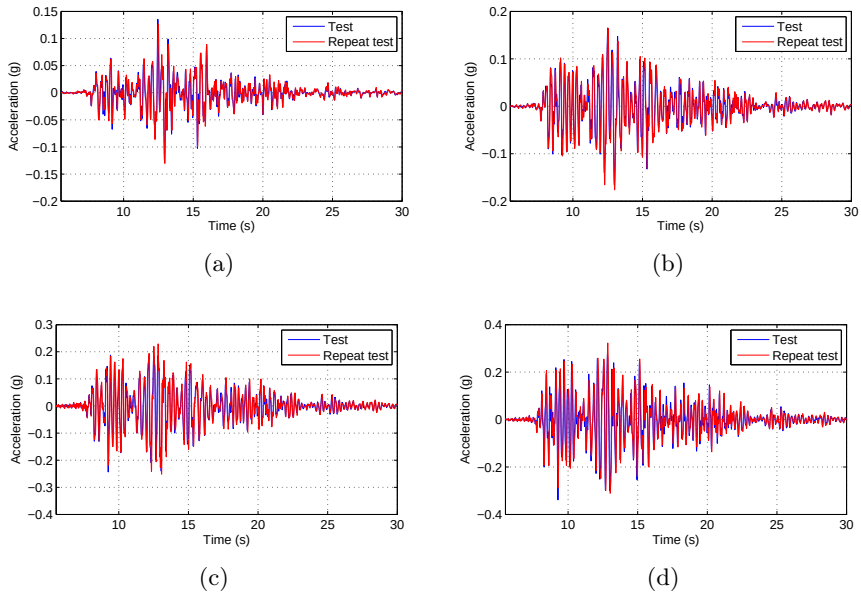

Figure G.1: Comparison of input signal on CH01 (input signal) (a), responses of soil column (middle) (b), responses of soil column (top) (c) and responses of container side-wall (d) – small earthquake, northridge -20 dB

2. Comparison of input signal in terms of acceleration (strong earthquake – Kobe -4 dB)

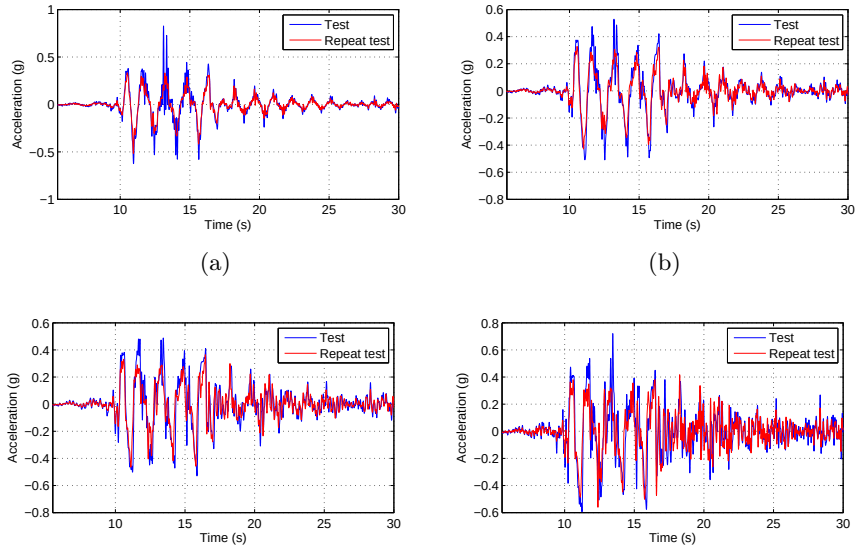

Figure G.2: Comparison of input signal on CH01 (input signal) (a), responses of soil column (middle) (b), responses of soil column (top) (c) and responses of container side-wall (d) – big earthquake, kobe -4 dB

G.2 Inclined pile group with short building

Original test	Repeat test 01	Repeat test 02
2011_06_24_inclined_short	2011_06_28_inclined_short	2011_10_20_inclined_short

Table G.1: Test ID for original test and repeat test

G.2.1 Comparison of Acceleration History

1. Comparison of input signal in terms of acceleration (small earthquake – Northridge -20 dB)

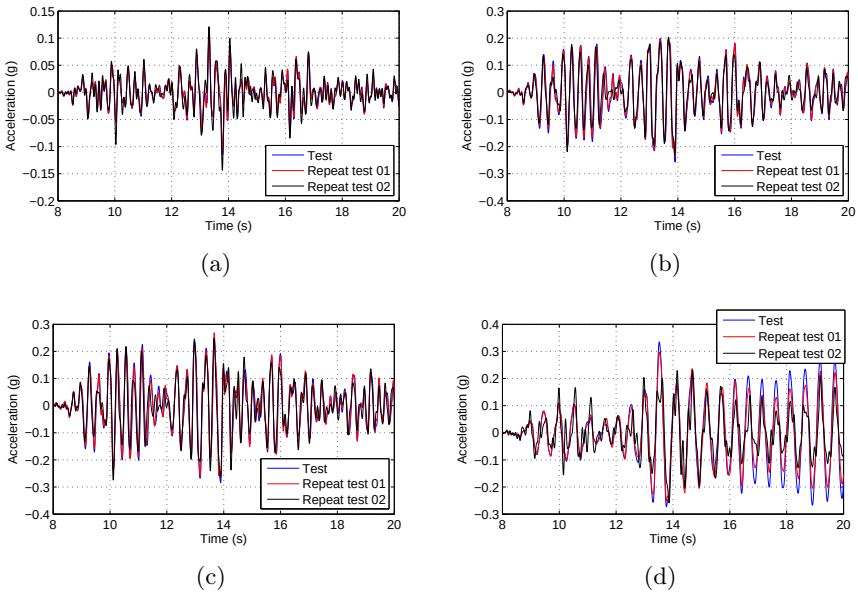

Figure G.3: Comparison of acceleration history: CH01 (input signal) (a), responses of soil column (top) (b), responses of pile cap (c) and responses of top building (d) – small earthquake, northridge -20 dB

2. Comparison of input signal in terms of acceleration (strong earthquake – Kobe -4 dB)

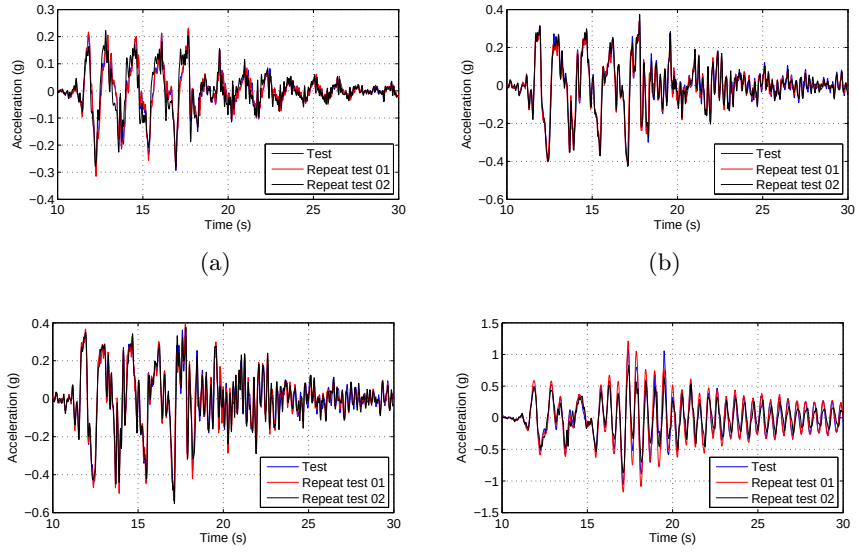

Figure G.4: Comparison of acceleration history: CH01 (input signal) (a), responses of soil column (top) (b), responses of pile cap (c) and responses of top building (d) – big earthquake, Kobe -4 dB

G.2.2 Comparison of bending moment

1. Comparison of residual bending moment

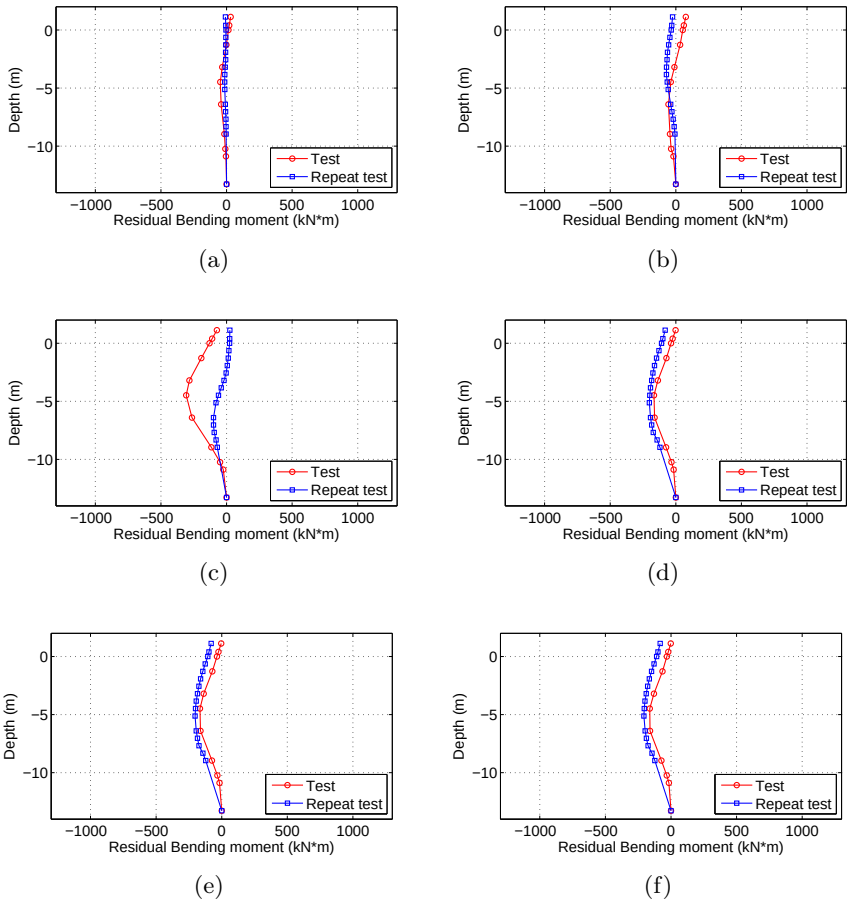

Figure G.5: Comparison of residual bending moments: Martinique Jara -1 dB (a), Northridge -20 dB (b), Northridge -9 dB (c), Kobe -4 dB (d), Martinique Jara -1 dB (e) and Northridge -20 dB (f)

2. Comparison of dynamic bending moment

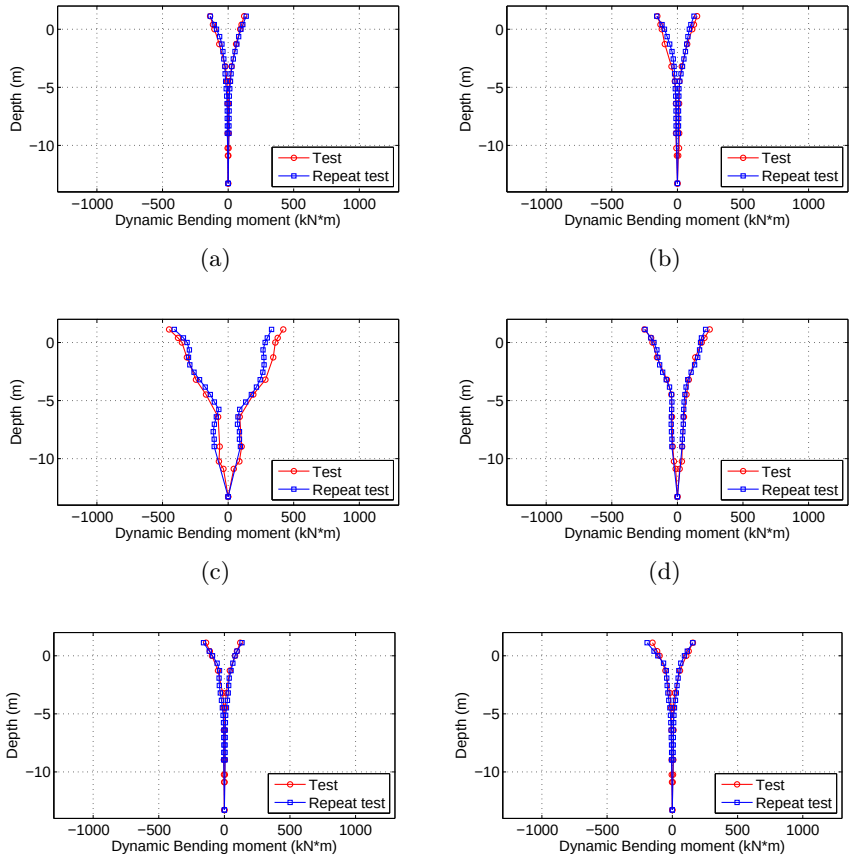

Figure G.6: Comparison of dynamic bending moments: Martinique Jara -1 dB (a), Northridge -20 dB (b), Northridge -9 dB (c), Kobe -4 dB (d), Martinique Jara -1 dB (e) and Northridge -20 dB (f)

3. Comparison of total bending moment

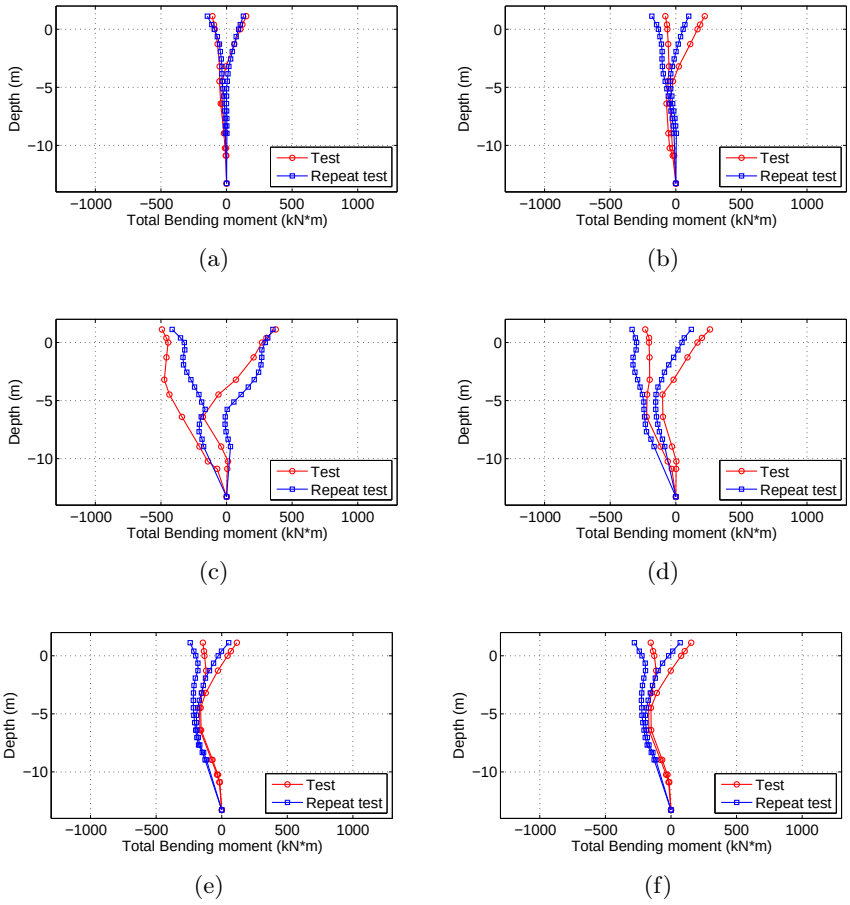

Figure G.7: Comparison of total bending moments: Martinique Jara -1 dB (a), Northridge -20 dB (b), Northridge -9 dB (c), Kobe -4 dB (d), Martinique Jara -1 dB (e) and Northridge -20 dB (f)

G.3 Cone Penetration Test

CPT tests were performed before and after the earthquakes. The results from CPT tests were compared between different tests. It can be seen that the sand properties are identical for each test.

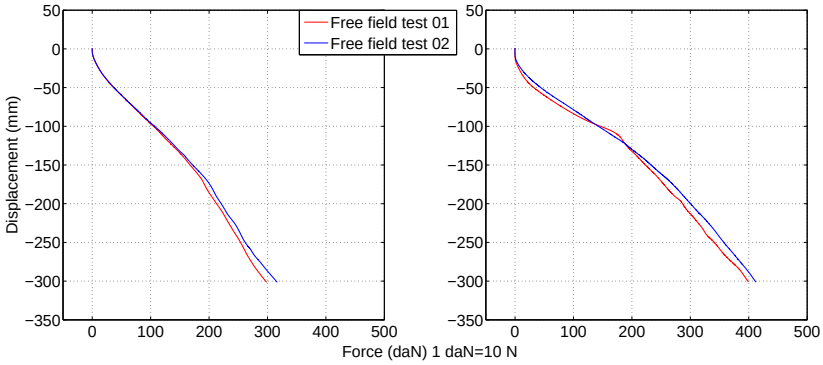

Figure G.8: CPT test before and after earthquakes (two free field test for example)

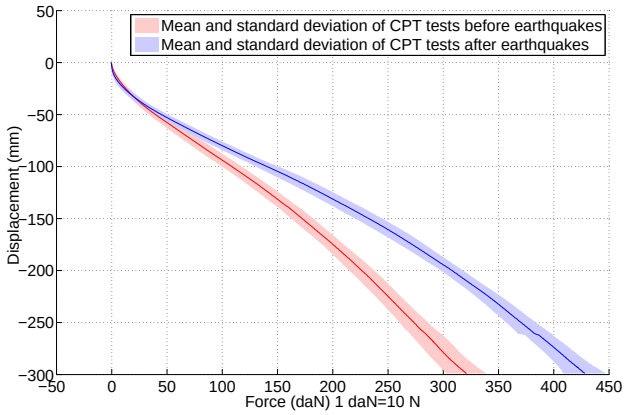

Figure G.9: CPT test before and after earthquakes (all test)

Appendix H

Strain gauges instrumented on piles

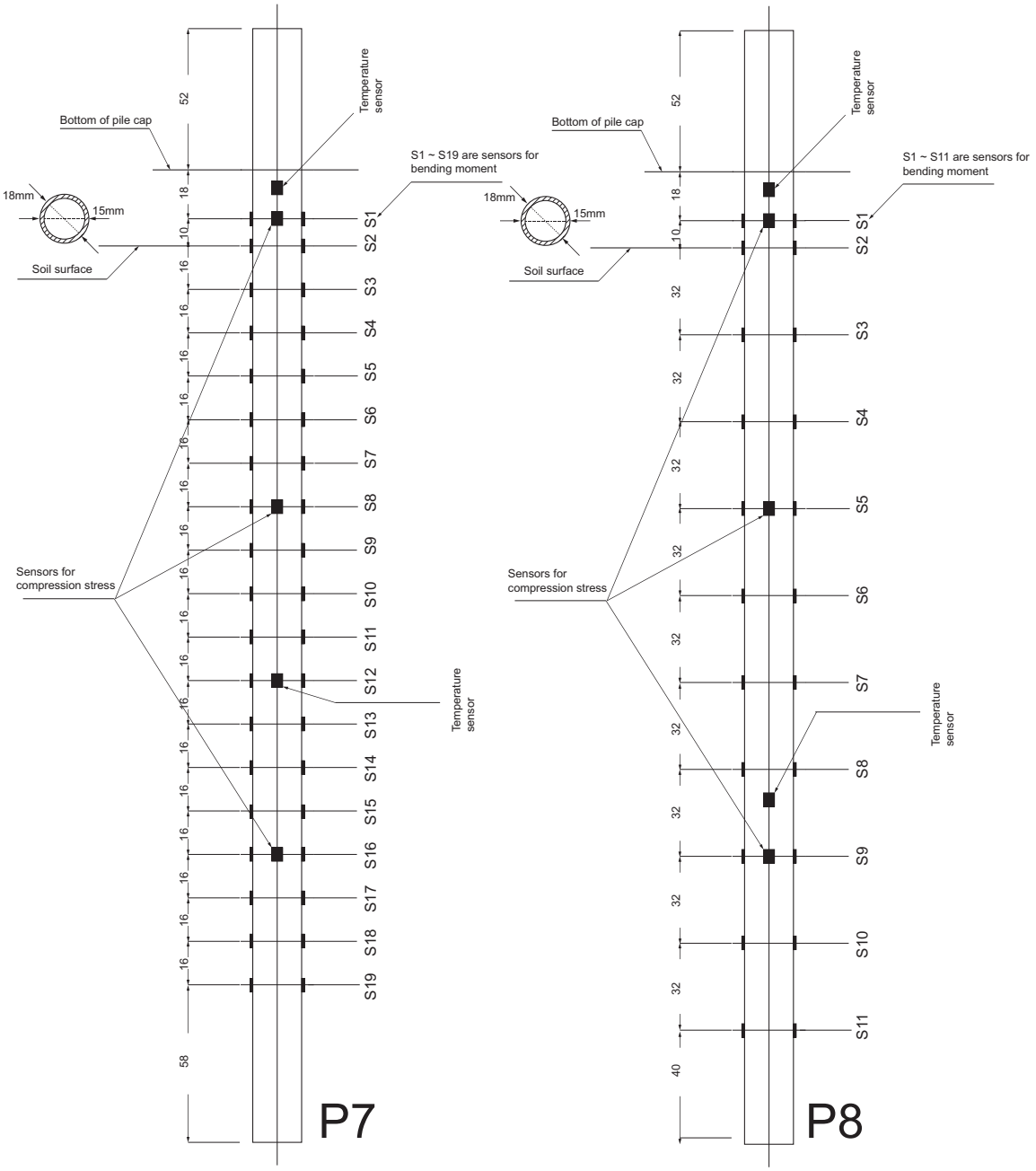

Figure H.1: Strain gauges instrumented on piles

Bibliography

[1] F. Rosquoët, *Pile under lateral cyclic load.* Ph.d. thesis, Ecole Centrale & Universitáe de Nantes, 2004. (Cited on pages vii, xv, xvi, 10, 6, 11, 12, 20, 21, 28 and 29.)

[2] R. B. Seed, S. E. Dickenson, and I. M. Idriss, "Principal geotechnical aspects of the 1989 Loma Prieta earthquake," *Soils and Foundations*, vol. 31, no. 1, pp. 1–26, 1991. (Cited on pages vii and 2.)

[3] SEAOC, "Reflections on the October 17, 1989 Loma Prieta Earthquake," tech. rep., Ad Hoc Earthquake Reconnaissance Committee, Sacramento, 1991. (Cited on pages vii and 2.)

[4] S. E. Dickenson, N. J. McCullough, M. G. Barkau, and B. J. Wavra, "Assessment and Mitigation of Liquefaction Harzards to Bridge Approach Embankments," tech. rep., Dept. of Civil Construction and Environmental Engineering Oregon State University, 2002. (Cited on pages vii and 3.)

[5] M. J. N. Priestley, J. P. Singh, T. L. Youd, and K. L. Rollins, "Costa Rica Earthquake of April 22, 1991 Reconnaissance Report," *Earthquake Spectra Supplement B to Volume 7*, pp. 59–91, 1991. (Cited on pages vii, 4 and 5.)

[6] E. Ovando-Shelley and M. P. Romo, "Behavior of the main wharf in San Pedrito Port in Manzanillo, Mexico," in *12th World Conference on Earthquake Engineering*, 2000. (Cited on pages vii, viii and 6.)

[7] GEER. Geotechnical Extreme Events Reconnaissance, "Geo-Engineering Reconnaissance of the February 27, 2010 Maule, Chile Earthquake," tech. rep., 2009. (Cited on pages viii, 7 and 8.)

[8] J. B. Berrill, S. A. Christensen, R. P. Keenan, W. Okada, and J. R. Pettinga, "Case study of lateral spreading forces on a piled foundation," *Geotechnique*, vol. 51, no. 6, pp. 501–517, 2001. (Cited on pages viii, 1, 4, 9, 10 and 11.)

[9] A. K. Giannakou, *Seismic Behavior of Inclined Piles.* Ph.d dissertation, National Technical University of Athens, 2007. (Cited on pages viii, 1, 2, 4, 5, 8, 10, 11, 12, 13, 23, 27, 26, 36 and 43.)

[10] G. G. Meyerhof and A. S. Yalcin, "Behaviour of flexible batter piles under inclined loads in layered soil," *Canadian Geotechnical Journal*, vol. 30, no. 2, pp. 247–256, 1993. (Cited on pages viii and 15.)

[11] M. C. McVay, R. Gardner, and L. Zhang, "Centrifuge Modeling of Laterally Loaded Battered Pile Groups in Sand," tech. rep., State of Florida department of Transportation, 1997. (Cited on pages viii and 16.)

[12] L. Zhang, M. C. McVay, and P. W. Lai, "Centrifuge modelling of laterally loaded single battered piles in sands," *Canadian Geotechnical Journal*, vol. 36, no. 6, pp. 1074–1084, 1999. (Cited on pages viii, ix, 16, 17, 25, 26, 27 and 24.)

[13] S. Escoffier, J.-L. Chazelas, and J. Garnier, "Centrifuge modelling of raked piles," *Bulletin of Earthquake Engineering*, vol. 6, pp. 689–704, Oct. 2008. (Cited on pages viii, 17, 18, 19 and 9.)

[14] T. Tazoh, M. Sato, J. Jang, Y. Taji, G. Gazetas, and I. Anastasopoulos, "Kinematic Response of Batter Pile Foundation: Centrifuge Tests," in *3rd Greece -Japan Workshop Seismic Design, Observation, and Retrofit of Foundations*, (Laboratory of Soil Mechanics, National Technical Univ. of Athens, Greece), 2009. (Cited on pages viii, 18, 19 and 33.)

[15] K. Okawa, H. Kamei, M. Kimura, and F. Zhang, "Dynamic behaviour of a group-pile foundation with inclined piles in loose sand," in *International conference on physical modelling in geotechnics: ICPMG'02*, pp. 729–736, 2002. (Cited on pages viii, 19, 20, 27 and 1.)

[16] J. C. Boland, S. M. Schlechter, N. J. Mccullough, S. E. Dickenson, B. L. Kutter, and D. W. Wilson, "Pile-supported Wharf Centrifuge Model (SMS02)," Tech. Rep. October, Center for Geotechnical Modeling University of California at Davis, 2001. (Cited on pages viii, 20 and 21.)

[17] J. C. Boland, S. M. Schlechter, N. J. Mccullough, S. E. Dickenson, B. L. Kutter, and D. W. Wilson, "Pile-supported Wharf Centrifuge Model (JCB01)," Tech. Rep. October, Center for Geotechnical Modeling University of California at Davis, 2001. (Cited on pages viii, 20 and 21.)

[18] A. Ohira, T. Tazoh, K. Dewa, K. Shimizu, and M. Shimada, "Observations of earthquake response behaviors of foundation piles for Road Bridge," in *8th World Conference on Earthquake Engineering*, pp. 577–584, 1984. (Cited on pages viii, ix, 24 and 28.)

[19] I. Andri-Ntoanina, J. Canou, and J. C. Dupla, "Caractérisation mécanique du sable de Fontainebleau NE34 à l'appareil triaxial sous cisaillement monotone," tech. rep., 2010. (Cited on pages xiii, 8 and 9.)

[20] A. Irina, "Caractérisationi dynamique de sables de référence en laboratoire - Application à la réponse sismique de massifs sableux en centrifugeuse," *Thése de Institue Français des Sciences et Technologies des Transports, de l'Aménagement et des Réseaux - IFSTTAR, Laboratoire NAVIER - Géotechnique (CERMES)*, 2011. (Cited on pages xxiii and 2.)

[21] "Recommandations AFPS 90." (Cited on pages 1 and 4.)

[22] Eurocode8-Part5, *Eurocode 8: Design of structures for earthquake resistance-Part 5: Foundations, retaining structures and geotechnical aspects*. Belgium:

European Committee for Standardization (CEN), 2003. (Cited on pages 1, 4 and 33.)

[23] N. Gerolymos, A. Giannakou, I. Anastasopoulos, and G. Gazetas, "Evidence of beneficial role of inclined piles: observations and summary of numerical analyses," *Bulletin of Earthquake Engineering*, vol. 6, pp. 705–722, 2008. (Cited on pages 1 and 4.)

[24] George Gazetas and G. Mylonakis, "Seismic Soil-Structure Interaction: New Evidence and Emerging Issues," in *Geotechnical Earthquake Engineering and Soil Dynamics III*, pp. 1119–1174, 1998. (Cited on pages 1 and 4.)

[25] M. Pender, "Aseismic pile foundation design analysis," *Bulletin of the NewZealand Society for Earthquake Engineering*, vol. 26, no. 1, pp. 49–61, 1993. (Cited on pages 1 and 4.)

[26] R. E. Harn, "Have Batter Piles Gotten a Bad Rap in Seismic Zones (Or Everything You Wanted to Know About Batter Piles But Were Afraid to Ask)," in *Ports 2004: Port Development in the Changing World*, pp. 1–10, 2004. (Cited on pages 1 and 4.)

[27] A. Giannakou, N. Gerolymos, G. Gazetas, T. Tazoh, and I. Anastasopoulos, "Seismic Behavior of Batter Piles : Elastic Response," *Journal of Geotechnical and Geoenvironmental Engineering*, vol. 136, no. 9, pp. 1187–1199, 2010. (Cited on pages 1, 2, 4, 5, 27 and 43.)

[28] I. Isao and Z. Xinjian, "Unified dynamic shear moduli and damping ratios of sand and clay," *Soils And Foundations*, vol. 33, no. 1, pp. 182–191, 1993. (Cited on pages 5, 1, 2, 14 and 17.)

[29] G. Gottardi, G. Houlsby, and R. Butterfield, "Plastic response of circular footings on sand under general planar loading," *Géotechnique*, vol. 49, no. 4, pp. 453–469, 1999. (Cited on pages 8, 2, 4 and 9.)

[30] A. Niemunis and I. Herle, "Hypoplastic model for cohesionless soils with elastic strain range," *Mechanics of Cohesive-Frictional Materials*, vol. 2, pp. 279–299, 1997. (Cited on pages 10, 6, 16 and 17.)

[31] A. Niemunis, *Extended hypoplastic models Dissertation submitted for habilitation.* PhD thesis, 2002. (Cited on pages 10, 1, 2, 6, 16 and 17.)

[32] P. J. Meymand, *Shaking table scale model tests of nonlinear soil-pile-superstructure interaction in soft clay.* PhD thesis, University of California, 1998. (Cited on page 1.)

[33] J. A. Egan, R. F. Hayden, L. Scheibel, M. Otus, and G. M. Serventi, "Seismic repair at Seventh Street marine terminal," in *Grouting, Soil Improvement, and Geosynthetics*, pp. 867–878, 1992. (Cited on page 1.)

[34] S. Yasuda and J. B. Berrill, "Observations of the earthquake response of foundations in soil profiles containing saturated sands," in *1st International Conference on Geotechnical and Geological Engineering - GeoENG2000*, pp. 1441–1470, 2000. (Cited on page 11.)

[35] GEER. Geotechnical Extreme Events Reconnaissance, "Geotechnical Reconnaissance of the Effects of the January 17, 1995 Hyogoken-Nanbu Earthquake, Japan. Report No. UCB/EERC-95/01," tech. rep., 1995. (Cited on page 11.)

[36] G. Kastranta, G. Gazetas, and T. Tazoh, "Performance of three quay walls in Maya Wharf: Kobe 1995," in *11th European Conference on Earthquake Engineering*, 1998. (Cited on page 11.)

[37] G. G. Meyerhof and G. Ranjan, "The bearing capacity of rigid piles under inclined loads in sand. I: Vertical piles," *Canadian Geotechnical Journal*, vol. 9, no. 4, pp. 430–446., 1972. (Cited on pages 15, 27, 5, 8 and 23.)

[38] G. G. Meyerhof and G. Ranjan, "The bearing capacity of rigid piles under inclined loads in sand. II: Batter piles," *Canadian Geotechnical Journal*, vol. 10, no. 3, pp. 430–446., 1973. (Cited on pages 15 and 16.)

[39] G. G. Meyerhof and G. Ranjan, "The bearing capacity of rigid piles under inclined loads in sand. III: Pile Groups," *Canadian Geotechnical Journal*, vol. 10, no. 3, pp. 428–438, 1973. (Cited on page 15.)

[40] G. G. Meyerhof, S. Yalcin, and S. K. Mathur, "Ultimate pile capacity for eccentric inclined load," vol. 109, pp. 408–423, 1983. (Cited on page 15.)

[41] G. G. Meyerhof and V. V. R. N. Sastry, "Bearing capacity of rigid piles under eccentric and inclined loads," *Canadian Geotechnical Journal*, vol. 22, no. 3, pp. 267–276, 1985. (Cited on page 15.)

[42] G. G. Meyerhof and A. S. Yalcin, "Behaviour of flexible batter piles under inclined loads in layered soil," *Canadian Geotechnical Journal*, vol. 30, no. 2, pp. 247–256, 1993. (Cited on page 15.)

[43] G. G. Meyerhof and A. S. Yalcin, "Bearing capacity of flexible batter piles under eccentric and inclined loads in layered soil," *Canadian geotechnical journal*, vol. 31, no. 4, pp. 583–590, 1994. (Cited on page 15.)

[44] L. C. Reese and v. I. Willem, *Single Piles and Pile Groups Under Lateral Loading*. Taylor & Francis, 2000. (Cited on page 15.)

[45] P. Pinto, M. McVay, M. Hoit, and P. Lai, "Centrifuge Testing of Plumb and Battered Pile Groups in Sand," *Transportation Research Record: Journal of the Transportation Research Board*, vol. 1569, no. 1, pp. 8–16, 1997. (Cited on page 16.)

[46] L. M. Zhang, M. C. Mcvay, S. J. Han, P. W. Lai, and R. Gardner, "Effects of dead loads on the lateral response of battered pile groups," vol. 575, pp. 561–575, 2002. (Cited on page 17.)

[47] S. Escoffier, "Experimental study of the effect of inclined pile on the seismic behavior of pile group," *Soil Dynamics and Earthquake Engineering*, vol. 42, pp. 275–291, Nov. 2012. (Cited on pages 19 and 40.)

[48] J. L. Chazelas, S. Escoffier, J. Garnier, L. Thorel, and G. Rault, "Original technologies for proven performances for the new LCPC earthquake simulator," *Bulletin of Earthquake Engineering*, vol. 6, pp. 723–728, Oct. 2008. (Cited on pages 19, 2 and 3.)

[49] I. Juran, A. Benslimane, and S. Hanna, "Engineering analysis of dynamic behavior of micropile system," *Transportation Research Record: Journal of the Transportation Research Board*, vol. 1772, no. 1, pp. 91–106, 2001. (Cited on page 22.)

[50] L. Feagin, "Lateral load tests on groups of battered and vertical piles," in *Proceeding Symp. on lateral Load Tests on Piles, ASTM*, (New York), pp. 12–20, 1953. (Cited on page 22.)

[51] G. P. Tschebotarioff, "The Resistance of Lateral Loading of Single Piles and of Pile Group," *ASTM special Publication*, vol. 38, no. 154, 1953. (Cited on page 23.)

[52] J. B. Kim and R. J. Brungraber, "Full-Scale Lateral Load Tests of Pile Groups," *Journal of the Geotechnical Engineering Division*, vol. 102, no. 1, pp. 87–105, 1976. (Cited on page 23.)

[53] O. L. Denisov, "Behavior of foundations using driven vertical and inclined piles under horizontal loading," *Soil Mechanics and Foundation Engineering*, vol. 19, no. 2, pp. 48–52, 1982. (Cited on page 23.)

[54] T. Tazoh, K. Shimizu, and T. Wakahara, "Seismic Observations and Analysis of Grouped Piles," in *Dynamic Response of Pile Foundations-Experiment, Analysis and Observation*, pp. 1–20. (Cited on page 24.)

[55] G. Gazetas, K. Fan, T. Tazoh, and K. Shimizu, "Seismic Response of the Pile Foundation of Ohba-Ohashi Bridge," in *Third International Conference on Case Histories in Geotechnical Engineering*, no. 2, (St. Luois, Missouri), 2013. (Cited on page 25.)

[56] H. G. Poulos, "Behavior of laterally loaded piles: II-Pile groups," *Journal of the Soil Mechanics and foundations Division*, vol. 97, no. 5, pp. 711–731, 1971. (Cited on page 25.)

[57] H. G. Poulos, "Approximate computer analysis of pile groups subjected to loads and ground movements," *International Journal for Numerical and Analytical Methods in Geomechanics*, vol. 23, pp. 1021–1041, Aug. 1999. (Cited on page 25.)

[58] K. Kubo, "Experimental study of the behaviour of laterally loaded piles," in *Proceeding of the 6th International Conference on Soil Mechanics and Foundation Engineering*, pp. 275–279, 1965. (Cited on page 25.)

[59] K. Awoshika, *Analysis of foundation with widely spaced piles.* Ph.d. thesis, 1971. (Cited on page 25.)

[60] M. A. Sherif, I. Ishibashi, and C. D. Lee, "Earth pressures against rigid retaining walls," *Journal of the Geotechnical Engineering Division*, vol. 108, no. 5, pp. 679–695, 1982. (Cited on page 26.)

[61] R. Jardine and F. Chow, *New design methods for off-shore piles.* London: Marine Technology Directorate, mtd public ed., 1996. (Cited on page 26.)

[62] H. Mroueh and I. Shahrour, "Numerical analysis of the response of battered piles to inclined pullout loads," *International Journal for Numerical and Analytical Methods in Geomechanics*, vol. 33, no. December 2008, pp. 1277–1288, 2009. (Cited on pages 27, 1 and 23.)

[63] I. Shahrour and I. Juran, "Seismic behaviour of micropile systems," *Ground Improvement*, vol. 8, pp. 109–120, Jan. 2004. (Cited on pages 27 and 1.)

[64] Z. Cheng and B. Jeremić, "Numerical modeling and simulation of pile in liquefiable soil," *Soil Dynamics and Earthquake Engineering*, vol. 29, pp. 1405–1416, Nov. 2009. (Cited on pages 27 and 1.)

[65] Y. F. Dafalias and M. T. Manzari, "Simple Plasticity Sand Model Accounting for Fabric Change Effects," *Journal of Engineering Mechanics*, vol. 130, no. 6, pp. 622 – 634, 2004. (Cited on page 27.)

[66] F. Zhang, K. Okawa, and M. Kimura, "Centrifuge model test on dynamic behavior of group-pile foundation with inclined piles and its numerical simulation," *Frontiers of Architecture and Civil Engineering in China*, vol. 2, pp. 233–241, July 2008. (Cited on pages 27 and 33.)

[67] T. Nakai, "An isotropic hardening elasto-plastic model for sand considering the stress path dependency in three-dimensional stresses," *Soils and Foundations*, vol. 29, no. 1, pp. 119–37, 1989. (Cited on page 27.)

[68] M. Novak and F. Aboul-Ella, "Impedance functions of piles in layered media," *Journal of Engineering Mechanics*, vol. 104, no. 3, pp. 289–304, 1978. (Cited on page 27.)

[69] H. G. Poulos and E. H. Davis, *Pile foundation analysis and design*. Wiley (John) & Sons, Limited, 1980. (Cited on pages 27 and 6.)

[70] S. M. Mamoon, A. M. Kaynia, and P. K. Banerjee, "Frequency domain dynamic analysis of piles and pile groups," *Journal of Engineering Mechanics*, vol. 116, pp. 2237–2257, 1990. (Cited on page 27.)

[71] G. Gazetas and N. Makris, "Dynamic pile-soil-pile interaction. Part I: analysis of axial vibration.," *Earthquake Engineering and Structural Dynamics*, vol. 20, pp. 115–132, 1991. (Cited on page 27.)

[72] N. Makris and G. Gazetas, "Dynamic pile-soil-pile interaction. Part II: lateral and seismic response," *Earthquake Engineering and Structural Dynamics*, vol. 21, pp. 145–162, 1992. (Cited on page 27.)

[73] A. Giannakou, N. Gerolymos, and G. Gazetas, "On the dynamics of inclined piles," in *Proceedings of the 10th International Conference on Piling and Deep Foundations*, (Amsterdam, Netherlands), pp. 286–295, 2006. (Cited on page 27.)

[74] L. A. Padrón, J. J. Aznárez, O. Maeso, and A. Santana, "Dynamic stiffness of deep foundations with inclined piles," *Earthquake Engineering & Structural Dynamics*, vol. 39, no. 12, pp. 1343–1367, 2010. (Cited on page 27.)

[75] M. McVay, C. Hays, and M. Hoit, "Development of a coupled bridge superstructure-foundation finite element code," tech. rep., Florida Department of Transportation by the University of Florida, 1996. (Cited on page 27.)

[76] R. Nova and L. Montrasio, "Settlements of shallow foundations on sand," *Geotéchnique*, vol. 41, no. 2, pp. 243–256, 1991. (Cited on pages 28, 29, 1 and 9.)

[77] M. Pender, L. Wotherspoon, N. M. Sa'don, and R. Orense, "Macro Element for Pile Head Cyclic Lateral Loading," in *Special Topics in Earthquake Geotechnical Engineering. Springer Netherlands* (M. A. Sakr and A. Ansal, eds.), vol. 16 of *Geotechnical, Geological and Earthquake Engineering*, pp. 129–145, Dordrecht: Springer Netherlands, 2012. (Cited on pages 28 and 29.)

[78] R. Paolucci, "Simplified Evaluation of Earthquake-Induced Permanent Displacements of Shallow Foundations," *Journal of Earthquake Engineering*, vol. 1, pp. 563–579, July 1997. (Cited on pages 29 and 1.)

[79] C. Cremer, A. Pecker, and L. Davenne, "Cyclic macro-element for soil-structure interaction: material and geometrical non-linearities," *International Journal for Numerical and Analytical Methods in Geomechanics*, vol. 25, pp. 1257–1284, Nov. 2001. (Cited on pages 29 and 1.)

[80] S. Grange, P. Kotronis, and J. Mazars, "A macro-element to simulate 3D soil-structure interaction considering plasticity and uplift," *International Journal of Solids and Structures*, vol. 46, no. 20, pp. 3651–3663, 2009. (Cited on pages 29 and 9.)

[81] C. Chatzigogos, a. Pecker, and J. Salençon, "Macroelement modeling of shallow foundations," *Soil Dynamics and Earthquake Engineering*, vol. 29, pp. 765–781, May 2009. (Cited on page 29.)

[82] M. Shirato, R. Paolucci, T. Kouno, S. Nakatani, J. Fukui, R. Nova, and C. di Prisco, "Numerical Simulation of Model Tests of Pier-Shallow Foundation Systems Subjected to Earthquake Loads Using an Elasto-Uplift-Plastic Macro Element," *Soils and Foundations*, vol. 48, no. 5, pp. 693–711, 2009. (Cited on page 29.)

[83] D. Salciarini and C. Tamagnini, "A hypoplastic macroelement model for shallow foundations under monotonic and cyclic loads," *Acta Geotechnica*, vol. 4, pp. 163–176, Apr. 2009. (Cited on pages 29, 1 and 16.)

[84] G. Cocchetti, C. di Prisco, A. Galli, and R. Nova, "Soil-pipeline interaction along unstable slopes: a coupled three-dimensional approach. Part 1: Theoretical formulation," *Canadian Geotechnical Journal*, vol. 46, pp. 1289–1304, Nov. 2009. (Cited on page 29.)

[85] E. Taciroglu, C. Rha, and J. W. Wallace, "A Robust Macroelement Model for Soil - Pile Interaction under Cyclic Loads," *Journal of geotechnical and geoenvironmental engineering*, vol. 132, no. 10, pp. 1304–1314, 2006. (Cited on page 29.)

[86] C. Rha and E. Taciroglu, "Coupled Macroelement Model of Soil-Structure Interaction," *Journal of Engineering Mechanics*, vol. 133, no. 12, pp. 1326–1340, 2007. (Cited on page 29.)

[87] R. W. Boulanger, C. J. Curras, S. Member, B. L. Kutter, D. W. Wilson, A. Member, and A. Abghari, "Seismic soil-pile-structure interaction experiments and analyses," *Journal of Geotechnical and Geoenvironmental Engineering*, vol. 125, no. 9, pp. 750–759, 1999. (Cited on page 29.)

[88] C. J. Curras, R. W. Boulanger, B. L. Kutter, and Daniel W. Wilson, "Dynamic experiments and analyses of a pile-group-supported structure," *Journal of Geotechnical and Geoenvironmental Engineering*, vol. 127, no. 7, pp. 585–596, 2001. (Cited on page 29.)

[89] N. Gerolymos and G. Gazetas, "Development of Winkler model for static and dynamic response of caisson foundations with soil and interface nonlinearities," *Soil Dynamics and Earthquake Engineering*, vol. 26, pp. 363–376, May 2006. (Cited on page 29.)

[90] N. Gerolymos and G. Gazetas, "Static and dynamic response of massive caisson foundations with soil and interface nonlinearities - validation and results," *Soil Dynamics and Earthquake Engineering*, vol. 26, pp. 377–394, May 2006. (Cited on page 29.)

[91] Varun, *A Non-linear Dynamic Macroelement for Soil Structure Interaction Analyses of Piles in Liquefiable Sites*. PhD thesis, 2010. (Cited on page 29.)

[92] T. G. Davies and M. Budhu, "Non-linear analysis of laterally loaded piles in heavily overconsolidated clays," *Géotechnique*, vol. 36, pp. 527–538, Jan. 1986. (Cited on page 29.)

[93] N. Gerolymos, A. Zafeirakos, and C. Souliotis, "Insight to Failure Mechanisms of Caisson Foundations under Combined Loading: A Macro-element Approach," in *Second International Conference on Perfromance-based Design in Earthquake Geotechnical Engineering*, no. 11, pp. 1267–1276, 2012. (Cited on page 29.)

[94] António Araújo Correia, *A Pile-Head Macro-Element Approach to Seismic Design of*. PhD thesis, Università degli Studi di Pavia & Istituto Universitario di Studi Superiori, 2011. (Cited on page 29.)

[95] D. Assimaki, W. Li, and a. Kalos, "A Wavelet-based Seismogram Inversion Algorithm for the In Situ Characterization of Nonlinear Soil Behavior," *Pure and Applied Geophysics*, vol. 168, pp. 1669–1691, Nov. 2010. (Cited on page 1.)

[96] A. J. Brennan, N. I. Thusyanthan, and S. P. G. Madabhushi, "Evaluation of Shear Modulus and Damping in Dynamic Centrifuge Tests," *Journal of Geotechnical and Geoenvironmental Engineering*, vol. 131, no. 12, pp. 1488–1497, 2005. (Cited on pages 1, 2, 7, 8 and 11.)

[97] M. Zeghal and A. Elgamal, "Analysis of Site Liquefaction Using Earthquake Records," *Journal of Geotechnical Engineering*, vol. 120, no. 6, pp. 996–1017, 1994. (Cited on pages 1, 7 and 8.)

[98] K. Pitilakis, E. Kirtas, A. Sextos, and M. Bolton, "Validation by centrifuge testing of numerical simulations for soil-foundation-structure systems," in *13th World Conference on Earthquake Engineering*, no. 2772, (Vancouver, Canada), 2004. (Cited on page 1.)

[99] A. Elgamal, Z. Yang, T. Lai, B. L. Kutter, and D. W. Wilson, "Dynamic Response of Saturated Dense Sand in Laminated Centrifuge Container," *Journal of Geotechnical and Geoenvironmental Engineering*, vol. 131, no. 5, pp. 598–609, 2005. (Cited on page 1.)

[100] R. Conti and G. M. B. Viggiani, "Evaluation of Soil Dynamic Properties in Centrifuge Tests," *Journal of Geotechnical and Geoenvironmental Engineering*, vol. 138, no. 7, pp. 850–859, 2012. (Cited on page 2.)

[101] A. N. Schofield and X. Zeng, "Design and performance of an equivalent-shear-beam container for earthquake centrifuge modelling," *Geotechnique*, vol. 46, no. 1, pp. 83–102, 1996. (Cited on pages 2 and 9.)

[102] B. Teymur and S. P. G. Madabhushi, "Experimental study of boundary effects in dynamic centrifuge modelling," *Géotechnique*, vol. 53, no. 7, pp. 655 –663, 2003. (Cited on pages 2 and 9.)

[103] E. Delfosse-Ribay, I. Djeran-Maigre, R. Cabrillac, and D. Gouvenot, "Shear modulus and damping ratio of grouted sand," *Soil Dynamics and Earthquake Engineering*, vol. 24, pp. 461–471, Aug. 2004. (Cited on pages 2 and 5.)

[104] H. Seed and I. Idriss, "Soil moduli and damping factors for dynamic response analyses," tech. rep., Univ. of California, Berkeley, California., 1970. (Cited on page 5.)

[105] B. O. Hardin and F. E. J. Richart, "Elastic wave velocities in Granular soils," *Journal of Soil Mechanics and Foundations Divisions, Proceedings of the American Society of Civil Engineers*, vol. 89, no. SM1, pp. 33–65, 1963. (Cited on page 5.)

[106] T. Iwasaki, F. Tatsuoka, Y. Takagi, and F. Tatsouka, "Hysteretic damping of sands under cyclic loading and its relation to shear modulus," *Soils and Foundations*, vol. 18, no. 1, pp. 39–56, 1978. (Cited on pages 5, 13 and 14.)

[107] B. Hardin, V. Drnevich, J. Wang, and C. Sams, "Resonant column testing at pressures up to 3.5 Mpa (500 psi)," *Dynamic Geotechnical Testing II*, vol. ASTM STP 1, pp. 222–233, 1994. (Cited on pages 5, 14 and 17.)

[108] Gaudin C., "Détermination de l'état de contrainte geostatique des massifs sableux centrifugés par des essais pénétrométriques," *Raport de DEA de l'école Centrale de Nantes et du Laboratoire Central de Ponts et Chaussées de Nantes*, p. 124, 1999. (Cited on page 5.)

[109] J. M. R. Wilson and M. D. Bolton, "Discussion: An experimental and theoretical comparison between static and dynamic torsional soil tests," *Géotechnique*, vol. 40, pp. 659–664, Jan. 1990. (Cited on page 13.)

[110] S. L. Kramer, *Geotechnical Earthquake Engineering*. New Jersey: Prentice Hall, 1996. (Cited on page 13.)

[111] T. Wichtmann, A. Niemunis, and T. Triantafyllidis, "Strain accumulation in sand due to cyclic loading : Drained cyclic tests with triaxial extension," *Soil Dynamics and Earthquake Engineering*, vol. 27, pp. 42–48, 2007. (Cited on page 13.)

[112] T. Kokusho, "The Japanese Geotechnical Society NII-Electronic Library Service," *Soils Found*, vol. 20, no. 2, pp. 45–60, 1980. (Cited on page 14.)

[113] I. Isao, "Discussion of "Effect of Soil Plasticity on Cyclic Response" by M. Vucetic and R. Dobry," *Journal of Geotechnical Engineering*, vol. 118, no. 5, pp. 830–832, 1992. (Cited on page 14.)

[114] F. Tatsuoka, T. Iwasaki, and Y. Takagi, "Hysteretic damping of sands under cyclic loading and its relation to shear modulus," *Soils And Foundations*, vol. 18, no. 2, pp. 25–40, 1978. (Cited on page 17.)

[115] G. Lanzo and M. Vucetic, "Effect of soil plasticity on damping ratio at small cyclic strains," *Soils And Foundations*, vol. 39, no. 4, pp. 131–141, 1999. (Cited on page 18.)

[116] R. L. Mokwa and J. M. Duncan, "Rotational Restraint of Pile Caps during Lateral Loading," *Journal of Geotechnical and Geoenvironmental Engineering*, vol. 129, no. 9, pp. 829–837, 2003. (Cited on page 5.)

[117] J. L. Liu, Z. L. Yuan, and K. P. Zhang, "Cap-pile-soil interaction of bored pile groups," in *Proc., 11th Int. Conf. on Soil Mech. and Found. Engrg.*, (Netherlands), pp. 1433–1436, 1985. (Cited on page 6.)

[118] C. I. Beatty, "Lateral test on pile groups," *Foundation Facts*, vol. 6, no. 1, pp. 18–21, 1970. (Cited on page 6.)

[119] Z. Zafir and W. E. Vanderpool, "Lateral response of large diameter drilled shafts: I-15/US 95 load test program," in *Proceedings of the 33rd Engineering Geology and Geotechnical Engineering Symposium*, (University of Nevada, Reno), pp. 161–176, 1998. (Cited on page 6.)

[120] C. M. Harris and A. G. Piersol, *Harris' shock and vibration handbook*. New York: McGraw-Hill, 2002. (Cited on page 8.)

[121] S. Escoffier, "Seismic and sinusoidal tests on pile group," tech. rep., IFSTTAR, 2011. (Cited on page 17.)

[122] O. Mohr, "Welche Umstände bedingen die Elastizitätsgrenze und den Bruch eines Materials?," *Zeitschrift des Vereins Deutscher Ingenieure*, vol. 46, pp. 1524–1530, 1900. (Cited on page 1.)

[123] D. Drucker and W. Prager, "Soil mechanics and plastic analysis or limit design," *Quarterly of applied mathematics*, vol. 10, no. 2, pp. 157–165, 1952. (Cited on page 1.)

[124] Y. F. Dafalias, "Bounding Surface Plasticity: I: Mathematical Foundation and Hypoplasticity," *Journal of Engineering Mechanics*, vol. 112, no. 9, pp. 966–987, 1986. (Cited on pages 1 and 3.)

[125] J. Bardet, "Hypoplastic model for sands," *Journal of engineering mechanics*, vol. 116, no. 9, pp. 1973–1994, 1990. (Cited on page 1.)

[126] D. Kolymbas, "An outline of hypoplasticity," *Archive of applied mechanics*, vol. 61, no. 3, pp. 143–151, 1991. (Cited on page 1.)

[127] P.-A. von Wolffersdorff, "A hypoplastic relation for granular materials with a predefined limit state surface," *Mechanics of Cohesive-Frictional Materials*, vol. 1, no. 4, pp. 251–271, 1996. (Cited on page 1.)

[128] F. Darve, *Une formulation incrémentale des lois rhéologiques. Application aux sols.* PhD thesis, INP Grenoble, 1978. (Cited on pages 2 and 17.)

[129] C. Tamagnini, G. Viggiani, and R. Chambon, *A review of two different approaches to hypoplasticity.* Springer Berlin Heidelberg, 2000. (Cited on pages 2 and 17.)

[130] B. O. Drnevich and V. P. Hardin, "Shear modulus and damping in soils: Design equations and curves," *Journal of the Soil Mechanics and Foundations Division*, vol. 98, pp. 667–692, 1972. (Cited on page 2.)

[131] T. Iwasaki and F. Tatsuoka, "Effects of Grain Size and Grading on Dynamic Shear Moduli of Sands," *Soils and Foundations*, vol. 17, no. 3, pp. 19–35, 1977. (Cited on page 2.)

[132] H. S. Yu, *Yu H S. Plasticity and geotechnics.* Springer, 2006. (Cited on page 3.)

[133] Y. Dafalias and L. Herrmann, *Bounding surface formulation of plasticity.* John Wiley and Sons, Ltd., 1982. (Cited on page 3.)

[134] J. P. Bardet, "Bounding surface plasticity model for sands," *Journal of engineering mechanics*, vol. 112, no. 11, pp. 1198–1217., 1986. (Cited on page 3.)

[135] Abaqus/Standard, *Abaqus 6.10 Documentation (SIMULIA Abaqus 6.10).* Dassault Systèmes, 2010. (Cited on pages 11 and 2.)

[136] A. Guefrech, G. Rault, N. Chenaf, L. Thorel, J. Garnier, and A. Puech, "Proceeding of the 7th International Conference on Offshore Site Investigation and Geotechnics," in *Stability of Cast in Place Piles in Sand under Axial Cyclic Loading*, (Royal Geographical Society, London, UK), pp. 239–334, 2012. (Cited on pages 11 and 12.)

[137] L. Montrasio and R. Nova, "Settlements of shallow foundations on sand: geometrical effects," *Settlements of shallow foundations on sand: geometrical effects*, vol. 47, no. 1, pp. 49–60, 1991. (Cited on page 1.)

[138] S. Grange, P. Kotronis, and J. Mazars, "A macro-element to simulate dynamic Soil-Structure Interaction," *Engineering Structures*, vol. 31, pp. 3034–3046, Dec. 2009. (Cited on pages 1 and 9.)

[139] C. Cremer, a. Pecker, and L. Davenne, *Modelling of Nonlinear Dynamic Behaviour of a Shallow Strip Foundation With Macro-Element*, vol. 6. Apr. 2002. (Cited on page 1.)

[140] FEDEASLab, *A Matlab Toolbox for Nonlinear Structural Response Simulations*. Department of Civil and Environmental Engineering University of California, Berkeley. (Cited on page 19.)

[141] M. Sadek and I. Shahrour, "Influence of the head and tip connection on the seismic performance of micropiles," *Soil Dynamics and Earthquake Engineering*, vol. 26, no. 5, pp. 461–468, 2006. (Cited on pages 1 and 33.)

[142] C. Di Prisco, A. Galli, and M. Vecchiotti, "Cyclic and dynamic mechanical behaviour of shallow foundations on granular deposits," *Coupled Site and Soil-Structure Interaction Effects with Application to Seismic Risk Mitigation NATO Science for Peace and Security Series C: Environmental Security*, pp. 139–150, 2009. (Cited on page 2.)

[143] G. Gazetas, "Seismic response of end-bearing piles," *Soil Dynamics and Earthquake Engineering*, vol. 3, pp. 89–93, 1984. (Cited on page 33.)

[144] K. Fan, G. Gazetas, A. Kaynia, E. Kausel, and S. Ahmad, "Kinematic seismic response of single piles and pile groups," *Journal of Geotechnical Engineering*, vol. 117, pp. 1860–1879, 1991. (Cited on page 33.)

[145] S. Nikolaou and G. Gazetas, "Seismic design procedure for kinematically loaded piles," in *Soil Mech. Found. Engng, hamburg, Special Volume, Earthquake geotechnical engineering*, pp. 253–260, 1997. (Cited on page 33.)

[146] K. J. Bentley and M. H. E. Naggar, "Numerical analysis of kinematic response of single piles," *Canadian Geotechnical Journal*, vol. 37, no. 6, pp. 1368–1382, 2000. (Cited on page 33.)

[147] S. Nikolaou, G. Mylonakis, G. Gazetas, and T. Tazoh, "Kinematic pile bending during earthquakes: analysis and field measurements," *Geotechnique*, vol. 51, no. 5, pp. 425–440, 2001. (Cited on page 33.)

[148] N. Deng, R. Kulesza, and F. Ostadan, "Seismic soil-pile group interaction analysis of a battered pile group," in *4th International Conference on Earthquake Geotechnical Engineering*, (Thessaloniki), 2007. (Cited on page 33.)